Imperial College London
Department of Electrical and Electronic Engineering

Resilience-Oriented Control and Communication Framework for Cyber-Physical Microgrids

Pudong Ge

Submitted in part fulfilment of the requirements for the degree of
Doctor of Philosophy in Electrical Engineering of Imperial College London and
the Diploma of Imperial College London, October 2023

Declaration of Originality

I hereby declare that the material contained within this thesis is my own work. Any ideas or quotations from the work of other people, published or otherwise, are fully acknowledged through standard referencing practices of the discipline.

Pudong Ge

Copyright Declaration

Pudong Ge

Abstract

Climate change drives the energy supply transition from traditional fossil fuel-based power generation to renewable energy resources. This transition has been widely recognised as one of the most significant developing pathways promoting the decarbonisation process toward a zero-carbon and sustainable society. Rapidly developing renewables gradually dominate energy systems and promote the current energy supply system towards decentralisation and digitisation. The manifestation of decentralisation is at massive dispatchable energy resources, while the digitisation features strong cohesion and coherence between electrical power technologies and information and communication technologies (ICT). Massive dispatchable physical devices and cyber components are interdependent and coupled tightly as a cyber-physical energy supply system, while this cyber-physical energy supply system currently faces an increase of extreme weather (e.g., earthquake, flooding) and cyber-contingencies (e.g., cyberattacks) in the frequency, intensity, and duration. Hence, one major challenge is to find an appropriate cyber-physical solution to accommodate increasing renewables while enhancing power supply resilience.

The main focus of this thesis is to blend centralised and decentralised frameworks to propose a collaboratively centralised-and-decentralised resilient control framework for energy systems i.e., networked microgrids (MGs) that can operate optimally in the normal condition while can mitigate simultaneous cyber-physical contingencies in the extreme condition. To achieve this, we investigate the concept of "*cyber-physical resilience*" including four phases, namely prevention/upgrade, resistance, adaption/mitigation, and recovery. Throughout these stages, we tackle different cyber-physical challenges under the concept of microgrid ranging from a centralised-to-decentralised transitional control framework coping with cyber-physical out of service, a cyber-resilient distributed control methodology for networked MGs, a UAV assisted post-contingency cyber-physical service restoration, to a fast-convergent distributed dynamic state estimation algorithm for a class of interconnected systems.

Acknowledgements

I would like to express my sincere gratitude to my supervisor, Dr. Fei Teng, who have guided me throughout these four years, for his invaluable insight, patience, and suggestions.

Furthermore, I would like to thank all those professors whom I have had the chance to visit over the years for their generous hospitality, and with whom I have been able to collaborate. More specifically, I would like to thank Dr. Boli Chen from University College London for his kind help and patience in explanations of control theory. I would like to thank Prof. Tim Green for his assistance on the experimental validation of my work in the Maurice Hancock Smart Energy Laboratory. I would like to thank Prof. Anna Korre and Dr. Michel-Alexandre Cardin from Energy Futures Lab for their valuable research advice on energy system analysis. I would like to thank Prof. Mingyang Sun from Zhejiang University for hosting me during a hard situation of Covid-19, Prof S. Y. Ron Hui, whom I have had the pleasure of visiting at Nanyang Technological University, Singapore. I would also like to thank Prof. Shiyan Hu from University of Southampton, Prof. Charalambos Konstantinou from KAUST (King Abdullah University of Science and Technology) and Prof. Peng Li from Harbin Institute of Technology, Shenzhen for their help, advice, and collaboration during my research life.

Special thanks go to Mr. Cesare Caputo and all other colleagues from Energy Futures Lab that give me much support on my research; Dr. Zhongda Chu, Dr. Yue Zhu, Dr. Mengxiang Liu, Mr. Wangkun Xu and all other colleagues that help me much on research and life from Control and Power Research Group at Imperial College London; Dr. Huawei Yuan and Mr. Hin Sang Raymond Lam from Nanyang Technological University for the collaboration and help during my visiting to Singapore.

A special thank goes to my family, who have supported me through all of my decisions, and who have been there for me throughout. I am particularly thankful to my wife, Mrs. Zhi Qiu, for her great support on my PhD study.

Contents

Nomenclature

$\mathcal{HS}$	Hilbert-Schmidt
3GPP	Third Generation Partnership Project
5G	the Fifth-Generation (technology standard for cellular networks)
ACPE	Adverse Cyber-Physical Effect
AC	Alternating Current
BF-NK	Bivariate Feedthrough Non-asymptotic Kernel
BS-UAV	Base Station Unmanned Aerial Vehicle
BS	Base Station
C2C	Controller-to-Controller
CERTS	the Consortium for Electric Reliability Technology Solutions
CIGRE	International Council on Large Electric Systems
CN	Complementary Neighbouring
CPS	Cyber-Physical System
D2D	Device-to-Device
DAPI	Distributed Averaging Proportional Integral
DC	Direct Current

DER	Distributed Energy Resource
DG	Distributed Generator
DMPC	Distributed Model Predictive Control
DoS	Denial of Service
EMS	Energy Management System
ESKBF	Extended State Kalman-Bucy Filter
EV	Electric Vehicle
FDD	Frequency Division Duplexing
FDI	False Data Injection
FTSM	Fast Terminal Sliding Mode
ICT	Information and Communication Technology
LCF	Inductor-Capacitor Filter
LTE	Long-Term Evolution
LTI	Linear Time-Invariant
MER	Mobile Energy Resource
MGCC	Microgrid Centre Controller
MG	Microgrid
MIMO	Multi-Input Multi-Output
MINLP	Mixed-Integer Non-Linear Programming
MPC	Model Predictive Control
NREL	National Renewable Energy Laboratory

PHIL	Power-Hardware-In-the-Loop
PIC	Proportional Integral Control
PoC	Persistency-of-Communication
PoDF	Persistency-of-Data-Flow
PV	Photovoltaic
QoS	Quality-of-Service
R-UAV	Relay Unmanned Aerial Vehicle
SCADA	Supervisory Control and Data Acquisition
SISO	Single-Input Single-Output
SNR	Signal-to-Noise Ratio
UAV	Unmanned Aerial Vehicle

List of Figures

List of Tables

List of Algorithms

Chapter 1

Introduction

1.1 Background and Motivation

1.1.1 Background

Climate change, a worldwide scientific consensus [8], drives the energy supply transition from traditional fossil fuel based power generation to renewable energy resources. This transition has been widely recognised as one of the most significant developing pathways to zero-carbon societies [9]. Rapidly developing renewable energy resources, penetrating into either transmission or distribution level, promotes the current energy supply system towards decentralisation and digitisation [10]. The manifestation of decentralisation is at massive dispatchable energy resources, both source-side distributed generator (DG) and load-side consumer participation, while the digitisation expresses itself by strong cohesion and coherence between electrical power technologies and information and communication technologies (ICT). Hence, massive dispatchable physical devices and cyber components enabling intelligent control are interdependent and coupled tightly as a cyber-physical energy supply system. The cyber components are powered by physical devices but provide intelligent logic to guarantee the whole energy system operations.

On the other hand, climate change has led to occurrence of severe weather events, which

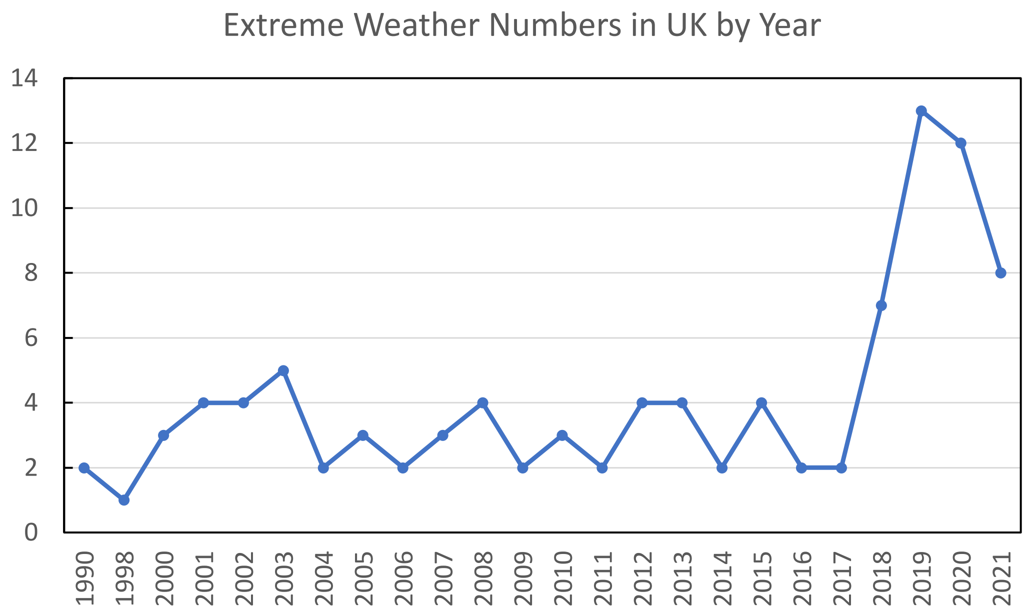

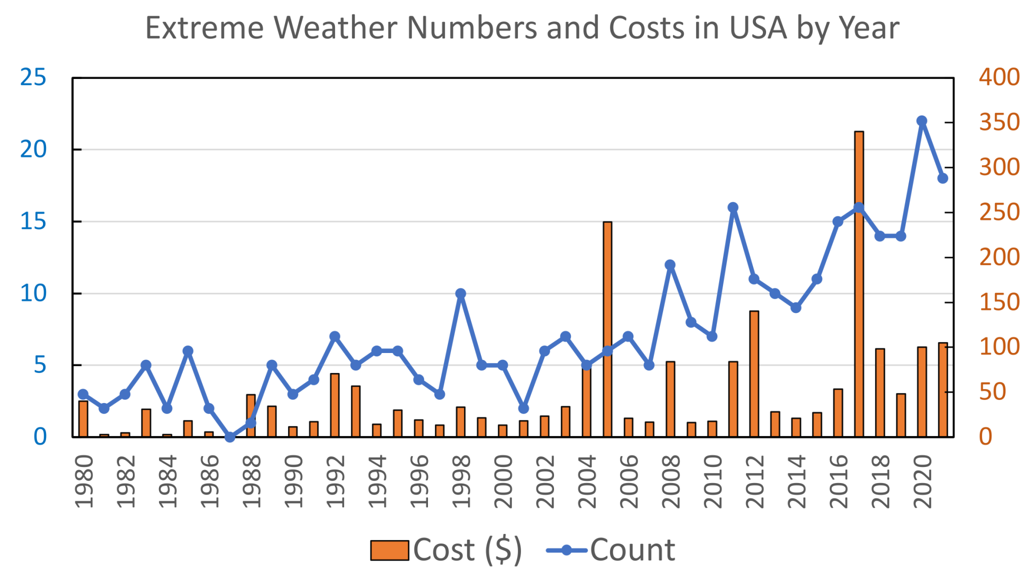

Figure 1.1: Numbers and costs of extreme events in UK and USA

are considered main causes of power grid infrastructure and communication facility damages, resulting in huge economic losses. In fact, severe weather caused approximately 80% of the large-scale power outage [11], and climate change has a trend of an increase in the frequency, intensity and duration of severe weather events [12]. As shown in Figure 1.1, both UK and USA witnessed a significantly increasing extreme weather events that causes severe damages. Due to the growing integration of cyber and physical layers of energy systems, the events that simultaneously affect both physical devices and cyber components lead to more significant damages on the energy supply and prolonged restoration duration. For instance, an ice storm in 2008 damaged over 36 thousand power transmission lines and 20 thousand mobile base stations in China [13], causing blackout for 200 million people, and direct cost was estimated to be more than 2.2 billion dollars.

Increasing extreme weather events poses huge threats to power supply infrastructures, both physical devices and cyber components, thereby leading to undesired power interruptions or blackouts [14]. Hence, the concept of resilience under extreme events has been gradually recognised as a key requirement for future energy systems [15–17]. According to NREL, a resilient power grid withstands, responds to, and recovers rapidly from major power disruptions as its designers, planners, and operators anticipate, prepare for, and adapt to changing grid conditions [18], while CIGRE defines power system resilience as the ability to limit the extent, severity, and duration of system degradation following an extreme event [19]. Considering the carbon neutrality target and the cyber-physical coupling, the concept of "*cyber-physical zero-carbon resilience*" should be analysed and emphasised in the future energy system. In this context, Section 1.1.2 will introduce the climate effects on both cyber and physical layers and Section 1.1.3 will analyse the resilience challenges.

1.1.2 Climate Effect

To provide a comprehensive and clear summary of the adverse effects on the future cyber-physical energy system, we have collected data from [20–22] and expressed them in terms of affected consumers by a time-sequential graphical format as Figure 1.2, which emphasises the power outage effects, and there is a clear increasing trend in the last decade for more frequent and severe (circle number and area) extreme weather events and the resulting widespread power outages.

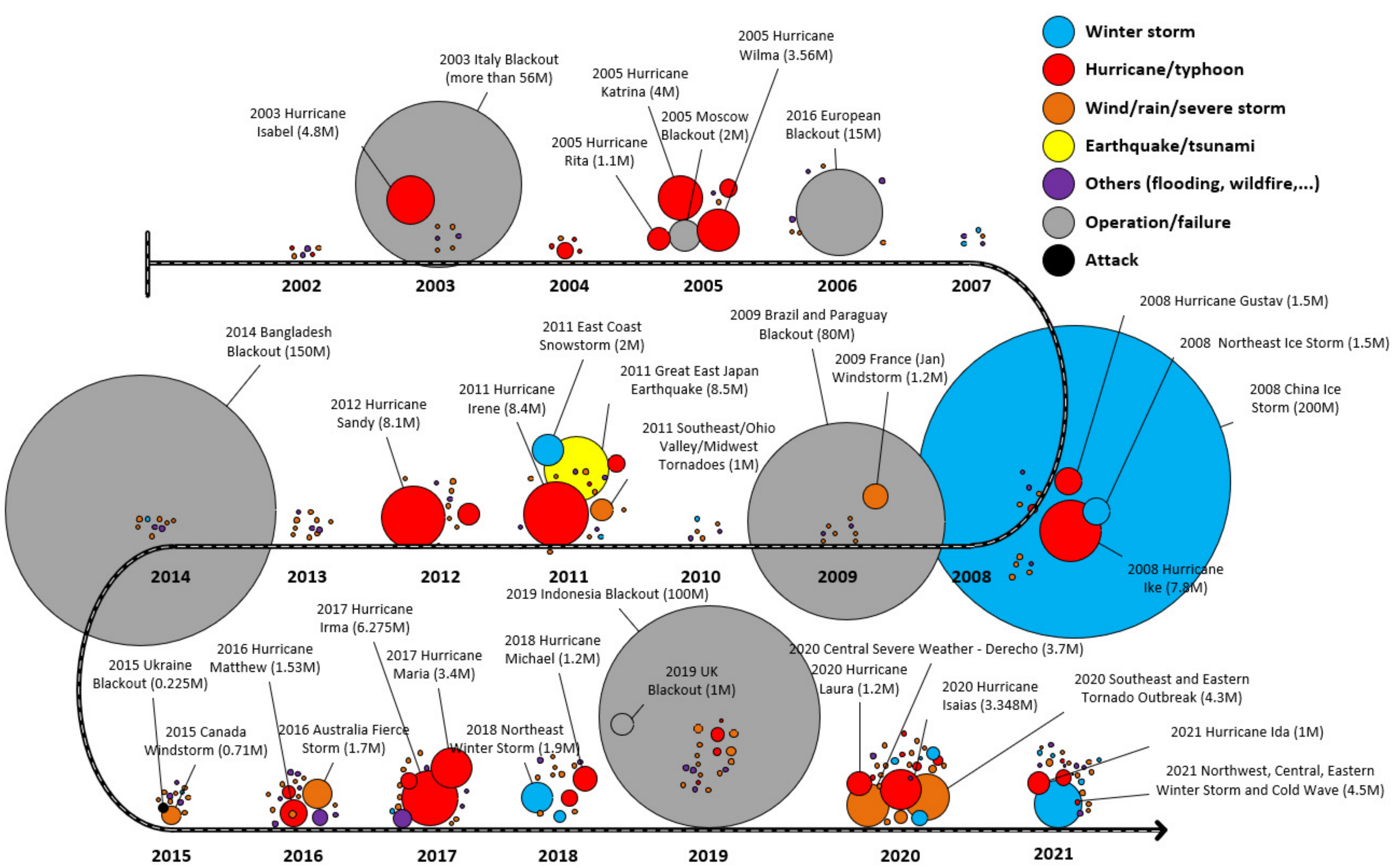

Figure 1.2: Worldwide examples of extreme events that affected energy systems (M: million)

Table 1.1: Cyber Climate Effects of Extreme Weather Events

Event	**Cyber Effects/Communication Damage**
Hurricane Katrina (Aug 2005) [23]	Many of the problems that arose developed from inadequate planning and back-up communication systems at various levels.
Hurricane Rita (Sep 2005) [24]	Damage to the entire region's electrical and communications infrastructure was severe, and authorities warned returning residents that restoration of services to some areas would take weeks to months.
China Ice Storm (Jan 2008) [13]	Destroyed 35000 telephone poles and 20000 mobile phone base stations
Great East Japan Earthquake (Mar 2011) [25]	Many types of communications equipment are affected by the power failures and destruction of communication lines; first 4-day period after the disaster, service to many of the base stations and landlines was cut.
Hurricane Sandy (Oct 2012) [26]	Wired communication: flooding damaged power back-up equipment including onsite diesel generators and fuel pumps in their basements or first floor; most wireless base stations, placed on buildings roofs had no permanent gensets but standard power sockets at the ground to access portable generator.
Louisiana Flooding (Aug 2016) [27]	A cellular network outage complicated rescues over the affected area.
Central Severe Weather - Derecho (Aug 2020) [28]	Wind gusts of 100 to 110 mph were also estimated over a small area near Princeton, Illinois, where a 150-foot communications tower collapsed and numerous power poles were snapped.
Hurricane Elsa (Jul 2021) [29]	20 of the 98 Flow telecommunication sites in Barbados were damaged and were offline.

Without doubt, the energy transition benefits from all cyber systems [30], however, undesired damage or vulnerability could also be brought. The cyber-physical energy system so highly depends on the cyber systems that a damaged or corrupted cyber system could cause severe consequences or even a widespread blackout. Firstly, more frequent natural disasters could cause direct damage to ICT infrastructure. In addition, the complexity and growth of cyber systems could induce hardware/software failures that affect the normal operation. Moreover, expanding cyber-attack surfaces are exposed to the cyber world. Either damage, failure or cyberattacks will add challenges especially in extreme conditions such as restoration. Several extreme weather events are selected, and their effects on the cyber system or the communication infrastructure are reported in Table 1.1. It can be concluded that either wired communication lines or wireless cellular network is vulnerable during the extreme weather. For example, China Ice Storm in 2008 destroyed communication infrastructure (35000 telephone poles and 20000 mobile phone base stations) as well as power grid facilities (36740 high-voltage transmission lines, 8381 towers and 2018 transformer stations). Collapsed communication systems were a factor in the initial sluggish governmental response, leading to ineffective controls in many industries such as ineffective traffic controls on highways, crowd management in railway stations, much less the large-scale outage restoration. Although the adverse effects on communication systems have been reported, the corresponding cascading influence on the energy system operation has not been discussed widely. As the localised distributed energy resource integration and wireless communication base station installation [14], the interdependent effects will become closer and require further investigations.

Cyber-physical coupling caused by energy decentralisation and digitisation leads to symbiotic influences between physical energy systems and cyber communication systems. The cyber-physical interaction makes it difficult to actively respond to the extreme weather because the damaged communication infrastructure and system cannot provide sufficient information flow supporting the energy supply maintaining and recovery. Even if the communication infrastructure is intact and has full functionality, the power shortage under such event may lead to limited or even no communication services, which may, in turn, exaggerate the power shortage. To conclude, the main effects towards the energy system operation are three parts:

- The system operators may face the corrupted cyber condition without data communication (of SCADA/EMS) or substation automation services during restoration.

- New systems such as photovoltaics (PVs) or electric vehicles (EVs) that have developed or been developing may fall into corrupted cyber systems, and the cascading consequences on critical deviations on energy systems may be existing.

- The unknown cyber-physical behaviour of new connected systems may increase difficulty in restoration.

Hence, the resilience of energy system can not be achieved in physical network only, and the cyber-physical cooperative response and recovery strategy is required to enhance the cyber-physical zero-carbon resilience.

1.1.3 Challenges on Cyber-Physical Resilience

The energy system operators and ICT engineers have been making efforts to prepare for physical damage and ICT issues respectively. However, a fundamental challenge still remains for the cyber-physical energy system being sufficiently prepared for the extreme event that simultaneously affect the cyber and physical layers. In this context, the response to extreme events can be partitioned in terms of time periods: pre-event period, during the event, post-event period and after-event period, as shown in Figure 1.3. In this figure, the cyber-physical resilience level is divided into three statuses, i.e., safe and optimal, safe and non-optimal, as well as unsafe. The "safe and optimal" is the system operating in the normal condition securely and economically with both critical and non-critical loads, the "safe and non-optimal" means the power system operating in a suboptimal condition but maintaining critical energy supply, while the "unsafe" denotes the status where the power system cannot guarantee fundamental critically power supply. Hence, the aims of cyber-physical resilience enhancement are summarised in different phases:

- **Preventative Phase (Post-/Pre-Event Period)**

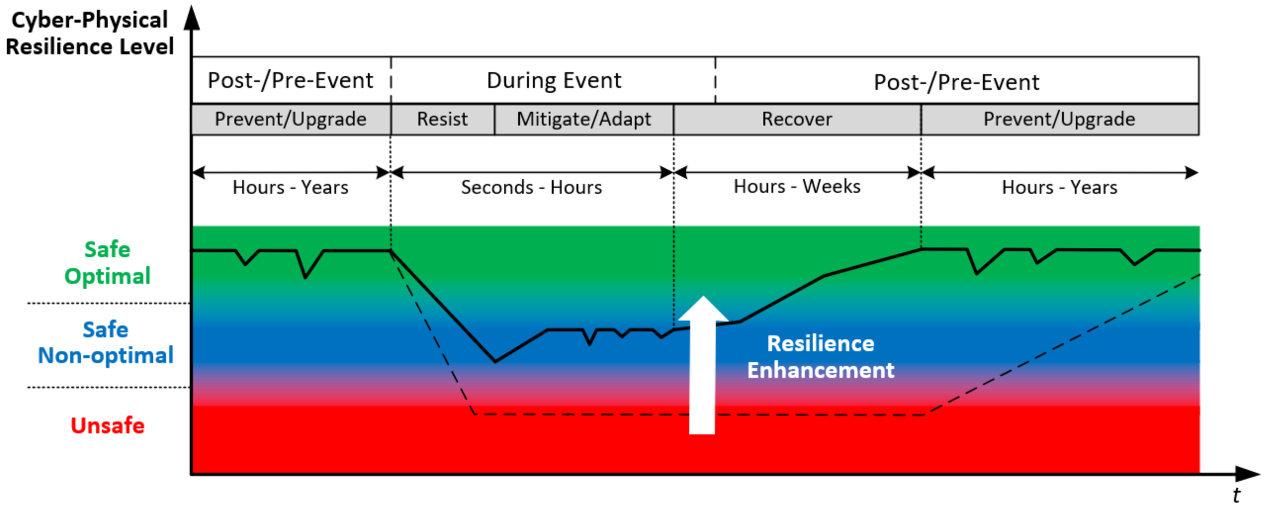

Figure 1.3: Resilience enhancement in terms of different periods

- Defensive preparation: optimise the cyber-physical operation to improve the cyber-physical redundancy, especially considering new connected systems such as PVs or EVs
- Active preparation: develop cyber-resilient back-up systems involving policymakers and regulators, especially regarding the necessary regulation for connected cyber-physical systems in order to avoid a collapse of the electrical system

- **Resistive Phase (During-Event Period)**
  - Fast cyber-physical detection: detect the occurrence of extreme events that damage the cyber components and physical devices by appropriate situational awareness
  - Fast cyber-physical isolation and localisation: cut down damaged parts to reduce the fault propagation and to ensure localised cyber-physical functionality

- **Adaptive/Mitigation Phase (During-Event Period)**
  - Regional critical power supply: utilise the pre-scheduled information and cyber-resilient back-up system to guide the cyber-physical response to maintain critical energy supply
  - Multi-regional service coverage: evaluate the limited cyber-physical service capability to enlarge the service range and to prolong the service duration

- **Recovery Phase (During-/Post-Event Period)**
  - Automatic restoration: well-organised restoration leveraging energy system digitisation tools and avoiding counter-acting of adverse cyber-physical effects
  - Manual restoration: efficient crew repair considering cyber-physical couplings
- **Upgrade Phase (Post-/Pre-Event Period)**
  - Model updating: update extreme event libraries considering behaviours and interactions between the increasing number of digital systems, and assess the possible risks
  - System expansion: evaluate the system redundancy margin to inform cyber-physical extension and renovation of stakeholders

The cyber-physical whole-system resilience enhancement should be implemented iteratively over time. In addition, such complex cyber-physical system requires common training of operators and specialists to adequately analyse, contain and restore the system after a power outage. The above four-phase[1] aims should be achieved by a series of appropriate methodologies that combines model-based and data-driven methods. How to reach these aims in detail through cyber-physical cooperation poses huge challenges to energy system operators and ICT engineers. Some key challenges can be summarised as

- Time-validity model synchronisation: how to utilise the information system to real-time update the cyber-physical energy system model in a high granularity?
- Fusion of model-based methods and data-driven algorithms: how does data-driven algorithms help cope with adverse cyber-physical effects?
- Cyber-physical validation platform: how to set up a comprehensive validation platform, by which the cyber-physical effects can be evaluated?
- Cyber-physical-social perspective: how does the human-in-the-loop (e.g., operator behaviours) affect the energy system operation?

[1]The preventative and upgrade phase is one phase of the post-/pre-event period.

The above analysis gives a grand overview of energy resilience from a cyber-physical perspective under the background of decarbonisation. However, this topic includes a wide array of research gaps needed to be bridged towards future resilient zero-carbon society. Therefore, this thesis only targets at a systematic solution of resilience-oriented communication and control framework using a concept of "microgrid (MG)" from a cyber-physical perspective because the distribution grids evolving into a combination of interconnected or networked MGs is gaining attention as a way to create a more flexible and resilient energy system [14, 31, 32]. Detailed problems that this thesis will focus on are outlined in Section 1.2 in terms of different phases as shown in Figure 1.3.

1.2 Problem Statement and Research Scope

This thesis analyses the limitations and issues of system operation, stability and resilience in high renewable penetrated networked MGs and proposes potential solutions from the perspective of grid resilience considering the inverter-based distributed energy resource (DER) control. In other words, the grid resilience is enhanced through an intelligent utilization of controllable grid-forming inverters without traditional diesel or synchronous generators considering a trend of future power electronics dominated power system.

The goal is to enhance grid resilience while maintaining system stability and cybersecurity when facing contingencies (e.g., natural disasters), system cyber-physical intrinsic disturbance (e.g., measurement noise and communication failure), and malicious cyberattacks (e.g., denial of service (DoS) attack) through a unified resilience-oriented control framework coordinating dispatchable DERs and cyber-layer communication devices. To achieve such a challenging objective for resilience, the secondary control of grid-forming inverter is considered based on the primary control while disregarding the tertiary control because of different characteristics and functions of such three control levels of grid-form inverters. To be more specific, these control levels differ in their (1) speed of response and the time frame in which they operate, and (2) infrastructure requirements (e.g., communication requirements) [33].

The foundation of this hierarchy, called primary control, must rapidly balance generation and demand, while sharing the load, synchronizing the AC voltage frequencies, and stabilizing their magnitudes. This is accomplished via decentralized droop control, where generators are controlled such that their power injections are proportional to their voltage frequencies and magnitudes. Droop controllers induce steady-state errors in frequency and voltage magnitudes, which are corrected in a secondary control layer. The operating point stabilized by primary and secondary control is scheduled in a tertiary control layer, to establish fair load sharing among the sources, or to dispatch the generation to minimize operational costs [34]. Owing to two reasons, i.e., the primary control only guaranteeing local stability and the tertiary economic dispatch may being impossible because of the major disruption, this thesis utilizes limited communication and energy resources to maintain critical power supply from a system-level perspective.

Based on above analyses, a wide array of research problems are identified below:

- The resilience against both damaged physical-layer power system infrastructures and nonfunctional cyber-layer information system devices in extreme contingencies after natural disasters, e.g., earthquake or flooding, is rarely studied. The interdependency of cyber-physical response could lead to inefficient mitigation and low resilience if we cannot cooperatively mitigate the adverse cyber-physical effects (ACPEs) in MGs. It is required to identify an appropriate information structure and communication system to enable the resilient control design of MGs, and further to form a resilient framework to efficiently and cooperatively cope with physical contingencies (e.g., earthquake, flooding, hurricane) and cyber contingencies (e.g., out-of-service information system). Considering existing centralised structure based on SCADA system, a blended centralised-and-decentralised framework is needed to make the best use of advanced communication and control structures. More specifically, it is necessary to design an efficient and cost-effective scheme from centralised framework to decentralised framework utilising collaborative transition of power electronic devices and flexible wireless communication technologies in response to cyber-physical contingencies.

- The resilience against co-existence of disturbances caused by different sources such as parameter perturbation and measurement noise in distributed controlled MG has not been fully mitigated. The existing methods tend to consider the multiple disturbances separately, while a systematic and unified disturbance modelling framework has yet to be developed. Moreover, with the uncertainty, plug-and-play operations in the multi-DG network may lead to frequent and significant fluctuations, which imposes a vast challenge on the fast restoration of the MG voltage. Under this circumstance, the convergence rate in the distributed control of MG has received increasing attention. The convergence of existing finite-time control protocol relies on its initial states, and the plug-and-play operation may cause unknown or diverse system initial states. For the MG system that emphasises on the plug-and-play capability, a novel control strategy for resilience enhancement is required to alleviate such impact by improving the convergence performance.

- The resilience against random packet loss existing in communication links of distributed controlled MGs has not been well investigated. Although existing distributed model predictive control (DMPC) can utilise prediction horizon to eliminate the effects of random packet loss, it will impose huge computation and communication burdens on the cyber solution. Hence, it is necessary to achieve a better trade-off between the control performance and communication and computation burden by appropriate event-triggered mechanism. At the same time, an efficient and non-continuous system state information acquisition and filtering, corresponding to an event-triggered mechanism, is also required to enhance the operational resilience against co-existence of multiple disturbances.

- The resilience against malicious data availability attacks among hierarchical communication links in MGs have not been systematically and theoretically mitigated. A hierarchical control framework adopted by networked MGs relies on more complex information network. On this occasion, besides the communication links among DGs and MGs, each DG involves information flows of (remote, e.g., telemetered) sensing and control actuation. Hence, cyberattacks could simultaneously occur on communication links for communication, measurement and actuation channels for intra-MG aggregation and distribution respectively. In particular, the adversary can erase the data sent to actuators or to block the sensor measurement. Existing mitigation is more focusing on the random communication failure and/or malicious DoS attack in the communication channels. The control performance can not been maintained if the data flow is blocked via multiple channels. This motivates a systematically preventative mitigation of DoS attacks for all data transmission channels of the information system and a resilience enhancement against multi-layer DoS for networked MGs within a hierarchical control framework.

- The digitisation tools in power systems provide more flexibility options in both cyber and physical aspects. The question is that how can we utilise the novel mobile (flexible) cyber-physical solutions to enhance grid resilience. Normally the post-contingency recovery mainly relies on crew repair, which may lead to long-term system operation under poor emergency communication. Thus, it is essential to investigate the potential functionality of mobile communication modules (e.g., UAV/drone) and mobile energy resources (MERs) for fast, automatic and efficient resilience enhancing capability in the post-contingency period.

- A comprehensive resilience enhancement relies on a well-designed dynamic state estimation for fault and malicious attack detection and isolation. The existing centralised dynamic state estimation and observer design cannot be directly applied to distributed controlled MGs due to lack of a centralised coordinator. A theoretical analysis of distributed fast-convergent state awareness algorithm for a large-scale system has not been investigated. Such a dynamic state awareness should be appropriate for the communication topology of connectivity in distributed control methods, while the time delay caused by distributed communication structure also needs to be considered.

1.3 Original Contributions

To tackle the challenges identified above, the contributions of this thesis are summarised as follows in terms of phases shown in Figure 1.4:

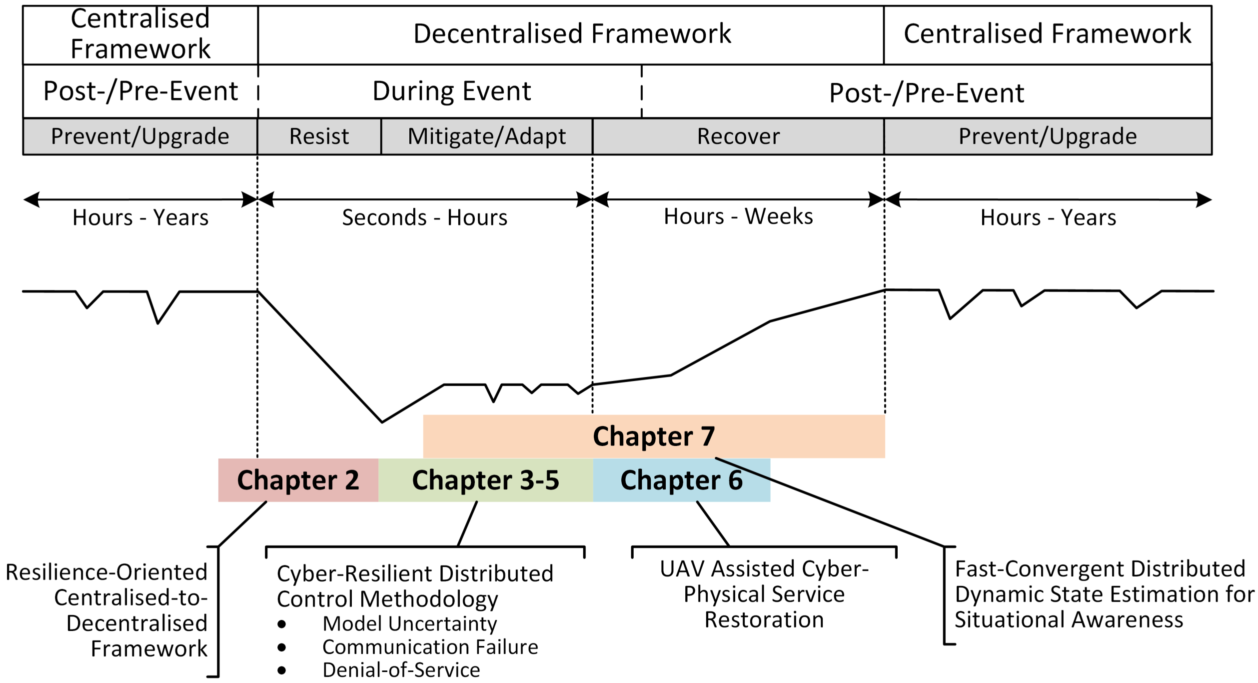

Figure 1.4: Structure of this thesis: original contribution and thesis outline.

- From the preventative phase to the resistive phase, a resilience-oriented centralised-to-decentralised framework is, for the first time, proposed in response to ACPEs, which triggers the islanding operation in the physical layer and the transition of the control and communication mode. The centralised-to-decentralised framework benefits from the advantages of centralised/decentralised frameworks. In such a centralised-to-decentralised framework, the cyber-physical response, i.e., dynamic emergency MGs and dynamic device-to-device (D2D) communication, is pre-scheduled in the centralised controller and allocated to the local controller periodically. The pre-scheduled D2D communication effectively and quantitatively optimises non-negligible delays and guides control law design.

- During the adaptive phase, a distributed robust fast terminal sliding mode (FTSM) secondary voltage control method based on extended state Kalman-Bucy filter (ESKBF) is proposed to achieve resilience against co-existence of multiple uncertainties including parameter perturbation, measurement noise and immeasurably external variables. Specifically, a linearised control-oriented model formulation significantly simplifies the observer design under multiple sources of uncertainties, while an ESKBF-based resilient observer with reasonable parameter selection process employs an extended state to denote the combination of multiple uncertainties. In addition, the proposed FTSM control improves the convergence rate of MG voltage control, where the settling time of the distributed controller can be reduced.

- During the adaptive phase, a distributed resilient voltage control against random packet loss for an islanded MG is designed based on an event-triggered DMPC and an adaptive non-asymptotic observer. Specifically, the prediction model of the DMPC compensates the effect of communication failure/random packet loss to enhance the system resilience by the update principle of the prediction sequence. In addition, two event triggering conditions which can be easily embedded into the DMPC are designed respectively to reduce computation and communication burdens in the cyber layer. Moreover, an adaptive non-asymptotic observer facilitates a cost-effective output-based control framework, which, unlike the Luenberger-like observer can operate in an intermittent way due to its deadbeat convergence property.

- During the adaptive phase, a novel resilient scheme addresses multi-layer DoS attacks targeting the neighbouring communication, sensor measurement and control actuation channels of networked MGs with hierarchically controlled DERs. In details, a unified notion of Persistency-of-Data-Flow (PoDF) characterises multi-layer DoS attacks, and the notion PoDF is of significance in evaluating the effects of multi-layer DoS attacks. Moreover, with an edge-based control logic, the proposed self-triggered ternary controller enables asynchronous data collection and processing for each MG from all its neighbours as opposed to existing methods in that relies on synchronous communication. This remarkable feature of asynchronous data collection and processing turns out to be of major significance to ensure consensus properties in the presence of multi-layer DoS attacks. Furthermore, the conservativeness of the edge-based self-triggered control designed from a global perspective can be significantly reduced by utilising timestamps of successful information exchange attempts in different information network links.

- During the recovery phase, a novel automatic post-contingency cyber-physical restoration based on mobile UAVs and MERs is proposed for resilience enhancement fully utilizing grid digitisation tools (e.g., wireless communication). The mobile UAVs, functioning as base station or relay node, are optimally positioned and deployed for an interconnected communication network coping with possible plug-and-play operations of DERs and MERs, thus enabling energy sharing throughout the whole grid instead of only inside each MG. The UAV base station operates in an event-based manner for energy efficiency, while the energy sharing is prioritized according to generation capacity even with poor communication conditions.

- A novel fixed-time convergent distributed observer is designed based on a cross-agent information sharing mechanism. The method provides an example of how distributed dynamic state estimation systems can benefit from fixed-time convergence properties. The key to the fixed-time observer is the Volterra integral operators with specialised kernel functions. In contrast to the majority of existing methods that require the full-dimensional state estimates to be shared among neighbouring nodes, the proposed distributed observer enables a reduction of the transmitted data over the communication links by invoking a rank-condition, and the effect of delays in communication networks is compensated, while the robustness of the proposed method against measurement noise and perturbations is characterised. The proposed distributed observer, as a fault detection algorithm, can provide real-time fault or damage locations D2D-based or UAV-based distributed communication network, thus leading to an efficient situational awareness during the adaptive phase or system manual repair process during the recovery phase.

1.4 Thesis Outline

This thesis is organised into six technical chapters corresponding to the contributions listed above corresponding to Figure 1.4. Due to the wide range of topics covered in this thesis, most of the relevant literature review is contained within each chapter.

- Chapter 2 focuses on the cyber solution based on wireless networks coordinating increasing and massive DERs for a resilience enhancement purpose. The comparison of (dis)advantages between centralised and decentralised frameworks is fully investigated, base on which a resilience-oriented centralised-to-decentralised framework is highlighted combing both benefits of centralised and decentralised frameworks. In this framework, a pre-scheduled resource allocation algorithm based on an iterative mixed-integer nonlinear programming (MINLP) and a delay-dependent distributed averaging proportional integral discrete controller based on linear feedback control are discussed.

- Chapter 3 proposes a distributed secondary voltage control method based on extended state Kalman-Bucy filter (ESKBF) and fast terminal sliding mode (FTSM) control for the resilient operation of an islanded MG with inverter-based DGs. A unified modelling framework is investigated to represent the set of different types of uncertainties by an extended state method, while Kalman-Bucy filter is then applied to accurately estimate the state information of the extended DG model. In addition, based on the accurate estimation, a FTSM surface with terminal attractors is designed to maintain the system stability and accelerate the convergence of consensus tracking, which significantly improves the performance of secondary voltage control under both normal and plug-and-play operation.

- Chapter 4 addresses the problem of distributed secondary voltage control of an islanded MG from a cyber-physical perspective. By discussing two novel event triggering conditions that can be easily embedded into the DMPC for the application of MG control, the computation and communication burdens are significantly reduced with negligible compromise of control performance. In addition, to reduce the sensor cost and to eliminate the negative effects of non-linearity, an adaptive non-asymptotic observer is investigated to estimate the internal and output signals of each DG. Thanks to the deadbeat observation property, the observer can be applied periodically to cooperate with the DMPC-based voltage regulator.

- Chapter 5 addresses a consensus problem in terms of frequency synchronisation in networked MGs subject to multi-layer DoS attacks, which could simultaneously affect communication, measurement and control actuation channels. A unified notion of Persistency-of-Data-Flow (PoDF) is proposed to characterise the data unavailability in different information network links, and further quantifies the multi-layer DoS effects on the hierarchical system. With PoDF, the consensus of the proposed edge-based self-triggered distributed control framework can be preserved with a sufficient condition of the DoS attacks. In addition, to mitigate the conservativeness of offline design against the worst-case attack across all agents, an online self-adaptive scheme of the control parameters is developed to fully utilise the latest available information of all data transmission channels.

- Chapter 6 focuses on an automatic cyber-physical restoration for post-contingency islanded MGs to improve service of both cyber and physical sides. The mobile UAVs are utilized to enlarge the communication coverage and inter-connectivity, based on which the MERs are prioritized to share their energy capacity throughout the whole grid. The UAV positioning algorithm is modelled through a mixed-integer linear programming optimization, while a two-level event-based DER control framework assisted by UAV-based ad-hoc network is developed to maximize the power supply. A bottom-level control targets at coordinate local dispatchable resources inside each MG, while an upper-level control puts an emphasis on multi-MG communication-efficient and poor-communication-tolerant cyber-physical operation.

- Chapter 7 focuses on the robust distributed state estimation for a class of continuous-time linear time-invariant systems such as networked MGs achieved by a novel kernel-based distributed observer, which ensures fixed-time convergence properties. The local observer estimates and broadcasts the observable states among neighbours so that the full state vector can be recovered at each node and the estimation error reaches zero after a predefined fixed time in the absence of perturbation. This represents a new distributed estimation framework that enables faster convergence speed and further reduced information exchange compared to a conventional Luenberger-like approach. The ubiquitous time-varying communication delay across the network is suitably compensated by a prediction scheme, while the robustness of the algorithm in the presence of bounded measurement and process noise is characterised.

Finally, Chapter 8 summarises the key findings of this thesis and suggests directions for future work.

1.5 Publications

The work presented in this thesis has been reported in the following publications:

Articles in peer-reviewed journals:

1. **P. Ge**, F. Teng, C. Konstantinou, and S. Hu, "A Resilience-Oriented Centralised-to-Decentralised Framework for Networked Microgrids Management", *Applied Energy*, 2022, 308: 118234, doi: 10.1016/j.apenergy.2021.118234.

2. **P. Ge**, Y. Zhu, T. C. Green, and F. Teng, "Resilient Secondary Voltage Control of Islanded Microgrids: An ESKBF-Based Distributed Fast Terminal Sliding Mode Control Approach", *IEEE Transactions on Power Systems*, vol. 36, no. 2, pp. 1059-1070, Mar. 2021, doi: 10.1109/TPWRS.2020.3012026.

3. **P. Ge**, B. Chen, and F. Teng, "Event-triggered distributed model predictive control for resilient voltage control of an islanded microgrid", *International Journal of Robust and Nonlinear Control*, vol. 31, no. 6, pp. 1979-2000, Apr. 2021, doi: 10.1002/rnc.5238.

4. **P. Ge**, B. Chen, and F. Teng, "Cyber-Resilient Distributed Self-Triggered Control of Networked Microgrids Against Multi-Layer DoS Attacks", *IEEE Transactions on Smart Grid*, vol. 14, no. 4, pp. 3114-3124, July 2023, doi: 10.1109/TSG.2022.3229486.

5. **P. Ge** and F. Teng, "Cyber-Physical Post-Contingency Service Restoration of Power Networks: A UAV Assisted Communication Coverage Approach", Under Review.

6. **P. Ge**, P. Li, B. Chen, and F. Teng, "Fixed-Time Convergent Distributed Observer Design of Linear Systems: A Kernel-Based Approach", *IEEE Transactions on Automatic Control*, 2022, Early Access, doi: 10.1109/TAC.2022.3212005.

Conference contributions:

7. **P. Ge**, C. Konstantinou, and F. Teng, "Cyber-Physical Disaster Response of Power Supply Using A Centralised-to-Distributed Framework", in *IEEE International Conference on Communications, Control, and Computing Technologies for Smart Grids,* Aachen, Germany, 25-28 October 2021.

Other publications during the course of the PhD studies with their content not included in the thesis:

8. **P. Ge**, C. Caputo, M.-A. Cardin, A. Korre, and F. Teng, "A Wireless-Assisted Hierarchical Framework to Accommodate Mobile Energy Resources", in *2022 IEEE International Conference on Communications, Control, and Computing Technologies for Smart Grids (SmartGridComm)*, IEEE, 2022, pp. 65–70.

9. F. Teng, S. Chhachhi, **P. Ge**, J. Graham, and D. Gunduz, "Balancing privacy and access to smart meter data: an Energy Futures Lab briefing paper", *White Paper of Energy Futures Lab, Imperial College London*, 2022.

10. C. Caputo, M.-A. Cardin, **P. Ge**, F. Teng, A. Korre, and E. A. del Rio Chanona, "Design and planning of flexible mobile Micro-Grids using Deep Reinforcement Learning", *Applied Energy*, vol. 335, p. 120707, 2023.

11. L. Castiglione, Z. Hau, **P. Ge**, K. Co, L. Muñoz-González, F. Teng, and E. Lupu, "HA-Grid: Security Aware Hazard Analysis for Smart Grids", in *2022 IEEE International Conference on Communications, Control, and Computing Technologies for Smart Grids (SmartGridComm)*, IEEE, 2022, pp. 446–452.

12. S. Rath, C. Konstantinou, B. Papari, C. S. Edrington, **P. Ge**, and F. Teng, "Microgrids in mission-critical applications", Book Chapter, *IET Digital Library, Cyber Security for Microgrids, Chap. 3*, pp. 39-58, 2022.

13. M. Liu, Z. Zhang, **P. Ge**, R. Deng, M. Sun, J. Chen, and F. Teng, "Enhancing Cyber-Resiliency of DER-based SmartGrid: A Survey", *arXiv preprint*, arXiv:2305.05338, 2023.

Chapter 2

Resilience-Oriented Centralised-to-Decentralised Framework for Networked Microgrids Management

2.1 Introduction

Global warming drives the energy supply transition from traditional fossil fuel based power generation to renewable energy resources. This transition has been widely recognised as one of the most significant developing pathways promoting low/zero-carbon societies [9]. Rapidly developing renewable energy generators gradually dominate power systems especially in distribution power networks [35, 36]. During the energy transition process, existing climate change leads to an increase in the frequency, intensity and duration of severe weather events [12, 31]. Extreme weather conditions pose huge threats to power supply infrastructures, thereby leading to undesired power interruptions or blackouts. Hence, the concept of resilience under extreme events has been gradually recognised as a key requirement for future energy systems [15–17,37].

Effectively utilising renewable distributed generators (DGs) to provide emergency power supply for critical loads in the form of microgrid (MG) is a widely used solution to enhance the resilience of power supply [33, 36]. For example, the Consortium for Electric Reliability Technology Solutions (CERTS)-enabled MG maintained power, water, heat of the Brevoort building in Greenwich Village, NY, USA, during the week of widespread utility outages due to Hurricane Sandy in late 2012 [38]. In Japan, Sendai MG and Roppongi Hills MG demonstrated that well-developed localised energy systems are essential to handle critical emergency resulting from earthquakes and tsunamis [39].

Currently, the research on regional MGs providing post-event power supply mostly focuses on the control strategy after islanding operation. The control methods of islanded MGs, either centralised or decentralised, have been widely investigated to regulate the frequency and voltage in the presence of renewable energy generators [40–43]. In addition, the concept of dynamic MGs, including reconfigurable cyber and physical layers, has been proposed to enable the autonomous operation of distribution systems [32], but the cyber solution and cyber-physical coordination, in the event of simultaneous cyber and physical damage, has not been clarified.

On the other hand, wireless communication technologies, e.g., the fifth-generation (5G), have been widely investigated to support the efficient operation and coordination of massive distributed energy resources (DERs) [44]. Leveraging advanced communication technologies, the operation of power systems is becoming intelligent towards a highly cyber-physical fusion [45, 46]. Although advanced communication technologies enable the real-time efficient centralised control framework, which is superior to the decentralised one in terms of control performance and implementation efficiency, such centralised framework suffers from a single-point failure. In addition, base stations that support the management of wireless resources are vulnerable to natural disasters or cyber-attacks, and they may fail to function if losing the backhaul connection to the core network or being physically damaged [47, 48]. Hence, for instance, ad-hoc communication technology has been utilised to realise the self-organised MGs in response to disasters [47, 49]. However, further detailed cyber-layer scheduling and implementation in response to contingencies have not been investigated.

Considering the limited occurrence of extreme events, the existing centralised control framework enabled by 5G networks should be fully utilised because of its advantages in achieving the global economic efficiency and easy integration into the existing centralised control framework (SCADA system). However, the vulnerability of centralised framework against single-point failure should be improved. The promising solution is to design a transition scheme from centralised framework to decentralised framework utilising the power electronic devices and the wireless communication technologies in response to extreme conditions because their configuration flexibility leads to the design of post-contingency communication topology with a high degree of freedom. The cyber-physical collaborative transition and response strategy during the pre-event and post-event periods, especially the cooperative design of communication network and control strategy, has not been examined in the literature. In this chapter, we design a resilience-oriented centralised-to-decentralised framework of networked MGs to maintain the critical power supply by utilising MG clusters isolated from the distribution system, thus enhancing the power supply resilience. Under such centralised-to-decentralised transition, the communication network is converted from base station supporting mode under normal operating conditions to controller-to-controller (C2C)[1] mode under extreme conditions. The C2C communication only requires wireless module equipped at the local controller, which is originally necessary for receiving the instructions in the pre-event normal condition. To summarise, the contributions of the chapter are listed as follows:

1. A centralised-to-decentralised framework is proposed to tackle adverse cyber-physical effects (ACPEs), which can simultaneously benefit from the efficiency of centralised framework (centralised controller and centralised communication) in normal operations and the resilience of decentralised framework (distributed controller and C2C communication) under extreme events.

2. In the cyber layer, a dynamic resource allocation based C2C communication protocol, over a limited wireless bandwidth, is proposed to facilitate emergency communication under

[1]C2C mode is based on the concept of Device-to-Device (D2D) communication, which can be enabled by various short-range wireless technologies like Bluetooth, WiFi Direct, LTE Direct and 5G defined by the Third Generation Partnership Project(3GPP).

extreme events. The communication resource allocation model effectively and quantitatively optimises the non-negligible delays and informs the design of the control algorithm.

3. A discrete-time distributed control system is co-designed along with the dynamically-scheduled wireless network solution. A delay-dependent sampling interval is proposed based on optimised communication resources, which simplifies the selection of control gains and enables the plug-and-play operation of MGs during the post-event period.

The remainder of this chapter is organised as follows: Section 2.2 introduces the detailed framework, while Section 2.3 and Section 2.4 provide the system design method from cyber layer and physical layer respectively. In Section 2.5, simulation results are given, and Section 2.6 concludes the chapter.

2.2 Centralised-to-Decentralised Resilient Framework: A Cyber-Physical Perspective

The resilient response to contingencies from a cyber-physical perspective consists of three scenarios: cyber contingencies, physical contingencies, cyber-physical contingencies. The research in this chapter focuses on resilience enhancement against failures or damages in both cyber and physical layers. For instance, natural disasters, e.g., earthquakes, hurricanes, and flooding, can destroy both power and communication infrastructures, and cyber-attacks can cause cascading failures leading to both power line damage and unreliable communication. Owing to cyber-physical couplings, DERs, the communication of which is supported by a stable power supply, will lost connection to the control centre after contingencies, especially under the circumstance where communication infrastructure is out of service. Inspired by [50], we can define such events as the following:

Definition 2.1. ***Adverse Cyber-Physical Effects (ACPEs)*** *involve single or the combination of the following extreme events, e.g., natural disasters such as hurricanes, earthquakes, wildfires, 'silent errors' due to components and manufacturing variability failures, hardware* *or software faults of smart monitoring devices due to bugs in the code (e.g., operating system, compilers, libraries, etc.), natural effects such as bit flips induced by hardware failures, drive failures, cosmic rays, cyber-attacks, or even faults involving the infrastructure design and implementation. ACPEs drastically affect the results of cyber-physical algorithms in power systems, and subsequently the operations of both cyber and physical components deployed in critical infrastructures.*

2.2.1 Overview of Centralised-to-Decentralised Framework

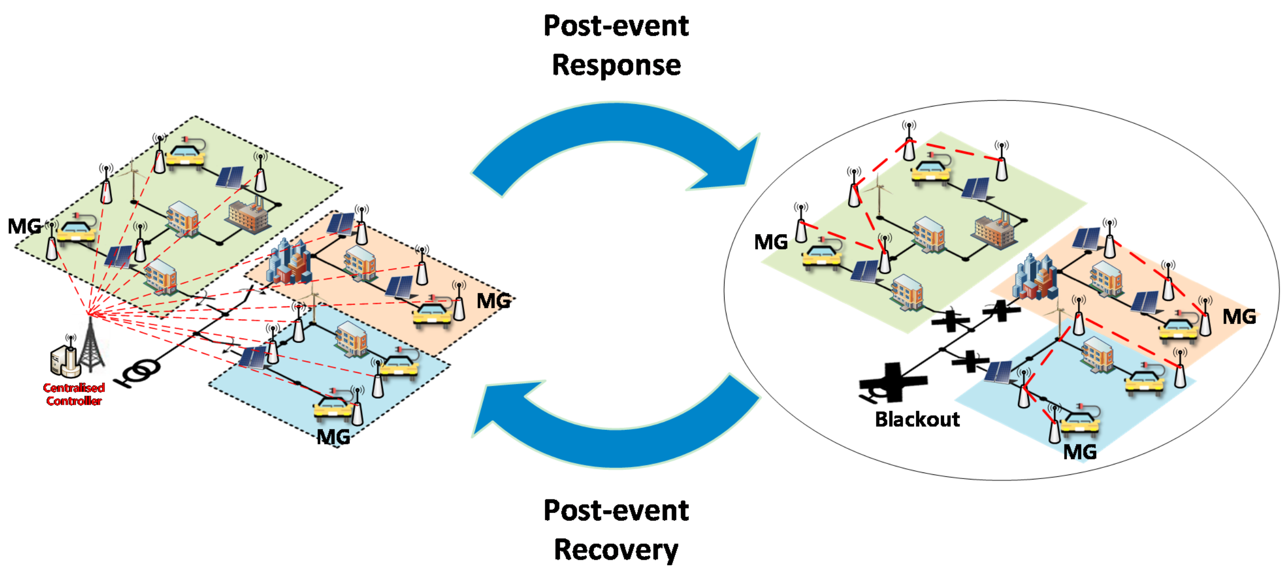

Figure 2.1: Blackout response framework – a centralised-to-decentralised method.

A resilience-oriented centralised-to-decentralised framework, as in Figure 2.1, is proposed in response to ACPEs, which trigger the islanding operation in the physical layer and transition of the control and communication mode from the centralised to the decentralised. The centralised control structure under normal operation is served by a centralised controller, normally implemented in the substation. Such centralised controller coordinates all dispatchable resources (e.g., DGs, controllable loads, EVs) to maintain the grid frequency, voltage stability, and economical dispatch through using wired or wireless communication, e.g., the 5G network[2] [52,53]

[2]Compared to wired communication, wireless communication is more affordable to coordinate massive distributed generators. Among wireless technologies, owing to massive distributed generators needed to be regulated, 5G with its abundant derivative technology [51] is a promising solution thanks to its high bandwidth and wide coverage.

supported by base stations. On the other hand, the decentralised structure under extreme events, whose priority is safety, is the emergency response to maintain the critical energy supply as much as possible by utilising available localised distributed resources and grid-forming techniques through device-to-device (D2D) ad-hoc wireless communication. Such a centralised-to-decentralised framework can complement existing centralised control structures, and benefit from the efficient and flexible grid formation of the decentralised structure. The detailed cyber-physical solution is outlined in Table 2.1.

Table 2.1: Cyber-Physical Solution of Centralised-to-Decentralised Framework

	Normal condition	Extreme condition
Physical solution	Main grid and DERs	DER-based MGs
Cyber solution	Wired/wireless	D2D-enabled wireless
	Centralised coordination	Decentralised/distributed
Objective	Economical operation	Critical power supply
Priority	Optimality	Safety

2.2.2 Centralised-to-Decentralised Post-Event Response Process

The centralised-to-decentralised transition functions as a post-event response against ACPEs. To form such transition, a dynamic cyber-physical scheduling scheme is required to clearly guide the immediate decentralised and localised energy supply. Under normal operation, the post-event cyber-physical response schedule is dynamically optimised in the central controller and sent, together with other control signals, to the local controllers. The sequential diagram of the cyber-physical collaborative response framework is outlined in Figure 2.2, and the centralised-to-decentralised framework focuses on the transition to the “response phase” using the proposed mitigation actions in this chapter.

Once damage or failure occurs after extreme events, the cyber-physical solution for power networks operating in the normal condition could be out of service. Physically, the main grid support is lost, which can be detected by the control and protection system using electrical state sensing. The successful detection triggers breakers switching off to enable networked

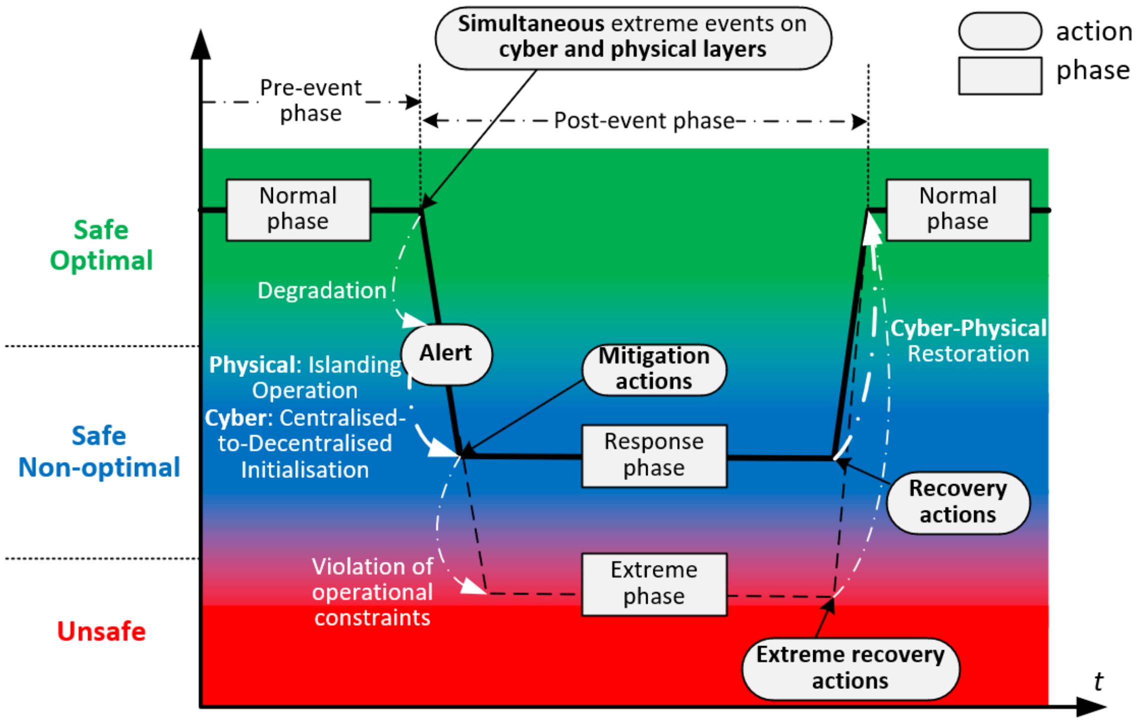

Figure 2.2: Time-sequential diagram of the centralised-to-decentralised framework.

MGs being split into islanded MGs. From a cyber perspective, if the local controller loses the connection to the centralised controller for a period of time (a threshold value), an emergency wireless network formation is triggered to form as the pre-scheduling. The controllers that enable direct D2D communication can move to the emergency mode to form an ad-hoc and self-organised emergency wireless network serving for a regional islanded MG. A reconfiguration protocol of the cyber layer can support the discovery of neighbour nodes [47,54] can be adopted or modified. The basic idea is to perform a handshake, i.e., scan and respond to a beacon signal from other nodes, or emit a beacon signal, wait for response, and then utilise the pre-scheduled frequency assignment to establish a communication link.

Hence, during the extreme conditions, each MG maintains the critical energy supply by limited energy capability under emergency scenarios and operates as that scheduled before in both cyber and physical layers. Followed by gradually repaired power supply infrastructure, the operation of networked MGs will recover to the normal condition. It should be noted that the recovery process is out of the scope of this chapter.

Remark 2.1. *The time and duration of the blackouts caused by extreme events vary case-by-*

case, from a short time of cyber-attack to a long time of hurricane for instance. The proposed framework can cope with the transition from centralised control to decentralised control when the blackout and cyber infrastructure damages occur simultaneously for both short-time and long-time disasters. However, the short-term and long-term responses require different energy capabilities and long-term response strategies, which are determined and optimised by the installation of renewable energy resources and portable storage connection design. The long-term response is the next step of our centralised-to-decentralised transition framework and is not inside the scope of this chapter. We will consider the long-term lasting post-event restoration in our future work.

2.3 Dynamic Cyber-Layer Scheduling Considering Time-Varying Dispatchable Resources

The dynamic cyber-physical response scheduling is performed during the pre-event stage in the normal condition. The objective of the scheduling is to design cyber-physical solutions in advance in order to accomplish seamless transformation once ACPEs occur. Owing to plug-and-play characteristic of EVs and time-varying availability of dispatchable loads, the scheduling needs to be dynamically optimised under different scenarios. The cyber-layer design utilises distributed C2C wireless communication in virtue of promising D2D techniques [49, 55], which efficiently benefits from flexible networking mode. The dynamic cyber-physical scheduling scheme, as shown in Figure 2.3 divides distributed power systems into regionally localised autonomous MGs according to line breakers.

In each region, cyber-layer solutions are designed independently in terms of bandwidth allocation. In other words, the total backup bandwidth that is reserved for emergency use can be reused because different regions have diverse physically geographic locations, and thus communication interregional collisions are assumed to be negligible [56]. On the other hand, the mitigation of intra-regional communication collisions is inspired by frequency division duplexing (FDD) techniques, which utilise frequency separation multiplexing technology to separate

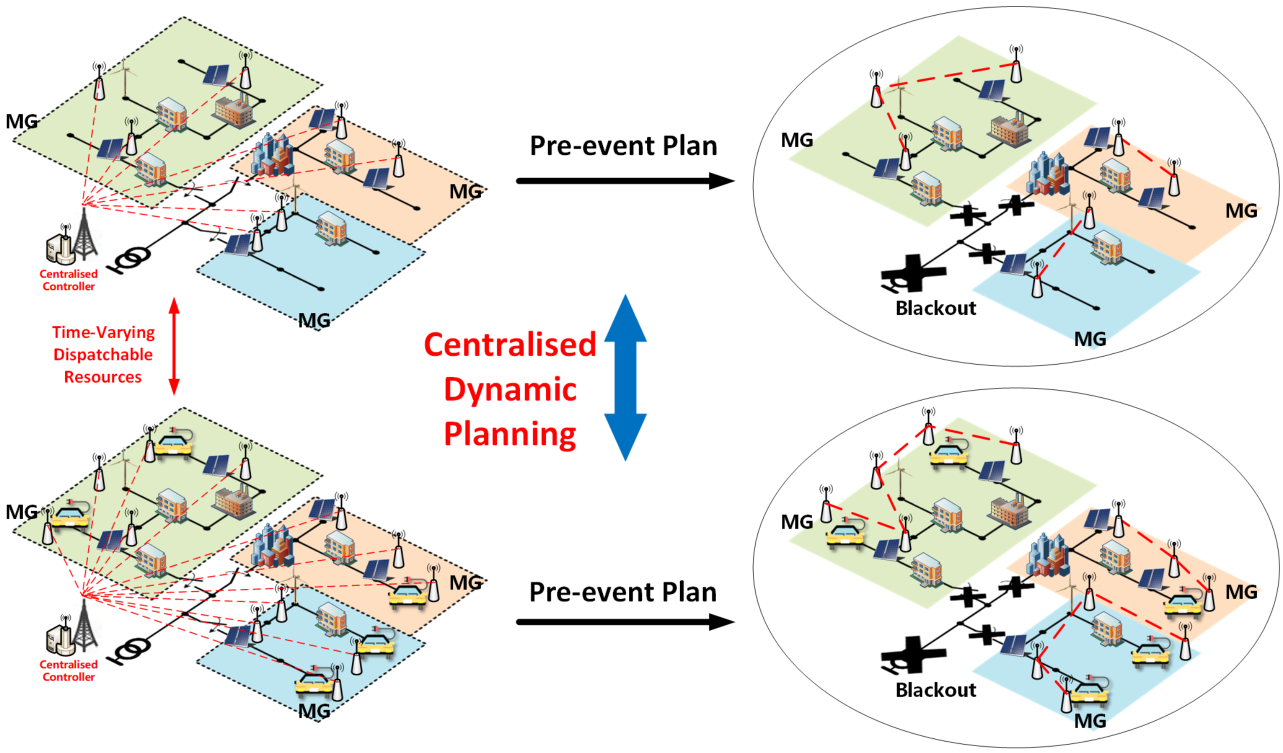

Figure 2.3: Centralised pre-event dynamic cyber-physical scheduling scheme.

the transmitted and received signals. Owing to the two-way data transmission among distributed control in the post-event MGs, FDD can decrease co-channel interference of two-way C2C communication, and hence avoid collisions in the intra-regional area [52].

In the remainder of this section, the details of dynamic cyber-physical scheduling are introduced with the objective of quantitatively determining the delay in each intra-regional wireless network, which will guide the control strategy design in Section 2.4.

2.3.1 Wireless Network Model

To enable each DER participating in post-contingency MG formations, there must be a distributed communication network for the secondary control inside each MG. Using a graph to model such a distributed communication network can explicitly depict its connectivity, which dominates the secondary control performance. As such, a time-varying wireless network of DGs that available for emergency use can be modelled by a dynamic undirected graph $\mathcal{G} = \{\mathcal{V}, \mathcal{E}, \mathcal{A}\}$, where $V = |\mathcal{V}|$ denotes the numbers of dispatchable emergency resources. Such graph $\mathcal{G}$ is certainly not connected because of switched-off breakers but contains $\phi = |\Phi|$ connected components representing MGs:

$$
\begin{aligned}
&\mathcal{G} = \bigcup_{\mu=1}^{\phi} \mathcal{G}_\mu \\
&\mathcal{G}_\mu \cup \mathcal{G}_\nu = 0,\ \ \mu \neq \nu,\ \ \forall \mu, \nu \in \Phi
\end{aligned}
\tag{2.1}
$$

where $\mathcal{G}_\mu = \{\mathcal{V}_\mu, \mathcal{E}_\mu, \mathcal{A}_\mu\}$ denotes a connected component representing one emergency MG with $V_\mu = |\mathcal{V}_\mu|$ DGs. Eq. (2.1) is equivalent to $\sum_{\mu=1}^{\phi} V_\mu = V$, and apparently adjacent matrix $\mathcal{A}$ has a block diagonalized form

$$
\mathcal{A} = \mathrm{blockdiag}\{\mathcal{A}_1, \mathcal{A}_2, \ldots, \mathcal{A}_\phi\} \tag{2.2}
$$

owing to none available interregional communication links.

For the sake of generality and convenience, wireless network $\mathcal{G}_\mu$ is discussed in details, and the combination of multi-graph ($\bigcup_{\mu=1}^{\phi} \mathcal{G}_\mu$) optimisation forms the dynamic cyber-layer scheduling in the centralised controller during the pre-event period.

For wireless network $\mathcal{G}_\mu$ modelling the μ_{th} autonomous MG, among V_μ DGs, the communication connection is described by a binary matrix $\mathcal{A}_\mu = [a_{ij}^\mu] \in \mathbb{R}^{V_\mu \times V_\mu}$, where all elements are 0 except for $a_{ij}^\mu = 1, i \neq j$ only if node j has access to data of node i, i.e. $(i, j) \in \mathcal{E}_\mu$. Through applying FDD technique modelled by undirected graph, there always exists $\mathcal{A}_\mu = \mathcal{A}_\mu^T$. In other words, any $a_{ij}^\mu = 1, i \neq j$ means two-way communication between nodes i, j. In addition, the component $\mathcal{G}_\mu$ has the undirected characteristic and connectivity [57, 58], leading to

$$
\lambda_2(\mathcal{L}_\mu) > 0 \tag{2.3}
$$

where $\lambda_2(\mathcal{L}_\mu)$ denotes the second-smallest eigenvalue of the Laplacian of a graph. This constraint can be relaxed using primal–dual variables and has been investigated in [58], so we omitted its discussion in this chapter.

The backup bandwidth dedicated to emergency use is divided into L sub-carriers in the set

$\mathcal{L} = \{1, 2, \ldots, L\}$. Let $g_{m,l}$ and $p_{m,l}$ be the channel gain and the transmit power for one C2C link $m = (i, j) \in \mathcal{E}_\mu$ on the sub-carrier $l \in \mathcal{L}$ respectively. Then, signal-to-noise ratio (SNR) for C2C link m on the sub-carrier l [59] is expressed as

$$\gamma_{m,l} = \frac{p_{m,l} g_{m,l}}{\sigma^2} \tag{2.4}$$

where σ^2 denotes the power of additive white Gaussian noise. The channel gain g_m of the C2C link $m = (i, j)$ is negatively related to the transmitting distance with fading effects [60]. Combining both path loss and log-normal shadowing, the channel gain is simply modelled as

$$g_m = h d_{i,j}^{-\alpha} \tag{2.5}$$

where h is the loss factor combining total fading effects; $d_{i,j}$ is the transmitting distance between the communication link $m = (i, j)$; α is the pathloss exponent.

The reachable instantaneous C2C data rates in bits per second (bps) are computed through the well-known Shannon formula

$$R_m = w \sum_{l=1}^{L} \beta_{m,l} \log_2(1 + \gamma_{m,l}) \tag{2.6}$$

where $\beta_{m,l}$ is a binary variable, and $\beta_{m,l} = 1$ if sub-carrier l is allocated to the C2C link; otherwise $\beta_{m,l} = 0$. w denotes the bandwidth of each sub-carrier.

In the emergency wireless network, normal Quality-of-Service (QoS) requirement is discarded in the constraints, and is reflected by transmission delay τ_m

$$\tau_m = \frac{L_{\text{packet}}}{R_m} \tag{2.7}$$

where L_{packet} denotes the packet size of data transmissions.

In addition, each controller of node i equipped with wireless communication module has its power limitation, which consists of constant circuit power and total transmit power

$$p_{i,\text{total}} = p_{i,\text{cst}} + \sum_{m \in \mathcal{E}_{\mu,i}} \sum_{l=1}^{L} p_{m,l} \leq p_{i,\max}, \ \forall j \in \mathcal{V}_i \tag{2.8}$$

where $\mathcal{E}_{\mu,i}$ denotes the edge/link set where node $i \in \mathcal{V}_\mu$ shares local information.

2.3.2 Service-Oriented Resource Allocation Problem

Algorithm 2.1: Overall Procedure of Resource Allocation for Dynamic Cyber-Layer Scheduling in the Centralised Controller

Input: w: sub-carrier bandwidth; L: number of sub-carriers;
σ^2: power of additive noise; g_m: channel gain of links;
V_μ: number of subnetwork nodes; L_{packet}: packet size;
$P_{i,\text{cst}}$: constant power of nodes; $P_{i,\max}$: maximum power of nodes;

Output: $\mathcal{A}$: scheduled wireless network;
$\boldsymbol{\tau}_{\max} = [\tau^{\mu}_{\max}] \in \mathbb{R}^{\phi}$: maximum communication delay;

Initialisation: maximum iterations $k_{\max}$; iteration index $k = 0$; convergence error ϵ; transmitting power of links on channels $\boldsymbol{p}$;
while $k < k_{\max}$ **do**
  repeat
    solve (2.10) using MATLAB/YALMIP with MOSEK;
    update wireless network matrix $\mathcal{A}$ and sub-carrier assignment matrix $\boldsymbol{\beta}$;
    solve (2.11) using MATLAB/YALMIP with MOSEK;
    update transmitting power of links on channels $\boldsymbol{p}$ and communication delay $\boldsymbol{\tau}_{\max}$;
  until $\mathcal{A}(k) - \mathcal{A}(k-1) = \mathbf{0}$ *and* $\|\boldsymbol{\tau}_{\max}(k) - \boldsymbol{\tau}_{\max}(k-1)\|_\infty \leq \epsilon$;
end

Inspired by the best-effort service of wireless network, the optimisation aims to minimise the total communication delay of wireless subnetworks $\{\mathcal{G}_1, \mathcal{G}_2, \ldots, \mathcal{G}_\phi\}$. Based on the analysis above, the optimisation problem can be formulated as

$$\min_{\mathcal{A},\boldsymbol{\beta},\boldsymbol{p}} \quad \sum_{\mu=1}^{\phi}\left(\tau_{\max}^{\mu}\right) \tag{2.9a}$$

subject to :

$$\mathrm{C}_1: \quad \mathcal{A} \in \{0,1\}^{V\times V} \tag{2.9b}$$

$$\mathrm{C}_2: \quad \mathcal{A} = \mathcal{A}^T \tag{2.9c}$$

$$\mathrm{C}_3: \quad \mathrm{tr}(\mathcal{A}) = 0 \tag{2.9d}$$

$$\mathrm{C}_4: \quad \lambda_2(\mathcal{L}_\mu) > 0, \forall \mu \in \Phi \tag{2.9e}$$

$$\mathrm{C}_5: \quad \beta_{m,l} \in \{0,1\}, \forall m \in \mathcal{E}, l \in \mathcal{L} \tag{2.9f}$$

$$\mathrm{C}_6: \quad \sum_{m\in\mathcal{E}_\mu} \beta_{m,l} \leq 1, \forall l \in \mathcal{L}, \mu \in \Phi \tag{2.9g}$$

$$\mathrm{C}_7: \quad p_{i,\mathrm{cst}} + \sum_{m\in\mathcal{E}_{\mu,i}} \sum_{l=1}^{L} p_{m,l} \leq p_{i,\max}, \forall i \in \mathcal{V}_i, \mu \in \Phi \tag{2.9h}$$

$$\mathrm{C}_8 - \mathrm{C}_{11}: \quad \text{Eqs. } (2.4)(2.5)(2.6)(2.7), \forall \mathcal{G}_\mu, \mu \in \Phi \tag{2.9i}$$

where $\tau_{\max}^{\mu} = \max_{m\in\mathcal{E}_\mu} \tau_m^{\mu}, \forall \mu \in \Phi$, $\boldsymbol{\beta} = [\beta_{m,l}] \in \{0,1\}^{E\times L}$, and $\boldsymbol{p} = [p_{m,l}] \in \mathbb{R}_{\geq 0}^{E\times L}$. Eqs. (2.9b) – (2.9e) are constraints derived from the undirected and connected sub-graphs. Eq. (2.9f) and Eq. (2.9g) are the exclusive sub-carrier allocation in the communication links. Eq. (2.9h) represents the wireless module in each DG controller should satisfy the maximum power consumption requirement. Constraints Eq. (2.9i) are basic resource allocation equations being a bridge among channels, power consumption and transmitting delay. The resource allocation optimisation of dynamic cyber-layer scheduling for emergency wireless network expressed by Eqs. (2.9) is a mixed-integer non-linear programming (MINLP). Due to inefficient solving of MINLP, and inspired by [61], we reduce the complex problem into two allocation sub-problems: sub-carrier allocation and power allocation.

Sub-carrier allocation sub-problem is optimised under a given power allocation:

$$\begin{aligned} &\min_{\mathcal{A},\boldsymbol{\beta}} \quad \sum_{\mu=1}^{\phi} \left(\tau_{\max}^{\mu}\right) \\ &\text{subject to}: \ \mathrm{C}_1 - \mathrm{C}_{11} \end{aligned} \tag{2.10}$$

and power allocation sub-problem is optimised under a given wireless network and corresponding sub-carrier assignment:

$$\begin{aligned} &\min_{\boldsymbol{p}} \quad \sum_{\mu=1}^{\phi} \left(\tau_{\max}^{\mu}\right) \\ &\text{subject to}: \ \mathrm{C}_7 - \mathrm{C}_{11} \end{aligned} \tag{2.11}$$

Both problems Eq. (2.10) and Eq. (2.11) are convex by utilising exponential cones for Eq. (2.6) and rotated quadratic cones for Eq. (2.7) specially. We solve the problem (2.9) by iteratively solving sub-problems (2.10) and (2.11) using MATLAB/YALMIP with MOSEK [62, 63]. The overall algorithm of proposed resource allocation problem is detailed in Algorithm 2.1.

Remark 2.2. *The optimised communication delay $\tau_{\max}^{\mu}$ considered in this chapter corresponds to the transmission delay, which defines the time taken to push the packet bits onto the scheduled channel. As it is well known, the communication delay typically consists of transmission delay, propagation delay, processing delay, and queuing delay. In our context, due to limited bandwidth capacity existing in the emergency C2C communication, transmission delay dominates the communication delay, which is why others are omitted here.*

2.4 Post-Event Response Based on Scheduled Cyber Network and Distributed Consensus Protocol

The operation of emergency MG clusters employs the wireless network that is scheduled by the centralised controller as a cyber solution. The physical solution enabling such post-event response utilises available localised energy sources to maintain the critical power supply. More specifically, inverter-based DGs using grid-forming techniques are considered due to its autonomous operation ability. The integrated cyber-physical modelling and structure of such MGs are detailed in Figure 2.4.

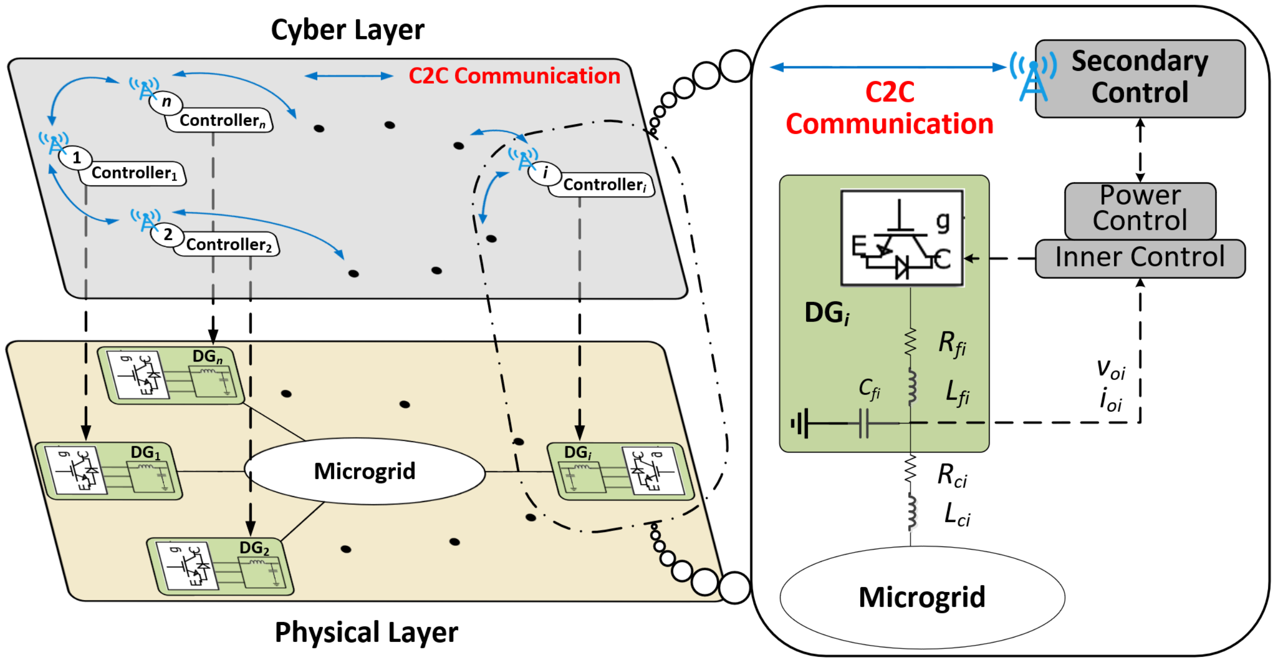

Figure 2.4: Diagram of a cyber-physical MG and control loops.

2.4.1 Physical-Layer Model and Post-Event Response Objectives

As an emergency response, the microgrids are modelled from the perspective of DG itself. In details, each DG supports the microgrid through supplying the power via an output impedance Z_o, as shown in Figure 2.5. The modelling of DGs is based on the well-known P/Q droop method [64]:

$$\begin{aligned} \omega_i &= \omega_i^* - m_{Pi}(P_i - P_i^*) \\ U_i &= U_i^* - n_{Qi}(Q_i - Q_i^*) \end{aligned} \tag{2.12}$$

where ω_i^*, U_i^* denote the nominal values of frequency and voltage of the i_{th} DG; P_i^*, Q_i^* are respectively active and reactive power set-points of the i_{th} DG. The model (2.12) is the conventional droop method where it is supposed that the output impedance is mainly inductive.

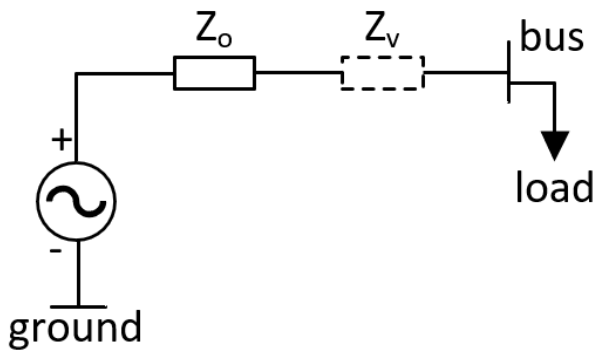

Figure 2.5: Equivalent circuit of an inverter-based DG with output-impedance loop.

However, in the low-voltage applications such as distribution network, such inductive characteristic is not satisfied. To mitigate the limitations of the conventional droop method, the control strategy including virtual impedance (Z_v in Figure 2.5) in the inner control loop has been widely investigated [64, 65]. The control loops are modified as shown in Figure 2.6 and the modified droops can be expressed as

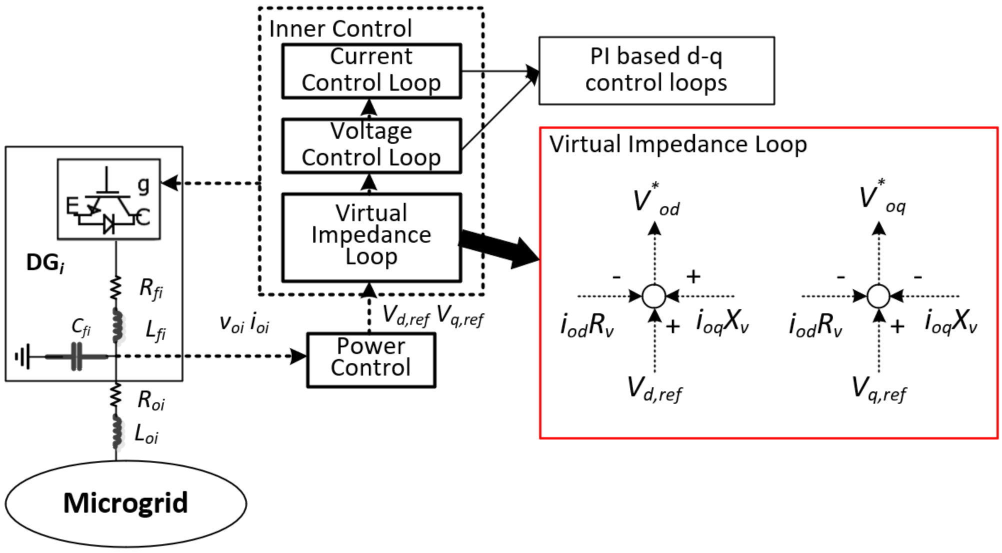

Figure 2.6: Virtual impedance control loops.

$$
\begin{aligned}
\omega_i &= \omega_i^* - m_{Pi}[(P_i - P_i^*)\sin\theta_i - (Q_i - Q_i^*)\cos\theta_i] \\
U_i &= U_i^* - n_{Qi}[(P_i - P_i^*)\cos\theta_i + (Q_i - Q_i^*)\sin\theta_i]
\end{aligned}
\tag{2.13}
$$

Fundamentally, in an inductive grid with $R \ll X$, frequency and voltage are dominated by active power and reactive power respectively, while in a resistive grid with $R \gg X$ frequency and voltage are dominated by reactive power and active power respectively. For a grid neither inductive nor resistive, an virtual impedance control loop is utilized as Figure 2.6, and the functionality of virtual impedance is to adjust the phase angle θ_i of (2.13), i.e., to ensure the equivalent output impedance $X_i \gg R_i$. Hence, the output power can be modelled by P/Q droop method approximately as an equivalent expression of (2.12) by integrating P_i^*, ω_i^*, Q_i^*, U_i^* into the primary control set points ω_{ni}, U_{ni}:

$$\begin{aligned} \omega_i &= \omega_{ni} - m_{Pi} P_i \\ U_i &= U_{ni} - n_{Qi} Q_i \end{aligned} \tag{2.14}$$

where ω_{ni}, U_{ni} are set points of primary frequency and voltage control; ω_i, U_i are angular frequency and voltage magnitude of the i_{th} DG; P_i, Q_i are respectively active and reactive power outputs of the i_{th} DG; m_{Pi}, n_{Qi} are droop coefficients and are selected based on the active and reactive power ratings [66].

Remark 2.3. *In the emergency condition, due to only maintaining the critical power supply, the line power flow exceeding to constraints is ignored. The microgrid modelling is an agent based method which focuses on the DG itself, i.e., the direct droop principle between power outputs and frequency, voltage regulations that can be obtained even in low-voltage networks via virtual impedance utilization. As for the optimised control that includes the power flow, it is not the focus of this chapter and will be considered in our future work.*

As depicted in Figure 2.4, the primary controller consists of power control of Eq. (2.14) and inner control [67], through which the frequency and voltage deviations from the reference cannot be eliminated without effectively adjusting set-points. Hence, the secondary control is employed to achieve frequency regulation, accurate active power sharing, and voltage regulation, i.e.,

$$\lim_{t\to\infty} \omega_i = \omega_{\text{ref}}, \quad \lim_{t\to\infty} \left| \frac{P_i}{P_{\max,i}} - \frac{P_j}{P_{\max,j}} \right| = 0 \tag{2.15}$$

$$\lim_{t\to\infty} U_i = U_{\text{ref}} \tag{2.16}$$

where $P_{\max,i}$ denotes the active power ratings of the i_{th} DG, and the second item of Eq. (2.15) is equivalent to $\lim_{t\to\infty} |m_{Pi}P_i - m_{Pj}P_j| = 0$ by appropriately setting $m_{Pi}P_{\max,i} = m_{Pj}P_{\max,j}$. Eq. (2.16) only focuses on voltage regulation because voltage quality is prioritised for the critical supply in the emergency response, and voltage regulation and reactive power sharing cannot be reached simultaneously due to impedance effects except for a perfect configuration [7].

2.4.2 Post-Event Response under Pre-Scheduled Wireless Network

Algorithm 2.2: Distributed Control Framework of Emergency MGs

Input: ω_{ref}, U_{ref}: reference values of angular frequency and voltage magnitude; $K_{\omega i}, K_{Pi}, K_{Ui}$: control gains of angular frequency, active power sharing and voltage magnitude; ω_i: local angular frequency; $m_{Pi}P_i$: local active power ratio; U_i: local voltage magnitude; $m_{Pj}P_j$: neighbouring active power ratio;

Output: ω_{ni}: set points of primary frequency control; U_{ni}: set points of primary voltage control;

```
for i ∈ V_μ, every T_s^μ do
    update input variables (including delayed neighbouring information);
    update set points in the primary control by Eq. (2.20);
    send updated m_Pi P_i to neighbours;
end
```

The control system of post-event response suffers from neighbouring communication delay because the wireless C2C network has limited reserved bandwidth and each controller hardware has limited transmit power, as analysed in Section 2.3. Therefore, we design a distributed control framework with sampling interval $T_s^\mu \geq \tau_{\max}^\mu, \mu \in \Phi$. The existing transmission delay, as analysed in Remark 2.2 restricts the selection of sampling interval, i.e., $T_s^\mu < \tau_{\max}^\mu, \mu \in \Phi$ could lead to the cumulative delay among the communication network, which makes the system suffer from unbounded time-varying delay, thereby raising the difficulty of controller design. Owing to the relatively low-frequency time-triggered control framework, for each emergency post-event MG, we model the dynamics of the system Eq. (2.14) in a discrete manner:

$$\omega_{ni}(k+1) = \omega_i(k+1) + m_{Pi}P_i(k+1) = \omega_i(k) + u_{\omega i}(k) + m_{Pi}P_i(k) + u_{Pi}(k) \tag{2.17}$$

$$U_{ni}(k+1) = U_i(k+1) + n_{Qi}Q_i(k+1) = U_i(k) + u_{Ui}(k) + n_{Qi}Q_i(k) + u_{Qi}(k) \tag{2.18}$$

Owing to the analysis for objective (2.16), reactive power sharing control is omitted. Then, we obtain the equivalent matrix-form discrete model

$$
\begin{cases}
\boldsymbol{x}_\omega(k+1) = \boldsymbol{x}_\omega(k) + \boldsymbol{u}_\omega(k) \\
\boldsymbol{x}_P(k+1) = \boldsymbol{x}_P(k) + \boldsymbol{u}_P(k) \\
\boldsymbol{x}_U(k+1) = \boldsymbol{x}_U(k) + \boldsymbol{u}_U(k)
\end{cases}
\tag{2.19}
$$

where $\forall \mu \in \Phi$,

$$
\begin{aligned}
\boldsymbol{x}_\omega &= [x_{\omega i}] = [\omega_i] \in \mathbb{R}^{\mathcal{V}_\mu}, & \boldsymbol{u}_\omega &= [u_{\omega i}] \in \mathbb{R}^{\mathcal{V}_\mu} \\
\boldsymbol{x}_P &= [x_{Pi}] = [m_{Pi}P_i] \in \mathbb{R}^{\mathcal{V}_\mu}, & \boldsymbol{u}_P &= [u_{Pi}] \in \mathbb{R}^{\mathcal{V}_\mu} \\
\boldsymbol{x}_U &= [x_{Ui}] = [U_i] \in \mathbb{R}^{\mathcal{V}_\mu}, & \boldsymbol{u}_U &= [u_{Ui}] \in \mathbb{R}^{\mathcal{V}_\mu}
\end{aligned}
$$

The distributed averaging proportional integral (DAPI) discrete controller is formulated inspired by extensively studied consensus protocol [68]:

$$
\begin{cases}
u_{\omega i}(k) = K_{\omega i}\big(x_{\omega,ref} - x_{\omega i}(k)\big) \\
u_{Pi}(k) = K_{Pi} \sum\limits_{(i,j)\in\mathcal{E}_{\mu,i}} a_{ij}\big(x_{Pj}(k-1) - x_{Pi}(k)\big) \\
u_{Ui}(k) = K_{Ui}\big(x_{U,ref} - x_{Ui}(k)\big)
\end{cases}
\tag{2.20}
$$

where $K_{\omega i}, K_{Pi}, K_{Ui} > 0$ are the designed control gains. Thanks to the design of $T_s \geq \tau_{\max}$, one time step of delay caused by emergency wireless network is induced in Eq. (2.20).

Theorem 2.1. *For emergency MGs controlled under Algorithm 2.2 and Eq.* (2.20) *with a distributed C2C communication structure modelled by an undirected graph $\mathcal{G}$, the distributed frequency regulation, active power sharing and voltage regulation can be achieved as Eqs.* (2.15) *and* (2.16) *asymptotically if the conditions*

$$0 < K_{\omega i}, K_{Ui} < 2 \tag{2.21a}$$

$$0 < |\mathcal{E}_{\mu,i}| K_{Pi} < 1 \tag{2.21b}$$

are satisfied.

Proof. Define $\boldsymbol{x}_\omega^e = \boldsymbol{x}_\omega - x_{\omega,ref}\mathbf{1}_N, \boldsymbol{x}_U^e = \boldsymbol{x}_U - x_{U,ref}\mathbf{1}_N$, where $\mathbf{1}_N$ denotes a column vector with all elements being ones, and $\boldsymbol{K}_\star = \text{diag}\{K_{\star i}\} \in \mathbb{R}^{V_\mu \times V_\mu}, \star \in \{\omega, P, U\}$ the dynamics of the system (2.19) can be expressed in a matrix form by identity matrix $\boldsymbol{I}$ of appropriate dimensions:

$$\boldsymbol{x}_\omega^e(k+1) = (\boldsymbol{I} - \boldsymbol{K}_\omega)\boldsymbol{x}_\omega^e(k) \tag{2.22a}$$

$$\boldsymbol{x}_P(k+1) = \boldsymbol{x}_P(k) - \boldsymbol{K}_P\mathcal{D}_\mu\boldsymbol{x}_P(k) + \boldsymbol{K}_P\mathcal{A}_\mu\boldsymbol{x}_P(k-1) \tag{2.22b}$$

$$\boldsymbol{x}_U^e(k+1) = (\boldsymbol{I} - \boldsymbol{K}_U)\boldsymbol{x}_U^e(k) \tag{2.22c}$$

where $\mathcal{D}_\mu = \text{diag}\{d_i\} \in \mathbb{R}^{V_\mu \times V_\mu}, d_i = |\mathcal{E}_{\mu,i}|$ is the diagonal out-degree matrix of $\mathcal{G}_\mu$.

Firstly, we give the proof of the stability of the frequency regulation. Taking z-transformation of the system (2.22a)

$$z\boldsymbol{X}_\omega^e(z) = (\boldsymbol{I} - \boldsymbol{K}_\omega)X_\omega^e(z)$$

the characteristic equation of which is

$$\det\big((z-1)\boldsymbol{I} + \boldsymbol{K}_\omega\big) = 0 \tag{2.23}$$

Owing to the diagonal form of $\boldsymbol{K}_\omega$, the characteristic equation (2.23) is equivalent to $z - 1 + K_{\omega i} = 0 \Longrightarrow z = 1 - K_{\omega i}$. By the stability criteria that the system (2.22a) is asymptotically stable if the roots of Eq. (2.23) have modulus less than unity, the asymptotic stability of the system (2.22a) is guaranteed if the following condition is satisfied:

$$|z| = |1 - K_{\omega i}| < 1 \Longrightarrow 0 < K_{\omega i} < 2$$

Similarly, an asymptotic stability of the system (2.22c) is guaranteed by $0 < K_{Ui} < 2$. Therefore, the proof with regard to Eq. (2.21a) is completed.

Then, we give the proof for the stability of the active power sharing. Taking z-transformation of the system (2.22b)

$$\begin{aligned} z\boldsymbol{X}_P(z) &= \boldsymbol{X}_P(z) - \boldsymbol{K}_P\mathcal{D}_\mu\boldsymbol{X}_P(z) + z^{-1}\boldsymbol{K}_P\mathcal{A}_\mu\boldsymbol{X}_P(z) \\ &= \boldsymbol{X}_P(z) - \widetilde{\boldsymbol{L}}_\mu\boldsymbol{X}_P(z) \end{aligned} \tag{2.24}$$

where

$$\widetilde{\boldsymbol{L}}_\mu(z) = \boldsymbol{K}_P\mathcal{D}_\mu - z^{-1}\boldsymbol{K}_P\mathcal{A}_\mu = \left\{\begin{array}{ll} -K_{Pi}a_{ij}z^{-1}, & (i,j)\in\mathcal{E}_\mu \\ K_{Pi}d_i, & i\in\mathcal{V}_\mu \\ 0, & \text{otherwise} \end{array}\right\} \in \mathbb{R}^{V_\mu\times V_\mu}$$

It should be noted that $\widetilde{\boldsymbol{L}}_\mu(1) = \boldsymbol{L}_\mu$ denotes the Laplacian matrix of $\mathcal{G}_\mu$. Define $p(z) = \det\big((z-1)\boldsymbol{I} + \widetilde{\boldsymbol{L}}_\mu(z)\big)$, then the asymptotic stability of the system (2.22b) is guaranteed by all the zeros of $p(z)$ having modulus less than unity except for a zero at $z = 1$ (see, e.g., *Lemma 1* in [68]).

Since graph $\mathcal{G}_\mu$ is undirected and connected, 0 is one eigenvalue of $\boldsymbol{L}_\mu$ and $\text{rank}(\boldsymbol{L}_\mu) = V_\mu - 1$ [69], thereby $p(1) = \det(\boldsymbol{L}_\mu) = 0$ showing that $z = 1$ is indeed one of zeros.

Next, we prove that the zeros of $f(z) = \det\big(\boldsymbol{I} + \frac{\widetilde{\boldsymbol{L}}_\mu(z)}{z-1}\big)$ have modulus less than unity. It is achieved if the eigenvalue loci of $\frac{\widetilde{\boldsymbol{L}}_\mu(e^{j\omega})}{e^{j\omega}-1}$, i.e., $\lambda\big(\frac{\widetilde{\boldsymbol{L}}_\mu(e^{j\omega})}{e^{j\omega}-1}\big), \forall\omega\in[-\pi,\pi]$ does not enclose $(-1, j0)$ in terms of the fact $K_{Pi}, a_{ij} > 0$ based on general Nyquist stability criteria. Using Gerschgorin disk theorem, we have

$$\lambda\left(\frac{\widetilde{\boldsymbol{L}}_\mu(e^{j\omega})}{e^{j\omega}-1}\right) \in \bigcup_{i\in\mathcal{V}_\mu}\mathcal{S}_i, \forall\omega\in[-\pi,\pi]$$

$$\mathcal{S}_i = \left\{ s\in\mathbb{C} : \left|s - \frac{K_{Pi}d_i}{e^{j\omega}-1}\right| \le \sum_{(i,j)\in\mathcal{E}_\mu}\left|\frac{K_{Pi}a_{ij}e^{-j\omega}}{e^{j\omega}-1}\right| \le \left|\frac{K_{Pi}d_i}{e^{j\omega}-1}\right| \right\}$$

Define

$$F(j\omega) = \frac{K_{Pi}d_i}{e^{j\omega}-1} = -\frac{K_{Pi}d_i}{2} - j\frac{K_{Pi}d_i\cos\frac{\omega}{2}}{2\sin\frac{\omega}{2}}$$

which is the centre of $\mathcal{S}_i$ and its modulus is the radius. The trajectory of $F(jw)$, i.e. Nyquist plot, and the corresponding Gerschgorin disks are shown in Figure 2.7, from which we find $\lambda\left(\frac{\widetilde{\boldsymbol{L}}_\mu(e^{j\omega})}{e^{j\omega}-1}\right), \forall\omega \in [-\pi,\pi]$ does not enclose $(-1,j0)$ as long as $(-1,j0)$ is outside $\mathcal{S}_i$, i.e., $(-1,j0) \notin \mathcal{S}_i$:

$$|-1-F(j\omega)|^2 - |F(j\omega)|^2 = 1 - K_{Pi}d_i = 1 - |\mathcal{E}_{\mu,i}|K_{Pi} > 0$$

which is satisfied by Eq. (2.21b).

Therefore, Theorem 2.1 is proved. $\square$

Remark 2.4. *The design principles Eqs.* (2.21a) *and* (2.21b) *in Theorem 2.1 are delay independent, owing to that bounded communication delay does not affect the selection of control gains in consensus problems [70, 71]. Such bounded communication delay in the MG control of wireless-based post-event response derives from $T_s^\mu \geq \tau_{\max}^\mu$ in Algorithm 2.2. Larger T_s^μ may slower consensus, while $T_s^\mu < \tau_{\max}^\mu$ will lead to cumulative delays among wireless communications. Such time-varying and unbounded communication delays could lead to complicated design*

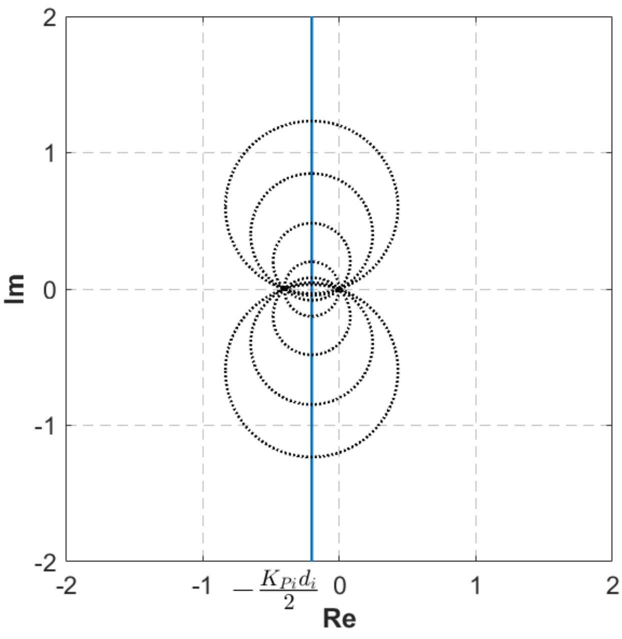

Figure 2.7: Nyquist plot of $F(jw)$.

and dynamics [70].

Remark 2.5. *From Eq.* (2.20)*, only active power sharing, which balances the reserved power among dispatchable resources, requires cyber-layer wireless communication. In other words, frequency and voltage regulation only requires localised measurement. This means, before backup wireless communication is absolutely initialised, decentralised controlled MG systems can be stabilised, which is significant for emergency wireless formation.*

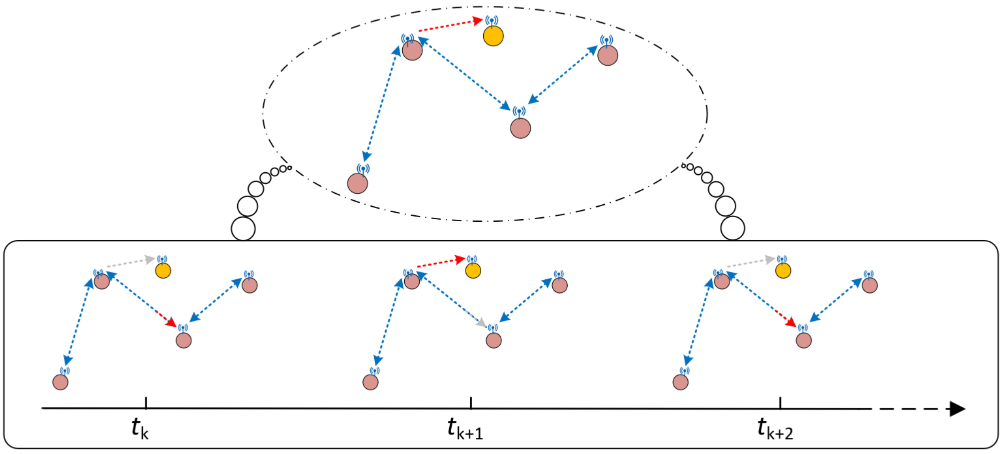

Figure 2.8: Cyber solution for mobile resources.

Mobile resources, e.g., portable energy storage and dispatchable electrified transportation have potentials to provide emergency response to extreme conditions [72, 73], and mobility requires the plug-and-play operation of MGs. Although plug-and-play operation has been widely investigated from a physical-layer perspective [41, 43, 67], it has not been investigated from a cyber-layer especially under extreme conditions. Due to limited communication bandwidth, just one-way communication is designed, i.e., mobile DGs only receive the information from networked DGs that have pre-designed in the cyber-layer network. One pre-designed and networked DG alternatively share information with one of previous fixed neighbours and one mobile DG, as shown in Figure 2.8, leading to second-order delay in the second item in Eq. (2.20). The stability remains guaranteed by the analysis in Remark 2.4 still using Theorem 2.1. It is worth noting that the cyber solution of such plug-and-play operation cannot handle massive mobile resources, which is reasonable because most mobile devices have been dynamically scheduled, only limited plug-and-play operation needs to be mitigated in the post-event period.

Remark 2.6. *The proposed framework can cope with the increasing DGs and MGs in both normal condition and extreme condition. In the normal condition, the increasing DGs can be efficiently coordinated and regulated by base stations through appropriate bandwidth allocation algorithms. In the extreme condition, the increase in MG number will not affect the intra-MG communication network as a connected subgraph because the inter-MG interference/collision between wireless links is limited. In other words, the communication network of the intra-regional MG can reuse bandwidth resources with other regional MGs. Inside the MG, the increasing DG numbers and distances lead to increasing time delays. Although it will not affect the control gain by Theorem 2.1 to guarantee the stability, the sampling interval increases as the time delay, thus decreasing the convergence rate.*

2.5 Results

In this section, the centralised-to-decentralised cyber-physical cooperative response to enable the critical power supply is verified through the power network detailed in Figure 2.9, where three emergency MGs, naturally clustered by geographical locations are available to maintain critical power supply.

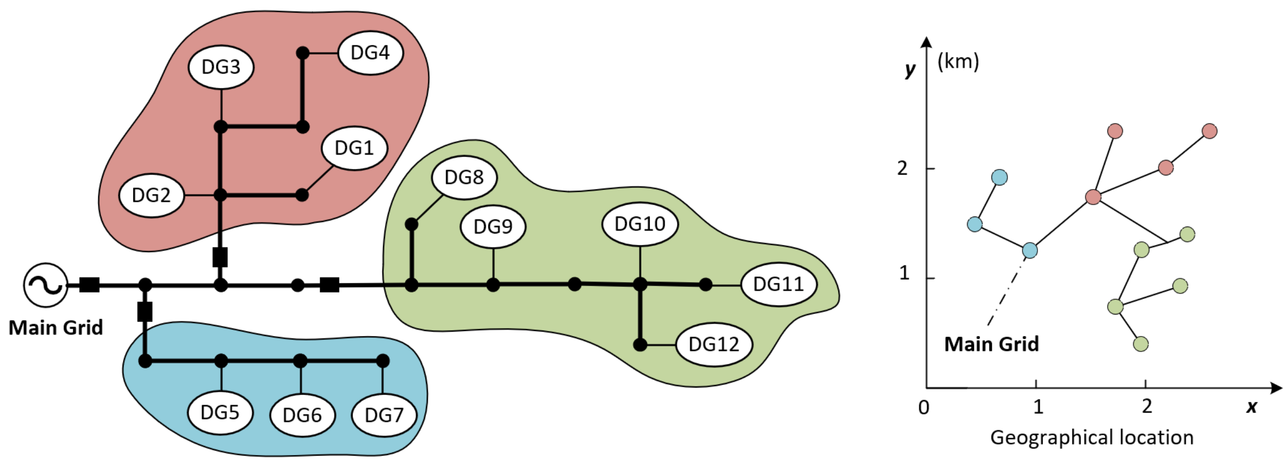

Figure 2.9: Diagram of the tested topology.

2.5.1 Results of Dynamic Cyber-Layer Pre-Event Scheduling

The parameters of the cyber layer are detailed by Table 2.2 and Eq. (2.25) [56, 61].

$$
\text{Distance Matrix (km)} = \\
\begin{bmatrix}
0 & 0.64 & 0.56 & 0.86 & & & & & & & & \\
0.64 & 0 & 0.72 & 1.20 & & & & & & & & \\
0.56 & 0.72 & 0 & 0.52 & & & & & & & & \\
0.86 & 1.20 & 0.52 & 0 & & & & & & & & \\
& & & & 0 & 0.55 & 0.72 & & & & & \\
& & & & 0.55 & 0 & 0.48 & & & & & \\
& & & & 0.72 & 0.48 & 0 & & & & & \\
& & & & & & & 0 & 0.45 & 0.93 & 0.62 & 1.10 \\
& & & & & & & 0.45 & 0 & 0.58 & 0.48 & 0.86 \\
& & & & & & & 0.93 & 0.58 & 0 & 0.48 & 0.41 \\
& & & & & & & 0.62 & 0.48 & 0.48 & 0 & 0.64 \\
& & & & & & & 1.10 & 0.86 & 0.41 & 0.64 & 0
\end{bmatrix}
\tag{2.25}
$$

Under the scenario with all DGs being dispatchable (Scenario 1), using Algorithm 2.1, the

Table 2.2: Parameters of Pre-Event C2C Wireless Network Scheduling

Parameters	Values
sub-carrier bandwidth (w)	25 kHz
number of sub-carriers (L)	40
maximum transmission power ($P_{i,\max}$)	24 dBm
constant power ($P_{i,\text{cst}}$)	0.1 dBm
noise power (σ^2)	-62 dBm
packet size (L_{packet})	32 bytes
pathloss exponent (α)	3
loss factor (h)	0.09

cyber layer of emergency MGs is scheduled by

$$\mathcal{A} = \begin{bmatrix} 0 & 1 & 1 & 0 & & & & & & & & \\ 1 & 0 & 0 & 0 & & & & & & & & \\ 1 & 0 & 0 & 1 & & & & & & & & \\ 0 & 0 & 1 & 0 & & & & & & & & \\ & & & & 0 & 1 & 0 & & & & & \\ & & & & 1 & 0 & 1 & & & & & \\ & & & & 0 & 1 & 0 & & & & & \\ & & & & & & & 0 & 1 & 0 & 0 & 0 \\ & & & & & & & 1 & 0 & 0 & 1 & 0 \\ & & & & & & & 0 & 0 & 0 & 1 & 1 \\ & & & & & & & 0 & 1 & 1 & 0 & 0 \\ & & & & & & & 0 & 0 & 1 & 0 & 0 \end{bmatrix}$$

From the adjacent matrix $\mathcal{A}$, we can find all three subgraphs are optimised to be connected as the emergency wireless network serving power supply locally. The minimised transmit delays $\boldsymbol{\tau}_{\max} = [87.5\ 55.4\ 44.6]^T$(ms), hence the sampling intervals in the localised controllers of DGs are set as $\boldsymbol{T}_s = [100\ 60\ 50]^T$(ms).

If DG 2, DG 9 and DG 11 are randomly out-of-service or non-dispatchable (Scenario 2), the corresponding cyber-layer scheduling result is

$$\mathcal{A} = \begin{bmatrix} 0 & - & 1 & 0 & & & & & & & & \\ - & - & - & - & & & & & & & & \\ 1 & - & 0 & 1 & & & & & & & & \\ 0 & - & 1 & 0 & & & & & & & & \\ & & & & 0 & 1 & 0 & & & & & \\ & & & & 1 & 0 & 1 & & & & & \\ & & & & 0 & 1 & 0 & & & & & \\ & & & & & & & 0 & - & 1 & - & 0 \\ & & & & & & & - & - & - & - & - \\ & & & & & & & 1 & - & 0 & - & 1 \\ & & & & & & & - & - & - & - & - \\ & & & & & & & 0 & - & 1 & - & 0 \end{bmatrix} \tag{2.26}$$

with the minimised transmit delays $\boldsymbol{\tau}_{\max} = [63.3\ 55.4\ 174]^T$(ms). Although the number of non-dispatchable DGs declines in the 3_{rd} MG compared to Scenario 1, the delay increases due to longer transmitting distances.

2.5.2 Results of Post-Event Response

Take Scenario 1 as an example, the post-event response algorithm is verified. The performance of the designed DAPI discrete controller is evaluated with different gains, and mobile resources are also discussed further under plug-and-play operations.

Response to Blackout

The control performance of the proposed C2C distributed control in response to blackouts is shown in Figure 2.10. After the occurrence of blackouts at t = 3 seconds, owing to the grid-forming techniques, DGs maintain the critical power supply by emergency MGs in terms of geographical locations using primary control, which leads to the control deviation. Then, the secondary control is activated at t = 4 seconds, when D2D-communication-based wireless network is completely initialised and only critical load demand is supplied. Followed by Theorem 2.1, the stability of MGs is guaranteed, and the control objectives of Eqs. (2.15) and (2.16) can be reached, though the load demand changes at $t = 6, 8$ seconds.

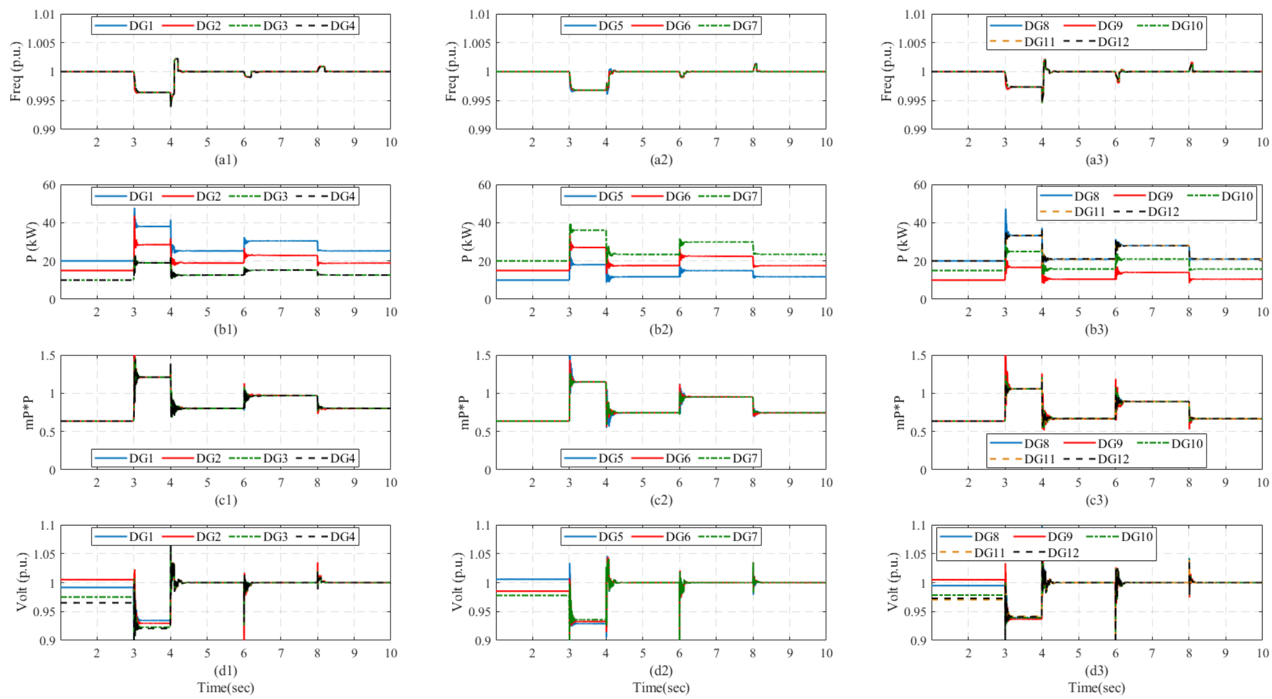

Figure 2.10: Control performance with reasonable $\boldsymbol{K}_\omega, \boldsymbol{K}_P, \boldsymbol{K}_U$.

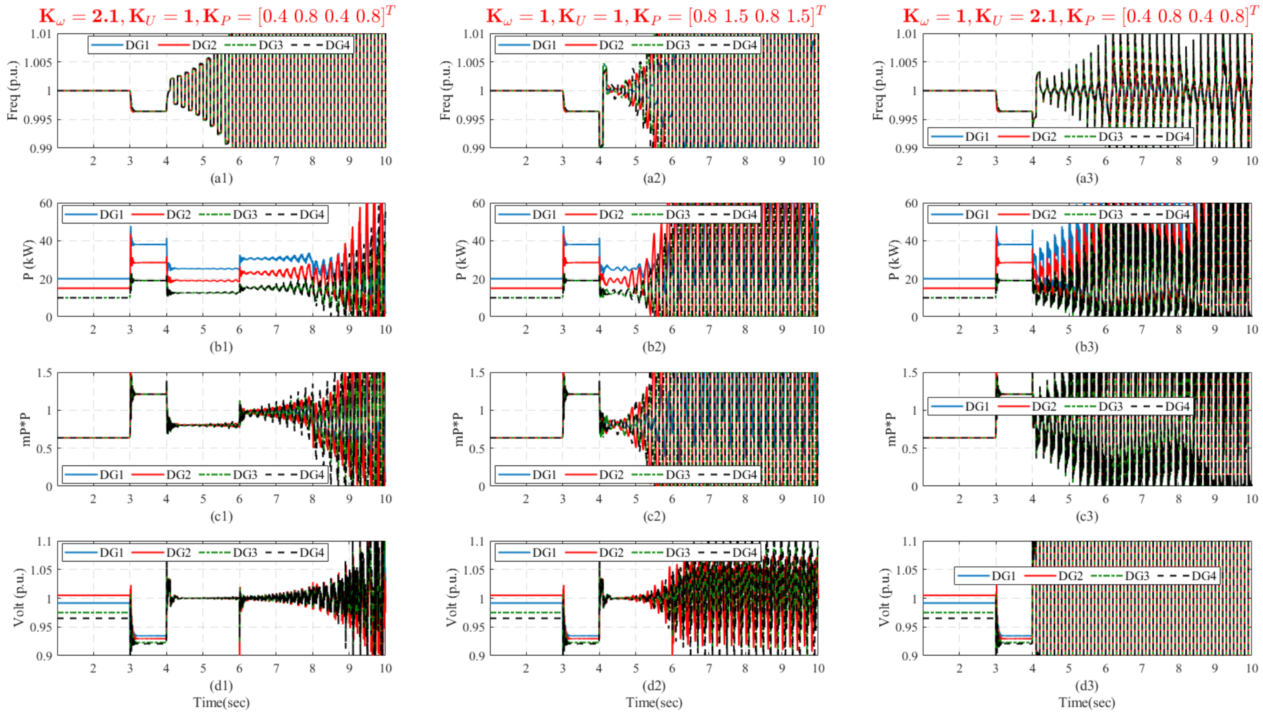

Figure 2.11: Control performance with unreasonable $\boldsymbol{K}_\omega, \boldsymbol{K}_P, \boldsymbol{K}_U$.

In order to verify the parameter design using Theorem 2.1, we set the control gains different from that in the benchmark Figure 2.10, i.e., $\boldsymbol{K}_\omega = \mathbf{1}, \boldsymbol{K}_U = \mathbf{1}, \boldsymbol{K}_P = [0.4\ 0.8\ 0.4\ 0.8]^T$ of the 1_{st} MG that satisfy Theorem 2.1. From Figure 2.11, it is clear that the control performance degrades in all scenarios. More specifically, $\boldsymbol{K}_\omega = \mathbf{2.1}, \boldsymbol{K}_U = \mathbf{2.1}$, and $\boldsymbol{K}_P = [0.8\ 1.5\ 0.8\ 1.5]^T$, exceeding to the boundaries of criteria Eqs. (2.21a) and (2.21b) respectively, lead to the divergence of frequency, voltage and active power sharing.

Response to Mobile Resources

The scheduled cyber-layer wireless enables mobile resources providing emergency power supply, which is illustrated by Figure 2.12. The 3_{rd} MG is islanded at $t = 3$ seconds and the proposed C2C-enabled cyber-physical control strategy is activated at $t = 4$ seconds. During $6 \leq t \leq 8$ seconds, the mobile resource, i.e., DG 13, is plugged in the MG, and frequency, voltage and active power sharing remains controlled as Eqs. (2.15),(2.16) though transient dynamics exist at the stage of emergency response. After disconnecting DG 13 from the MG at $t = 8$ seconds, the cyber-physical post-event response remains effective.

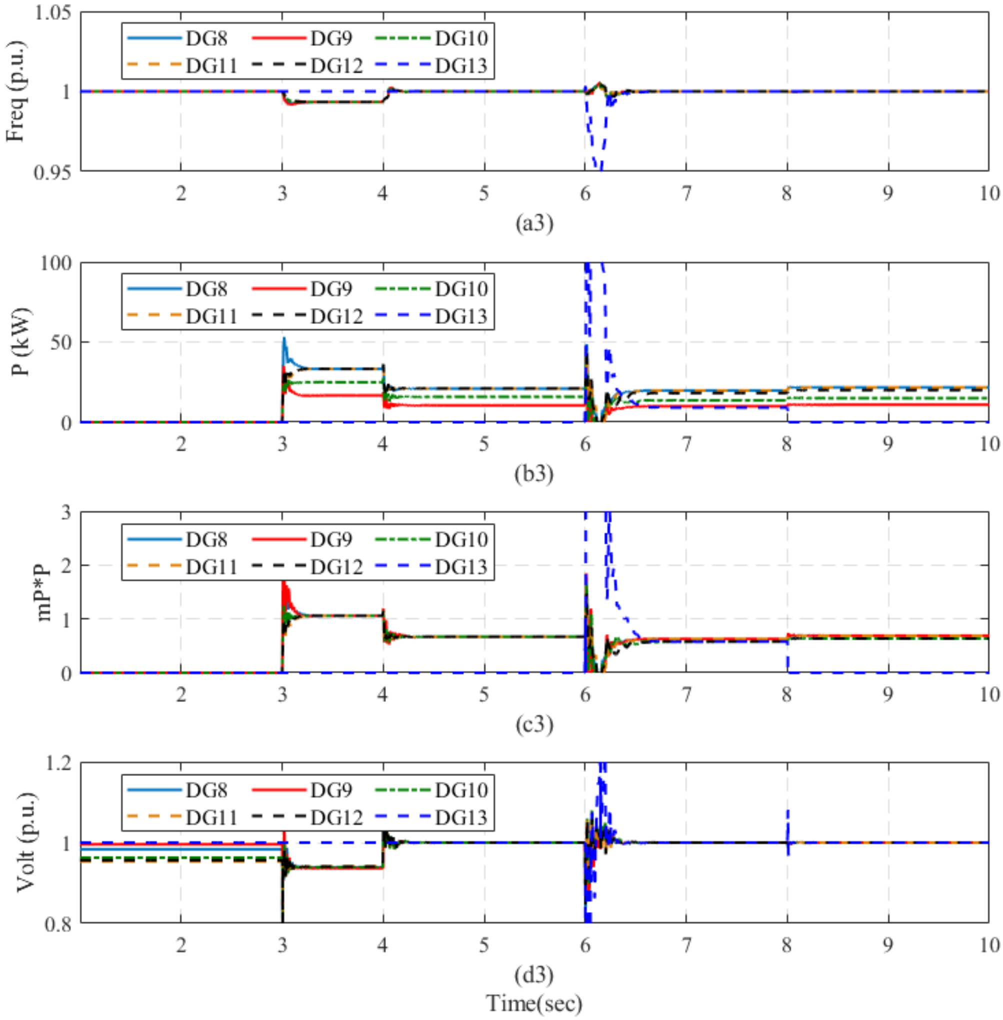

Figure 2.12: Control performance with mobile resources.

2.5.3 Comparison of Post-Event Response Performance

As shown in Figure 2.13, the post-event response performance of the 1*st* MG under proposed framework is compared with other solutions, including decentralised strategy without neighbouring communication, centralised strategy and centralised-to-decentralised mitigation without dynamic pre-event schedule. The decentralised mitigation without neighbouring communication (first column) regulates the frequency and voltage to their references, while the power sharing is not accurately guaranteed, see the third row. The centralised mitigation utilises the same bandwidth that is allocated in Section 2.5.2. Due to the long distance of data flow in the centralised framework, the delays (8.35 seconds) induced by the limited bandwidth lead to the uncontrollable period between two sampling intervals. If the centralised-to-decentralised

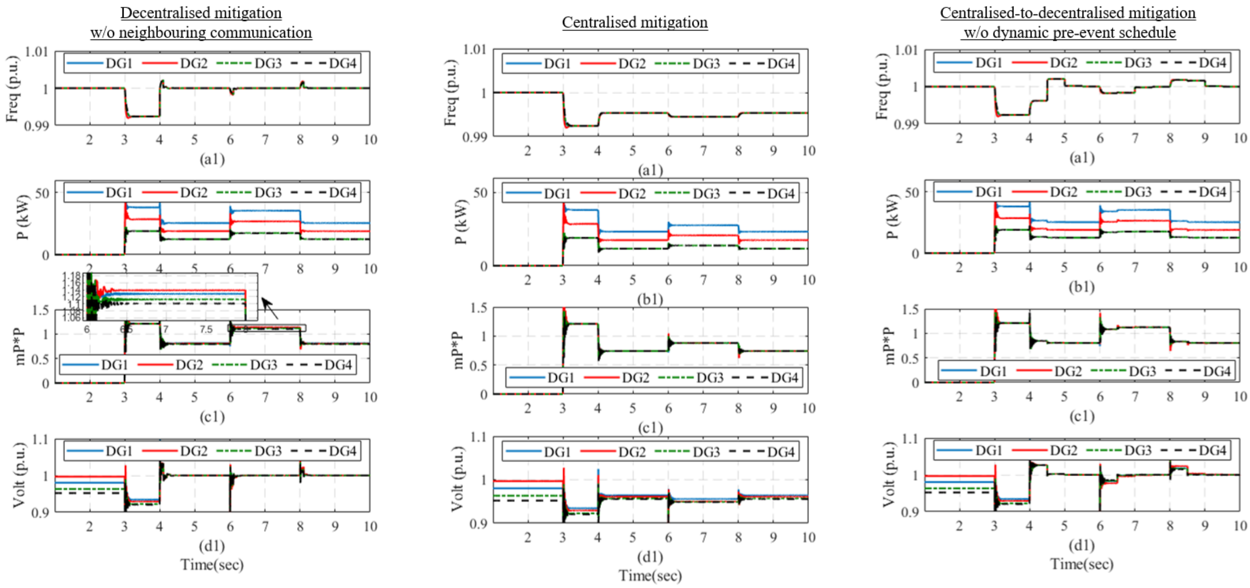

Figure 2.13: Comparisons of post-event response performance.

mitigation without dynamic schedule strategy is applied, the scheduled delays should be conservative by the consideration of the worst case, leading to a large sampling interval. Such design degrades the post-event response performance as shown in the third column. All three solutions have not achieved the optimised response performance, compared to Figure 2.10. Although the basic stability can be guaranteed by the grid-forming technique, optimised voltage, frequency, and power sharing may be compromised under such emergency conditions.

2.6 Conclusion

This chapter proposes a centralised-to-decentralised framework to enhance the resilience of power supply in response to possible failures/blackouts caused by ACPEs. In the proposed resilient framework, the cyber-physical response plan is dynamically updated in the centralised controller of networked MGs under the normal operation, where cyber-layer C2C communication and physical-layer emergency MGs formation are pre-scheduled. Considering the possible damage to base stations, the backup communication employs dedicated wireless network to provide reliable services for real-time control. The inevitable delay derived from the backup bandwidth is then considered in the distributed control system design. At last, the whole pre-event scheduling process and post-event response performance are evaluated through the case studies.

Chapter 3

Resilient Secondary Voltage Control of Islanded Microgrids: An ESKBF-Based Distributed Fast Terminal Sliding Mode Control Approach

3.1 Introduction

Microgrid (MG) is a promising concept that supports the integration of distributed generators (DGs) into traditional bulk electric power systems [33, 74]. A MG, a group of interconnected loads and distributed energy resources within clearly defined electrical boundaries, acts as a single controllable entity with respect to the grid, and it can connect and disconnect from the grid to enable it to operate in both grid-connected and islanded (autonomous) modes [75]. While the dynamics of grid-connected MG are determined by the main grid, the stability of islanded MG highly relies on the underlining control strategy [33, 76].

To stabilize islanded MGs, a three-layer control structure has been proposed, including primary, secondary and tertiary control [64, 77, 78]. Primary control [77] is implemented locally to guarantee the stability of MGs by only using the local DG's information [79], while at the same time, secondary and tertiary control [64, 80, 81] are employed to ensure the voltage and frequency of MG being regulated to the references and the optimal power sharing. In general, the different levels differ in control goals and infrastructure requirements (i.e., communication requirements) [33]. The microgrid can benefit from this control hierarchy by decoupling control goals in terms of response speed and time frame, and DGs can respond to the load change independently thanks to the primary control that does not require communication.

The conventional secondary control is designed in a centralized mode [82, 83], where DGs receive control commands from a center controller. Due to the reliance on the communication network, the key drawbacks of centralized approach are: 1) high communication delays that might degrade the control performance; 2) poor plug-and-play capability; 3) low fault tolerance due to all-to-one control scheme [33, 84].

These drawbacks have been overcome by the development of distributed control scheme [85,86] and multi-agent system [84, 87]. In the existing literature for the distributed control of MG, the feedback linearization has been widely used to simplify the modelling of DG inner control loops by transferring the highly-nonlinear MG voltage control model into a single-input single-output second-order model [7,88]. Nevertheless, after the application of feedback linearization, one complex variable is required to represent the total non-linearity, consisting of many voltage and current variables. This complex variable is contaminated by inevitable measurement noise, the effect of which on the linearised MG control model has not been fully investigated. Thus, it is vital to evaluate and potentially eliminate the influence of measurement noise in the control system design.

Moreover, the co-existence of disturbances caused by different sources such as parameter perturbation and measurement noise has not been fully investigated. Although robust distributed control [89, 90] and noise-resilient control [67, 91] have been applied respectively, these control methods cannot simultaneously consider multiple types of disturbances efficiently. The effect of the measurement noise on the MG secondary control has not been considered in [7,88,92,93], though these methods show good robustness against parameter perturbation or other unmodeled uncertainty. The existing methods tend to consider the multiple disturbances separately, while a systematic and unified disturbance modelling framework has yet to be developed. The recent development of advanced disturbance-resilient methods in control theory, such as adaptive filter algorithms [94, 95], provides a strong theoretical basis to develop such modelling framework.

In addition, plug-and-play operation in the multi-DG network may lead to frequent and significant voltage fluctuations, which imposes a vast challenge on the fast restoration of the MG voltage. In this circumstance, the convergence rate in the distributed control of MG has received increasing attention. Some distributed control methods [7, 92, 93] has been designed for MGs to achieve finite-time convergence rate. However, the convergence of finite-time control protocol relies on its initial states, and the plug-and-play operation may cause unknown or diverse system initial states. For the MG system that emphasizes on the plug-and-play capability, a novel control strategy for resilience enhancement is required to alleviate such impact by improving the convergence performance.

To mitigate the aforementioned problems, a distributed robust fast terminal sliding mode (FTSM) secondary voltage control method based on extended state Kalman-Bucy filter (ESKBF) is proposed in this chapter. The ESKBF employs an extended state to denote the combination of different types of uncertainties, including parameter perturbation, measurement noise and immeasurably external variables. The proposed FTSM control enhances the convergence rate of MG voltage control, where the settling time of the distributed controller can be reduced. The main features and contributions of the proposed control method is summarised as follows:

1. linearised control-oriented model formulation under a unified modelling framework for multiple sources of disturbances: unlike the traditional disturbance observer that targets at filtering out exact disturbance magnitude, we integrate the multiple disturbances related to parameter perturbation, immeasurable variables and measurement noise into one extended state which was originally used to only represent the complicated nonlinear part of MG model caused by feedback linearization. This formulation significantly simplifies the observer design under multiple sources of disturbance.

2. Multi-disturbance resilient observer design: to obtain the accurate model state for the control implementation, the impact of multiple-source disturbance is first described by a combination of process noise and observation noise in the system model. Kalman-Bucy filter is then utilized to design a multi-disturbance resilient observer that can estimate the extended state value and cope with stochastic measurement noise without complicated parameter selection process required in the existing extended state observer design [96].

3. Faster convergence rate: to accelerate the convergence rate in the MG distributed voltage control for plug-and-play operation, a FTSM surface is designed by employing nonlinear terminal attractors to guarantee a faster convergence rate when the system is close to equilibrium. To achieve this, we propose a nonlinear control protocol and prove its global stability. Through the coordination of FTSM control and the proposed nonlinear control protocol, the voltage control of MG can achieve globally consensus stability with short settling time. In addition, this control framework can be extended to balance voltage regulation and accurate reactive power sharing.

This chapter is structured as follows. In Section 3.2, preliminary notions of graph theory and the detailed model of islanded MG are introduced. Section 3.3 introduces the ESKBF-based observer for MG voltage control, and in Section 3.4, the FTSM secondary voltage control is discussed. Then, Section 3.5 illustrates the implementation structure of the proposed control scheme. Finally, simulation and experimental results are analyzed in Section 3.6 and the conclusion and future work are discussed in Section 3.7.

3.2 Preliminaries and Model Description

3.2.1 Preliminary of Graph Theory

The communication topology among DGs in a MG can be modeled as a weighted graph $\mathcal{G} = \{\mathcal{V}, \mathcal{E}, \mathcal{A}\}$ with a DG node set $\mathcal{V} = \{v_1, v_2, \cdots, v_N\}$, a communication edge set $\mathcal{E} \subset \mathcal{V} \times \mathcal{V}$, and a weighted adjacent matrix $\mathcal{A} = [a_{ij}] \in \mathbb{R}^{N\times N}$. If DG node v_i can receive information

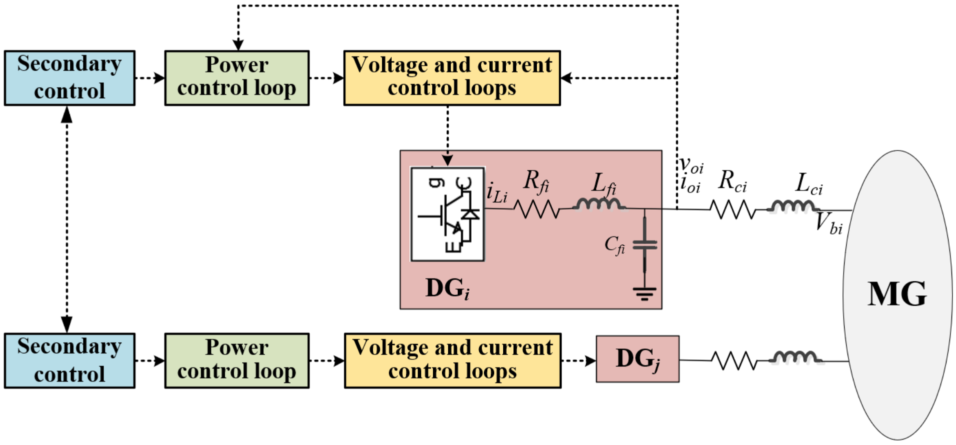

Figure 3.1: Block diagram of an inverter-based MG.

from DG node v_j, edge $(v_j, v_i) \in \mathcal{E}$ and set $N_i = \{j|(v_j, v_i) \in \mathcal{E}\}$ means neighbors of node i. For adjacent matrix $\mathcal{A}$, elements $a_{ii} = 0$ and $a_{ij} \geq 0$. $a_{ij} > 0$ if and only if $(v_i, v_j) \in \mathcal{E}$. The Laplacian matrix of $\mathcal{G}$ is defined as $\mathcal{L} = [l_{ij}] = \mathcal{D} - \mathcal{A} \in \mathbb{R}^{N\times N}$, where $\mathcal{D} = \text{diag}\{d_i\}$ denotes the in-degree matrix with $d_i = \sum_{j\in N_i} a_{ij}$ [97]. The eigenvalues of the Laplacian matrix $\mathcal{L}$ of a distributed communication topology are highly related to control performance, which will be analysed for the control design later in Section 3.4.2.

A MG can be modeled as a leader-following multi-agent system with N DGs. In this leader-following structure, the frequency and voltage references are only available to a small portion of DGs (as "leader"). Other DGs (as "followers") have neighboring information through a sparse communication structure, and then "followers" can track to the "leader" DGs' frequency and voltage. The adjacency matrix extended by the reference node is denoted as $\mathcal{B} = \text{diag}\{b_i\} \in \mathbb{R}^{N\times N}$, in which if the reference node is a neighbor of node v_i, $b_i > 0$; otherwise, $b_i = 0$. The corresponding Laplacian matrix $\overline{\mathcal{L}} = \mathcal{L} + \mathcal{B}$.

3.2.2 Large-Signal Dynamic Model of MGs with Inverter-Based DGs

As depicted in Figure 3.1, each DG unit contains a DC/AC inverter, an inductor-capacitor filter (LCF) and a resistor-inductor connection, and its controller is composed of three control loops formulated on its own direct-quadrature frame $(d - q)_i$ at rotating frequency ω_i: power control loop, voltage control loop and current control loop [7, 88].

The power control loop of each DG controller generates the angular frequency and voltage references for the whole DG system, while voltage and current loops enable the inverter system to track the angular frequency and voltage references. Droop control [79] is typically used in the power control loop, and it can describe the relationship between angular frequency, output voltage magnitude and power output:

$$\omega_i = \omega_{ni} - m_{Pi} P_i \tag{3.1}$$

$$v^*_{o,magi} = v^*_{odi} = V_{ni} - n_{Qi} Q_i \tag{3.2}$$

$$v^*_{oqi} = 0 \tag{3.3}$$

where ω_i is the angular frequency of the ith DG; v^*_{odi} and v^*_{oqi} are the d-axis and q-axis components of $v^*_{o,magi}$, and $v^*_{odi} = v^*_{o,magi}$ due to the fact that $v^*_{o,magi}$ often aligns itself on the d-axis; P_i and Q_i are the active power and reactive power; m_{Pi} and n_{Qi} are the frequency and voltage droop coefficients, which are selected based on the active and reactive power ratings of each DG [64]; ω_{ni} and V_{ni} are references for primary control that are generated from the secondary control.

The power elements P_i and Q_i are obtained by instantaneous power calculation and low-pass filter, which can be expressed as follows:

$$P_i = \frac{\omega_{ci}}{s + \omega_{ci}} (v_{odi} i_{odi} + v_{oqi} i_{oqi}) \tag{3.4}$$

$$Q_i = \frac{\omega_{ci}}{s + \omega_{ci}} (v_{oqi} i_{odi} - v_{odi} i_{oqi}) \tag{3.5}$$

where $v_{odi}, v_{oqi}, i_{odi}, i_{oqi}$ are the d-axis and q-axis components of output voltage v_{oi} and output current i_{oi}. ω_{ci} is the cut-off frequency of low-pass filter.

To model all DG inverters synchronized in the common frequency frame with the rotating frequency ω_{com}, δ_i is employed to represent the angular frequency difference of the ith DG unit compared to the common reference frame:

$$\dot{\delta}_i = \omega_i - \omega_{com} \tag{3.6}$$

The dynamics of voltage and current control loops have been discussed in [7, 88, 93], and are omitted here. By combining dynamic models of the three control loops and LCF, the large-signal dynamic model of the ith DG over a MG system can be detailed as the following multi-input multi-output (MIMO) nonlinear system:

$$\dot{\boldsymbol{x}}_i = \boldsymbol{f}_i(\boldsymbol{x}_i) + \boldsymbol{g}_i(\boldsymbol{x}_i)\boldsymbol{u}_i + \boldsymbol{k}_i(\boldsymbol{x}_i)\boldsymbol{d}_i \tag{3.7}$$

where the state vector is

$$\boldsymbol{x}_i = [\delta_i \ P_i \ Q_i \ \phi_{di} \ \phi_{qi} \ \gamma_{di} \ \gamma_{qi} \ i_{ldi} \ i_{lqi} \ v_{odi} \ v_{oqi} \ i_{odi} \ i_{oqi}]^T$$

and system input $\boldsymbol{u}_i = [\omega_i \ V_{ni}]^T$; $\boldsymbol{d}_i = [\omega_{com} \ v_{bdi} \ v_{bqi}]^T$ are the considered disturbance.

It should be noted that the dispatchable DGs considered in this chapter are controlled by grid-forming inverters [98]. A class of grid-forming inverters with the droop control loop have been widely adopted in the current secondary control scheme of MGs [92, 93, 99]. The DGs that operate in maximum power tracking mode are normally controlled by grid-supporting or grid-feeding inverters, and dispatched in different layers [66].

3.3 Extended State Observer Design for Secondary Voltage Control

In this section, to enhance the resilience and robustness of secondary voltage control of MG, an extended state observer is designed to mitigate the influence of multiple sources of disturbance on the control performance. As for a distributed control structure, each DG should consider their control design from a local perspective. Hence, from a point view of each DG, the state of the point of connection is seen as external signals hereafter in this section.

3.3.1 Model Linearization of Nonlinear Systems

For the secondary voltage control of MG, the ith DG system model (3.7) can be described as the following single-input single-output (SISO) system:

$$\begin{cases} \dot{\boldsymbol{x}}_i = \boldsymbol{f}_i(\boldsymbol{x}_i) + \boldsymbol{g}_i(\boldsymbol{x}_i)u_i + \boldsymbol{k}_i(\boldsymbol{x}_i)\boldsymbol{d}_i \\ \quad = \boldsymbol{F}_i(\boldsymbol{x}_i) + \boldsymbol{g}_i(\boldsymbol{x}_i)u_i \\ y_i = v_{odi} = h_i(\boldsymbol{x}_i) \end{cases} \tag{3.8}$$

where $u_i = V_{ni}$.

By applying feedback linearization method, the nonlinear system (3.8) can be transformed into:

$$\begin{cases} \dot{y}_{i,1} = \dot{v}_{odi} = y_{i,2} \\ \dot{y}_{i,2} = \ddot{v}_{odi} = L^2_{\boldsymbol{F}_i} h_i(\boldsymbol{x}_i) + L_{\boldsymbol{g}_i} L_{\boldsymbol{F}_i} h_i(\boldsymbol{x}_i) u_i \\ \quad y_i = y_{i,1} = v_{odi} \end{cases} \tag{3.9}$$

and

$$\begin{cases} L_{\boldsymbol{F}_i} h_i(\boldsymbol{x}_i) = \dfrac{\partial h_i}{\partial \boldsymbol{x}_i} \boldsymbol{F}_i(\boldsymbol{x}_i) \\ L^k_{\boldsymbol{F}_i} h_i(\boldsymbol{x}_i) = \dfrac{\partial L^{k-1}_{\boldsymbol{F}_i} h_i}{\partial \boldsymbol{x}_i} \boldsymbol{F}_i(\boldsymbol{x}_i) \\ L_{\boldsymbol{g}_i} L^{k-1}_{\boldsymbol{F}_i} h_i(\boldsymbol{x}_i) = \dfrac{\partial L^{k-1}_{\boldsymbol{F}_i} h_i}{\partial \boldsymbol{x}_i} \boldsymbol{g}_i(\boldsymbol{x}_i) \end{cases} \tag{3.10}$$

where $L_{\boldsymbol{F}_i} h_i(\boldsymbol{x}_i)$ represents the Lie derivative [100] of $h_i(\boldsymbol{x}_i)$ along $\boldsymbol{F}_i(\boldsymbol{x}_i)$.

Define $z_i = L^2_{\boldsymbol{F}_i} h_i(\boldsymbol{x}_i) + L_{\boldsymbol{g}_i} L_{\boldsymbol{F}_i} h_i(\boldsymbol{x}_i) u_i$, the system (3.9) can be expressed as a second-order linear system:

$$\begin{cases} \dot{y}_{i,1} = y_{i,2} \\ \dot{y}_{i,2} = z_i \\ \quad y_i = y_{i,1} = v_{odi} \end{cases} \tag{3.11}$$

and the input of the nonlinear system (3.8) is

$$u_i = \frac{z_i - L_{\boldsymbol{F}_i}^2 h_i(\boldsymbol{x}_i)}{L_{\boldsymbol{g}_i} L_{\boldsymbol{F}_i} h_i(\boldsymbol{x}_i)} \tag{3.12}$$

3.3.2 Control-Oriented Model Formulation Considering System Disturbances

Although the second-order linear system model (3.11) is simple and convenient for the design of distributed secondary voltage control, it is difficult to obtain the accurate value of system state $y_{i,2}$ in (3.11) and the original system input u_i in (3.12).

The state $y_{i,2} = \dot{v}_{odi}$ is in the differential form and can not be directly obtained in the industrial practice. Therefore, to avoid the differential operation, the state can be accessed by the equation described in (3.7):

$$\dot{v}_{odi} = \omega_i v_{oqi} + \frac{i_{ldi} - i_{odi}}{C_{fi}} \tag{3.13}$$

To obtain the original input u_i in (3.12), the two variables, $L_{\boldsymbol{F}_i}^2 h_i(\boldsymbol{x}_i)$ and $L_{\boldsymbol{g}_i} L_{\boldsymbol{F}_i} h_i(\boldsymbol{x}_i)$, which consist of numerous measurement variables, can be expressed as

$$\begin{aligned} L_{\boldsymbol{F}_i}^2 h_i(\boldsymbol{x}_i) = {} & (-\omega_i^2 - \frac{K_{Pci}K_{Pvi}+1}{C_{fi}L_{fi}} - \frac{1}{C_{fi}L_{ci}})v_{odi} - \frac{\omega_b K_{Pci}}{L_{fi}} v_{oqi} + \frac{R_{ci}}{C_{fi}L_{ci}} i_{odi} - \frac{2\omega_i}{C_{fi}} i_{oqi} \\ & - \frac{R_{fi}+K_{Pci}}{C_{fi}L_{fi}} i_{ldi} + \frac{2\omega_i - \omega_b}{C_{fi}} i_{lqi} - \frac{K_{Pci}K_{Pvi}n_{Qi}}{C_{fi}L_{fi}} Q_i + \frac{K_{Pci}K_{Ivi}}{C_{fi}L_{fi}} \phi_{di} + \frac{K_{Ici}}{C_{fi}L_{fi}} \gamma_{di} + \frac{1}{C_{fi}L_{ci}} v_{bdi} \end{aligned} \tag{3.14}$$

$$L_{\boldsymbol{g}_i} L_{\boldsymbol{F}_i} h_i(\boldsymbol{x}_i) = \frac{K_{Pci}K_{Pvi}}{C_{fi}L_{fi}} \tag{3.15}$$

where ω_b is the rated frequency of the MG; v_{bdi} represents q-axis voltage at the connection bus between DG and MG; i_{ldi}, i_{lqi} denote the d-axis and q-axis currents of filter inductance; K_{Pvi}, K_{Ivi} and K_{Pci}, K_{Ici} denote the proportional, integral gains of voltage and current control loops respectively; R_{fi}, L_{fi}, C_{fi} denote resistance, inductance and capacitance values of LCF; R_{ci}, L_{ci} denote output resistance and inductance values.

From (3.13)-(3.15), it is clear that the intermediate variables $\dot{v}_{odi}$, $L^2_{\boldsymbol{F}_i} h_i(\boldsymbol{x}_i)$ and $L_{\boldsymbol{g}_i} L_{\boldsymbol{F}_i} h_i(\boldsymbol{x}_i)$ mainly consist of three different parts, measurable variables, immeasurable variables and parameters. To fully investigate the effects of the existing disturbances, we consider three corresponding uncertain factors: measurement noise, exogenous disturbance and parameter perturbation.

For the secondary voltage control of MG, the influence of measurement noise cannot be ignored as such noise can be amplified by inductance and capacitance values that are relatively small (order of magnitude: 10^{-3} or 10^{-6}). Exogenous disturbance from immeasurable variables and parameter perturbation can bring deviation to $L^2_{\boldsymbol{F}_i} h_i(\boldsymbol{x}_i)$ and $L_{\boldsymbol{g}_i} L_{\boldsymbol{F}_i} h_i(\boldsymbol{x}_i)$, thus reducing system controlling accuracy. Moreover, for those measurable variables such as voltages and currents inside the inverters, if the intermediate variables by (3.13)-(3.15) are introduced in the control system, a large number of measurement units need to be deployed for direct measurements. Therefore, to overcome negative effects of the aforementioned disturbance, an extended state observer is employed to observe accurate values of $\dot{v}_{odi}$, $L^2_{\boldsymbol{F}_i} h_i(\boldsymbol{x}_i)$ and $L_{\boldsymbol{g}_i} L_{\boldsymbol{F}_i} h_i(\boldsymbol{x}_i)$.

The linearised model considering system disturbance for the ith DG (3.9) can be extended as:

$$\begin{cases} \dot{y}_{i,1} = y_{i,2} \\ \dot{y}_{i,2} = \xi_i + g_{i,0} u_i \\ \quad \dot{\xi}_i = \psi_i \\ \quad y_i = y_{i,1} = v_{odi} \end{cases} \tag{3.16}$$

where

$$g_i = g_{i,0} + \Delta g_i = L_{\boldsymbol{g}_i} L_{\boldsymbol{F}_i} h_i(\boldsymbol{x}_i) \tag{3.17}$$

$$\xi_i = L^2_{\boldsymbol{F}_i} h_i(\boldsymbol{x}_i) + \Delta g_i u_i \tag{3.18}$$

$[y_{i,1}\ y_{i,2}]^T$ is the original state vector, while ξ_i is the extended state; $g_{i,0}$ and Δg_i denote nominal value and the deviation caused by parameter perturbation of g_i respectively.

Through introducing ξ_i, the effect of the uncertainty in g_i is removed by using the constant nominal value. More importantly, the extended state ξ_i represents the sum of DG inner control loops' dynamics and total uncertainties caused by exogenous disturbance, parameter perturbation and the measurement noise. As a result, the problem of calculating the three variables (3.13)-(3.15) is converted to obtain the values of ξ_i and $y_{i,2}$, which can be directly obtained as the state variables in the system (3.16) by filtering out the influence of zero-mean and high-frequency measurement noise.

3.3.3 Multi-Disturbance Resilient Extended State Observer Design Based on Kalman-Bucy Filter

The extended state system model (3.16) can be written in a matrix form:

$$\begin{cases} \begin{bmatrix} \dot{\boldsymbol{x}}_{v,i} \\ \dot{\xi}_i \end{bmatrix} = \begin{bmatrix} \mathbf{A} & \mathbf{E} \\ \mathbf{0} & 0 \end{bmatrix} \begin{bmatrix} \boldsymbol{x}_{v,i} \\ \xi_i \end{bmatrix} + \begin{bmatrix} \mathbf{B} \\ 0 \end{bmatrix} u_i + \begin{bmatrix} \mathbf{0} \\ \psi_i \end{bmatrix} + \boldsymbol{w}_i \\ \boldsymbol{y}_i = \begin{bmatrix} \mathbf{C} & 0 \end{bmatrix} \begin{bmatrix} \boldsymbol{x}_{v,i} \\ \xi_i \end{bmatrix} + \boldsymbol{\nu}_i \end{cases} \tag{3.19}$$

where $\boldsymbol{x}_{v,i} = [v_{odi}\ \dot{v}_{odi}]^T$ denotes original state vector in the second-order system; $\boldsymbol{w}_i = [\boldsymbol{w}_{\boldsymbol{x},i}\ 0]^T$ and $\boldsymbol{\nu}_i$ respectively represent the process noise and the observation noise; the corresponding constant matrices are

$$\mathbf{A} = \begin{bmatrix} 0 & 1 \\ 0 & 0 \end{bmatrix}, \mathbf{B} = \begin{bmatrix} 0 \\ g_{i,0} \end{bmatrix}, \mathbf{C} = \begin{bmatrix} 1 & 0 \end{bmatrix}, \mathbf{E} = \begin{bmatrix} 0 \\ 1 \end{bmatrix}.$$

To simplify the observer design, system (3.19) can be expressed as

$$\begin{cases} \dot{\boldsymbol{x}}_{\text{ex},i} = \mathbf{A}_{\text{ex}} \boldsymbol{x}_{\text{ex},i} + \mathbf{B}_{\text{ex}} u_i + \boldsymbol{\Psi}_i + \boldsymbol{w}_i \\ \boldsymbol{y}_i = \mathbf{C}_{\text{ex}} \boldsymbol{x}_{\text{ex},i} + \boldsymbol{\nu}_i \end{cases} \tag{3.20}$$

where

$$\boldsymbol{x}_{\mathrm{ex},i} = \begin{bmatrix} \boldsymbol{x}_{v,i} \\ \xi_i \end{bmatrix}, \boldsymbol{\Psi}_i = \begin{bmatrix} \mathbf{0} \\ \psi_i \end{bmatrix}, \mathbf{A}_{\mathrm{ex}} = \begin{bmatrix} \mathbf{A} & \mathbf{E} \\ \mathbf{0} & 0 \end{bmatrix}, \mathbf{B}_{\mathrm{ex}} = \begin{bmatrix} \mathbf{B} \\ 0 \end{bmatrix}, \mathbf{C}_{\mathrm{ex}} = \begin{bmatrix} \mathbf{C} & 0 \end{bmatrix}.$$

Assumption 3.1: The process noise and the observation noise are energy limited:

$$E\{\boldsymbol{w}_{\boldsymbol{x},i}\boldsymbol{w}_{\boldsymbol{x},i}^T\} \leq \boldsymbol{Q}_{\boldsymbol{x}} \tag{3.21}$$

$$E\{\boldsymbol{\nu}_i\boldsymbol{\nu}_i^T\} \leq \boldsymbol{R}_{\boldsymbol{x}} \tag{3.22}$$

where $\boldsymbol{Q}_{\boldsymbol{x}} > 0$ and $\boldsymbol{R}_{\boldsymbol{x}} > 0$; $\boldsymbol{Q}_{\boldsymbol{x}}$ and $\boldsymbol{R}_{\boldsymbol{x}}$ are upper bounded.

Assumption 3.2: The unknown dynamics are upper bounded: $E\{\psi_i\psi_i^T\} \leq Q_\xi$ and $Q_\xi > 0$.

To design multi-disturbance resilient observer based on the model (3.20), a novel observer, combining extended stated observer with Kalman-Bucy filter, can be fomulated as follows:

$$\begin{cases} \dot{\hat{\boldsymbol{x}}}_{\mathrm{ex},i} = \mathbf{A}_{\mathrm{ex}}\hat{\boldsymbol{x}}_{\mathrm{ex},i} + \mathbf{B}_{\mathrm{ex}}u_i + \boldsymbol{K}_i(\boldsymbol{y}_i - \mathbf{C}_{\mathrm{ex}}\boldsymbol{x}_{\mathrm{ex},i}) \\ \dot{\boldsymbol{P}}_i = \mathbf{A}_{\mathrm{ex}}\boldsymbol{P}_i + \boldsymbol{P}_i\mathbf{A}_{\mathrm{ex}}^T - \boldsymbol{K}_i\mathbf{C}_{\mathrm{ex}}\boldsymbol{P}_i + \boldsymbol{Q}_i \\ \boldsymbol{K}_i = \boldsymbol{P}_i\mathbf{C}_{\mathrm{ex}}^T\boldsymbol{R}_i^{-1} \end{cases} \tag{3.23}$$

where

$$\boldsymbol{Q}_i = \begin{bmatrix} \boldsymbol{Q}_{\boldsymbol{x}} & \mathbf{0} \\ \mathbf{0} & Q_\xi \end{bmatrix}, \boldsymbol{R}_i = \boldsymbol{R}_{\boldsymbol{x}}$$

It is noted that the estimation error of the initial state is bounded, and the initial parameter $\boldsymbol{P}_{i,0}$ is selected by satisfying $E\{(\boldsymbol{x}_{\mathrm{ex},i} - \hat{\boldsymbol{x}}_{\mathrm{ex},i})(\boldsymbol{x}_{\mathrm{ex},i} - \hat{\boldsymbol{x}}_{\mathrm{ex},i})^T\} \leq \boldsymbol{P}_{i,0}$, Furthermore, the conditions in *Assumption 3.1* and *Assumption 3.2* can be met due to the limited power of the systems in practice [101]. Thus, parameters $\boldsymbol{Q}_i, \boldsymbol{R}_i$ can be selected accordingly, supported by the simple dynamics of the extended system (3.19).

3.4 Distributed Robust Fast Terminal Sliding Mode Secondary Voltage Control

In this section, a distributed fast terminal sliding mode (FTSM) control strategy is introduced to select the appropriate voltage control input V_{ni} to guarantee the voltage magnitude of DGs following the voltage reference v_{ref}, $v_{o,magi} = v_{odi} \to v_{ref}$. The proposed FTSM control strategy can address the consensus tracking problem of linear second-order system (3.11) with the reference v_{ref}. Then, to realize the trade-off between voltage regulation and accurate reactive power sharing, the extension of the proposed FTSM control strategy is also provided.

3.4.1 Voltage Regulation

The corresponding reference with regard to the second-order system (3.11) is

$$\begin{cases} y_0 = v_{ref} \\ \dot{y}_0 = 0 \end{cases} \tag{3.24}$$

which is commonly accessible to one DG node, thus the tracking errors of local neighborhood state for the ith DG node can be denoted as

$$\begin{cases} e_{i,1} = \sum_{j \in N_i} a_{ij}(y_{i,1} - y_{j,1}) + b_i(y_{i,1} - y_0) \\ e_{i,2} = \sum_{j \in N_i} a_{ij}(y_{i,2} - y_{j,2}) + b_i y_{i,2} \end{cases} \tag{3.25}$$

To solve the above tracking control problem, the following FTSM surface is designed

$$s_i = e_{i,2} + c e_{i,1}^{m/n} + d e_{i,1}^{p/q} \tag{3.26}$$

where $c, d > 0$, and m, n, p, q are positive odd integers satisfying $m > n, p < q$. The nonlinear terminal attractors $e_{i,1}^{m/n}$ and $e_{i,1}^{p/q}$ are applied to improve the convergence rate. More especially, the term $e_{i,1}^{p/q}$ can improve the convergence rate when the system is close to the equilibrium [102].

To solve the sliding mode surface (3.26), nonlinear function $\mathrm{sig}(x)^a = \mathrm{sgn}(x)\,|x|^a$ with signum $\mathrm{sgn}(x)$ [103] is employed to design the control law for the system (3.11) as follows:

$$z_i = \left(\sum_{j\in N_i} a_{ij} + b_i\right)^{-1}\left[\sum_{j\in N_i} a_{ij}z_j - \alpha\mathrm{sig}(s_i)^2 - \beta\mathrm{sgn}(s_i) - \left(c\frac{m}{n}e_{i,1}^{m/n-1} + d\frac{p}{q}e_{i,1}^{p/q-1}\right)e_{i,2}\right] \tag{3.27}$$

where $\alpha, \beta > 0$.

Using the control law (3.27) under the sliding model surface (3.26), the distributed secondary voltage regulation problem can be solved with the stability guaranteed.

Proof. To verify the system stability under the control law (3.27), consider the following Lyapunov candidate function:

$$V = \frac{1}{2}\sum_{i=1}^{N} s_i^2 \tag{3.28}$$

and the time derivative of V can be obtained as

$$\begin{aligned}\dot{V} = \sum_{i=1}^{N} s_i\dot{s}_i &= \sum_{i=1}^{N} s_i\left[\dot{e}_{i,2} + \left(c\frac{m}{n}e_{i,1}^{m/n-1} + d\frac{p}{q}e_{i,1}^{p/q-1}\right)e_{i,2}\right] \\ &= \sum_{i=1}^{N} s_i\left(-\alpha\mathrm{sig}(s_i)^2 - \beta\mathrm{sgn}(s_i)\right) = -\alpha\sum_{i=1}^{N}\left(s_i^2\right)^{\frac{3}{2}} - \beta\sum_{i=1}^{N}\left(s_i^2\right)^{\frac{1}{2}}\end{aligned} \tag{3.29}$$

Based on *Lemma 3.3* and *Lemma 3.4* in [99], we obtain

$$\dot{V} \le -\alpha N^{-\frac{1}{2}}\left(\sum_{i=1}^{N} s_i^2\right)^{\frac{3}{2}} - \beta\left(\sum_{i=1}^{N} s_i^2\right)^{\frac{1}{2}} \le -\alpha N^{-\frac{1}{2}}\left(2V\right)^{\frac{3}{2}} - \beta\left(2V\right)^{\frac{1}{2}} \tag{3.30}$$

Since $V > 0, \dot{V} < 0$, following *Lemma 4.1* in [99], the convergence of (3.28) towards 0 is guaranteed. Thus, $s = 0$ will be maintained under the control law (3.27).

After the sliding mode surface has been reached, the dynamics of tracking errors $e_{i,1}$ can be described by

$$s_i = \dot{e}_{i,1} + ce_{i,1}^{m/n} + de_{i,1}^{p/q} = 0 \Longrightarrow \dot{e}_{i,1} = -ce_{i,1}^{m/n} - de_{i,1}^{p/q} \tag{3.31}$$

Based on the stability proof of system (3.31) in [102], the stability of the designed FTSM secondary voltage control is proved. □

3.4.2 Trade-off between Voltage Regulation and Reactive Power Sharing

The exact voltage restoration and accurate reactive power sharing cannot be achieved simultaneously due to the line impedance effect [92], except for a perfectly symmetric configuration [7]. However, the exact voltage regulation and accurate reactive power sharing could compromise with each other based on the practical circumstances. For the cases that sensitive loads require operation at the nominal voltage or the overloading of DGs is not the primary concern, voltage regulation should be prioritised [7, 41, 88, 92, 93]. However, if the concerned system has low ratings of DGs, small electrical distances between DGs or limited capacitive compensation, the reactive power sharing needs to be maintained to prevent overloading [65, 104–106]. Thus, in this subsection, the extension of the proposed secondary control scheme is provided for the case that a trade-off between voltage regulation and accurate reactive power sharing needs to be achieved.

The FTSM surface (3.26) and the control law (3.27) can be respectively modified as

$$\begin{aligned} s_i =& e_{i,2} + ce_{i,1}^{m/n} + de_{i,1}^{p/q} + c_q e_{qi}^{m1/n1} + d_q e_{qi}^{p1/q1} \\ e_{qi} =& \sum_{j \in N_i} a_{ij}(n_{Qi}Q_i - n_{Qj}Q_j) \end{aligned} \tag{3.32}$$

$$z_i = \left(\sum_{j\in N_i} a_{ij} + b_i\right)^{-1} \left[\sum_{j\in N_i} a_{ij} z_j - \alpha \mathrm{sig}(s_i)^2 - \beta \mathrm{sgn}(s_i) - \left(c\frac{m}{n} e_{i,1}^{m/n-1} + d\frac{p}{q} e_{i,1}^{p/q-1}\right) e_{i,2}\right] \tag{3.33}$$

where $c_q, d_q > 0$, and $m1, n1, p1, q1$ are positive odd integers satisfying $m1 > n1, p1 < q1$ similarly.

To express the control trade-off, the Laplacian matrix of the distributed system is redefined as $\overline{\mathcal{L}}_V$ and $\mathcal{L}_Q$:

$$\begin{cases} \overline{\mathcal{L}}_V = \mathcal{L}_V + \mathcal{B}_V \\ [e_{i,1}]_{N\times 1} = \mathcal{L}_V [y_{i,1}]_{N\times 1} + \mathcal{B}_V [y_{i,1} - y_0]_{N\times 1} \\ [e_{i,2}]_{N\times 1} = \mathcal{L}_V [y_{i,2}]_{N\times 1} + \mathcal{B}_V [y_{i,2}]_{N\times 1} \end{cases} \tag{3.34}$$

$$[e_{qi}]_{N\times 1} = \mathcal{L}_Q [n_{Qi} Q_i]_{N\times 1} \tag{3.35}$$

where $[*]_{N\times 1}$ denotes the column vector composed of states of all DG units. If $\overline{\mathcal{L}}_V \neq \mathbf{0}, \mathcal{L}_Q = \mathbf{0}$, the control system is the same as that only emphasizes voltage regulation. If $\overline{\mathcal{L}}_V = \mathbf{0}, \mathcal{L}_Q \neq \mathbf{0}$, the control system is the same as that only emphasizes accurate reactive power sharing. However, $\overline{\mathcal{L}}_V = \mathbf{0}$ could lead to poor voltage regulation. Let $\mathcal{L}_V = 0, \mathcal{L}_Q \neq \mathbf{0}, \mathcal{B}_V \neq \mathbf{0}$, the accurate reactive power sharing is guaranteed, while the voltages are regulated all around the reference. Regarding this trade-off, how to select an optimal $\mathcal{B}_V$ would be an interesting problem, and we will consider this by an optimization algorithm in the future work.

3.5 Controller Implementation for MGs

The diagram of the proposed ESKBF-based distributed robust voltage control of MGs is detailed in Figure 3.2. The ESKBF only requires the local voltage information to observe the corresponding information related to the inverter's dynamics. Once the observed information against disturbance and uncertainties is obtained and transmitted to its neighbors, the nominal control input V_{ni} can be updated to respond to system operation changes through

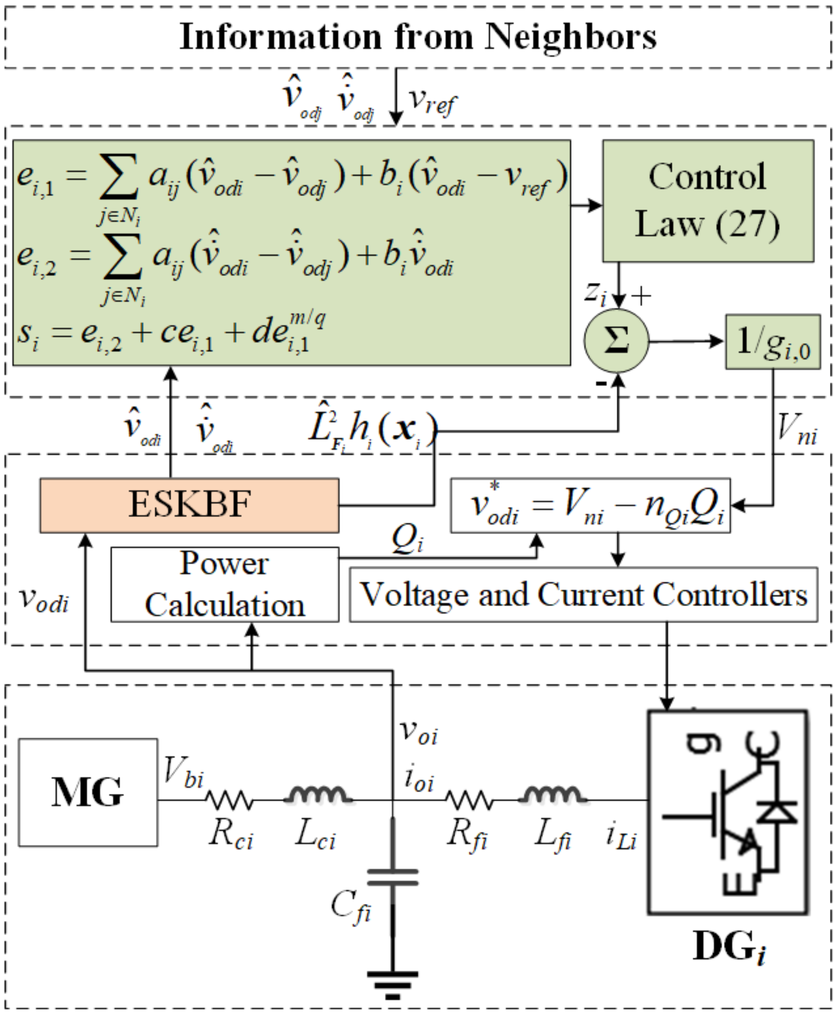

Figure 3.2: Block diagram of the proposed distributed robust FTSM voltage control.

the FTSM-based secondary voltage control law accordingly. Similarly, if the reactive power sharing is considered, the control implementation should also be modified as that analyzed in Section 3.4.2.

3.6 Simulation and Experimental Results

In this section, to verify the effectiveness of the proposed ESKBF-based distributed FTSM secondary voltage control method, both simulation and experimental studies are developed. More specifically, the proposed control scheme is firstly tested on a 4-DG islanded MG. Then, the scalability and practical performance of the proposed method are evaluated by a modified IEEE 37 bus system and an experimental MG testbed respectively.

The 4-DG islanded MG, as shown in Figure 3.3, is developed in the MATLAB/Simulink and parameters are detailed in Table 3.1. In this 4-bus MG system, the following simulation scenario is designed to evaluate the performance of the proposed voltage control strategy:

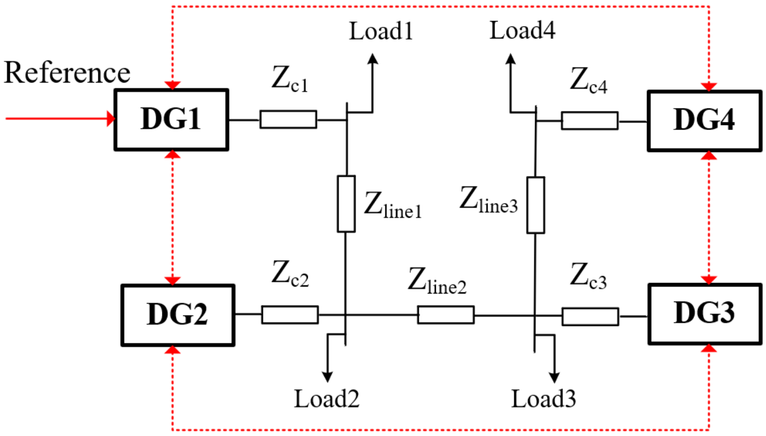

Figure 3.3: Diagram of a 4-bus MG.

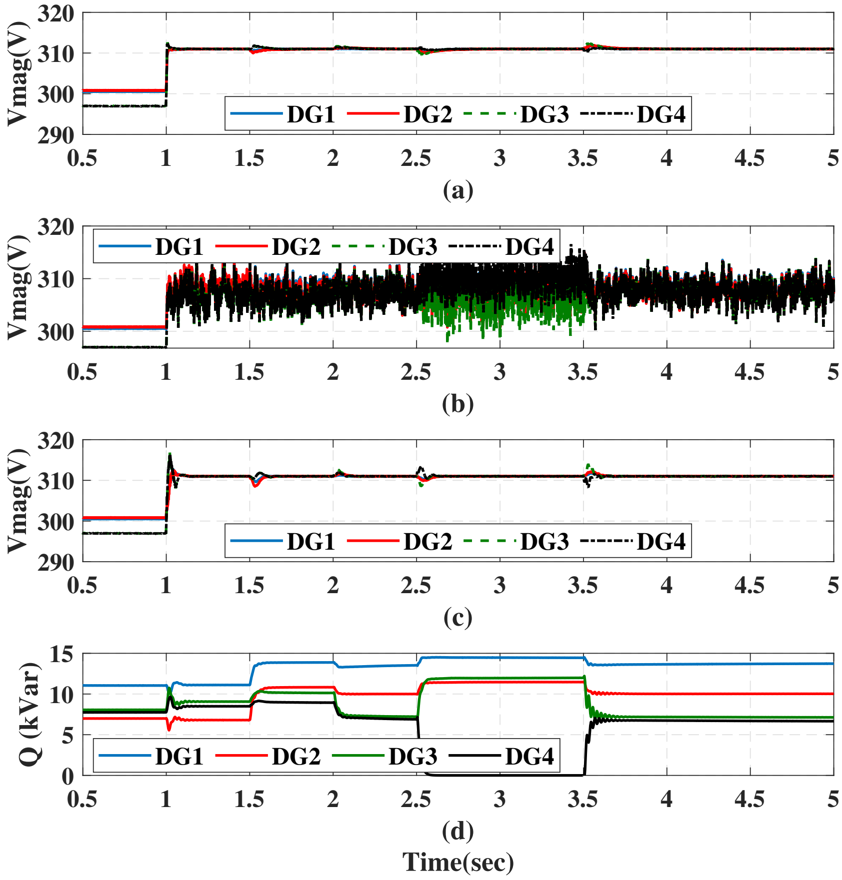

Figure 3.4: General performance evaluation of ESKBF-based distributed voltage control: (a) noise-free environment without observer, (b) noise-containing environment without observer, (c) noise-containing environment with ESKBF, (d) reactive power output in the noise-containing environment with ESKBF.

Table 3.1: Parameters of the Tested 4-bus MG System for ESKBF-Based Distributed FTSM Control Simulation [7]

		DG1	DG2	DG3 & DG4
DG power ratings		40kW, 30kVar	27kW, 20kVar	20kW, 15kVar
DGs	m_P	6.28×10^{-5}	9.42×10^{-5}	12.56×10^{-5}
	n_Q	0.5×10^{-3}	0.75×10^{-3}	1×10^{-3}
	R_f	0.1 Ω	0.1 Ω	0.1 Ω
	L_f	1.35 mH	1.35 mH	1.35 mH
	C_f	47μF	47μF	47 μF
	R_c	0.02 Ω	0.02 Ω	0.02 Ω
	L_c	2 mH	2 mH	2 mH
	K_{Pv}	0.05	0.05	0.1
	K_{Iv}	390	390	420
	K_{Pc}	10.5	10.5	15
	K_{Ic}	1.6×10^4	1.6×10^4	2×10^4
Lines	Line1	R = 0.23 Ω, L = 318 μH		
	Line2	R = 0.35 Ω, L = 1847 μH		
	Line3	R = 0.23 Ω, L = 318 μH		
RL Loads	Load1	R = 4 Ω, L = 9.6 mH		
	Load2	R = 8 Ω, L = 12.8 mH		
	Load3	R = 6 Ω, L = 12.8 mH		
	Load4	R = 12 Ω, L = 25.6 mH		
Control Parameters		$c = 600, m = 13, n = 11$		
		$d = 100, p = 3, q = 5$		
		$\alpha = 100, \beta = 400, v_{ref} = 311$ V		

1. $t = 0.0$ s: simulation initialization period, when only the primary controller is applied with constant control input $V_{ni} = 311$V, and Load2 is not connected into the MG.

2. $t = 1.0$ s: the proposed ESKBF-based distributed robust FTSM secondary voltage control is activated;

3. $t = 1.5$ s: Load2 is connected into the MG (100% increment of the load);

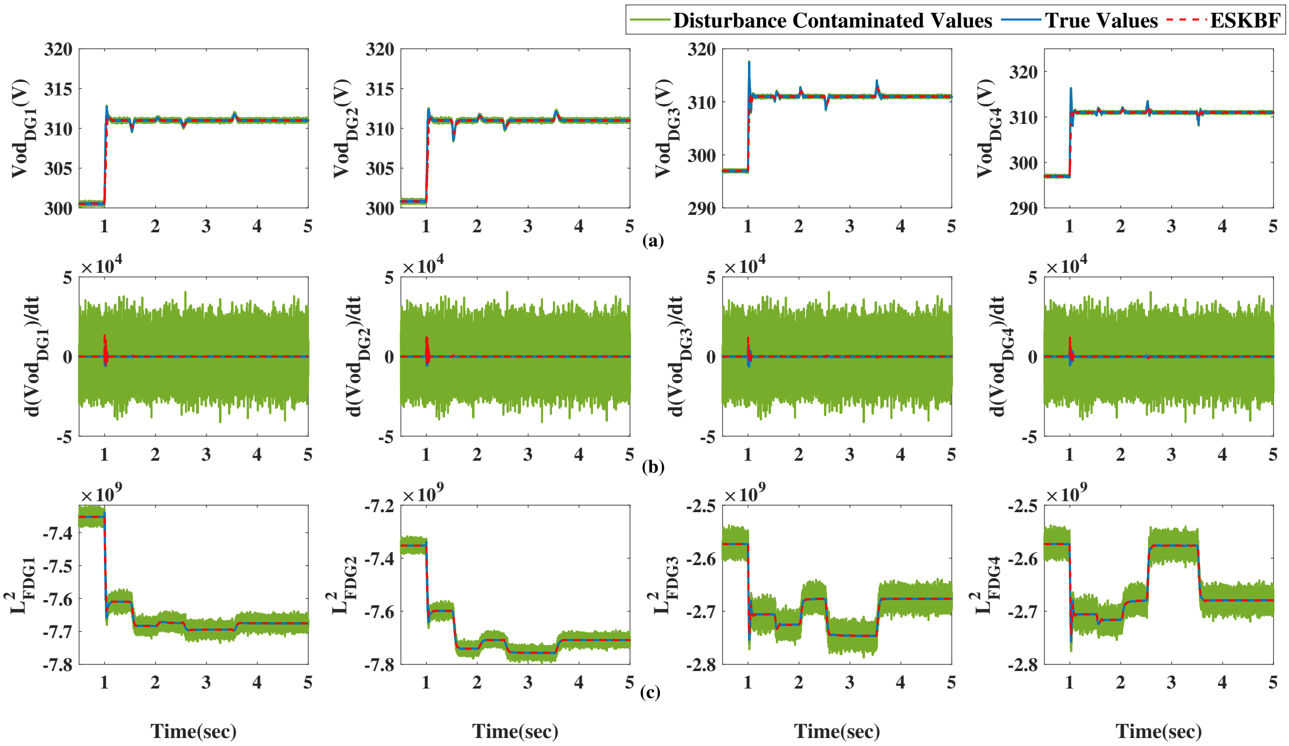

Figure 3.5: ESKBF-based observer performance evaluation: (a) v_{odi}, (b) $\dot{v}_{odi}$, (c) $L^2_{\boldsymbol{F}_i} h_i(\boldsymbol{x}_i)$.

4. $t = 2.0$ s: Load3 is decreased (50% decrement of the load);
5. $t = 2.5$ s: DG4 is disconnected (plugged out);
6. $t = 3.5$ s: DG4 is re-connected (plugged in).

3.6.1 General Performance Analysis

To demonstrate the negative effects of ignoring measurement noise when designing the controller, we simulate the MG system operation with the controller designed without considering the measurement noise in both noise-free and noise-containing environments. In the noise-containing environment, the additive measurement noise with $\sigma^2 = 0.01$ is added throughout the simulation. In the case without noise, the controller accurately regulates the system voltage according to the reference (Figure 3.4(a)). However, as demonstrated in Figure 3.4(b), although the noise amplitude is very small, the voltage control performance is significantly degraded, which is mainly driven by amplification effect of the linearised model.

In the same noise-containing environment, simulation results of the proposed ESKBF-based distributed robust FTSM voltage control are detailed in Figure 3.4(c), and the corresponding reactive power output is shown in Figure 3.4(d). At the initial phase, the secondary control is not activated, causing a static voltage deviation. Once the proposed secondary control is applied at $t = 1$ s, the voltage is restored to its reference. Then, at $t = 1.5$ s and $t = 2$ s, the control system rapidly responds to the change of load, and the voltage is accurately regulated to the reference. When DG4 is plugged out and in at $t = 2.5$ s and $t = 3.5$ s respectively, the voltage restoration can be guaranteed as well. Although some transient still occurs when DG4 is re-connected, the voltage can be rapidly regulated to the reference.

By employing the proposed ESKBF, the negative effects of the disturbance can be eliminated, as shown in Figure 3.5. More specifically, the impact of ESKBF-based observer is emphasized by the comparisons among true values, ESKBF observed values and disturbance contaminated values that are obtained from indirect measurement. If the MG voltage controller operates without ESKBF, the control performance will degrade as Figure 3.4(b), where the voltage fluctuation is undesired and unacceptable.

3.6.2 Robustness against Different Disturbance Scenarios

To illustrate the robustness of the proposed control method against uncertainties, different levels of measurement noise, $\sigma^2 = 0.01, \sigma^2 = 0.1, \sigma^2 = 1$ are employed in the system. For the sake of simplification, only ESKBF-based observation performance of DG1 is selected, and the corresponding comparisons are shown in Figure 3.6. Although the noise variance is varying, the ESKBF remains effective to filter out the additive noise. Moreover, as shown in Figure 3.7(d), the proposed ESKBF-based observer enables the voltages being accurately regulated in all cases, demonstrating the robustness of proposed control strategies against unknown level of bounded noise. If ESKBF-based observer is not activated in the secondary voltage controller, the voltages will degrade as Figure 3.7(a), (b), (c) respectively.

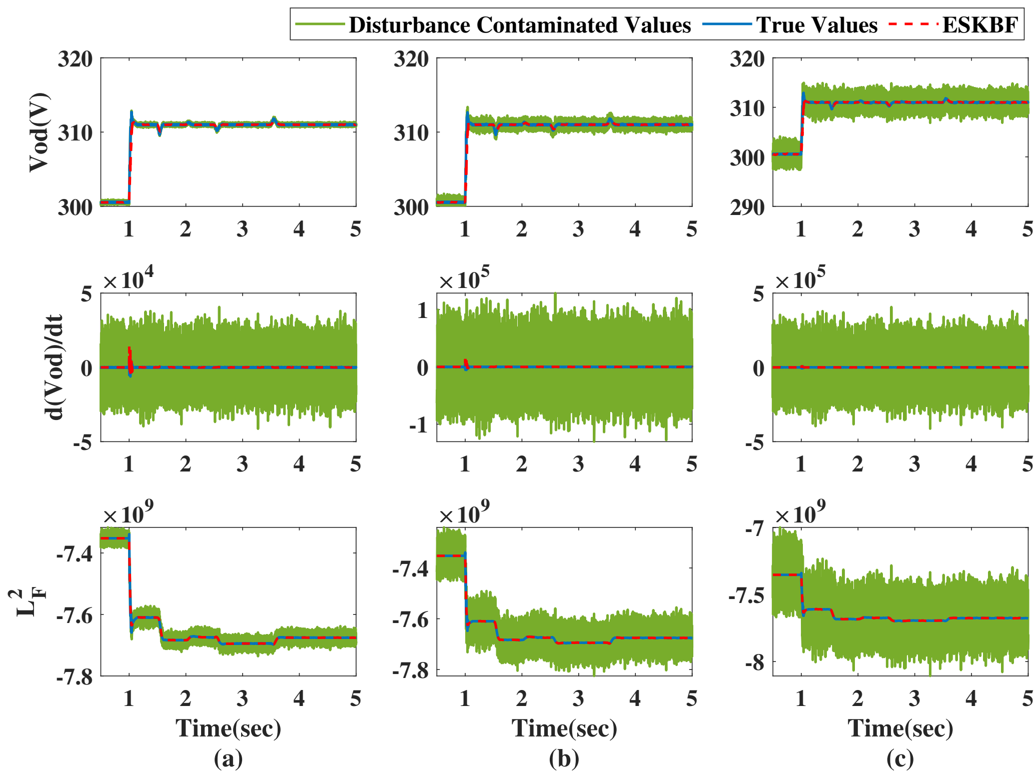

Figure 3.6: Robustness evaluation of ESKBF-based observer: (a) noise $\sigma^2 = 0.01$, (b) noise $\sigma^2 = 0.1$, (c) noise $\sigma^2 = 1$.

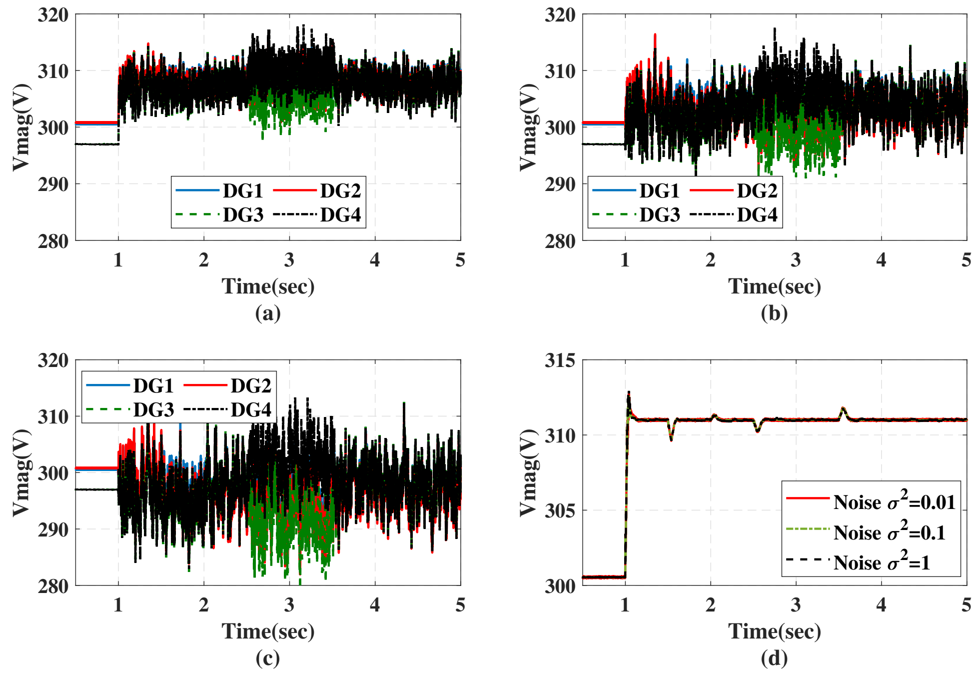

Figure 3.7: Voltage control performance analysis: (a) noise $\sigma^2 = 0.01$, (b) noise $\sigma^2 = 0.1$, (c) noise $\sigma^2 = 1$, (d) voltage comparison of all scenarios.

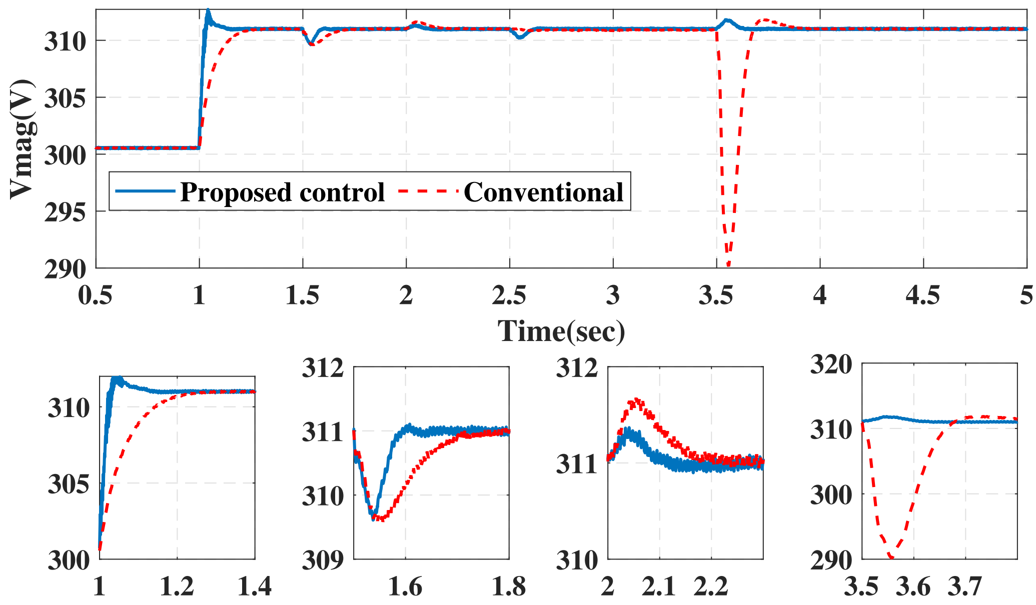

Figure 3.8: Comparison with conventional finite-time control.

3.6.3 Control Performance of Distributed FTSM Secondary Voltage Control

To show the faster convergence of the proposed distributed FTSM secondary voltage control, we compared it with the existing MG distributed finite-time control law [92]. Take DG1's control performance as an example, the comparison is detailed in Figure 3.8, where both consensus convergence rate and undesired control dynamics are improved by employing the proposed secondary voltage control method, although there may be a slight overshoot when system operation conditions change. It is also worth noting that during plug-in operation at 3.5s, the control performance achieves the most significant improvement, demonstrating the merit of the proposed control framework in supporting plug-and-play operation.

3.6.4 Trade-off between Voltage Regulation and Reactive Power Sharing

To show the conflict between voltage regulation and accurate reactive power sharing and to demonstrate the effectiveness of the proposed control framework under alternative control objectives, this subsection compares the performance in the noise-containing environment (load

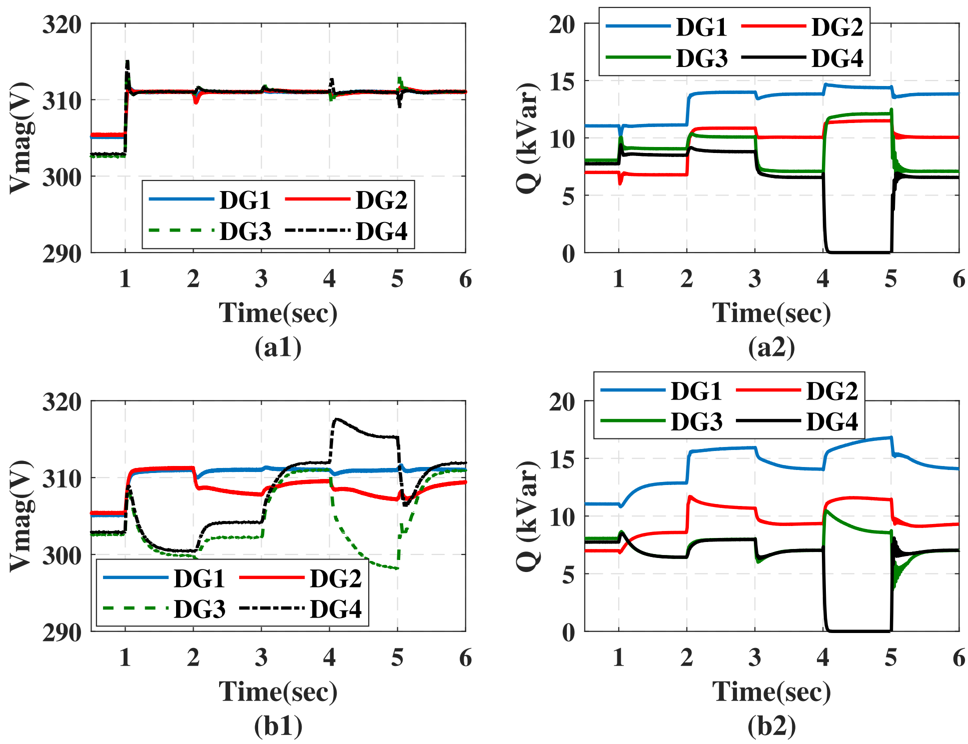

Figure 3.9: Voltage regulation and reactive power sharing: (a) voltage regulation without reactive power sharing, (b) accurate reactive power sharing with tight voltage regulation around reference value.

change at 2 s and 3 s; plug-and-play at 4 s and 5 s) under the control laws that emphasize either voltage regulation or reactive power sharing. Compared to Figure 3.9(a) that only guarantees exact voltage regulation without considering reactive power sharing, the results in Figure 3.9(b) demonstrate the feasibility to achieve the accurate reactive power sharing with tight voltage regulation around reference value.

3.6.5 Scalability Test

The scalability of the proposed control method is investigated in the modified IEEE 37 bus system [107], as shown in Figure 3.10. Before $t = 1.5$ s, the 37-node MG system operates in the islanded model with the total loads of 122.10 kW and 70.35 kVar, and DGs are controlled under the primary control only. After $t = 1.5$ s, the proposed secondary voltage control is activated. The loads of 15.75 kW and 7.88 kVar are increased and decreased on node 2 at $t = 3$ s and $t = 4.5$ s respectively, and DG4 is disconnected and re-connected at $t = 6$ s and $t = 7.5$ s respectively.

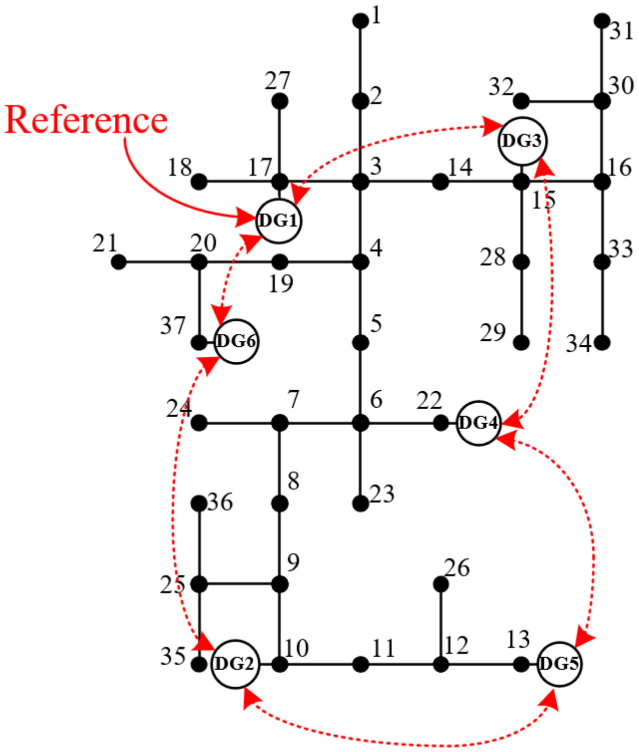

Figure 3.10: Diagram of the modified IEEE 37-bus system.

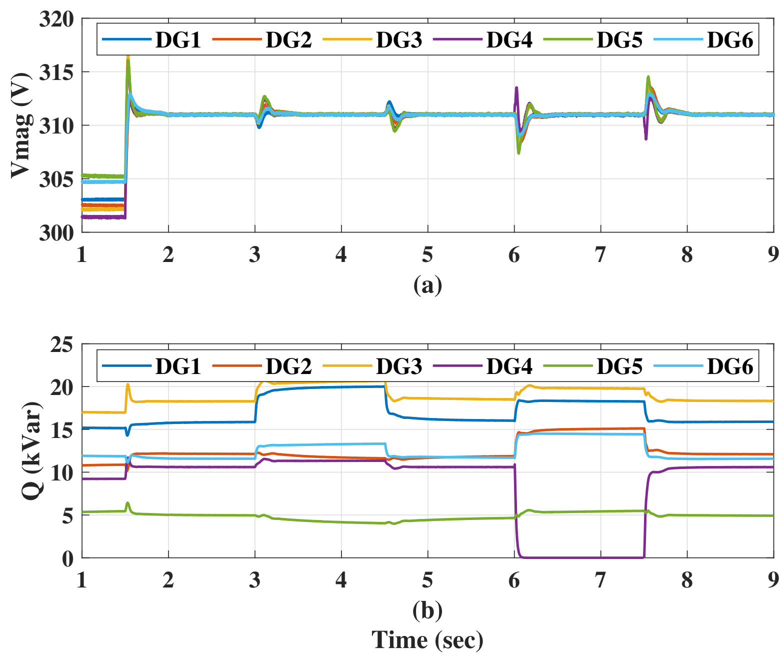

Figure 3.11: Scalability evaluation: (a) voltage magnitude, (b) reactive power output.

As shown in Figure 3.11, by applying the proposed secondary voltage control method, the output voltages of DGs can be regulated to the reference when load change and plug-and-play occur. Moreover, the performance of ESKBF is similar to that in the 4-bus MG system, so for the sake of simplification, only the observation performance of DG1 is shown in Figure 3.12.

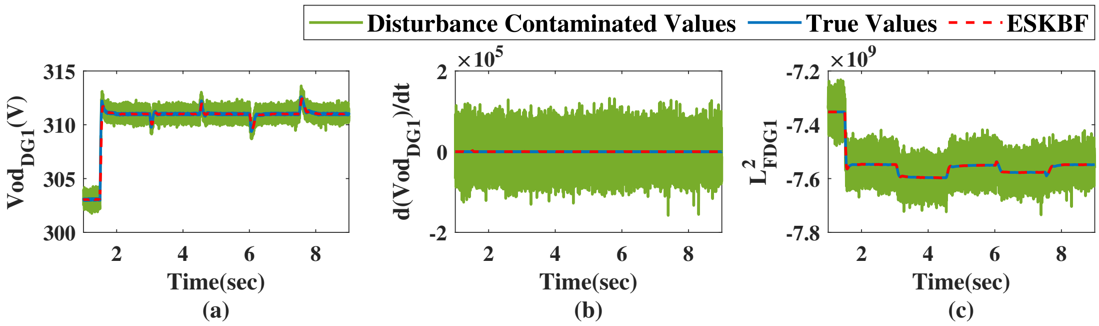

Figure 3.12: ESKBF-based observer performance evaluation (DG1) of the scalability test: (a) v_{odi}, (b) $\dot{v}_{odi}$, (c) $L^2_{\boldsymbol{F}_i} h_i(\boldsymbol{x}_i)$.

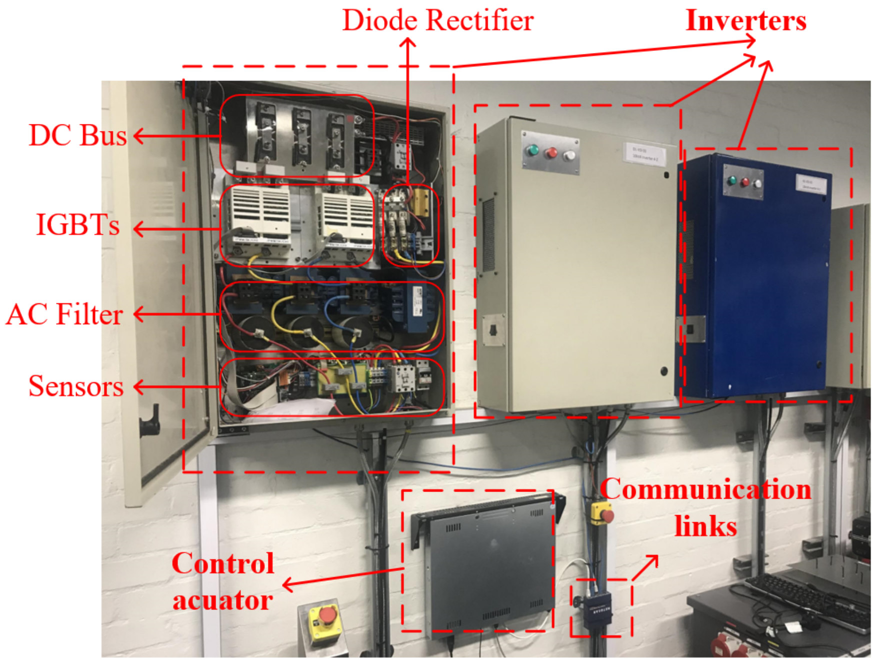

Figure 3.13: Experimental testbed of the MG with three inverters.

3.6.6 Experimental Verification

To validate the effectiveness of the proposed control method in a practical scenario, an experimental MG testbed, as shown in Figure 3.13 with three inverters has been developed to test the control performance. The topology of the MG testbed is shown in Figure 3.14, and the parameters of the inverter are the same as the Table I in [108] ($v_{ref} = 381$ V).

Two experimental cases are designed, including load change and plug-and-play capability test. The control performance is detailed as in Figure 3.15 when load change occurs. Throughout the whole experiment, the active power load (Load3) connected at DG3 is 3 kW. DG2 and

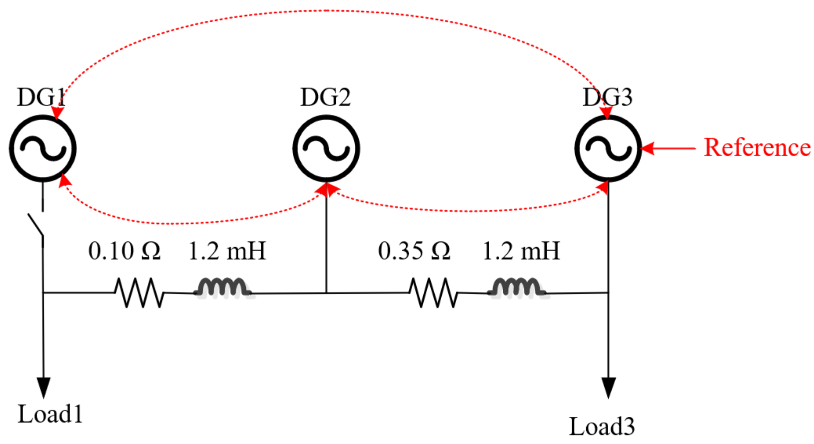

Figure 3.14: Topology of the experimental testbed.

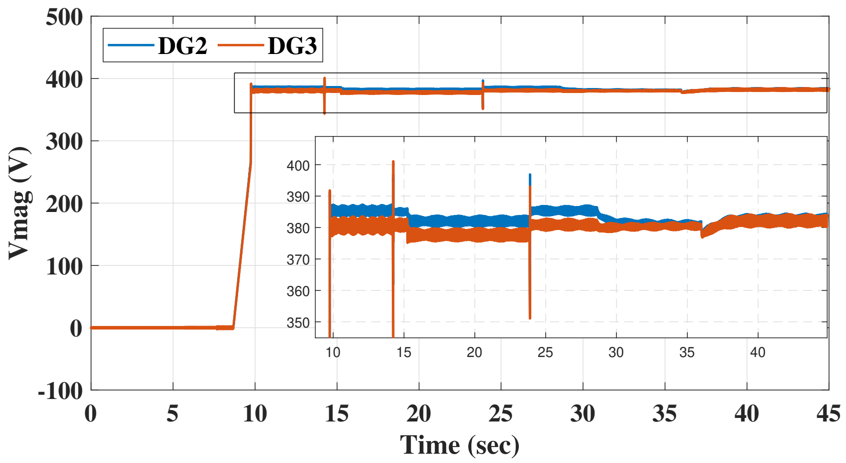

Figure 3.15: Voltage control performance in the experimental scenario with load change.

DG3 are switched in and started up during the periods $8.5 - 10$ s and $14 - 16$ s respectively. A capacitance ($50\ \mu F$) is connected to the grid at $t = 24$ s, driving the increase of the output voltages of DG2 and DG3 due to the capacitive reactive power output. The voltages of two DGs are regulated to the reference when the proposed secondary control is activated at $t = 28.5$ s. At $t = 36$ s, the capacitance is disconnected from the MG, and the voltages are restored as well. The performance of ESKBF during this experiment is detailed in Figure 3.16, demonstrating its fast convergence tracking property.

The voltage control performance of the plug-and-play capability test is shown in Figure 3.18, and the corresponding ESKBF-based observer performs as in Figure 3.17. Three DGs are switched in and started up during the periods $16 - 18$ s, $20 - 22$ s and $26 - 27.5$ s respectively. The proposed secondary control is activated at $t = 32.5$ s, when the voltages of three DGs

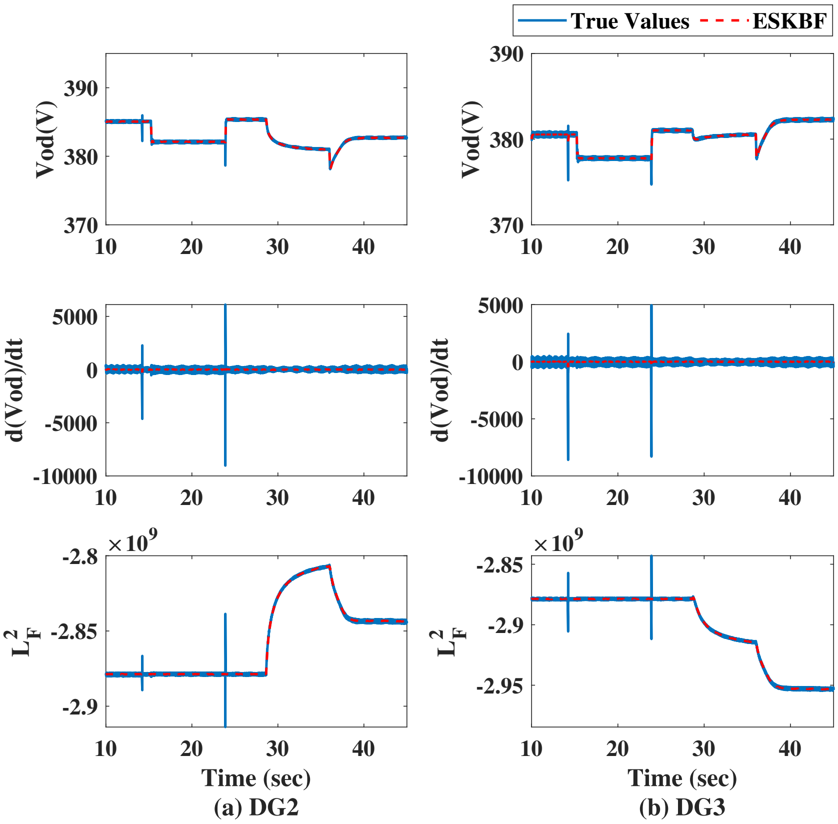

Figure 3.16: ESKBF performance in the experimental scenario with load change.

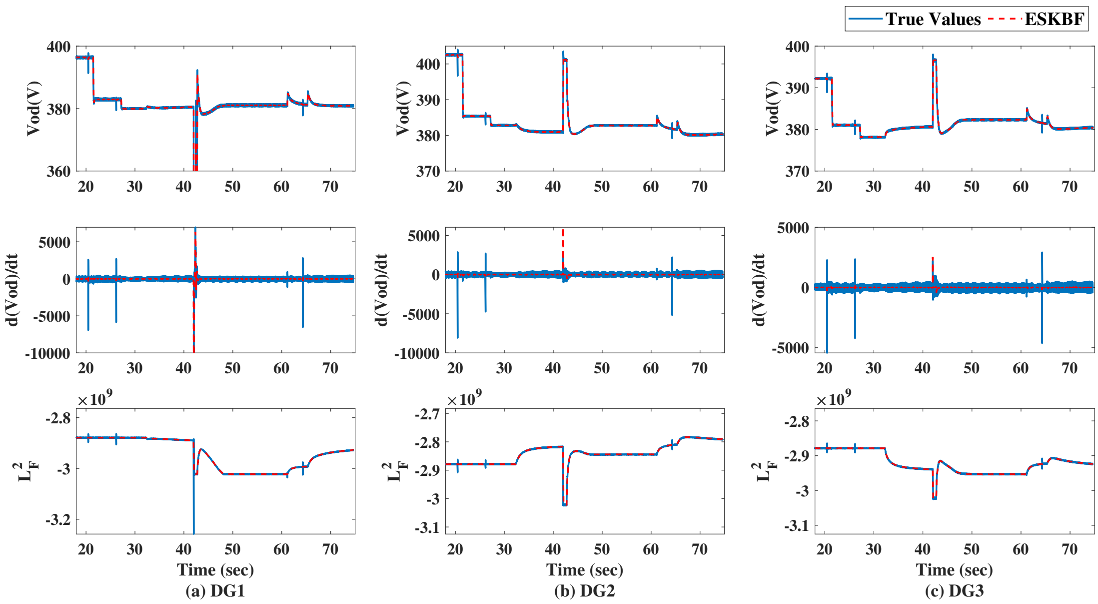

Figure 3.17: ESKBF performance of plug-and-play capability test in the experimental scenario.

start to synchronized to the reference. The DG1 is disconnected at $t = 42$ s, after a very short transient, the voltages are correctly restored. The re-connection of DG1 occurs from $t = 61$ s to $t = 64.5$ s, including the re-connection of LCF and the re-activation of DG1 inner control loops. The corresponding voltage restoration illustrates the effectiveness of the proposed secondary

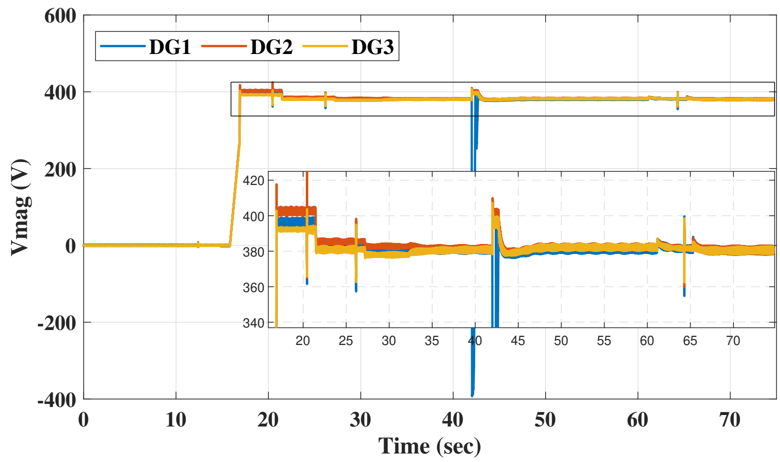

Figure 3.18: Voltage control performance of plug-and-play capability test in the experimental scenario.

voltage control when the plug-in process occurs.

3.7 Conclusion

This chapter proposes a distributed secondary voltage control method for the resilient operation of an islanded microgrid, where each inverter-based DG is modeled as an agent and the MG is seen as a multi-agent system by using the sparse communication network. Firstly, a Kalman-Bucy filter based extended state observer is designed to overcome the disturbance caused by three different sources, namely measurement noise, parameter perturbation and immeasurable variables. The ESKBF locally observes the control variables that are related to MG secondary voltage control. Then, based on the locally observed states of the DGs and distributed communication network, the proposed FTSM control employs nonlinear terminal attractors to enhance the consensus convergence rate of the system. Finally, the effectiveness of the proposed control method is illustrated by simulation and experimental studies.

Chapter 4

Event-Triggered Distributed MPC for Resilient Voltage Control of An Islanded microgrid

4.1 Introduction

A microgrid (MG) is a single controllable entity with interconnected loads and distributed energy resources [33, 74, 75]. Combining these physical plants with indispensable measurement and control loops, MG has been investigated as a typical cyber-physical system (CPS) [109]. A MG can connect and disconnect from the grid to operate in either grid-connected or islanded mode [75, 110]. When in the islanded mode, MG control architecture can be divided into three parts: primary control, secondary control and tertiary control [64, 111]. The primary control is implemented locally, whereas the secondary and tertiary control coordinate the controllable distributed generators (DGs) in the MG to achieve respective control objectives: commonly the objective of the secondary control is to regulate the voltage/frequency to its references and to guarantee the accurate power sharing, while the objective of the tertiary control is to achieve the economic dispatch [33, 80, 111].

This chapter focuses on the secondary control of the MGs. Initial research on this topic investigates the centralized control strategies [82], where DGs receive control commands from a centre controller. However, due to the fact that the centralized control structure suffers communication delays and requires extensive communication and computation infrastructure, the distributed control strategies, which allow each DG to communicate only with neighbouring DGs, have received increasing attention [85, 86]. In particular, distributed control strategies such as linear feedback control [88, 105, 112], finite-time control [93, 113], fixed-time control [114], have been applied to improve the secondary control in the MG with sparse communication network. Model predictive control (MPC) [115] has been recently introduced to distributed MG voltage control and demonstrated its superior performance. However, MPC algorithm exacerbates the burden on the online computation and real-time communication due to its prediction mechanism. Most of existing distributed secondary control methods of the MG [7, 43, 93, 114] are still designed and implemented in a time-triggered fashion, where the measuring and the controlling are conducted periodically. The time-triggered control could lead to inefficient utilization of computation and communication resources as many data transmissions and calculations are not actually essential to guarantee the control performance.

In this context, the event-triggered control has been proposed for distributed model predictive control (DMPC) to achieve a better trade-off between the control performance and communication and computation burden [116–118]. The event-triggered mechanism can ease the burden on the communication and even keep resilient against reduced communication resources caused by cyber contingency. So far, several event-triggered secondary control methods have been developed in the MG system with droop-based DGs. However, several problems still remain: (i) the triggering conditions for simultaneously reducing computation and communication have not been fully considered; (ii) the resilience brought by the prediction mechanism of the DMPC to the possible cyber events has not been fully discussed; (iii) the existing event-triggered MG control methods [105, 119] are designed with the assumption that the system state information are fully available, which may not be the case for certain system configuration or requires continuously running of an observer.

To mitigate the aforementioned problems, a distributed resilient voltage control of an islanded

MG is designed based on an event-triggered DMPC and an adaptive non-asymptotic observer. The main contributions of this chapter are as follows:

(i) A novel distributed event-triggered DMPC framework is proposed to restore the voltage for islanded MGs in the secondary control level, which is resilient to the random packet loss and communication failure. The prediction model of the DMPC also can compensate the effect of communication failure to enhance the system resilience by the update principle of the prediction sequence. In addition, two event triggering conditions which can be easily embedded into the DMPC are designed respectively to reduce computation and communication burden in the cyber layer.

(ii) An adaptive non-asymptotic observer is designed to facilitate a cost-effective output-based control framework, which, unlike the Luenberger-like observer [67, 96], can operate in an intermittent way due to its deadbeat convergence property; Moreover, the integrated control framework that coordinates the proposed DMPC voltage regulator and the non-asymptotic observer is designed from a timing sequence perspective.

The remainder of this chapter is organized as follows. Section 4.2 is concerned with the cyber-physical modelling of the islanded MG and the corresponding problem formulation. In Section 4.3, the DMPC with specific event-triggered mechanism and the adaptive non-asymptotic observer are detailed. The corresponding simulation cases are provided in Section 4.4, and the conclusions are collected in Section 4.5.

Primary notations and definitions are given as follows. The set of real numbers is denoted by $\mathbb{R}$. For any vector $\boldsymbol{x}$, $\|\boldsymbol{x}\|$ denotes the Euclidean norm and $\|\boldsymbol{x}\|_{\mathbf{Q}} = \sqrt{\boldsymbol{x}^T\mathbf{Q}\boldsymbol{x}}$ stands for $\mathbf{Q}$-weighted norm, where $\mathbf{Q}$ is a matrix with appropriate dimension. The notation $\mathbf{Q} > 0$ denotes that $\mathbf{Q}$ is a positive definite matrix. For any set N, $|N|$ denotes the number of elements in N. For any nth order differentiable $y(t)$, $y^{(n)}(t)$ denotes the nth order differential value. The notation $\mathbf{1}_n \in \mathbb{R}^n$ denotes a column vector with all elements being ones, i.e., $\mathbf{1}_n = [1, 1, \cdots, 1]^T$. The notation $\mathbf{I}_n$ denotes the nth order identity matrix.

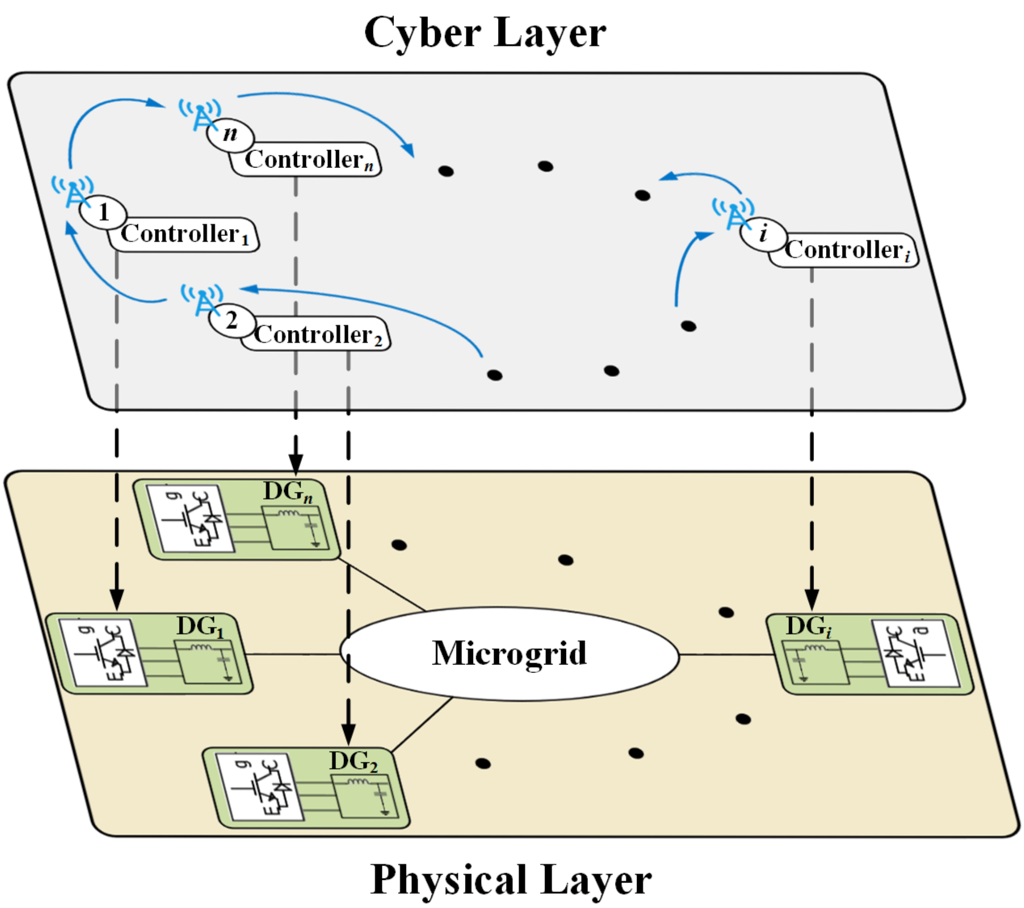

Figure 4.1: Distributed control structure of a cyber-physical coupling MG.

4.2 Problem Formulation

In this section, the model for designing distributed control method of an islanded microgrid is detailed from a cyber-physical coupling system perspective. The physical system contains the electrical topology of the MG and its local controllers, while the cyber layer of the MG can be modelled as a graph with edges being interconnecting communications, as shown in Figure 4.1.

4.2.1 Physical System

The MG physically contains multiple DGs that are interconnected through the electrical network. If there is a line between DG i and DG j with the impedance $Z_{ij} = R_{ij} + jX_{ij}$, due to the inductive impedance [105, 106], the output active power and reactive power of DG i can be expressed as follows:

$$P_i = P_{iL} + \sum_{j=1}^{N_i} \frac{V_i V_j}{X_{ij}} \sin(\theta_i - \theta_j) \tag{4.1}$$

$$Q_i = Q_{iL} + \sum_{j=1}^{N_i} \left[\frac{V_i^2}{X_{ij}} - \frac{V_i V_j}{X_{ij}} \cos(\theta_i - \theta_j) \right] \tag{4.2}$$

where P_{iL} and Q_{iL} are active and reactive power of the load at bus i; and V_i and θ_i are the bus voltage and the angle at bus i. In practice, the electrical network connecting DG i and DG j is usually more complicated. However, it is reasonable to model each single MG system by using approximate modelling approaches, where the line impedance is modelled as the equivalent impedance of the network [120, 121].

Due to the fact that the phase difference $(\theta_i - \theta_j)$ is small [65], $\sin(\theta_i - \theta_j) \approx (\theta_i - \theta_j)$ and $\cos(\theta_i - \theta_j) \approx 1$, which means the active and reactive power can be controlled by the difference of phase angle and voltage magnitude respectively. Thus, the conventional droop control can be obtained:

$$\omega_i = \omega_{ni} - m_{Pi} P_i \tag{4.3}$$

$$V_i = v_{odi}^* = V_{ni} - n_{Qi} Q_i \tag{4.4}$$

where ω_i, V_i are the angular frequency and the voltage magnitude provided for the inner control loops. m_{Pi}, n_{Qi} are droop coefficients and are selected based on the active and reactive power ratings of each DG [64]. ω_{ni}, V_{ni} are the nominal references of the primary control, which can be generated from the secondary control. It should be noted that each DG is controlled under itself d-q (direct-quadrature) axis, which guarantees the voltage magnitude V_i is equivalent to the d-axis voltage v_{odi}, which means $v_{oqi}^* = 0$. Through the droop control principle, each inverter is controlled with its rotating angular reference. To model the MG in a uniform frame, a specifically chosen DG is considered as the common reference ω_{com}, and the angular frequency

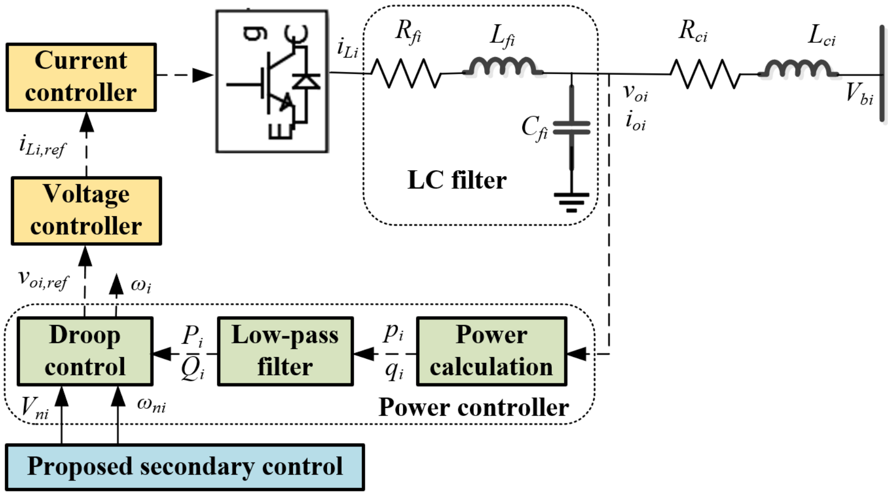

Figure 4.2: Block diagram of the primary control loops in the inverter-based DG.

difference of the ith DG can be denoted by δ_i:

$$\dot{\delta}_i = \omega_i - \omega_{com} \tag{4.5}$$

Combining detailed models in the DG control loops as shown in Figure 4.2 (including models of inner loops detailed in [7,88,93]), the large-signal dynamic model of the ith DG can be detailed as the following multi-input multi-output (MIMO) nonlinear system:

$$\dot{\boldsymbol{x}}_i = \boldsymbol{f}_i(\boldsymbol{x}_i) + \boldsymbol{g}_i(\boldsymbol{x}_i)\boldsymbol{u}_i + \boldsymbol{k}_i(\boldsymbol{x}_i)\boldsymbol{d}_i(\boldsymbol{x}_j) \tag{4.6}$$

with the state vector

$$\boldsymbol{x}_i = [\delta_i \; P_i \; Q_i \; \phi_{di} \; \phi_{qi} \; \gamma_{di} \; \gamma_{qi} \; i_{ldi} \; i_{lqi} \; v_{odi} \; v_{oqi} \; i_{odi} \; i_{oqi}]^T,$$

where the system input is denoted by $\boldsymbol{u}_i = [\omega_{ni} \; V_{ni}]^T$ with ω_{ni} and V_{ni} the input variables for frequency control and voltage control, respectively. $\boldsymbol{d}_i(\boldsymbol{x}_j) = [\omega_{com} \; v_{bdi} \; v_{bqi}]^T$ represents the interconnection with other DGs, modelled as a disturbance in a single DG system, and v_{bdi}, v_{bqi} denote the d-q-axis voltages at the connection bus in Figure 4.2, which reflects the external disturbance acting on DG i.

4.2.2 Cyber System

To realize the implementation of the secondary controllers, we assume each DG is equipped with a transceiver for information exchange among sparsely distributed DGs. Thus, as depicted in Figure 4.1, the communication network in the multi-DG MG can be modelled as a weighted graph $\mathcal{G}_c = \{\mathcal{V}_c, \mathcal{E}_c\}$, where $\mathcal{V}_c = \{v_1, v_2, \ldots, v_N\}$ is a set of nodes, $\mathcal{E}_c \subseteq \mathcal{V}_c \times \mathcal{V}_c$ is a set of edges, and N is the number of controllable DG nodes. An edge (v_j, v_i) means that the ith node can receive information from the jth node and v_j is a neighbour of v_i. The set of neighbours of node i is described by $N_i = \{j : (v_j, v_i) \in \mathcal{E}_c$. The corresponding adjacency matrix $\mathcal{A} = [a_{ij}] \in \mathbb{R}^{N\times N}$ is denoted by $a_{ii} = 0$; $a_{ij} > 0$ if $(v_j, v_i) \in \mathcal{E}_c$, otherwise $c_{ij} = 0$. For the graph representing a MG, there exists a virtual leader (reference node), whose adjacency matrix is denoted by $\mathcal{B} = \text{diag}\{b_i\} \in \mathbb{R}^{m\times m}$, and the Laplacian matrix $\mathcal{L} = \mathcal{D} - \mathcal{A} + \mathcal{B}$, where $\mathcal{D} = \text{diag}\{\sum_{j\in N_i} a_{ij}\}$ [7, 84].

The objective of the secondary voltage control designed in the cyber system is to regulate the output voltage magnitude V_i of each DG to a unified reference v_{ref} through a leader-following scheme, in the sense that $v_{ref,1} = v_{ref}$ and $v_{ref,i} = V_{i-1}, \forall i > 1$. In other words, each DG tracks its neighbours' voltage to achieve the reference tracking. In the cyber layer design, it is meaningful and desirable to limit the computation and communication, especially with the wireless embedded control systems [116]. From this point of view, this chapter proposes an event-triggered control framework, where, as opposed to the conventional control with continuous (or periodic) observation and control of the system, control tasks are executed only when certain conditions are met in order to minimise the computation and communication costs.

4.3 Linear DMPC Based Resilient Voltage Control Algorithm Design

The proposed control scheme, as shown in Figure 4.3, is mainly consisted of three parts: distributed model predictive control (DMPC) based voltage regulator, event triggering mechanism

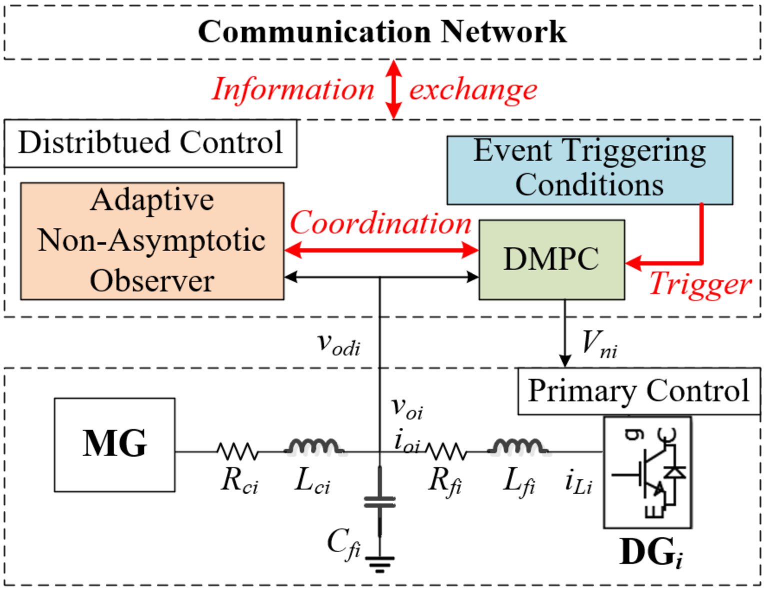

Figure 4.3: Scheme of the DMPC based noise-resilient voltage control.

design and adaptive non-asymptotic observer. The voltage regulator is designed based on the DMPC framework, where the event-triggered mechanism can be easily embedded to alleviate the computation burden. In addition, the information exchange among DGs is also governed by the event-triggered scheme in order to reduce communication cost. Finally, to reduce sensor cost, an adaptive non-asymptotic observer is utilized for the reconstruction of internal and output signals. Owing to its fast convergence property, the observer can be operated in an intermittent way, and consequently, it can be integrated into the overall event-triggered control framework.

4.3.1 DMPC-Based Voltage Restoration

The system model (4.6) is a MIMO nonlinear system, but when voltage control is considered, instead of using such a sophisticated model, feedback linearization [88] is utilized to simplify the model into a linearized form:

$$\begin{cases} \dot{y}_{i,1} = \dot{v}_{odi} = y_{i,2} \\ \dot{y}_{i,2} = \ddot{v}_{odi} = f_i(\boldsymbol{x}_i) + g_i u_i \\ y_{i,o} = y_{i,1} = v_{odi} \end{cases} \tag{4.7}$$

$$f_i(\boldsymbol{x}_i) = L^2_{\boldsymbol{F}_i} h_i(\boldsymbol{x}_i), \quad g_i = L_{\boldsymbol{g}_i} L_{\boldsymbol{F}_i} h_i(\boldsymbol{x}_i)$$

where $f_i(\boldsymbol{x}_i)$ represents the system non-linearity.

Let us define an auxiliary control variable $\xi_i = f_i(\boldsymbol{x}_i) + g_i u_i$, then $u_i = (g_i)^{-1}(\xi_i - f_i(\boldsymbol{x}_i))$ and the dynamic system (4.7) can be rewritten as

$$\begin{cases} \dot{\boldsymbol{y}}_i = \mathbf{A}\boldsymbol{y}_i + \mathbf{B}\xi_i \\ y_{i,o} = \mathbf{C}\boldsymbol{y}_i \end{cases} \tag{4.8}$$

$$\boldsymbol{y}_i = \begin{bmatrix} y_{i,1} \\ y_{i,2} \end{bmatrix}, \mathbf{A} = \begin{bmatrix} 0 & 1 \\ 0 & 0 \end{bmatrix}, \mathbf{B} = \begin{bmatrix} 0 \\ 1 \end{bmatrix}, \mathbf{C} = \begin{bmatrix} 1 & 0 \end{bmatrix}$$

The distributed voltage regulation problem is to find appropriate input ξ_i to achieve $y_{i,o} \longrightarrow v_{ref,i}$. To implement DMPC, the discrete-time model of (4.8) is obtained through Euler discretization:

$$\begin{cases} \boldsymbol{y}_i(k+1) = \mathbf{A}_z\boldsymbol{y}_i(k) + \mathbf{B}_z\xi_i(k) \\ y_{i,o}(k) = \mathbf{C}_z\boldsymbol{y}_i(k) \end{cases} \tag{4.9}$$

where $\mathbf{A}_z = \mathbf{I} + \mathbf{A}T_s, \mathbf{B}_z = \mathbf{B}T_s, \mathbf{C}_z = \mathbf{C}$ and T_s denotes the sampling time interval. However, after feedback linearization, the dynamics of the discretized system and the real system inevitably differ. An increase in sampling rate will increase the model accuracy whereas computational efficiency degrades. To balance the model accuracy and the computational complexity, we design a two-time-scale DMPC model where two time intervals T_s, T_s^{mpc} are defined. T_s denotes the discretization time interval, while T_s^{mpc} denotes the sampling time interval of the DMPC algorithm, and $T_s^{mpc} = rT_s, r \in \mathbb{Z}^+$. Define $h = 1, 2, \cdots, H$ as the prediction time steps of the DMPC, the full model-based prediction at the time-step k ($t_{k+1} - t_k = T_s^{mpc}$) is expressed

$$
\begin{bmatrix} y_{i,o}(k+1|k) \\ y_{i,o}(k+2|k) \\ \cdots \\ y_{i,o}(k+Hr|k) \end{bmatrix} = \begin{bmatrix} \mathbf{C}_z\mathbf{A}_z \\ \mathbf{C}_z\mathbf{A}_z^2 \\ \cdots \\ \mathbf{C}_z\mathbf{A}_z^{Hr} \end{bmatrix} \boldsymbol{y}_i(k)
+ \begin{bmatrix} \mathbf{C}_z\mathbf{B}_z & & & \\ \mathbf{C}_z\mathbf{A}_z\mathbf{B}_z & \mathbf{C}_z\mathbf{B}_z & & \\ \vdots & \vdots & \ddots & \\ \mathbf{C}_z\mathbf{A}_z^{Hr-1}\mathbf{B}_z & \mathbf{C}_z\mathbf{A}_z^{Hr-2}\mathbf{B}_z & \cdots & \mathbf{C}_z\mathbf{B}_z \end{bmatrix} \begin{bmatrix} \xi_i(k|k) \\ \xi_i(k+1|k) \\ \cdots \\ \xi_i(k+Hr-1|k) \end{bmatrix} \tag{4.11}
$$

$$
\begin{aligned}
\boldsymbol{Y}_{i,o}(k) &= \begin{bmatrix} y_{i,o}(k+r|k) \\ y_{i,o}(k+2r|k) \\ \cdots \\ y_{i,o}(k+Hr|k) \end{bmatrix} = \left(\mathbf{I}_H \otimes \begin{bmatrix} \mathbf{0}_{1\times(r-1)} & 1 \end{bmatrix}\right) \begin{bmatrix} y_{i,o}(k+1|k) \\ y_{i,o}(k+2|k) \\ \cdots \\ y_{i,o}(k+Hr|k) \end{bmatrix} \\
&= \left(\mathbf{I}_H \otimes \begin{bmatrix} \mathbf{0}_{1\times(r-1)} & 1 \end{bmatrix}\right) \begin{bmatrix} \mathbf{C}_z\mathbf{A}_z \\ \mathbf{C}_z\mathbf{A}_z^2 \\ \cdots \\ \mathbf{C}_z\mathbf{A}_z^{Hr} \end{bmatrix} \boldsymbol{y}_i(k) \\
&+ \left(\mathbf{I}_H \otimes \begin{bmatrix} \mathbf{0}_{1\times(r-1)} & 1 \end{bmatrix}\right) \begin{bmatrix} \mathbf{C}_z\mathbf{B}_z & & & \\ \mathbf{C}_z\mathbf{A}_z\mathbf{B}_z & \mathbf{C}_z\mathbf{B}_z & & \\ \vdots & \vdots & \ddots & \\ \mathbf{C}_z\mathbf{A}_z^{Hr-1}\mathbf{B}_z & \mathbf{C}_z\mathbf{A}_z^{Hr-2}\mathbf{B}_z & \cdots & \mathbf{C}_z\mathbf{B}_z \end{bmatrix} (\mathbf{I}_H \otimes \mathbf{1}_r) \begin{bmatrix} \xi_i(k|k) \\ \xi_i(k+1|k) \\ \cdots \\ \xi_i(k+H-1|k) \end{bmatrix} \\
&= \mathbf{F}_i\boldsymbol{y}_i(k) + \mathbf{G}_i\boldsymbol{\Xi}_i(k)
\end{aligned} \tag{4.12}
$$

---

as

$$
y_{i,o}(k+h_d|k) = \mathbf{C}_z\mathbf{A}_z^{h_d}\boldsymbol{y}_i(k) + \sum_{i=0}^{h_d-1} \mathbf{C}_z\mathbf{A}_z^{h_d-i-1}\mathbf{B}_z\xi_i(k+i|k), h_d = 1, 2, \cdots, Hr \tag{4.10}
$$

where h_d denotes the detailed prediction time steps with length Hr for the discretization model, and the model (4.10) also can be expressed in a matrix form (4.11).

However, only the prediction at each DMPC time step $k = r$, $2r$, $\ldots$ is required, and therefore the order of the model-based prediction can be reduced and expressed as (4.12), where $\boldsymbol{Y}_{i,o} \in \mathbb{R}^{H\times 1}, \mathbf{F}_i \in \mathbb{R}^{H\times 2}, \mathbf{G}_i \in \mathbb{R}^{H\times H}$ and $\boldsymbol{\Xi}_i \in \mathbb{R}^{H\times 1}$, and more specifically

$$
\begin{bmatrix} \xi_i(k|k) & \xi_i(k+1|k) & \cdots & \xi_i(k+Hr-1|k) \end{bmatrix}^T = (\mathbf{I}_H \otimes \mathbf{1}_r)\,\boldsymbol{\Xi}_i(k) \tag{4.13}
$$

This guarantees the dimension of prediction model (4.12) does not increase, although the full prediction model (4.11) is applied to ensure the prediction accuracy of discretization model. In other words, the prediction sequence $\boldsymbol{Y}_{i,o}(k)$ can be obtained directly from (4.12) instead of (4.11), and this can save the computation for both prediction and optimization. Due to the fact that the proposed DMPC tracking voltage reference by eliminating the difference between local and neighbouring DGs' voltage magnitudes, the objective function is designed as follows:

$$\min_{\boldsymbol{\Xi}_i(k)} J_i(\boldsymbol{y}_i(k), \boldsymbol{\Xi}_i(k)) = \left\| \frac{1}{|N_i|} \sum_{j \in N_i} \boldsymbol{Y}_{i,o}(k) - \boldsymbol{Y}_{j,o}(k) \right\|_{\mathbf{Q}}^2 + \|\boldsymbol{\Xi}_i(k)\|_{\mathbf{R}}^2 \tag{4.14}$$

where $|N_i|$ denotes the neighbour number of the ith DG; the weighting matrix $\mathbf{Q} > 0, \mathbf{R} > 0$ are designed to balance the tracking performance and the control effort. It is noteworthy that when solving the optimization problem, the output of the virtual leader (reference node) is a constant vector $\boldsymbol{Y}_{0,o}(k) = \mathbf{1}_H v_{ref}$. The synchronization of the voltage signals represents the main target of the application addressed in this chapter. For this reason, the weighting factors $\mathbf{Q}, \mathbf{R}$ are selected to emphasize the former term in (4.14).

Finally, the DMPC framework is completed by the following constraint

$$0.97p.u. \leq V_i \leq 1.03p.u. \tag{4.15}$$

which restricts the voltage tracking error to 3% so as to enable fast restoration of the voltage to the acceptable range. This constraint can maintain the control performance especially under an exceptional circumstance (e.g., a huge voltage drop or an overvoltage). According to IEEE standard 1547, it is not necessary for the power system to strictly fulfil the constraint (4.15) during the operation. However, the tracking error is not permitted to exceed the 3% limit for more than $\bar{T} = 0.166$s. In order to meet this requirement, the two sampling interval T_s and T_s^{mpc} calibrated, such that T_s^{mpc} is reasonably smaller than $\bar{T}$ to ensure smooth operation of the system. The optimization problem (4.14) is solved recursively at each time step k subject to (4.15), and the first control input $\xi_i(k|k)$ of the optimal control sequence $\boldsymbol{\Xi}_i(k)$ is applied at the ith DG.

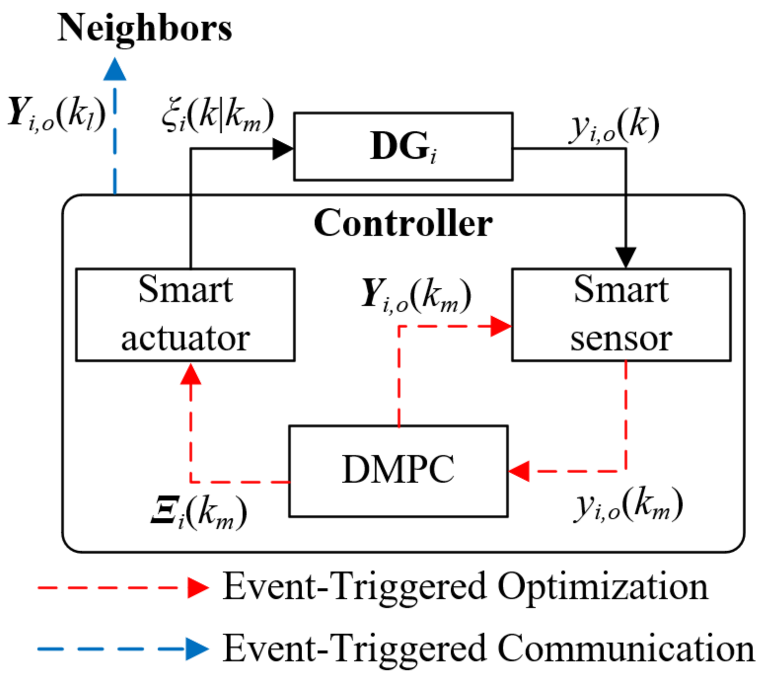

Figure 4.4: Event-triggered DMPC scheme.

4.3.2 Event Triggering Condition Design

Traditionally, the DMPC-based voltage regulation algorithm relies on the iterative finite-horizon optimization and information exchange among DGs at each time step k, which heavily increase the computation and communication burdens. In this connection, an event-triggered scheme is designed and integrated into the DMPC framework to effectively save computation and communication power without sacrificing control performance. The overall scheme of a single DG is shown in Figure 4.4. To better demonstrate the event triggering mechanisms, two sets of samples, are defined: $\mathcal{O} = \{k|\Phi(k)\}$ collects the time steps when the DMPC optimization is triggered, where $\Phi(k)$ and $\Psi(k)$ denote the event-trigger rules for optimization and communication, respectively. The design of these rules is introduced next.

The event-trigger conditions for the DMPC optimization is discussed at first. With the aim of reducing the number of optimization iterations, the DMPC can be made active only when the control performance is not satisfactory. Considering the DMPC is triggered at k_mth step ($k_m \in \mathcal{O}$), then for any $k > k_m$ the DMPC is disabled unless 1) the prediction of the system behaviour based on the previously calculated control is not reliable any more, or 2) the maximum horizon is reached:

$$\Phi(k): \ \ \|y_{i,o}(k) - y_{i,o}(k|k_m)\| \geq e_{opt} \ \textbf{OR} \ k \geq k_m + H \tag{4.16}$$

where $e_{opt} > 0$ is the user designed threshold for the prediction error. By using this event-triggered optimization mechanism (4.16), the stability proof has been discussed in [117] and the tracking error is bounded. Assuming the DMPC is reactivated at $k_m + n$th step with $1 \leq n \leq H$, the control input is not updated by optimization for any steps in between (i.e., $k_m + m$, $1 \leq m < n$). Without loss of generality, the input sequence $\boldsymbol{\Xi}_i(k_m + m)$ is updated by

$$1 \leq m < n \leq H, \ \boldsymbol{\Xi}_i(k_m + m) = \begin{bmatrix} \xi_i(k_m + m|k_m) & \cdots & \xi_i(k_m + H - 1|k_m) & 0 \cdots 0 \end{bmatrix}^T \tag{4.17}$$

and based on (4.17) the output predictions are reevaluated by (4.12).

On the other hand, to eliminate unnecessary date exchange, the communication between DGs is also regulated by an event-triggered mechanism. Considering the fact that the communication is not required when the consensus among voltage signals of each DG is achieved, after any communication triggered time step k_l, the communication is enabled only when the prediction error meets the following condition:

$$\Psi(k): \ \ \|\boldsymbol{Y}_{i,o}(k) - \boldsymbol{Y}_{i,o}(k|k_l)\|_\infty \geq e_{com}, \qquad k > k_l \tag{4.18}$$

$$\star := \left[\boldsymbol{Y}_{i,o}(k_l)^T\right], \quad \boldsymbol{Y}_{i,o}(k|k_l) = [\star(k - k_l + 1) \quad \cdots \quad \star(H) \quad \cdots \quad \star(H)]^T \tag{4.19}$$

where $[*](i)$ denotes the ith element of the vector. If the communication is not triggered, the neighbours can update the voltage prediction sequence using (4.19). This can avoid unnecessary communication if a slight change between two consecutive voltage prediction sequences is captured. As such, if the condition (4.18) is triggered at k_lth time step ($k_l \in \mathcal{C}$), the voltage predictions $\boldsymbol{Y}_{i,o}(k_l)$ are updated through the communication network. For any $j \in N_i$, the differences between the voltage of DG i and the information transmitted to DG j in the DMPC algorithm are bounded by the threshold e_{com} for all t.

It should be noted that the voltage prediction remains updated by (4.19) in presence of communication failure (caused by e.g. packet loss) between neighbours as the failure interrupts the communication (i.e. communication is not triggered). In such case, the control terminal value will be the last value in the prediction sequence, which can maintain the performance and enhance the system resilience.

Based on the discussion above, the event-triggered DMPC-based voltage regulation algorithm is illustrated in Algorithm 4.1. The impacts of the event triggering thresholds e_{opt} and e_{com} on the system behaviour will be numerically investigated in Section 4.4 to provide further insights into the selection of the thresholds.

Algorithm 4.1: Event-Triggered Voltage Regulation Algorithm

foreach *Time step* k **do**
    foreach *DG* i **do**
        Collect $\boldsymbol{y}_i(k), \boldsymbol{Y}_{j,o}(k), j \in N_i, \Xi_i(k-1)$ (update $\boldsymbol{Y}_{j,o}(k)$ from $\boldsymbol{Y}_{j,o}(k-1)$ as (4.19) if there is no data received);
        if (4.16) *holds* **then**
            Solve (4.14) and (4.15) to update the control input sequence $\Xi_i(k)$ and the voltage magnitude output sequence $\boldsymbol{Y}_{i,o}(k)$;
        else
            Update $\Xi_i(k), \boldsymbol{Y}_{i,o}(k)$ according to (4.17) and (4.12) respectively;
        end
        Apply $\xi_i(k|k)$ to DG i;
        if (4.18) *holds* **then**
            Transmit $\boldsymbol{Y}_{i,o}(k)$ to the neighbours through the communication network;
    end
end

4.3.3 Finite-time Adaptive Observer Design for Enhancing Noise-Resilience

The mismatch between the continuous-time system (4.8) and the discretized system (4.9) is highly influenced by the non-linearity $f_i(\boldsymbol{x}_i)$ embedded in ξ_i due to the variation of f_i within two samples. As such, the evaluation of the $\boldsymbol{y}_i(k+1)$ based on the given control input at $k+1$ may be inaccurate, and in turn, affects the upcoming optimization and prediction. In addition, after generating the auxiliary control variable ξ_i, the actual control input u_i is obtained by

$u_i = (g_i)^{-1}(\xi_i - f_i(\boldsymbol{x}_i))$, where the term $f_i(\boldsymbol{x}_i)$ need to be evaluated, and additional sensors may be required to monitor the internal states, such as v_{odi}, v_{oqi}. In fact, to obtain the state $\boldsymbol{y}_i$ and the term $f_i(\boldsymbol{x}_i)$, a more cost-effective solution is to use a system observer for reconstructing the real-time state $\boldsymbol{y}_i$ and the time-varying variable $f_i(\boldsymbol{x}_i)$, where the influence of measurement noise can also be highly attenuated [67]. The linearized model (4.7) considering system disturbance for the ith DG can be rewritten as:

$$\begin{cases} \dot{y}_{i,1} = y_{i,2} \\ \dot{y}_{i,2} = f_i'(\boldsymbol{x}_i) + g_{i,0}u_i \\ y_{i,o} = y_{i,1} = v_{odi} \end{cases} \tag{4.20}$$

$$g_i = g_{i,0} + \Delta g_i = L_{\boldsymbol{g}_i} L_{\boldsymbol{F}_i} h_i(\boldsymbol{x}_i), f_i'(\boldsymbol{x}_i) = f_i(\boldsymbol{x}_i) + \Delta g_i u_i$$

where $[y_{i,1}\ y_{i,2}]^T$ is the original state vector; $g_{i,0}$ and Δg_i denote nominal value and the deviation caused by parameter perturbation of g_i, respectively. Moreover, $f_i'(\boldsymbol{x}_i)$ represents the system uncertainty that collects the dynamics of DG inner control loops $f_i(\boldsymbol{x}_i)$, total uncertainties caused by exogenous disturbance, parameter perturbation and the measurement noise.

In the sequel, to streamline the notation, let us consider $\boldsymbol{y}_i(t) = \boldsymbol{z}(t) = [z_0(t) \quad z_1(t)]^T$ and $y_{i,o}(t) = y(t)$. Then, the single DG system (4.7) can be rewritten in the following observer-canonical form:

$$\begin{cases} \dot{\boldsymbol{z}}(t) = \mathbf{A}\boldsymbol{z}(t) + \mathbf{B}u(t) + \mathbf{B}_w w(t) \\ y(t) = \mathbf{C}\boldsymbol{z}(t) \end{cases}$$
$$\mathbf{A} = \begin{bmatrix} a_1 & 1 \\ a_0 & 0 \end{bmatrix}, \mathbf{B} = \begin{bmatrix} b_1 \\ b_0 \end{bmatrix}, \mathbf{C} = \begin{bmatrix} 1 & 0 \end{bmatrix}, \quad \mathbf{B}_w = \begin{bmatrix} \alpha_1 \\ \alpha_0 \end{bmatrix} = \begin{bmatrix} 0 \\ f'(\boldsymbol{x}(t)) \end{bmatrix}, w(t) = 1 \tag{4.21}$$

with $a_0 = a_1 = b_1 = 0, b_0 = 1$.

Motivated by a recently proposed deadbeat adaptive observer [122], which offers nearly instantaneous convergence property with high noise immunity, the intermittent (over short time-interval) state and parameter estimation can be enabled to cooperate with the proposed DMPC algorithm. Assuming the short time-interval can guarantee that $f'(\boldsymbol{x}(t))$ can be seen as a constant parameter, we can convert the linear time-varying (LTV) system (4.21) to a linear time-invariant system (LTI) with an unknown parameter $\alpha_0 = f$.

To proceed with the analysis, the state-space system (4.21) is expressed as the combination of the input-output derivatives:

$$y^{(n)}(t) = \sum_{i=0}^{n-1} a_i y^{(i)}(t) + \sum_{i=0}^{n-1} b_i u^{(i)}(t) + \sum_{i=0}^{n-1} \alpha_i w^{(i)}(t) \tag{4.22}$$

$$z_r(t) = y^{(r)}(t) - \sum_{j=0}^{r-1} a_{n-r+j} y^{(j)}(t) - \sum_{j=0}^{r-1} b_{n-r+j} u^{(j)}(t) - \sum_{j=0}^{r-1} \alpha_{n-r+j} w^{(j)}(t) \tag{4.23}$$

where $n = r = 2$ and $\sum_{j=0}^{k} \{\cdot\} = 0, k < 0$. $y^{(n)}(t)$ denotes the nth differential value of $y(t)$ and $z_r(t)$ denotes the rth element of the state in (4.21).

Let us introduce the Volterra integral operator V_K induced by a bivariate function $K(t, \tau)$ to the output and its derivatives:

$$[V_K y^{(i)}](t) \triangleq \int_0^t K(t, \tau) y^{(i)}(\tau) d\tau, \forall i \in \{0, \cdots, n\} \tag{4.24}$$

where $K(t, \tau)$ is the nth order non-asymptotic kernel [123] subject to

$$K^{(i)}(t, 0) = 0, \forall i \in \{0, \cdots, n\} \tag{4.25}$$

After some algebra, we get:

$$[V_K y^{(i)}](t) = \sum_{j=0}^{i-1} (-1)^{i-j-1} y^{(j)}(t) K^{(i-j-1)}(t, t) + (-1)^i [V_{K^{(i)}} y](t) \tag{4.26}$$

which can be obtained by applying the integral by parts and (4.25). If $i = 1$,

$$[V_{K^{(1)}} y](t) = y(t) K(t, t) - [V_K y^{(1)}](t) \tag{4.27}$$

Replacing $y(t)$ with $y^{(n-1)}(t)$, (4.27) becomes

$$[V_{K^{(1)}}y^{(n-1)}](t) = y^{(n-1)}(t)K(t,t) - [V_K y^{(n)}](t)$$

which can be further expanded by substituting (4.22)

$$\begin{aligned}(-1)^{n-1}[V_{K^{(n)}}y](t) = &-\sum_{j=0}^{n-2}(-1)^{n-2-j}y^{(j)}(t)K^{(n-j-1)}(t,t) + y^{(n-1)}(t)K(t,t)\\ &-\sum_{i=0}^{n-1}a_i[V_K y^{(i)}](t) - \sum_{i=0}^{n-1}b_i[V_K u^{(i)}](t) - \sum_{i=0}^{n-1}\alpha_i[V_K w^{(i)}](t)\end{aligned} \tag{4.28}$$

Substituting (4.26) and its same forms with $u(t), w(t)$ into (4.28), we obtain

$$\begin{aligned}(-1)^{n-1}[V_{K^{(n)}}y](t) + \sum_{i=0}^{n-1}(-1)^i a_i[V_{K^{(i)}}y](t) + \sum_{i=0}^{n-1}(-1)^i b_i[V_{K^{(i)}}u](t)\\ = -\sum_{i=0}^{n-1}(-1)^i\alpha_i([V_{K^{(i)}}w](t) + \sum_{r=0}^{n-1}(-1)^{n-r-1}K^{(n-r-1)}(t,t)z_r(t)\end{aligned} \tag{4.29}$$

where the state variables $z_r(t)$ and the unknown parameters α_i appear explicitly, and can be obtained by the casual filtering of the signals $y(t), u(t)$.

Considering the specific parameters of (4.21), the following expression can be inferred from (4.29):

$$(-1)[V_{K^{(2)}}y](t) + [V_K u](t) = f[V_K w](t) + (-1)K^{(1)}(t,t)z_0(t) + K(t,t)z_1(t) \tag{4.30}$$

To estimate the state and unknown parameter, let us define

$$\lambda(t) \triangleq (-1)[V_{K^{(2)}}y](t) + [V_K u](t) \tag{4.31}$$

$$\boldsymbol{\gamma}(t) \triangleq \big[[V_K w](t), (-1)K^{(1)}(t,t), K(t,t)\big] \tag{4.32}$$

Then, (4.30) can be rewritten as

$$\lambda(t) = \boldsymbol{\gamma}(t) \begin{bmatrix} f \\ \boldsymbol{z}(t) \end{bmatrix} \tag{4.33}$$

To find the estimates of $\begin{bmatrix} f & \boldsymbol{z}(t) \end{bmatrix}^T$ (of dimension 3), we can apply three different non-asymptotic kernel functions to augment (4.33) into three linearly independent equations

$$\boldsymbol{\Lambda}(t) = \boldsymbol{\Gamma}(t) \begin{bmatrix} f \\ \boldsymbol{z}(t) \end{bmatrix} \tag{4.34}$$

where $\boldsymbol{\Lambda}(t) = [\lambda_0(t), \lambda_1(t), \lambda_2(t)]^T$ and $\boldsymbol{\Gamma}(t) = \left[\boldsymbol{\gamma}_0^T(t), \boldsymbol{\gamma}_1^T(t), \boldsymbol{\gamma}_2^T(t)\right]^T$, and $\lambda_h(t), \boldsymbol{\gamma}_h(t), h \in \{0, 1, 2\}$ are (4.31) and (4.32) induced with the kernel functions respectively. The three kernel functions are designed as follows [123]:

$$K_h(t, \tau) = e^{-\omega_h(t-\tau)}(1 - e^{-\varpi\tau})^2, h \in \{0, 1, 2\} \tag{4.35}$$

which meets the non-asymptotic condition (4.25). Finally, the estimates are obtained by:

$$\begin{bmatrix} \hat{f} \\ \hat{\boldsymbol{z}}(t) \end{bmatrix} = \boldsymbol{\Gamma}^{-1}(t)\boldsymbol{\Lambda}(t), \forall t_\epsilon < t < t_\epsilon + \Delta t \tag{4.36}$$

where t_ϵ is the observer initialization time to guarantee the invertibility of $\boldsymbol{\Gamma}(t)$ ($\boldsymbol{\Gamma}(0) = 0$) and Δt is the active time of the observer. The observer ensures finite and instantaneous convergence of the state estimates to the true state with high level of noise immunity. The detailed discussion about the robustness of the observer is show in [124].

The non-asymptotic observer is sampled at T_s, and it cooperates with the event-triggered DMPC voltage regulation in a periodical manner, as shown in Figure 4.5. To ensure the estimates, $\hat{f}_i$ and $\hat{\boldsymbol{y}}_i$, available for the voltage regulator at each DMPC sampling instant. The observer is always enabled $\Delta t + t_\epsilon$ seconds ahead of an MPC step. For example, assuming the time at the k-th MPC step is t_{k_o}, the proposed observer is enabled at $t_{k_o} - \Delta t - t_\epsilon$, and after

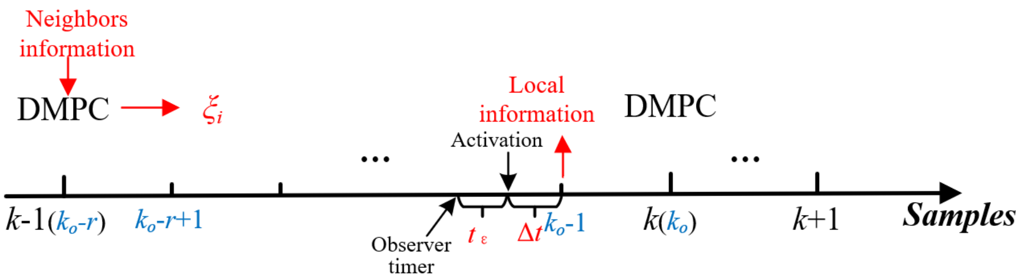

Figure 4.5: Time-sequence cooperation between the event-triggered DMPC and the non-asymptotic observer.

the holding time t_ϵ the estimates start updating. Both estimates $\hat{f}_i(t_{k_o})$ and $\hat{\boldsymbol{y}}_i(t_{k_o})$ are fed to the voltage regulator at t_{k_o} when the observer is disabled.

4.4 Simulation Results

In this section, the proposed event-triggered control method is tested on a simple MG configuration with 4 DGs and on the modified IEEE-13 test system.

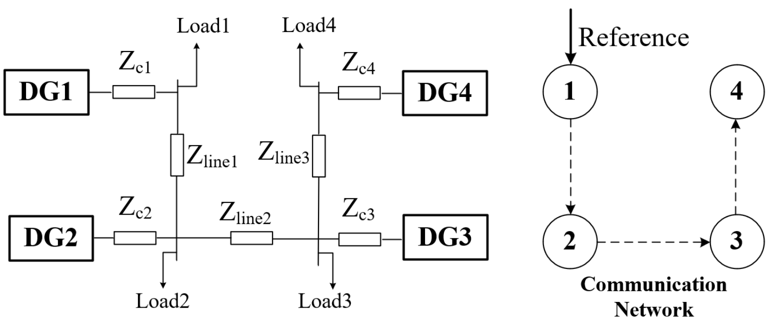

Figure 4.6: Diagram of the tested 4-bus MG system.

4.4.1 Case 1: 4-DG MG system

The single line diagram of the 4-DG MG and its communication topology is shown in Figure 4.6. The parameters of the tested MG system and the proposed controllers is shown in Table 4.1. The simulation test involves a few representative scenarios by which the effectiveness of the proposed methodology can be reflected.

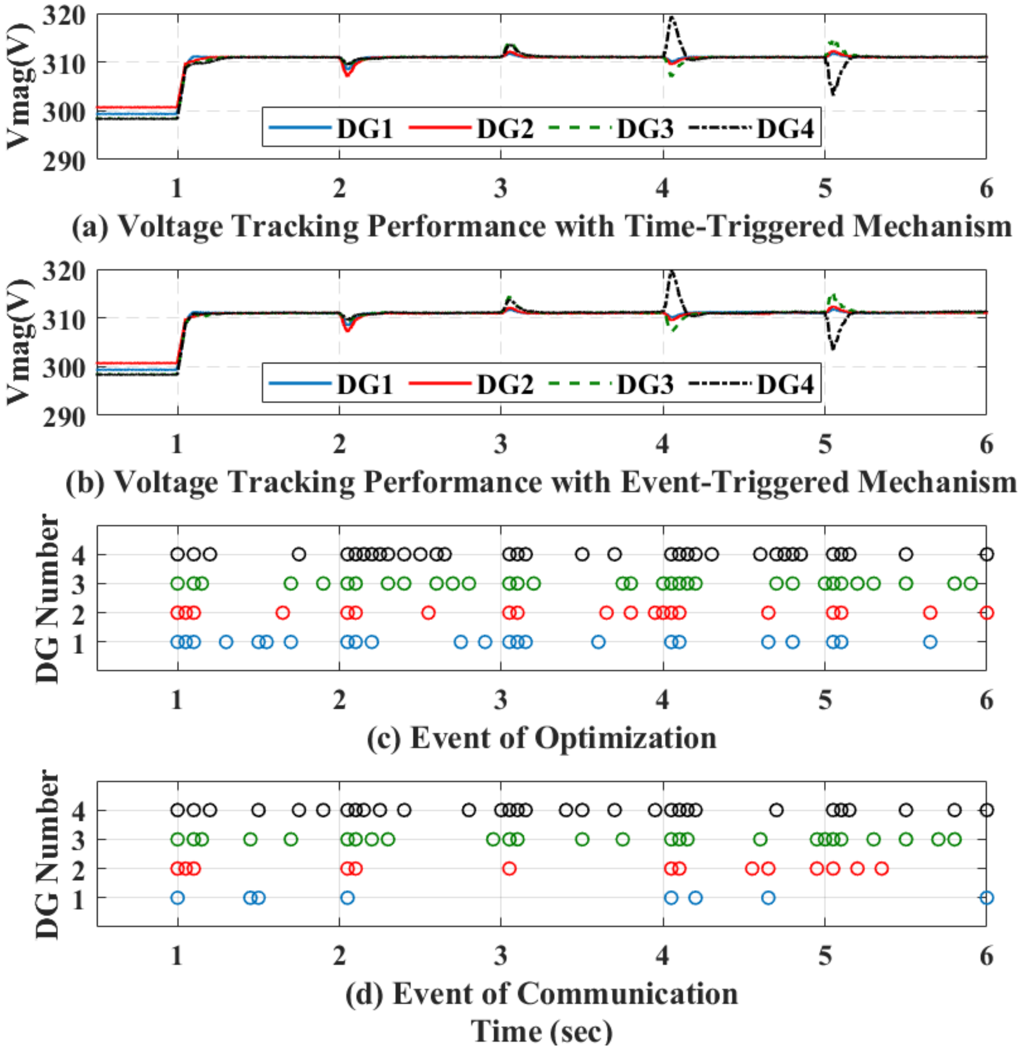

Figure 4.7: Voltage control performance by using event-triggered mechanism: (a) voltage tracking performance with time-triggered mechanism; (b) voltage tracking performance with event-triggered mechanism; (c) event-triggered time of DMPC optimization; (d) event-triggered time of neighbouring communication.

Scenario 1: Load Change and Plug-and-Play Capability Test

In this Scenario, the control performance of the proposed control is illustrated under load change and DG's plug-and-play operation: in the beginning, Load2 is disconnected from the system and only primary control is applied; at $t = 1$s, the proposed secondary control is activated; Load2 and half of Load3 are connected and disconnected at $t = 2$s and $t = 3$s respectively, and DG4 is disconnected and re-connected at $t = 4$s and $t = 5$s respectively. The performance of voltage tracking is shown in Figure 4.7 and the reductions of computation and communication are detailed in Table 4.2.

Table 4.1: Parameters of the Tested 4-bus MG System for DMPC Simulation ($T_s^{mpc} = 0.05$s, $T_s = 0.01$s)

	DG1	DG2	DG3 & DG4
m_P	6.28×10^{-5}	9.42×10^{-5}	12.56×10^{-5}
n_Q	0.5×10^{-3}	0.75×10^{-3}	1×10^{-3}
R_f	0.1 Ω	0.1 Ω	0.1 Ω
L_f	1.35 mH	1.35 mH	1.35 mH
C_f	47μF	47μF	47 μF
R_c	0.02 Ω	0.02 Ω	0.02 Ω
L_c	2 mH	2 mH	2 mH
K_{Pv}	0.05	0.05	0.1
K_{Iv}	390	390	420
K_{Pc}	10.5	10.5	15
K_{Ic}	1.6×10^4	1.6×10^4	2×10^4
Line1	$R = 0.23\ \Omega,\ L = 318\ \mu$H		
Line2	$R = 0.35\ \Omega,\ L = 1847\ \mu$H		
Line3	$R = 0.23\ \Omega,\ L = 318\ \mu$H		
Load1	$R = 2\ \Omega,\ L = 6.4$ mH		
Load2	$R = 4\ \Omega,\ L = 9.6$ mH		
Load3	$R = 6\ \Omega,\ L = 12.8$ mH		
Load4	$R = 6\ \Omega,\ L = 12.8$ mH		
DMPC	$v_{ref} = 311(220\sqrt{2}),\ H = 10$		
Thresholds	$e_{opt} = 0.1, e_{com} = 0.1$		
Observer	$\varpi = 2.5, [\omega_0, \omega_1, \omega_2] = [1, 2, 3]$		

Table 4.2: Computation and Communication Reductions Using Event-Triggered Mechanism

	DG1	DG2	DG3	DG4	Average
Computation Reduction	77%	80%	68%	66%	72.75%
Communication Reduction	92%	86%	74%	69%	80.25%

By using the event-triggered mechanism, the sacrifice of control performance is limited, whereas the computation and communication are both considerably reduced. By employing the pro-

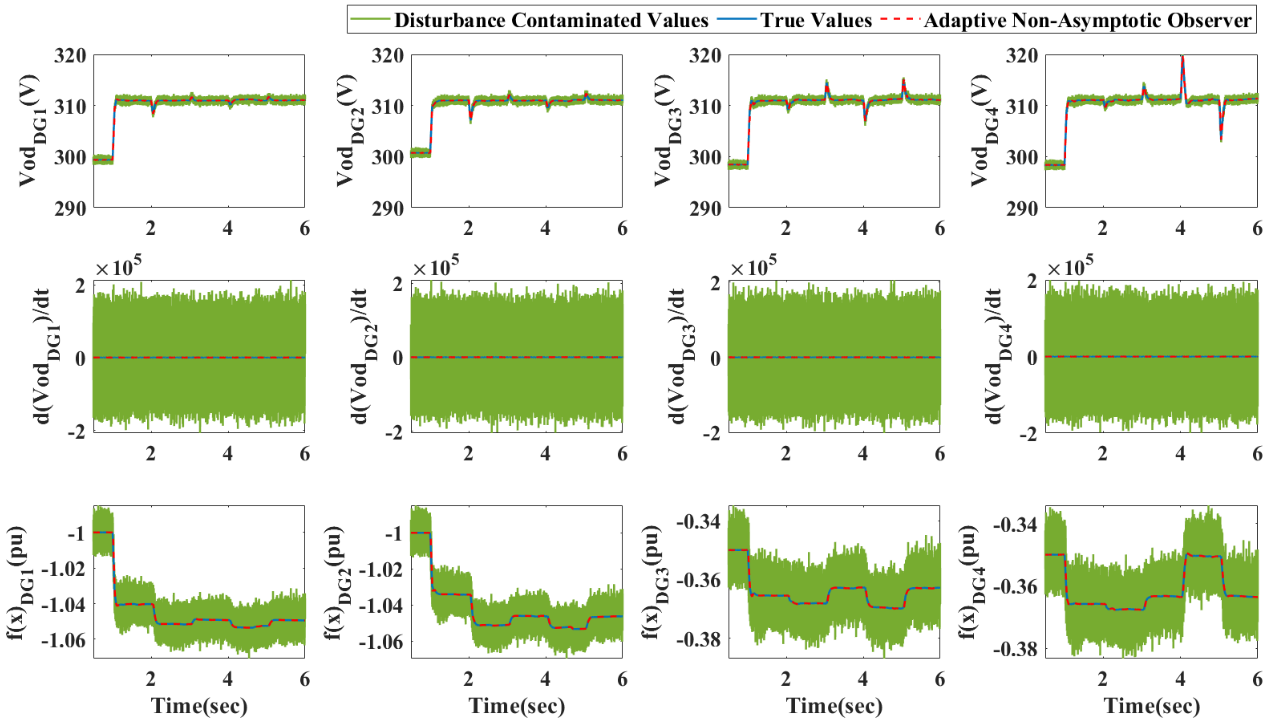

Figure 4.8: Non-asymptotic observer performance (base value of $f(x)$: 7.35×10^9).

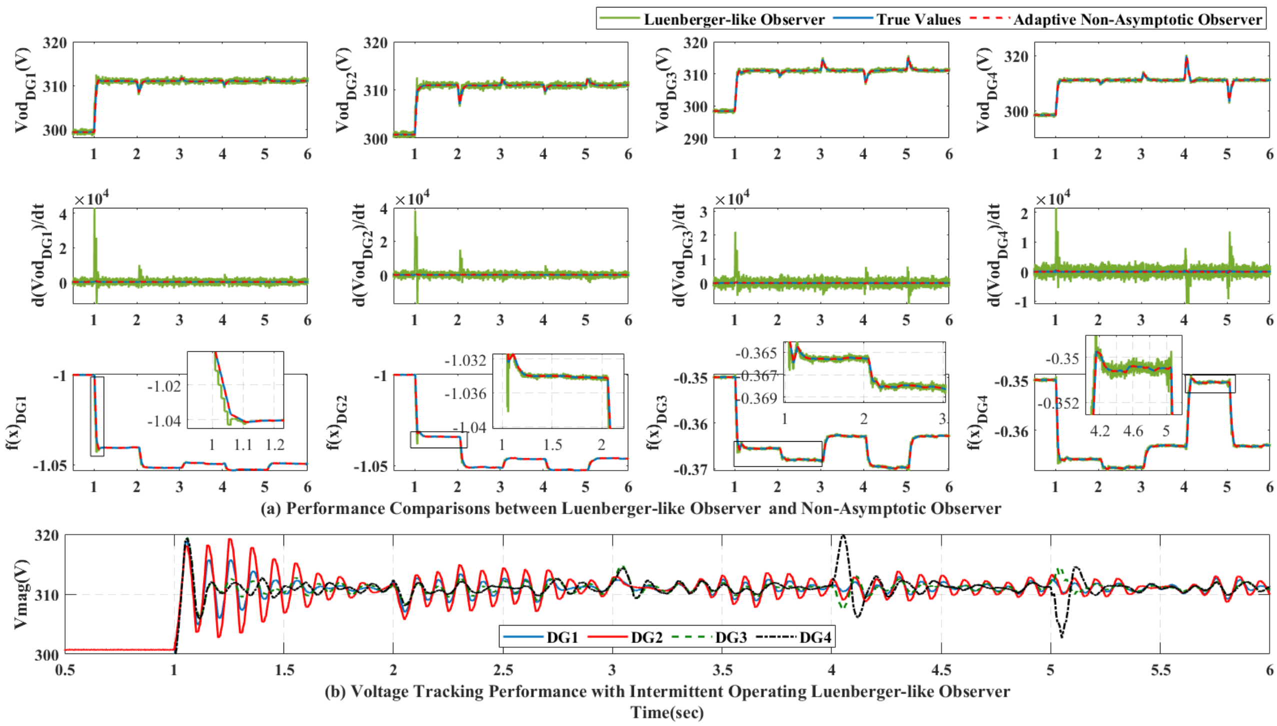

Figure 4.9: Voltage control performance with intermittent operating Luenberger-like observer.

posed non-asymptotic observer, the negative effects of the disturbance can be eliminated, as shown in Figure 4.8. The performance of the proposed observer is emphasized by the comparisons among true values, observed values and disturbance contaminated values that are obtained from indirect measurement in the noisy environment. Compared to the previous Luenberger-like extended state observer [67], the proposed non-asymptotic observer benefits from its intermittent operating characteristic. The performance comparisons between intermittent operating Luenberger-like observer and the proposed non-asymptotic observer is shown in Figure 4.9, where we can see that Luenberger-like Observer cannot estimate the state precisely when the system responses to the physical events. If the Luenberger-like extended state observer is working intermittently as the proposed non-asymptotic observer, the voltage tracking performance will degrade as Figure 4.9(b).

To further illustrate the resilient performance of the DMPC-based algorithm, an extreme condition with a dramatic voltage drop has been simulated. At t=2s, DG4 is disconnected from the MG while the loads increase, thus the DG output voltage may drop to the unacceptable sections (out of the constraint (4.15)). Figure 4.10 compares the control performance between DMPC-based and PIC (Proportional Integral Control)-based algorithms. When using DMPC-based algorithm, the voltage magnitudes are restored into the constraints faster due to the voltage constraints. However, the PIC-based algorithm, as a linear control method, cannot handle such a voltage drop efficiently.

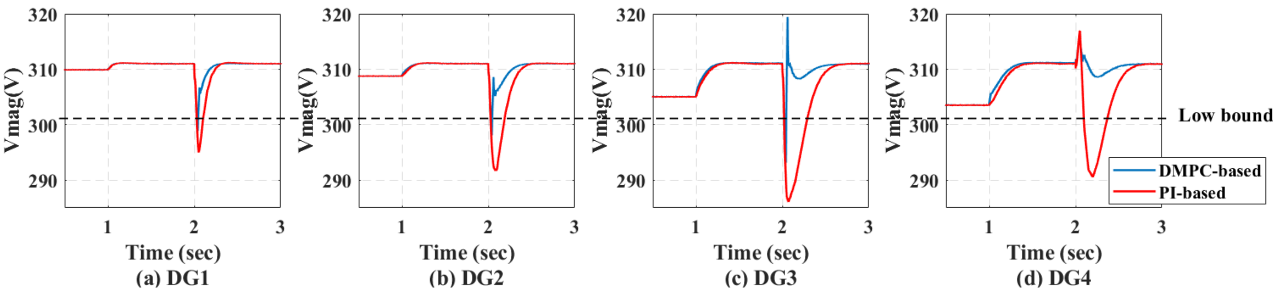

Figure 4.10: Voltage control performance under the extreme condition.

Scenario 2: Control Performance with Different Event Triggering Thresholds

The control performance of proposed event-triggered mechanism may be influenced by the selection of thresholds for both computation and communication event generators. Therefore, in Scenario 2, case studies as Scenario 1 are carried out with different triggering thresholds.

The control performance with fixed e_{com} ($e_{com} = 0.1$) but different thresholds e_{opt} is detailed

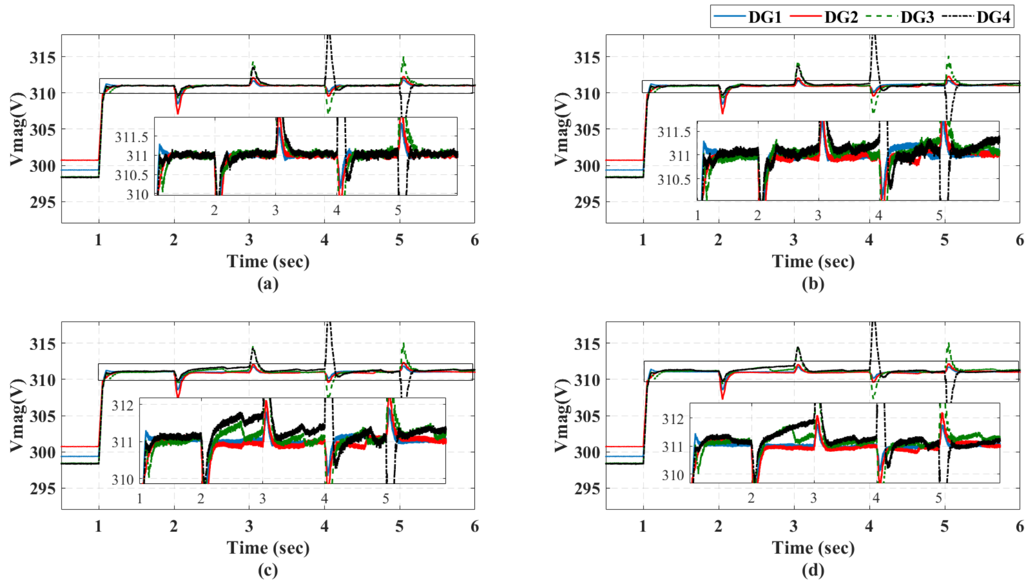

Figure 4.11: Event-triggered condition with fixed e_{com} ($e_{com} = 0.1$) but different thresholds e_{opt}: (a) $e_{opt} = 0.05$; (b) $e_{opt} = 0.1$; (c) $e_{opt} = 0.15$; (d) $e_{opt} = 0.2$.

Table 4.3: Computation and Communication Reductions with Fixed e_{com} ($e_{com} = 0.1$) but Different Thresholds e_{opt}

	e_{opt}	DG1	DG2	DG3	DG4	Average
Computation	0.05	24%	24%	34%	34%	29%
	0.1	77%	80%	68%	66%	72.75%
	0.15	83%	84%	83%	81%	82.75%
	0.2	87%	84%	85%	83%	84.75%
Communication	0.05	95%	89%	84%	84%	88%
	0.1	92%	86%	74%	69%	80.25%
	0.15	88%	77%	65%	64%	73.5%
	0.2	86%	78%	64%	65%	73.25%

in Figure 4.11 and Table 4.3. As e_{opt} increases, the optimization computation of each DG controller decreases largely, but from Figure 4.11, we can also see the control performance will clearly degrade when $e_{opt} = 0.2$ and $e_{opt} = 0.3$. Thus, the selection of e_{opt} is a trade-off between the tracking performance and the computation reduction. The control performance with fixed e_{opt} ($e_{opt} = 0.1$) but different thresholds e_{com} is detailed in Figure 4.12 and Table 4.4. As e_{com} increases, the communication among DGs is reduced with the gradually degraded control performance.

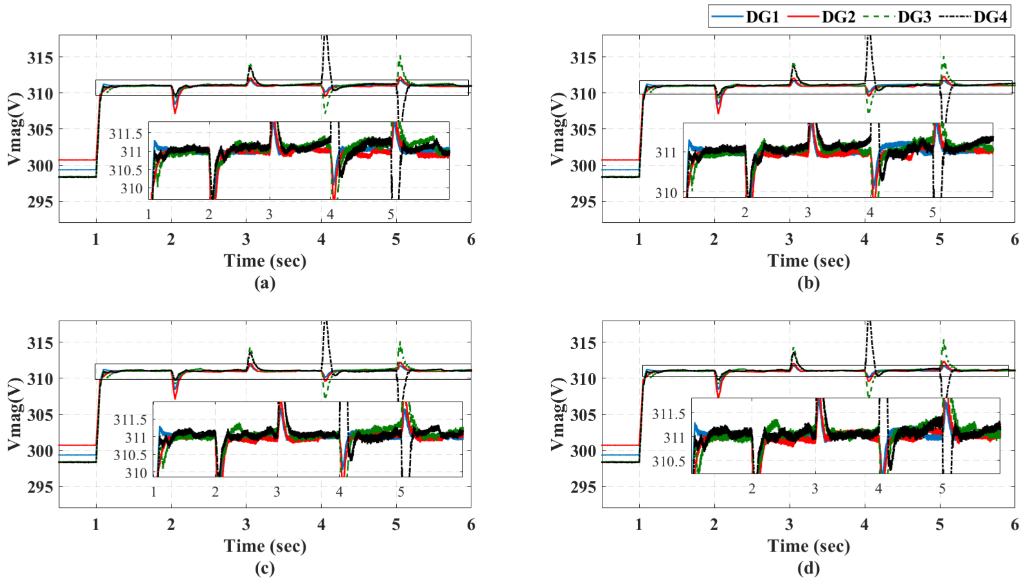

Figure 4.12: Event-triggered condition with fixed e_{opt} ($e_{opt} = 0.1$) but different thresholds e_{com}: (a) $e_{com} = 0.05$; (b) $e_{com} = 0.1$;(c) $e_{com} = 0.15$; (d) $e_{com} = 0.2$.

Table 4.4: Computation and Communication Reductions with Fixed e_{opt} ($e_{opt} = 0.1$) but Different Thresholds e_{com}

	e_{com}	DG1	DG2	DG3	DG4	Average
Computation	0.05	77%	79%	69%	71%	74%
	0.1	77%	80%	68%	66%	72.75%
	0.15	79%	80%	73%	64%	74%
	0.2	78%	75%	69%	71%	73.25%
Communication	0.05	67%	42%	42%	41%	48%
	0.1	92%	86%	74%	69%	80.25%
	0.15	96%	91%	81%	80%	87%
	0.2	96%	93%	86%	88%	90.75%

Scenario 3: Effects of Information Update Frequency and Prediction Horizons

In Scenario 3, the effects of information update frequency and prediction horizon on the control performance are investigated, shown in Figure 4.13. Figure 4.13(a) illustrates the voltage response for different update intervals ($T_s^{mpc} = 0.05\text{s}, 0.1\text{s}, 0.15\text{s}$). Although the voltage control performance degrades slightly on convergence time as the update interval increases, the computation and communication ($T_s^{mpc} = 0.15\text{s}$) are reduced significantly by 32.1% and 68.4%

respectively compared to that of $T_s^{mpc} = 0.05$s. The effect of the prediction horizon is shown on the voltage control performance as prediction horizon decreases. It can be noted that the declining prediction horizon leads to degrading control performance and at the same time higher computation and communication rates (increasing by 70.6% and 81.0% respectively as horizon decreases from 10 to 2).

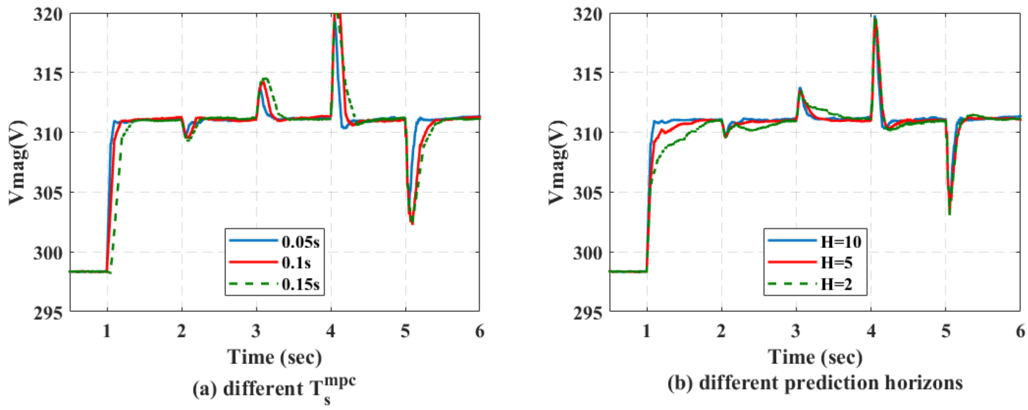

Figure 4.13: Effects of information update frequency and prediction horizon.

Scenario 4: Communication Topology Change

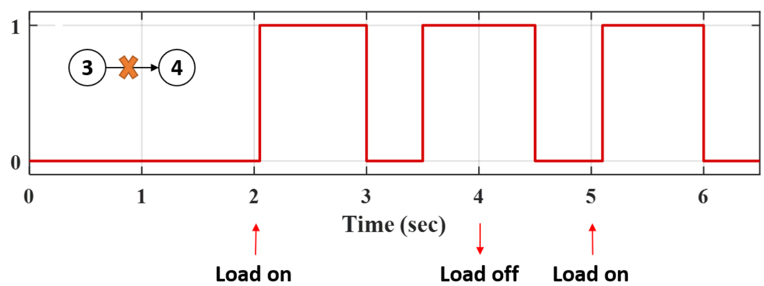

Figure 4.14: Physical and cyber events of the 4-DG MG system: value "1" represents that the communication channel between DG3 and DG4 is unavailable; the load change occurs at 2s, 4s and 5s respectively.

In Scenario 4, we consider communication interruptions which may occur in the distributed operation, and the physical and cyber events is shown in Figure 4.14. In the cyber layer, the communication change mimics the failure and recovery of cyber links. In practice, the recovery of communication links takes a finite period of time depending on the numbers of attacked nodes and broken communication links [125]. In this scenario, from 2s to 6s, several failure and recovery events occur. The corresponding control performance is shown in Figure 4.15. The

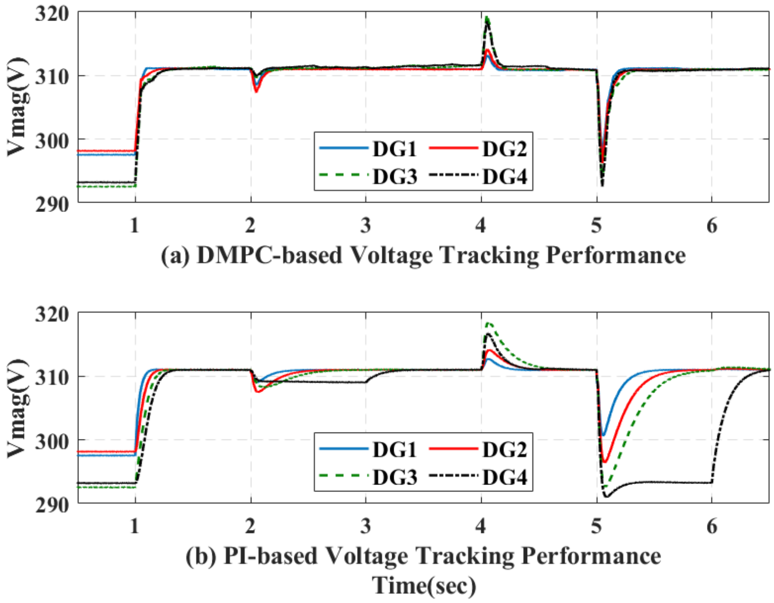

Figure 4.15: Voltage control performance with cyber and physical events.

voltage tracking performance is maintained during the whole event, although DG4 does not always have the neighbouring information over the time period $2\text{s} < t < 6\text{s}$. This is due to the prediction mechanism in the DMPC algorithm, under which DG4 can update the neighbouring information according to the information received before the communication failure occurs. In other words, the prediction model in the event-triggered DMPC helps maintain the control performance in this extreme condition, which enhances the operational resilience. However, the PIC-based control can only use the last received information before the communication failure, so it could lead to the tracking error if the system has not entered into the steady state at the time instant when the communication failure occurs. Due to that communication failure can be caused by many practical reasons such as actual fault, it is reasonable that there exists load change during the communication failure, thus the proposed DMPC-based control will show better resilience in practice.

4.4.2 Case 2: Modified IEEE-13 bus system

A real MG system is utilized to further test the effectiveness of the proposed method. The electrical and communication topology of the modified IEEE-13 bus test system [126] is shown in Figure 4.16, where there is a breaker between node 671 and 692. The parameters of 6 DGs

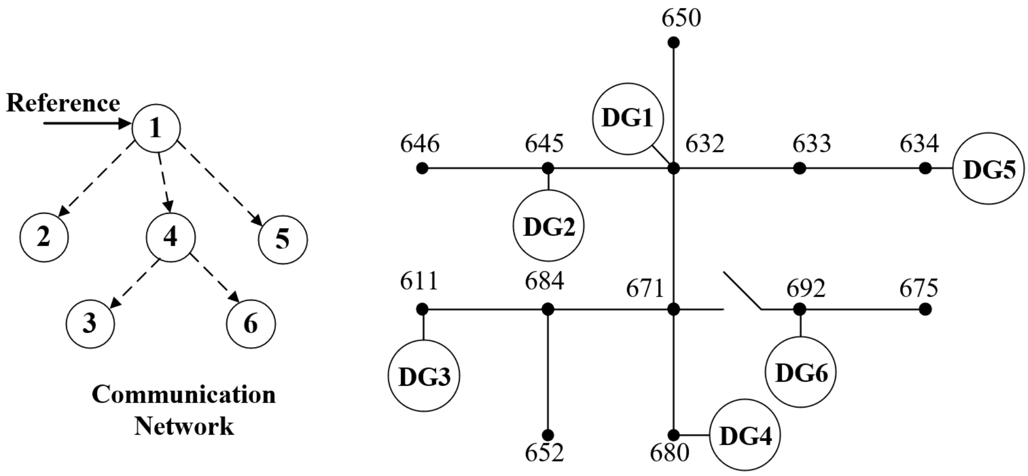

Figure 4.16: Diagram of modified IEEE-13 bus MG system

are the same as those shown in Table 4.1 (DG5 is the same as DG4, DG6 is the same as DG1). The controller parameters remain the same as well. Due to the fact that this subsection focuses on the scalability and especially the resilience against potential system reconfiguration. The event triggering thresholds are set to $e_{opt} = 0.1, e_{com} = 0.1$ by following a similar tuning process elaborated in subsection 4.1.2.

Scenario 1: Scalability Test

In this Scenario, the breaker between nodes 671 and 692 is always switched on, and the scalability of the proposed control is illustrated by load change and DG's plug-and-play scenario: loads at bus 645 and bus 675 are decreased and increased at $t = 2\text{s}, 3\text{s}$ respectively; and DG4 is disconnected and re-connected at $t = 4\text{s}$ and $t = 5\text{s}$ respectively. The voltage tracking performance is shown in Figure 4.17 and the average reductions of computation and communication are 57.42% and 88.48%.

Scenario 2: Resilience Illustration with System Reconfiguration

To evaluate the resilience of the proposed voltage regulation method when the system reconfiguration occurs on both physical and cyber layers, we design the physical and cyber events (including breaker switched off and on) as shown in Figure 4.18. The corresponding control per-

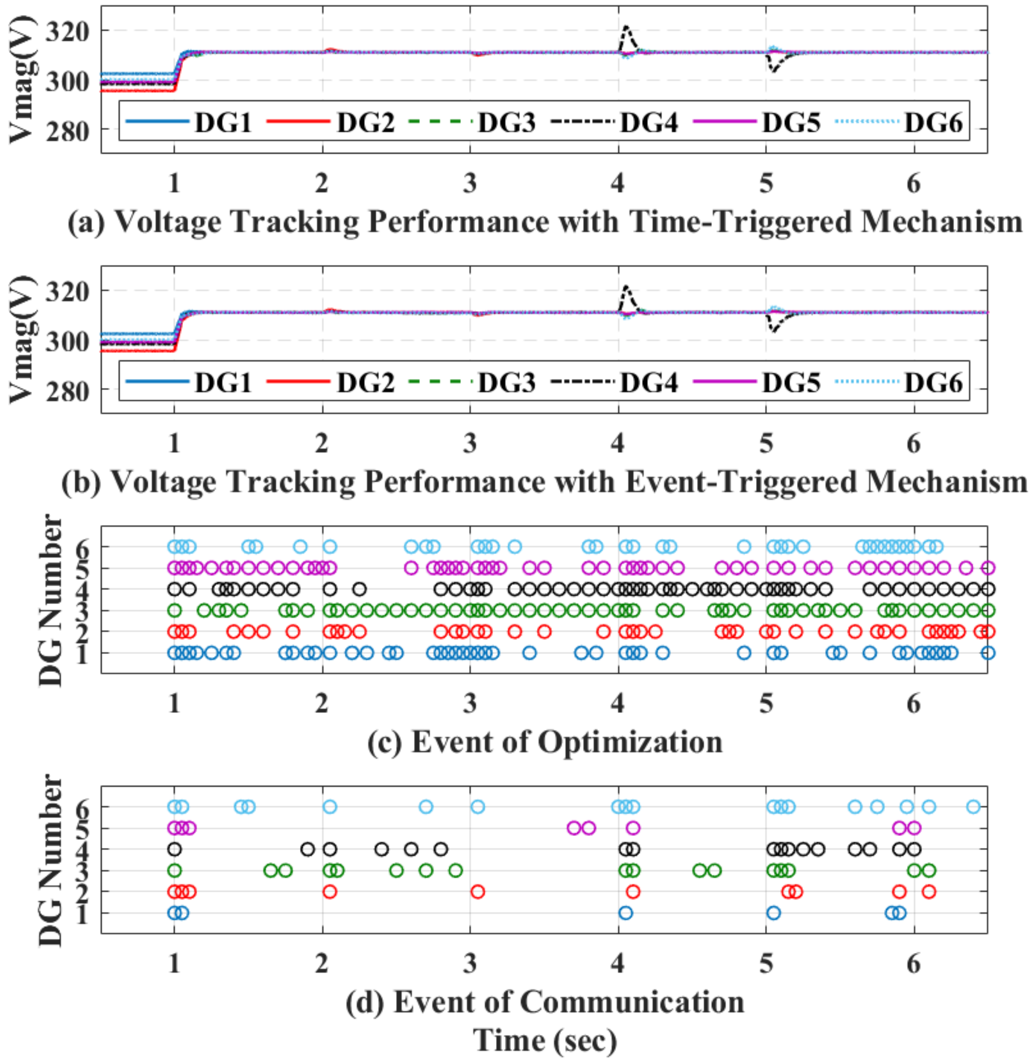

Figure 4.17: Voltage control performance of modified IEEE-13 bus MG system: (a) voltage tracking performance with time-triggered mechanism; (b) voltage tracking performance with event-triggered mechanism; (c) event-triggered time of DMPC optimization; (d) event-triggered time of neighbouring communication.

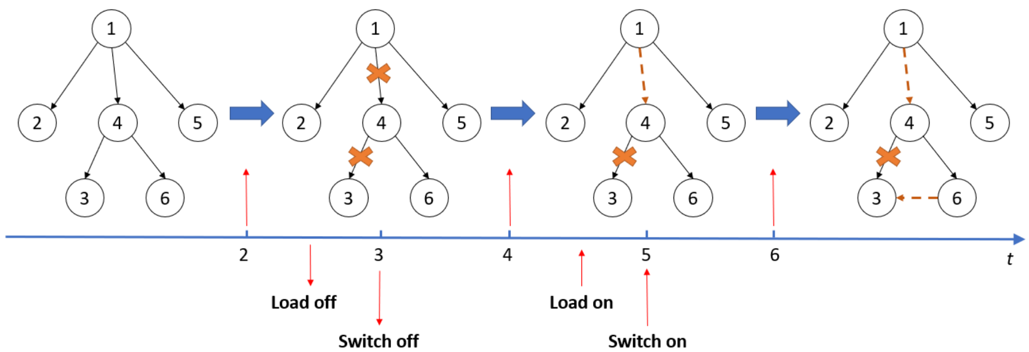

Figure 4.18: Physical and cyber events of modified IEEE-13 bus MG system

formance is shown in Figure 4.19. Although there are both physical and cyber events, similar to the subsection 4.1.4, the voltage tracking performance is guaranteed by using event-triggered

DMPC method, and the average reductions of computation and communication are 63.94% and 88.03%. The oscillations at $t = 5$s are incurred by the re-synchronization after the break is switched on.

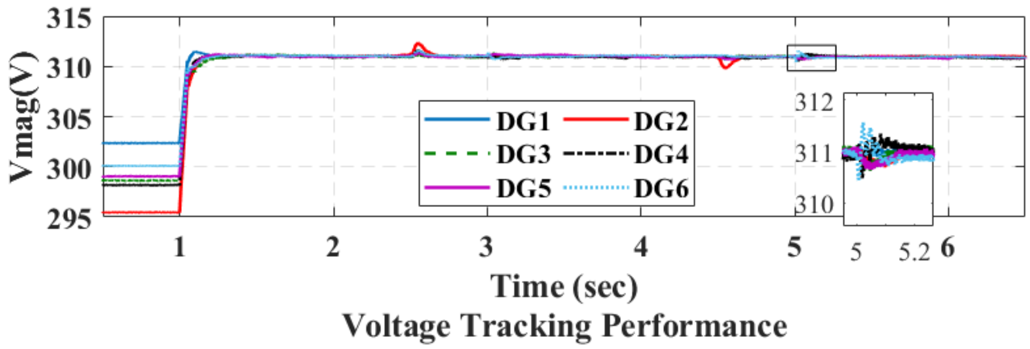

Figure 4.19: Voltage control performance with system reconfiguration in the modified IEEE-13 bus system

4.5 Conclusion

This chapter proposes an event-triggered DMPC for secondary voltage control scheme in a cyber-physical coupled MG system, which explicitly considers the model non-linearity and the system noise-resilience. In the control design, based on the event-triggered DMPC, two thresholds are designed to trigger the local DMPC computation and neighbouring communications among DGs. To facilitate a cost-effective and noise-resilient control, an adaptive observer that features the non-asymptotic convergence characteristic is utilized, and this designed adaptive non-asymptotic observer can be coordinated with the DMPC voltage regulator in a timing sequence. Finally, the effectiveness of the proposed control method is verified on a 4-DG MG system and the modified IEEE-13 system.

Chapter 5

Cyber-Resilient Self-Triggered Distributed Control of Networked Microgrids Against Multi-Layer DoS Attacks

5.1 Introduction

The energy source has been transforming from traditional fossil fuel based power generations to inverter-based renewable energy resources driven by the development of low/zero-carbon societies [9]. Rapidly developing inverter-based distributed energy resources (DERs) gradually dominate power systems [36, 127]. Reconstructing high-DER-penetrated power systems into multi-microgrids, i.e., networked microgrids (MGs) is one of the significant pathways of improving the resilience [14, 128]. However, the integration of increasing DERs (using the concept of networked MGs) has lead to more complicated information flows and tighter cyber-physical fusion [129] between DER devices and information systems in order to support efficient control logic. The large scale integration of distributed DERs restricts the applicability of traditional centralised control methods due to the communication constraints and vulnerability against single-point failure, which drives the rapid development of distributed control methods [41,43].

Such cyber-physical system has inevitably left multi-MG systems exposed to uncertainties from the physical environment and malicious cyberattacks from cyberspace. One of the most significant cyber-layer issues is known as denial-of-service (DoS) or jamming attacks, which intend to disrupt communication and data exchange among networked MG information systems to deteriorate control and operation performance. Therefore, resilient distributed control has been receiving significant attention in recent years. Various control methods have been proposed to enhance the resilience of cyber-physical MGs against DoS attacks, including time-varying sampling strategies [130–132], Lyapunov-based analysis [133–135], H_∞ control [136,137], switched system design [138–140] and reinforcement learning [141]. To efficiently manage the information flow, the concept of event-/self-triggered control strategies [116] is developed to enable aperiodic communication, sensing and actuation [142]. With the event-/self-triggered framework, a class of effective DoS countermeasures are designed by constructing suitable triggering mechanisms inferred from Lyapunov arguments [1–4,131,132]. For instance, the works presented in [131,132] propose an adaptive sampling mechanism whereby the impact of DoS attacks can be mitigated by increasing the sampling rate under attacks.

Existing literature on DoS attacks can be generalised into two categories: 1) attacks only over neighbouring communication links, 2) attacks over the sensing-communication-actuation chain. The neighbouring communication links admittedly are the most vulnerable to attackers as discussed in [3,4,130–132,135,139]. Ref. [2], though mentioning multi-layer DoS attacks, still focuses on the effects on communication channels. However, the sensing and actuation channels are also worthy of consideration. Some recent works start to investigate the attacks over sensing-communication-actuation chains, by either focusing on the single-layer sensing and actuation channels while ignoring communication channels [133], or simply regarding DoS attack effects on the chains as overdue input updates [134,137,138]. In this context, there is still a lack of understanding of the diverse impact of DoS attacks against different layers of the sensing-communication-actuation chain in a hierarchical control framework of power systems.

In fact, a hierarchical control framework adopted by networked MGs relies on more complex information network. On this occasion, each DG involves remote (e.g., telemetered) sensing and control actuation with its MG centre controller (MGCC). Hence, cyberattacks could simultaneously occur on communication links for inter-MG data sharing, measurement and actuation channels for intra-MG aggregation and distribution respectively. In particular, the adversary can erase the data sent to actuators or to block the sensor measurement. This motivates the resilience enhancement against multi-layer DoS for networked MGs within a hierarchical control framework. In this context, this chapter proposes a novel scheme that, for the first time, addresses multi-layer DoS attacks targeting the neighbouring communication, sensor measurement and control actuation channels of networked MGs with hierarchically controlled DERs. The main contributions are summarised as follows:

1. To characterise multi-layer DoS attacks within different data flow channels among networked MGs, we propose a unified notion of Persistency-of-Data-Flow (PoDF). The notion PoDF is of significance in evaluating the effects of multi-layer DoS attacks.

2. With an edge-based control logic, the proposed self-triggered ternary controller enables asynchronous data collection and processing for each MG from all its neighbours as opposed to existing methods that relies on synchronous communication. This remarkable feature of asynchronous data collection and processing turns out to be of major significance to ensure consensus properties in the presence of multi-layer DoS attacks.

3. An adaptive scheme of the control and communication policies is devised by utilising timestamps of successful information exchange attempts in different information network links. As such, the conservativeness of the edge-based self-triggered control designed from a global perspective can be significantly reduced.

The remainder of this chapter is organized as follows. In Section 5.2, the cyber-physical model of networked MGs and the self-triggered consensus concept are provided. Section 5.3 introduces the adaptive distributed self-triggered consensus controller with reduced conservativeness that is proved to be resilient against multi-layer DoS attacks. Simulation results are presented in Section 5.4 and Section 5.5 concludes this chapter.

5.2 Preliminaries and Problem Formulation

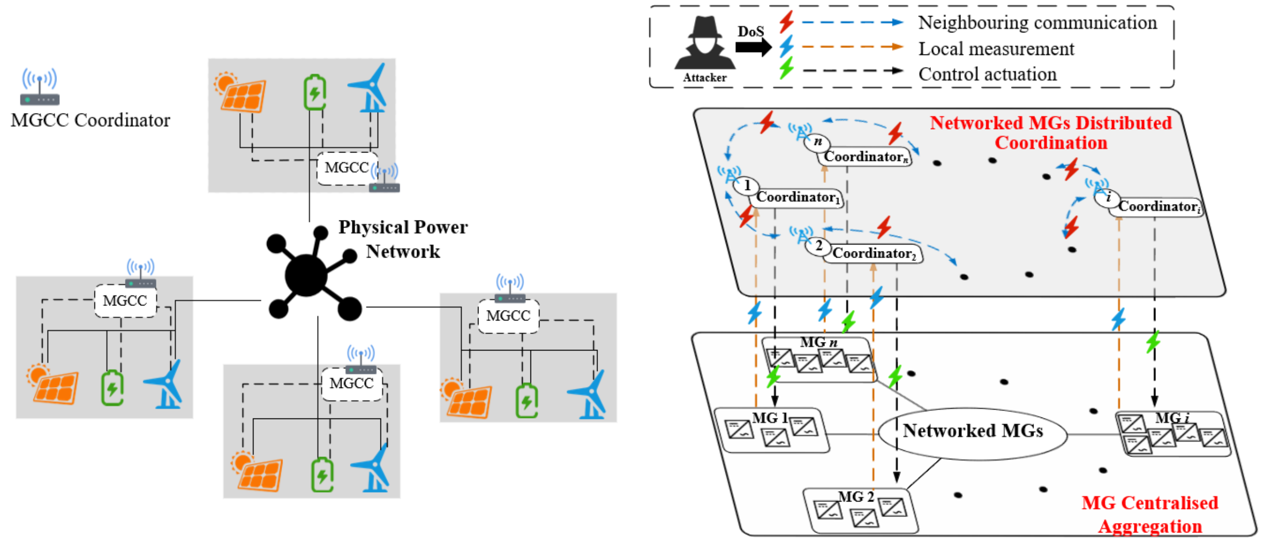

Figure 5.1: Hierarchically controlled networked MGs.

5.2.1 Problem Statement

The networked MGs discussed in this chapter are controlled under a hierarchical framework, as shown in Figure 5.1, where each MG employs one central coordinator called MGCC to aggregate the measured information and to distribute the calculated commands. In each MG shown in Figure 5.1(a), one MGCC manages all dispatchable DERs and aggregates their operational states. Each MGCC exchanges its own aggregated state information with other neighbouring MGCCs through a distributed communication network, to enable distributed coordination, as depicted in Figure 5.1(b).

The basic idea of such a hierarchical framework is to aggregate DGs, with small capacities but in large quantities inside one MG to support system operation. Such a hierarchical framework [143] avoids a curse of dimensionality within a fully centralised control, while modularized distributed control avoids the large-scale complex communication network of a fully distributed framework.

To effectively regulate each MG, an aggregated dynamic model can be built through some equivalent methods [128, 144, 145], even if there exist nodes without DGs (refer to [121]). To summarise, consider a droop-controlled equivalent modelling, for each MG i, we have the equivalent parameters

$$m_{Pi} = \frac{1}{\sum_{j \in \mathcal{C}_i} \frac{1}{m_i^{Pj}}}, \ \omega_i = \frac{\sum_{j \in \mathcal{C}_i} \frac{\omega_i^j}{\omega_c m_i^{Pj}}}{\sum_{j \in \mathcal{C}_i} \frac{1}{\omega_c m_i^{Pj}}} \tag{5.1}$$

where $\mathcal{C}_i$ contains all DGs of MG i. In MG i, m_i^{Pj}, ω_i^j denote the frequency droop coefficient and angular frequency of DG j, and m_{Pi}, ω_i are respectively the equivalent frequency droop coefficient and the equivalent angular frequency of MG i (similar to the concept of the Center of Inertia). ω_c denotes the cut-off frequency of low-pass filter in the inverter control loop.

The objective is to enable each MG to participate frequency synchronisation using

$$\omega_{ni} = \omega_i + m_{Pi} P_i \tag{5.2}$$

where ω_{ni} is the nominal set point for frequency regulation; P_i is the summation of active power output of the ith MG.

The primary control through (5.2) can not eliminate the frequency deviations from the reference, and the secondary control is employed to achieve frequency synchronisation and accurate active power sharing, i.e.,

$$\lim_{t \to \infty} |\omega_i - \omega_j| = 0, \lim_{t \to \infty} \omega_i = \omega_{\text{ref}} \tag{5.3}$$

$$\lim_{t \to \infty} \left| \frac{P_i}{P_{\max,i}} - \frac{P_j}{P_{\max,j}} \right| = 0 \tag{5.4}$$

where $P_{\max,i}$ denotes the active power ratings of the ith generator, and (5.4) is equivalent to $\lim_{t \to \infty} |m_{Pi} P_i - m_{Pj} P_j| = 0$ by approximately setting frequency droop coefficients.

To formulate the control problem, we differentiate (5.2) and choose the changing rates of frequency and active power output as control variables $\dot{\omega}_{ni} = \dot{\omega}_i + m_{Pi} \dot{P}_i = u_{\omega i} + u_{Pi}$ with $u_{\omega i}, u_{Pi}$ being the auxiliary control inputs that have been widely utilised in [66, 92]. Such that, we can obtain

$$\dot{\boldsymbol{x}}_\omega = \boldsymbol{u}_\omega, \dot{\boldsymbol{x}}_P = \boldsymbol{u}_P \tag{5.5}$$

where $\boldsymbol{x}_\omega = [\omega_1, \ldots, \omega_n]^\top$, $\boldsymbol{x}_P = [m_{P1}P_1, \ldots, m_{Pn}P_n]^\top$, $\boldsymbol{u}_\omega = [u_{\omega 1}, \ldots, u_{\omega n}]^\top$ and $\boldsymbol{u}_P = [u_{P1}, \ldots, u_{Pn}]^\top$. Owing to the similar formulation of modelling (5.5) for frequency and active power, we hereafter omit the subscript ω, P, i.e., $x_i := \omega_i$ or $x_i := m_{Pi}P_i$, to design the control algorithm that can be applied to both frequency regulation and active power sharing.

The communication topology of networked MGs can be modelled by an undirected graph $\mathcal{G} = \{\mathcal{I}, \mathcal{E}\}$, where $\mathcal{I} = \{1, 2, \ldots, m\}$ is a set of MGs, $\mathcal{E} \subseteq \mathcal{I} \times \mathcal{I}$ is a set of edges, and m is the number of MGs. An edge (j, i) means that the ith MG can receive information from the jth MG and j is a neighbour of i. The set of neighbours of MG i is described by $\mathcal{N}_i = \{j : (j, i) \in \mathcal{E}\}$ with $d_i = |\mathcal{N}_i|$ denoting the cardinality of $\mathcal{N}_i$. The corresponding adjacency matrix $\mathcal{A} = [a_{ij}] \in \mathbb{R}^{m \times m}$ is formed by $a_{ii} = 0$; $a_{ij} > 0$ if $(j, i) \in \mathcal{E}$, otherwise $a_{ij} = 0$. The communication topology is denoted by the matrix $\mathcal{A}$, which is assumed to be connected to guarantee the consensus performance [146].

As shown in Figure 5.1, different channels, i.e., measurement, communication and actuation are vulnerable to cyberattacks due to the hierarchical structure. In this chapter, we consider data unavailability issues affecting all channels. Under multi-layer DoS attacks, the frequency synchronisation problem based on dynamics (5.5) becomes: *how to design efficient control laws to update input vectors* $\boldsymbol{u}_\omega, \boldsymbol{u}_P$ *to reach both* (5.3) *and* (5.4) *under DoS attacks?*

5.2.2 Preliminary of Distributed Ternary Control

System (5.5) can be recast in the form of (5.6), which has been addressed in the literature by a distributed ternary control mechanism. Some basic concepts concerning the ternary control are presented below with more detailed discussion in [4] and [1]. The system is formed by a triplet of n-dimensional variables $(x, u, \theta) \in \mathbb{R}^n \times \mathbb{R}^d \times \mathbb{R}^d$, where x, u, θ are the vectors of node states, controls and clock variables respectively. u, θ are both edge-based variables with $d := \sum_{i=1}^n d_i$

defined in Section 5.2.1. The system dynamics of distributed ternary control are governed by:

$$\dot{x}_i = u_i = \sum_{j \in \mathcal{N}_i} u_{ij} \tag{5.6}$$

$$\begin{cases} x_i(t) = x_i(t^-) \quad \forall i \in \mathcal{I} \\ u_{ij}(t) = \begin{cases} \text{sign}_\varepsilon \left(D_{ij}(t) \right), & \text{if } (i,j) \in \mathcal{J}(\theta, t) \\ u_{ij}(t^-), & \text{otherwise} \end{cases} \\ \theta_{ij}(t) = \begin{cases} f_{ij} \left(x(t) \right), & \text{if } (i,j) \in \mathcal{J}(\theta, t) \\ \theta_{ij}(t^-), & \text{otherwise} \end{cases} \end{cases} \tag{5.7}$$

where $i \in \mathcal{I}$, $j \in \mathcal{N}_i$. The control input u_i aggregates contributions of all edges $(j,i) \in \mathcal{E}$, and u_{ij} represents the control action on node i of the communication link from node j to node i. Through (5.7), u_{ij}, θ_{ij} are updated only when the clock variable θ_{ij} reaches zero, i.e., $(i,j) \in \mathcal{J}(\theta, t) = \{(i,j) : j \in \mathcal{N}_i \wedge \theta_{ij}(t^-) = 0\}$ where $\theta_{ij}(t^-) = \lim_{\tau \to t} \theta_{ij}(\tau)$. Specifically,

$$\begin{aligned} & f_{ij} \left(x(t) \right) = \max \left\{ \frac{|D_{ij}(t)|}{2(d_i + d_j)}, \frac{\varepsilon}{2(d_i + d_j)} \right\} \\ & D_{ij}(t) = x_j(t) - x_i(t) \\ & \text{sign}_\varepsilon(z) := \begin{cases} \text{sign}(z), & \text{if } |z| \geq \varepsilon \\ 0, & \text{otherwise} \end{cases} \end{aligned} \tag{5.8}$$

with $\varepsilon > 0$, a user designed sensitivity parameter (consensus error bound); $u_{ij} \in \{-1, 0, 1\}$ from a quantiser $\text{sign}_\varepsilon(z)$.

5.3 Resilient Frequency Regulation of MGs Against Multi-Layer DoS Attacks

In this section, we design a DoS-resilient control strategy for global consensus to mitigate the joint impacts of multi-layer DoS attacks in the networked MGs frequency control. We firstly model the multi-layer DoS attacks and analyse the effects on the data flow serving for the frequency regulation. Inspired by the concept of self-triggered control, the adaptive distributed self-triggered control is proposed, and its consensus stability and convergence time are theoretically analysed. Before proposing the DoS-resilient control, we give a comprehensive modelling of multi-layer DoS attacks.

5.3.1 Denial-of-Service Attacks Modelling

To model DoS attacks, $\Xi(t_1, t_2)$ and $\Theta(t_1, t_2)$ are respectively defined as the under-attack and healthy subsets of the time interval $[t_1, t_2)$. By $n(t_1, t_2)$ denoting the incidence of DoS inactive/active transitions within the time interval $[t_1, t_2)$, the following assumption are introduced [2, 4], where a more comprehensive information on DoS frequency and duration is provided.

Assumption 5.1 (DoS Frequency and Duration). *There exist* $\eta \in \mathbb{R}_{\geq 0}, \kappa \in \mathbb{R}_{\geq 0}$ *and* $\tau^f \in \mathbb{R}_{\geq 0}, \tau^d \in \mathbb{R}_{\geq 0}$ *such that*

$$\text{Frequency}: \quad n(t_1, t_2) \leq \eta + \frac{t_2 - t_1}{\tau^f}, \tag{5.9}$$

$$\text{Duration}: \quad |\Xi(t_1, t_2)| \leq \kappa + \frac{t_2 - t_1}{\tau^d}. \tag{5.10}$$

To model multi-layer DoS attacks in a unified form, the Persistency-of-Communication (PoC) in [4] is generalised and extended to a notion of PoDF owing to the independence of DoS on diverse channels of data transmission.

Proposition 5.1 (Persistency-of-Data-Flow (PoDF)). *For any transmission channel* $\mu \in \{\mathcal{I} \cup \mathcal{E}\}$[1] *serving for the distributed control, if multi-layer DoS sequences satisfy Assumption 5.1 respectively with coefficients* τ_μ^f, τ_μ^d, *such that* $\phi_\mu(\tau_\mu^f, \tau_\mu^d, \Delta_\mu^*) := \frac{1}{\tau_\mu^d} + \frac{\Delta_\mu^*}{\tau_\mu^f} < 1$, *where* $\Delta_\mu^* := \min \Delta_\mu$. *Then, for any unsuccessful data transmission attempt* t_μ^k, *at least one successful transmission occurs within the time interval* $[t_\mu^k, t_\mu^k + \Phi_\mu]$ *with* $\Phi_\mu := \frac{\kappa_\mu + (\eta_\mu + 1)\Delta_\mu^*}{1 - \phi_\mu(\tau_\mu^f, \tau_\mu^d, \Delta_\mu^*)}$.

[1] $\mu := ij$, communication channel $(i, j) \in \mathcal{E} : j \in \mathcal{N}_i$; $\mu := i$, measurement channel of subsystem $i \in \mathcal{I}$; $\mu := i0$, control actuation channel of subsystem $i \in \mathcal{I}$.

Proof. The proof is similar to that in the Appendix A of [4], thus omitted here. □

Proposition 5.1 describes the impact of multi-layer DoS attacks on each data flow channel. Δ_μ^* denotes the minimum time interval between two sequential attempts of data flow, which is different for the three different types of data transmissions. In practice, Δ_μ^* can be known a priori, though conservatively, based on the specification of the system. More specifically, $\Delta_i^*, \Delta_{i0}^*$ depend on the performance of each MGCC, while Δ_{ij}^* is determined by (5.13), which is introduced later.

Assumption 5.2. *Assuming that both local-level DoS attacks (measurement and control actuation DoS) occur with similar chance, which is less frequent than that on the neighbouring communication channels, such that* $\tau_i^f \approx \tau_{i0}^f, \tau_i^d \approx \tau_{i0}^d \implies \Phi_i \approx \Phi_{i0}$ *and* $\Phi_i \leq \Phi_{ij}, \Phi_{i0} \leq \Phi_{ij}$ *according to the definition in Proposition 5.1 and its footnotes.*

5.3.2 DoS Resilient Consensus Control Algorithm

The distributed control protocol (5.6)–(5.8) is based on the hypothesis that the MGCC has access to both local state $x_i(t)$ and neighbouring state $x_j(t)$ at the triggering time, and therefore not valid for multi-layer DoS attacks. To ensure the cyber-resilient consensus in such a scenario, we design an adaptive self-triggered control protocol to achieve resilience under multi-layer DoS attacks (the corresponding stability criteria will be discussed later in Section 5.3.3 and

Section 5.3.4). The nominal discrete transition (5.7) is modified as follows:

$$\begin{cases} x_i(t) = x_i(t^-) \quad \forall i \in \mathcal{I} \\ u_{ij}(t) = \begin{cases} \operatorname{sign}_\varepsilon\left(D_{ij}(\bar{t})\right), & (i,j) \in \mathcal{J}(\theta,t) \wedge t \in \Theta_{ij}(0,t) \\ 0, & (i,j) \in \mathcal{J}(\theta,t) \wedge t \in \Xi_{ij}(0,t) \\ u_{ij}(t^-), & \text{otherwise} \end{cases} \\ \theta_{ij}(t) = \begin{cases} f_{ij}\left(x(\bar{t})\right), & (i,j) \in \mathcal{J}(\theta,t) \wedge t \in \Theta_{ij}(0,t) \\ \dfrac{\varepsilon_{ij}}{2(d_i + d_j)}, & (i,j) \in \mathcal{J}(\theta,t) \wedge t \in \Xi_{ij}(0,t) \\ \theta_{ij}(t^-), & \text{otherwise} \end{cases} \end{cases} \tag{5.11}$$

with asynchronous clock rate across all network links $\dot{\theta}_{ij}(t) = -R_{ij}$ and individual sensitivity parameters ε_{ij} satisfying:

$$0 < \varepsilon \le \varepsilon_{ij}. \tag{5.12}$$

where ε represents the minimally acceptable consensus error that avoids Zeno-behaviour of all edges. The utilization of R_{ij} and ε_{ij}, for each edge as opposed to the uniform parameters used in the nominal scheme (5.6)-(5.8) is a remarkable feature, and it turns out to be useful in the context of consensus performance as will be discussed in Section 5.3.4. The map $f_{ij} : \mathbb{R}^2 \to \mathbb{R}_{>0}$ is defined as $f_{ij}\left(x(\bar{t})\right) = \max\left\{\frac{|D_{ij}(\bar{t})|}{2(d_i+d_j)}, \frac{\varepsilon_{ij}}{2(d_i+d_j)}\right\}$.

Let $\{t_{ij}^k\}_{k\in\mathbb{Z}_{\ge 0}}$ be the sequence of communication-triggering attempt. It is immediate to show that a dwell-time property is ensured between consecutive sequences:

$$\Delta_{ij} := t_{ij}^{k+1} - t_{ij}^k \ge \frac{\varepsilon_{ij}}{2R_{ij}(d_i + d_j)} \ge \frac{\varepsilon}{4R_{ij}d_{\max}} \tag{5.13}$$

where $d_{\max} = \max_{i\in\mathcal{I}} d_i$. This ensures the adaptive self-triggered control (5.11) to be Zeno-free. The item $D_{ij}(\bar{t})$ of (5.11) is designed to mitigate the cooperative impacts of multi-layer DoS, i.e., $D_{ij}(\bar{t}) = x_j(\bar{t}_j) - x_i(\bar{t}_i)$, where "$\bar{t}$" denotes the latest time instant when the state is available.

For the sake of further analysis, we define

Definition 5.1 (Secure Consensus). *Given the system* (5.6)*, a graph $\mathcal{G}$ and a distributed self-triggered resilient consensus controller with edge-based control u_{ij}, the networked systems are said to be consensus under multi-layer DoS attacks if for any initial condition, $x(t)$ converges in finite time to a point belonging to the set by defining $\delta = \varepsilon(n-1)$*

$$\{x \in \mathbb{R}^n : |x_i(t) - x_j(t)| < \delta \quad \forall (i,j) \in \mathcal{I} \times \mathcal{I}\}. \tag{5.14}$$

Remark 5.1. *The consensus error bound of the distributed system δ derives from edges and can be designed appropriately as small as possible to ensure the system consensus performance, i.e., frequency regulation and active power sharing accuracy, just for being Zeno-free.*

In the following, the distributed control system stability will be analysed in terms of parameter design, followed by the convergence analysis in line with (5.14). The network behaviour of the networked system (5.6), (5.11)-(5.13) is analysed in the presence of multi-layer DoS attacks. The analysis is carried out in two steps: 1) we assume uniform clock rate and consensus error bound, such that $R_{ij} = R$, $\varepsilon_{ij} = \varepsilon$, $\forall i \in \mathcal{I}$, $j \in \mathcal{N}_i$ and provide the stability condition in a global sense, and 2) with the additional degrees of freedom endowed by ε_{ij} and R_{ij}, we provide less conservative design criteria by which the consensus remains guaranteed.

5.3.3 Control Parameter Design and Stability Analysis

After the MGCC i updates the associated input u_{ij} related to its neighbour j by (5.11), its transmission through the actuation channels could also be blocked due to DoS attacks. To better demonstrate the effects of DoS attacks on the actuation channels, two sequences of time instants for any $(i,j) \in \mathcal{E}$ are defined: $\{t_{ij}^k : k \in \mathbb{N}\}$ and $\{s_{ij}^k : k \in \mathbb{N}\}$. The sequence t_{ij}^k denotes the time instants at which both local and neighbouring states are updated after $(i,j) \in \mathcal{J}(\theta, t)$ satisfies, while the sequence s_{ij}^k denotes the corresponding time instants at which transmission attempts of control actuation from (5.11) are successful. Then, two sequences have the property of $0 \leq s_{ij}^k - t_{ij}^k \leq \Phi_{i0}$.

Theorem 5.1. *Consider the distributed control system* (5.6), (5.11) *subject to multi-layer DoS attacks. If Assumption 5.1 and Assumption 5.2 hold and*

$$\varepsilon > 2d_{\max}\Phi_{\mathcal{I}+2\mathcal{I}0}^{\max},\ R > \frac{\varepsilon}{2\left[\varepsilon - 2d_{\max}\Phi_{\mathcal{I}+2\mathcal{I}0}^{\max}\right]} \tag{5.15}$$

with $\Phi_{\mathcal{I}+2\mathcal{I}0}^{\max} = \Phi_{\mathcal{I}}^{\max} + 2\Phi_{\mathcal{I}0}^{\max}$, $\Phi_{\mathcal{I}}^{\max} = \max_{i\in\mathcal{I}} \Phi_i$, $\Phi_{\mathcal{I}0}^{\max} = \max_{i\in\mathcal{I}} \Phi_{i0}$, *then* $x(t)$ *reaches consensus in finite time as described in* (5.14).

Proof. Consider any time t, there exists two successive time instants of successful control actuation that satisfy $s_{ij}^k \le t < s_{ij}^{k+1}$. During the time period $[s_{ij}^k, s_{ij}^{k+1})$, the control input that is updated through (5.11) at the time instant t_{ij}^k will be applied. For each $(i,j) \in \mathcal{E} : j \in \mathcal{N}_i$, we have the following inequality:

$$t - t_{ij}^k \le \frac{f_{ij}(x(\bar{t}_{ij}^k))}{R} + 2\Phi_{i0} \tag{5.16}$$

Then if $D_{ij}(\bar{t}_{ij}^k) \ge \varepsilon$,

$$\begin{aligned} D_{ij}(t) &= x_j(t) - x_i(t) \\ &\overset{(a1)}{\ge} D_{ij}(t_{ij}^k) - (d_i + d_j)(t - t_{ij}^k) \\ &\overset{(a2)}{\ge} D_{ij}(\bar{t}_{ij}^k) - d_i\Phi_i - d_j\Phi_j - (d_i + d_j)(t - t_{ij}^k) \\ &\overset{(a3)}{\ge} D_{ij}(\bar{t}_{ij}^k)(1 - \frac{1}{2R}) - d_i(\Phi_i + 2\Phi_{i0}) - d_j(\Phi_j + 2\Phi_{i0}) \end{aligned} \tag{5.17}$$

where (a1) derives from identifiable neighbours and control inputs, and (a2), (a3) are from Proposition 5.1 and (5.16) respectively, then (5.17) can be expressed as

$$D_{ij}(t) \ge D_{ij}(\bar{t}_{ij}^k)(1 - \frac{1}{2R}) - 2d_{\max}\Phi_{\mathcal{I}+2\mathcal{I}0}^{\max} > 0 \tag{5.18}$$

If $D_{ij}(\bar{t}_{ij}^k) \le -\varepsilon$, an analogous inequality holds

$$D_{ij}(t) \le D_{ij}(\bar{t}_{ij}^k)(1 - \frac{1}{2R}) + 2d_{\max}\Phi_{\mathcal{I}+2\mathcal{I}0}^{\max} < 0 \tag{5.19}$$

Define error terms as $e_i = x_i - \frac{1}{n}\sum_{i=1}^{n} x_i$ and $\boldsymbol{e} = [e_i]_{N\times 1}$. Consider a candidate Lyapunov function $V(t) = \frac{1}{2}\boldsymbol{e}^T\boldsymbol{e}$ and define $\mathcal{S} := |D_{ij}(\bar{t}_{ij}^k)| \geq \varepsilon \wedge t_{ij}^k \in \Theta_{ij}(0,t)$, then the derivative of $V(t)$ under the controller (5.11):

$$
\begin{aligned}
\dot{V}(t) &= \sum_{i=1}^{n} e_i \dot{e}_i = \sum_{i=1}^{n} e_i \sum_{j\in\mathcal{N}_i:\mathcal{S}} \operatorname{sign}_\varepsilon\left(D_{ij}(\bar{t})\right) \\
&= -\frac{1}{2}\sum_{(i,j)\in\mathcal{E}:\mathcal{S}} D_{ij}(t)\operatorname{sign}_\varepsilon\left(D_{ij}(\bar{t})\right) \\
&\leq -\frac{1}{2}\sum_{(i,j)\in\mathcal{E}:\mathcal{S}} \left[\varepsilon\left(1-\frac{1}{2R}\right) - 2d_{\max}(\Phi_{\mathcal{I}}^{\max} + 2\Phi_{\mathcal{I}0}^{\max})\right] \overset{(b)}{<} 0
\end{aligned}
\tag{5.20}
$$

where (b) derives by applying (5.15) in Theorem 5.1. As a result, (5.20) shows the convergence of Theorem 5.1. Thus, *secure consensus* defined in Definition 5.1 can be reached. □

Based on the results stated in Theorem 5.1, the convergence time can be characterised.

Corollary 5.1 (Convergence Time)**.** *Consider $T_\star$ as the convergence time of the distributed control system* (5.6)*,* (5.11)*. It holds that*

$$
T_\star \leq \frac{2\varepsilon(d_{\max}+d_{\min}) + 8Rd_{\max}d_{\min}\Phi_{\mathcal{IJ}+2\mathcal{I}0}^{\max}}{\varepsilon d_{\min}\left[\varepsilon(1-\frac{1}{2R}) - 2d_{\max}\Phi_{\mathcal{I}+2\mathcal{I}0}^{\max}\right]} V(0) \tag{5.21}
$$

where $\Phi_{\mathcal{IJ}+2\mathcal{I}0}^{\max} = \Phi_{\mathcal{IJ}}^{\max} + 2\Phi_{\mathcal{I}0}^{\max}$, $\Phi_{\mathcal{IJ}}^{\max} = \max_{i\in\mathcal{I},j\in\mathcal{N}_i}\Phi_{ij}$, $d_{\min} = \min_{i\in\mathcal{I}} d_i$.

Proof. Consider the Lyapunov function based stability analysis (5.20), for any successful communication attempt t_{ij}^k with $|D_{ij}(\bar{t}_{ij}^k)| \geq \varepsilon$, the function V decreases at least with the rate of $\rho := \frac{1}{2}\left[\varepsilon(1-\frac{1}{2R}) - 2d_{\max}\Phi_{\mathcal{I}+2\mathcal{I}0}^{\max}\right]$ by at least $(\varepsilon/4Rd_{\max})$ units of time (as inferred from (5.13)) under the enhanced adaptive controller (5.11).

We consider any $t > 0$ the consensus has not yet been reached and $u_{ij}^\star(t) = 0$, thus the next communication attempt through edge $(i,j) \in \mathcal{E}$ will occur at the following time period $[t, t+\varepsilon/4Rd_{\min}]$. The most conservative scenario is that over this time period $u_{ij}^\star = 0$. Due to the effect of DoS on communication channels, one successful communication attempt will certainly occur before $(t + \varepsilon/4Rd_{\min} + \Phi_{ij})$ even at the most conservative scenario.

Then, we consider the effect of DoS on control actuation channels. After u_{ij} is updated at t_{ij}^k, the successful control actuation attempt $u_{ij}^\star(s_{ij}^k) = u_{ij}(\bar{t}_{ij}^k)$ occurs at $s_{ij}^k \in \left[t_{ij}^k, t_{ij}^k + \Phi_{i0}\right]$. The time-duration of $u_{ij}^\star(s_{ij}^k)$ contributing to the consensus is determined by the next successful control actuation attempt, which can be defined as $s_{ij}^{k+1} \in \left[t_{ij}^{k+1}, t_{ij}^{k+1} + \Phi_{i0}\right]$. We assume $u_{ij}^\star(s_{ij}^k)$ will be lasting for at least $(\varepsilon/4Rd_{\max} + \Delta t)$ with $0 \leq \Delta t \leq \Phi_{i0}$, thus, we conclude that V decreases by at least $[\rho(\varepsilon/4Rd_{\max} + \Delta t)]$ every $(\Phi_{ij} + \varepsilon/4Rd_{\min} + \varepsilon/4Rd_{\max} + \Delta t)$ units of time. Therefore, the convergence time

$$
\begin{aligned}
T_\star &\leq \frac{\varepsilon/4Rd_{\min} + \Phi_{ij} + \Phi_{i0} + \varepsilon/4Rd_{\max} + \Delta t}{\rho(\varepsilon/4Rd_{\max} + \Delta t)} V(0) \\
&\leq \frac{\varepsilon/4Rd_{\min} + \Phi_{ij} + 2\Phi_{i0} + \varepsilon/4Rd_{\max}}{\rho\varepsilon/4Rd_{\max}} V(0) \\
&\leq \frac{2\left(\varepsilon/4Rd_{\min} + \varepsilon/4Rd_{\max} + \Phi_{\mathcal{I}\mathcal{J}}^{\max} + 2\Phi_{\mathcal{I}0}^{\max}\right)}{\left[\varepsilon(1 - \frac{1}{2R}) - 2d_{\max}(\Phi_{\mathcal{I}}^{\max} + 2\Phi_{\mathcal{I}0}^{\max})\right] \varepsilon/4Rd_{\max}} V(0) \\
&= \frac{2\varepsilon(d_{\max} + d_{\min}) + 8Rd_{\max}d_{\min}(\Phi_{\mathcal{I}\mathcal{J}}^{\max} + 2\Phi_{\mathcal{I}0}^{\max})}{\varepsilon d_{\min}\left[\varepsilon(1 - \frac{1}{2R}) - 2d_{\max}(\Phi_{\mathcal{I}}^{\max} + 2\Phi_{\mathcal{I}0}^{\max})\right]} V(0)
\end{aligned}
\tag{5.22}
$$

□

5.3.4 Conservativeness Mitigation under DoS Attacks

The global consensus criteria (5.15) given in Theorem 5.1, though can be designed offline, are inferred from the global worst case analysis in terms of PoDF (uniform bounds across all the MGCC nodes), thereby being conservative and could lead to degraded consensus accuracy. In this section, under the procedure of DoS resilient control protocol summarised in Algorithm 5.1, less conservative criteria are derived from a local perspective (Theorem 5.2) to further improve the control performance.

Theorem 5.2. *Consider the distributed system* (5.6) *subject to multi-layer DoS attacks and the edge-based control* (5.11)*. If each subsystem can individually choose its parameters* ε_{ij} *and*

Algorithm 5.1: DoS Resilient Distributed Consensus Control

Initialisation: for all $i \in \mathcal{I}$ and $j \in \mathcal{N}_i$, set $\theta_{ij}(0^-) = 0$, $u_{ij}(0^-) = 0$, $u^\star_{ij}(0^-) = 0$;
`/* Local State Update from Sensors to Controllers */`
foreach $i \in \mathcal{I}$ **do**
    if $t \in \Theta_i(0, t)$ **then**
        i updates $x_i(\bar{t}) = x_i(t)$;
    end
end
`/* Edge-Based Control Update in Controllers */`
foreach $i \in \mathcal{I}$ **do**
    foreach $j \in \mathcal{N}_i$ **do**
        while $\theta_{ij}(t) > 0$ **do**
            i applies the control $u_i(t) = \sum_{j \in \mathcal{N}_i} u_{ij}(t)$;
        end
        if $\theta_{ij}(t) \leq 0 \wedge t \in \Theta_{ij}(0, t)$ **then**
            i updates $u_{ij}(t) = \text{sign}_\varepsilon(D_{ij}(\bar{t}))$;
            i updates $\theta_{ij}(t) = f_{ij}(x(\bar{t}))$;
        else if $\theta_{ij}(t) \leq 0 \wedge t \in \Xi_{ij}(0, t)$ **then**
            i updates $u_{ij}(t) = 0$;
            i updates $\theta_{ij}(t) = \frac{\varepsilon_{ij}}{2(d_i + d_j)}$;
        end
    end
end
`/* Control Actuation */`
foreach $i \in \mathcal{I}$ **do**
    if $u_i(t)$ *is updated* $\wedge\ t \in \Theta_{i0}(0, t)$ **then**
        $u^\star_i(t) = u_i(t)$;
    end
end
`// note:` $u_i(t)$ `denotes the desired control output, while` $u^\star_i(t)$ `denotes the actual control input of the subsystem.` $u_i(t) = u^\star_i(t)$ `if the actuation channel is not attacked.`

R_{ij}, such that $\forall\, i \in \mathcal{I}, \forall\, j \in \mathcal{N}_i$,

$$\begin{aligned} &\varepsilon_{ij} > d_i(\Phi_i + 2\Phi_{i0}) + d_j(\Phi_j + 2\Phi_{i0}) \\ &R_{ij} > \frac{\varepsilon_{ij}}{2\left[\varepsilon_{ij} - d_i(\Phi_i + 2\Phi_{i0}) - d_j(\Phi_j + 2\Phi_{i0})\right]} \end{aligned} \tag{5.23}$$

then the global consensus (5.14) *can be guaranteed.*

Proof. From the proof of Theorem 5.1, the inequality (5.18) and (5.19) can be replaced by

$$\begin{cases} D_{ij}(t) \geq D_{ij}(\bar{t}_{ij}^k)(1-\dfrac{1}{2R_{ij}}) - d_i(\Phi_i + 2\Phi_{i0}) \\ \qquad\qquad - d_j(\Phi_j + 2\Phi_{i0}), \text{ if } D_{ij}(\bar{t}_{ij}^k) \geq \varepsilon_{ij} \\ D_{ij}(t) \leq D_{ij}(\bar{t}_{ij}^k)(1-\dfrac{1}{2R_{ij}}) + d_i(\Phi_i + 2\Phi_{i0}) \\ \qquad\qquad + d_j(\Phi_j + 2\Phi_{i0}), \text{ if } D_{ij}(\bar{t}_{ij}^k) \leq -\varepsilon_{ij} \end{cases} \tag{5.24}$$

Then, (5.20) can be replaced by

$$\dot{V}(t) \leq -\frac{1}{2}\sum_{(i,j)\in\mathcal{E}:\mathcal{S}} \left[\varepsilon_{ij}(1-\frac{1}{2R_{ij}}) - d_i(\Phi_i + 2\Phi_{i0}) - d_j(\Phi_j + 2\Phi_{i0})\right] < 0 \tag{5.25}$$

which shows the convergence using (5.23) in Theorem 5.2. Thus, the secure consensus (5.14) is achieved. □

For the reason that the cyber vulnerability of different links may vary, there exists $\Phi_i \leq \Phi_{\mathcal{I}}^{\max}, \Phi_{i0} \leq \Phi_{\mathcal{I}0}^{\max}, \forall i \in \mathcal{I}$, thus the condition (5.23) is less conservative than (5.15). Furthermore, although Proposition 5.1 gives bounded time interval Φ_μ that can be utilised to design parameters, not every attack attempt leads to the worst data flow block, i.e., the time to achieve a successful data flow would not be Φ_μ all the time. Using the bounds to stabilise the system as Theorem 5.1 may lead to excessive conservativeness. Therefore, a self-adaptive scheme is utilised to mitigate the conservativeness.

For the controller of each subsystem i, assume the kth communication attempt is successful at t_{ij}^k, we define the following time instants:

$$t_{i,i}^k := t_{ij}^k - \bar{t}_i^k, \quad t_{i,j}^k := t_{ij}^k - \bar{t}_j^k, \quad t_{i0}^k := s_{ij}^k - t_{ij}^k \tag{5.26}$$

where $t_{i,i}^k, t_{i,j}^k$ are available at t_{ij}^k whereas t_{i0}^k is not know until $t = s_{ij}^k$. To estimate t_{i0}^k, let us consider an unsuccessful control actuation attempt at $\breve{s}_{ij} \in [t_{ij}^k, s_{ij}^k)$ and $\hat{t}_{i0}^k$ the estimate of t_{i0}^k. As we know that the next attempt will be made at $\breve{s}_{ij} + \Delta_{i0}^*$, we keep updating $\hat{t}_{i0}^k$ via $\hat{t}_{i0}^k = \breve{s}_{ij} + \Delta_{i0}^* - t_{ij}^k$ until the next successful attempt. As such, there always exists a time instant

$\bar{t} < s_{ij}^k$, such that for all $t \in [\bar{t}, s_{ij}^k)$, $\hat{t}_{i0}^k = t_{i0}^k$. It implies that t_{i0}^k is known prior to s_{ij}^k.

Proposition 5.2. *For any control actuation during* $[s_{ij}^k, s_{ij}^{k+1})$*, the following control inputs are equivalent to the system:*

$$
\begin{aligned}
u'_{ij}(t) &= \operatorname{sign}_\varepsilon\left(D_{ij}(\bar{t}_{ij}^k)\right)\frac{\vartheta_{ij}^k}{\vartheta_{ij}^k + \Phi_{i0}}, s_{ij}^k \le t < s_{ij}^{k+1} \\
\iff u_{ij}(t) &= \begin{cases} \operatorname{sign}_\varepsilon\left(D_{ij}(\bar{t}_{ij}^k)\right), & s_{ij}^k \le t < t_{ij}^{k*} \\ 0, & t_{ij}^{k*} \le t < s_{ij}^{k+1} \end{cases}
\end{aligned}
\tag{5.27}
$$

where $\vartheta_{ij}^k = \frac{\theta_{ij}^k}{R_{ij}^k} = \frac{f_{ij}(x(\bar{t}_{ij}^k))}{R_{ij}^k}$ *and* $s_{ij}^k + \frac{(\vartheta_{ij}^k)^2}{\vartheta_{ij}^k + \Phi_{i0}} \le t_{ij}^{k*} \le t_{ij}^{k+1}$.

Proof. By the inequality $s_{ij}^{k+1} - t_{ij}^{k+1} = t_{i0}^{k+1} \le \Phi_{i0}$ and $t_{ij}^{k+1} - s_{ij}^k = \vartheta_{ij}^k$, if $\operatorname{sign}_\varepsilon\left(D_{ij}(\bar{t}_{ij}^k)\right) = 1 \Rightarrow u'_{ij}(t) > 0, t \in [s_{ij}^k, s_{ij}^{k+1})$,

$$
\int_{s_{ij}^k}^{s_{ij}^{k+1}} u'_{ij}(t)dt \le \int_{s_{ij}^k}^{t_{ij}^{k+1}+\Phi_{i0}} u'_{ij}(t)dt \tag{5.28}
$$

if $\operatorname{sign}_\varepsilon\left(D_{ij}(\bar{t}_{ij}^k)\right) = -1 \Rightarrow u'_{ij}(t) < 0, t \in [s_{ij}^k, s_{ij}^{k+1})$,

$$
\int_{s_{ij}^k}^{s_{ij}^{k+1}} u'_{ij}(t)dt \ge \int_{s_{ij}^k}^{t_{ij}^{k+1}+\Phi_{i0}} u'_{ij}(t)dt \tag{5.29}
$$

Combining (5.28) and (5.29), the contribution of control actuation during $[s_{ij}^k, s_{ij}^{k+1})$ is limited:

$$
\int_{s_{ij}^k}^{s_{ij}^{k+1}} \left|u'_{ij}(t)\right| dt \le \left|\operatorname{sign}_\varepsilon\left(D_{ij}(\bar{t}_{ij}^k)\right)\right| \vartheta_{ij}^k = \int_{s_{ij}^k}^{t_{ij}^{k+1}} \left|\operatorname{sign}_\varepsilon\left(D_{ij}(\bar{t}_{ij}^k)\right)\right| dt + \int_{t_{ij}^{k+1}}^{s_{ij}^{k+1}} 0 \;\, dt \tag{5.30}
$$

Thus, from (5.30), we can know if u'_{ij} is actuated, it has the equivalent contribution of

$$
u_{ij}(t) = \begin{cases} \operatorname{sign}_\varepsilon\left(D_{ij}(\bar{t}_{ij}^k)\right), & s_{ij}^k < t < t_{ij}^{k*} \\ 0, & t_{ij}^{k*} < t < s_{ij}^{k+1} \end{cases}
$$

where $s_{ij}^k + \frac{(\vartheta_{ij}^k)^2}{\vartheta_{ij}^k + \Phi_{i0}} \le t_{ij}^{k*} \le t_{ij}^{k+1}$. In particular, $t_{ij}^{k*} = s_{ij}^k + \frac{(\vartheta_{ij}^k)^2}{\vartheta_{ij}^k + \Phi_{i0}}$ implies $t_{ij}^{k+1} = s_{ij}^{k+1}$. □

Although the consensus error bound ε_{ij} guaranteed in Theorem 5.2 is less conservative than

(5.15), it still relies on the PoDF conditions, which is inevitably conservative. Next, we show that a tighter consensus error bound can be achieved if an online self-adaptation mechanism of ε_{ij} and R_{ij} is permitted after each successful communication attempt.

Corollary 5.2 (Self-Adaptive Scheme)**.** *Consider the distributed system* (5.6) *subject to multi-layer DoS attacks and the edge-based control* (5.11) *with control input u'_{ij} in Proposition 5.2, if ε_{ij} and R_{ij} can be adapted after each successful communication attempt, such that*

$$\varepsilon_{ij}^k > \Gamma_{ij}^k,\ R_{ij}^k > \frac{\varepsilon_{ij}^k}{2\left[\varepsilon_{ij}^k - \Gamma_{ij}^k\right]} \tag{5.31}$$

where $\Gamma_{ij}^k = d_i(t_{i,i}^k + t_{i0}^k) + d_j(t_{i,j}^k + t_{i0}^k)$ with $t_{i,i}^k$, t_{i0}^k, $t_{i,j}^k$ defined in (5.26)*, then the secure consensus condition* (5.14) *can be preserved.*

Proof. If $D_{ij}(\bar{t}_{ij}^k) \geq \varepsilon_{ij}^k$, (5.17) in Theorem 5.1 can be modified as the following

$$\begin{aligned}
D_{ij}(t) &\geq D_{ij}(t_{ij}^k) - (d_i + d_j)(t - t_{ij}^k) \\
&\overset{(c)}{\geq} D_{ij}(\bar{t}_{ij}^k) - d_i t_{i,i}^k - d_j t_{i,j}^k - (d_i + d_j)(t_{i0}^k + \vartheta_{ij}^k) - 0 \times \Phi_{i0} \\
&= D_{ij}(\bar{t}_{ij}^k)(1 - \frac{1}{2R_{ij}^k}) - d_i(t_{i,i}^k + t_{i0}^k) - d_j(t_{i,j}^k + t_{i0}^k)
\end{aligned}$$

where (c) comes from Proposition 5.2. Followed by the similar process as (5.18)-(5.20), we obtain $\dot{V}(t) < 0$ remains guaranteed with (5.31). Similarly, secure consensus (5.14) is achieved.

□

After the kth successful communication attempt of edge $(i,j) \in \mathcal{E} : j \in \mathcal{N}_i$, Γ_{ij}^k is already known before the control actuation attempt. Then we can choose appropriate $\varepsilon_{ij}^k, R_{ij}^k$ to satisfy (5.31), and the corresponding clock variable θ_{ij}^k and control variable $u_{ij}^k = u'_{ij}$ can be obtained from (5.11) and (5.27) respectively. To make the proposed self-adaptive scheme clear, we summarise it in Algorithm 5.2.

Remark 5.2. *The conditions shown in* (5.31) *are equivalent to $\varepsilon_{ij}^k > \left[1 + \frac{1}{2R_{ij}^k - 1}\right]\Gamma_{ij}^k, R_{ij}^k >$ 0.5, which explicitly shows the relationship between two designed parameters. The selection of $\varepsilon_{ij}^k, R_{ij}^k$ is subject to a trade-off between consensus accuracy and computation burden. More* *specifically, smaller ε_{ij}^k leads to more accurate consensus performance in terms of* (5.12) *but requires larger R_{ij}^k, which means more frequent communication between MGCCs. Hence, the parameter selection in practice should consider both the communication capability and accuracy requirement of networked MGs case-by-case.*

Algorithm 5.2: Self-Adaptive Scheme for DoS Resilient Distributed Consensus Control

foreach $(i, j) \in \mathcal{E}$ **do**
    foreach *communication attempt k* **do**
        if *attempt is unsuccessful* **then**
            apply (5.11) and Algorithm 5.1 to the unsuccessful solution;
        else if *attempt is successful* **then**
            design $\varepsilon_{ij}^k, R_{ij}^k$ using (5.31);
            calculate θ_{ij}^k as (5.11) and $u_{ij}^k = u_{ij}'$ as (5.27);
        end
    end
end

Remark 5.3. *Under Corollary 5.2, the adverse effects of multi-layer DoS attacks can be classified as "identifiable" and "non-identifiable" depending on the extent to which the convervativeness of global consensus criteria* (5.15) *can be mitigated, as shown in Figure 5.2. More specifically, the "identifiable" means those DoS attacks can be noticed before control command calculation by the definition of* (5.26) *(e.g., communication and measurement DoS), while the "non-identifiable" means the actuated commands are not updated as desired due to DoS attacks that block the next actuation attempt (e.g., actuation DoS). The "non-identifiable" effects always come with actuation DoS attacks and are mitigated by using Proposition 5.2, which brings extra conservativeness. Besides the desired effects, such separation of identifiable and non-identifiable effects can effectively avoid the over conservative design using the fully worst scenario owing to intensive DoS attacks are a low-frequency event.*

Remark 5.4. *Compared to [2–4], the main contributions of the proposed method are: 1) consideration of the multi-layer DoS attacks in all channels of local measurement, neighbouring communication and control actuation, 2) consideration of asynchronous data collection and processing, as major significance, to ensure consensus properties in the presence of multi-layer DoS attacks, 3) the proposed adaptive scheme can significantly reduce the conservativeness in-*

volved in the algorithm [4]. These contributions lead to a dedicated resilient control design with rigorous analysis for resilience guarantees. To show the superior of the proposed method, comprehensive comparisons with [1–4] will be provided in Section 5.4.1.

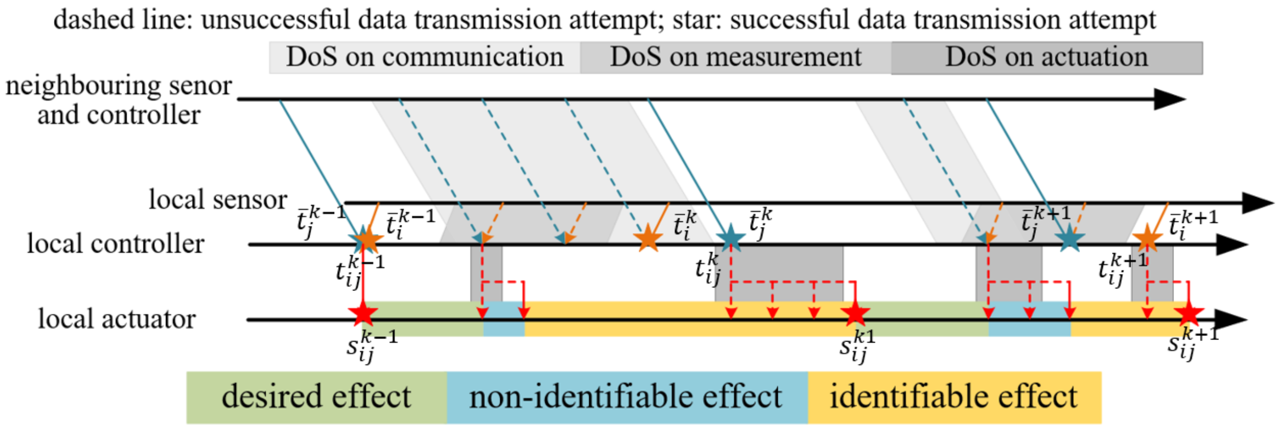

Figure 5.2: Sequential control scenarios under multi-layer DoS attacks.

5.4 Results

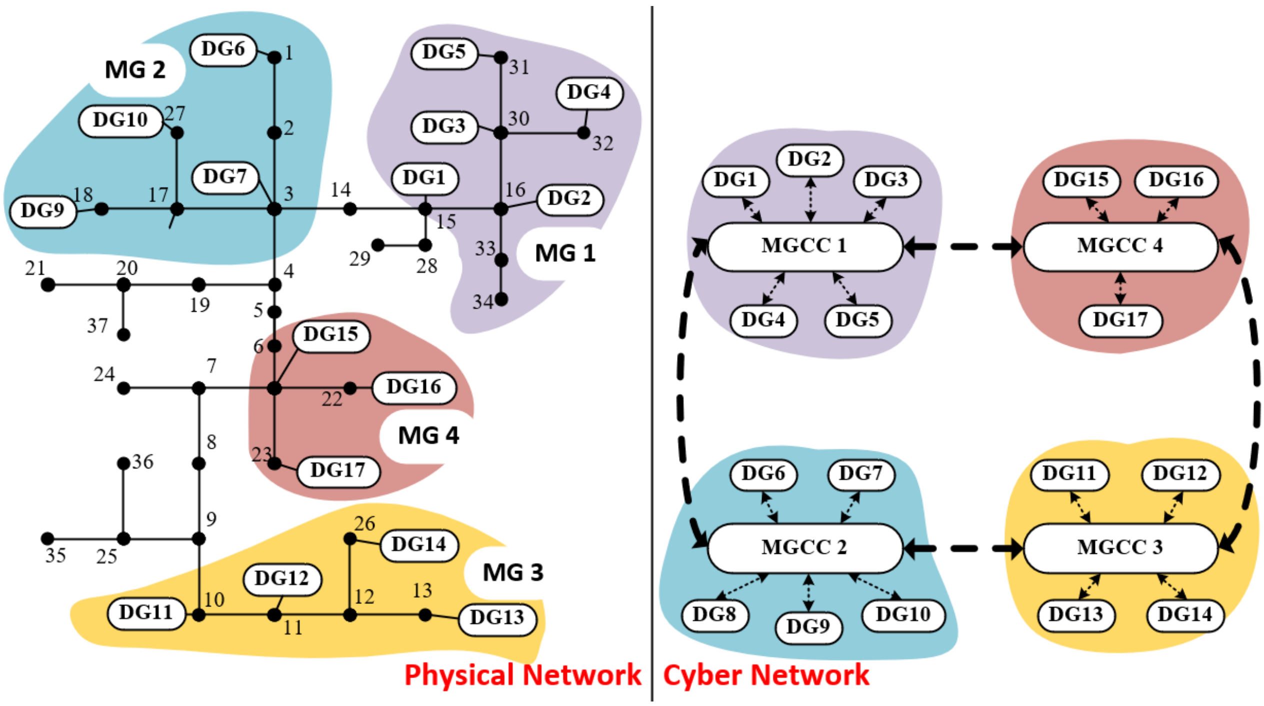

Figure 5.3: A networked MGs topology modified by IEEE 37 bus test system.

To verify the effectiveness of the proposed DoS resilient control of networked MGs, a modified IEEE 37 nodes system [67] with four MGs is established in MATLAB/Simulink as shown in

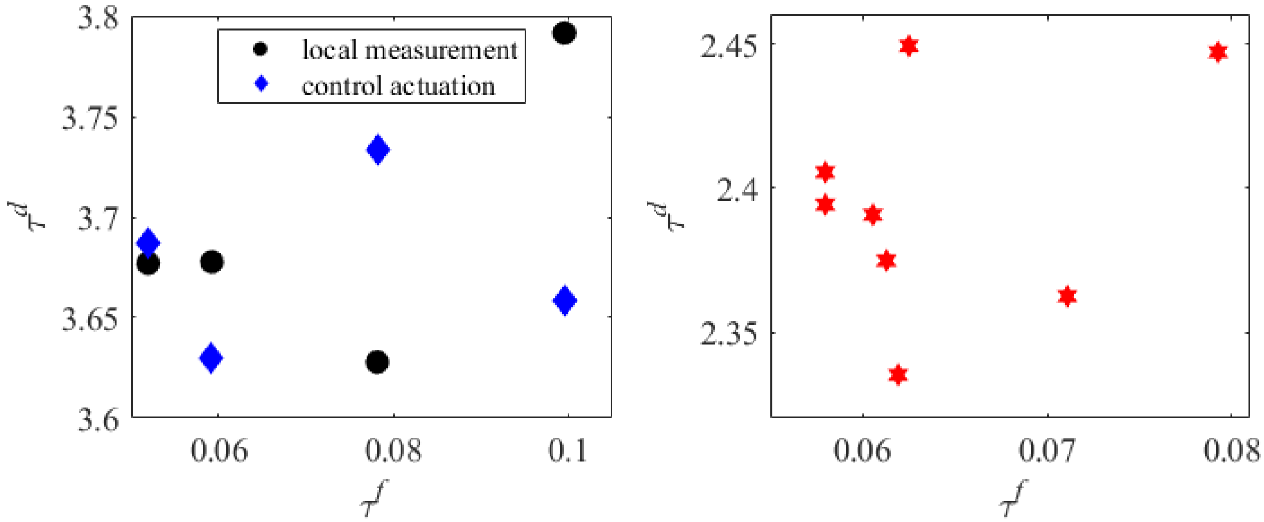

(a) local DoS (b) neighbouring DoS

Figure 5.4: τ^f and τ^d values among networked MGs: (a) measurement and control actuation; (b) neighbouring communication.

Table 5.1: Power Ratings of DGs

MG 1		MG 2		MG 3		MG 4	
DG 1	20 kW	DG 6	20 kW	DG 11	15 kW	DG 15	10 kW
DG 2	15 kW	DG 7	20 kW	DG 12	20 kW	DG 16	10 kW
DG 3	15 kW	DG 8	15 kW	DG 13	20 kW	DG 17	15 kW
DG 4	15 kW	DG 9	15 kW	DG 14	15 kW		
DG 5	15 kW	DG 10	10 kW				

Figure 5.3. The network topology follows

$$\mathcal{A} = \begin{bmatrix} 0 & 1 & 0 & 1 \\ 1 & 0 & 1 & 0 \\ 0 & 1 & 0 & 1 \\ 1 & 0 & 1 & 0 \end{bmatrix}$$

, which satisfies the consensus requirement discussed in Section 5.2.1 . Each MG incorporates several inverter-based DGs, the power ratings of which are detailed in Table 5.1. In the simulation, the proposed secondary controller is activated at $t = 5\,\mathrm{s}$, and before only the primary controller is used, which tends to lead to larger frequency synchronous deviations. Furthermore, the load changes (prevalent in the power networks) are introduced at $t = 30\,\mathrm{s}$ and $t = 45\,\mathrm{s}$, respectively. Finally, multi-layer DoS attacks acting on local and neighbouring links of the power network are illustrated in Figure 5.4.

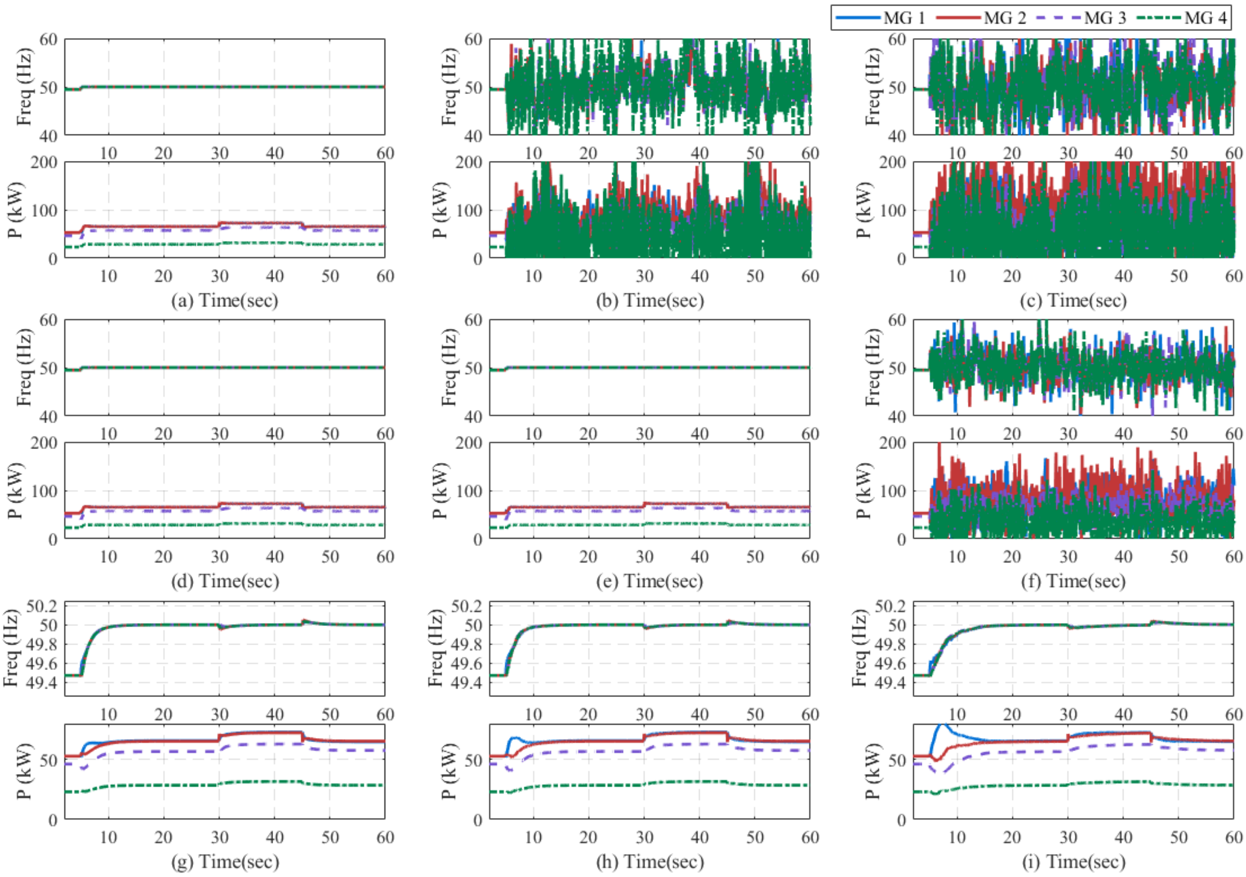

Figure 5.5: Performance evaluation of frequency synchronisation and active power sharing. 1st row, i.e., (a), (b), (c) are using (5.7) designed without considering any DoS attacks [1]; 2nd row, i.e., (d), (e), (f) are using ternary control (5.7) designed only considering neighbouring DoS attacks [2–4]; 3rd row, i.e., (g), (h), (i) are using the proposed resilient control designed considering multi-layer DoS attacks; 1st column, i.e., (a), (d), (g): none DoS attacks exist; 2nd column, i.e., (b), (e), (h): only communication DoS attacks exist; 3rd column, i.e., (c), (f), (i): multi-layer DoS attacks exist.

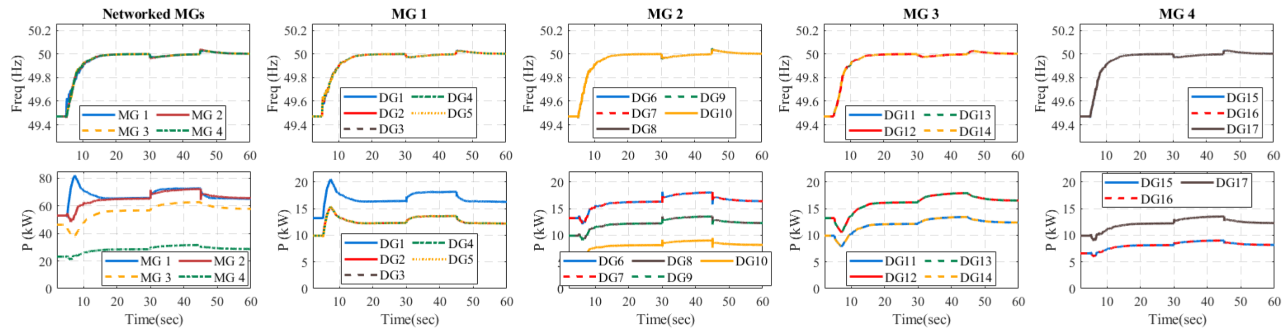

Figure 5.6: Frequency synchronisation and active power sharing inside MGs.

5.4.1 Validation of the Proposed Method

To show the impact of multi-layer DoS attacks and the performance of the proposed resilient

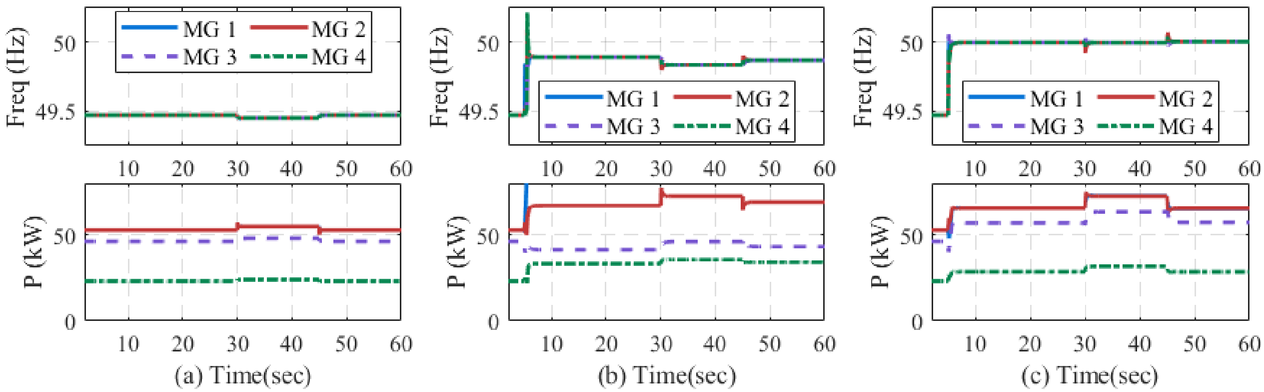

Figure 5.7: Conservativeness validation of Theorem 5.1. (a): intensive DoS attacks using controller satisfying Theorem 5.1; (b) and (c): less intensive DoS attack using controllers satisfying Theorem 5.1 and Corollary 5.2, respectively.

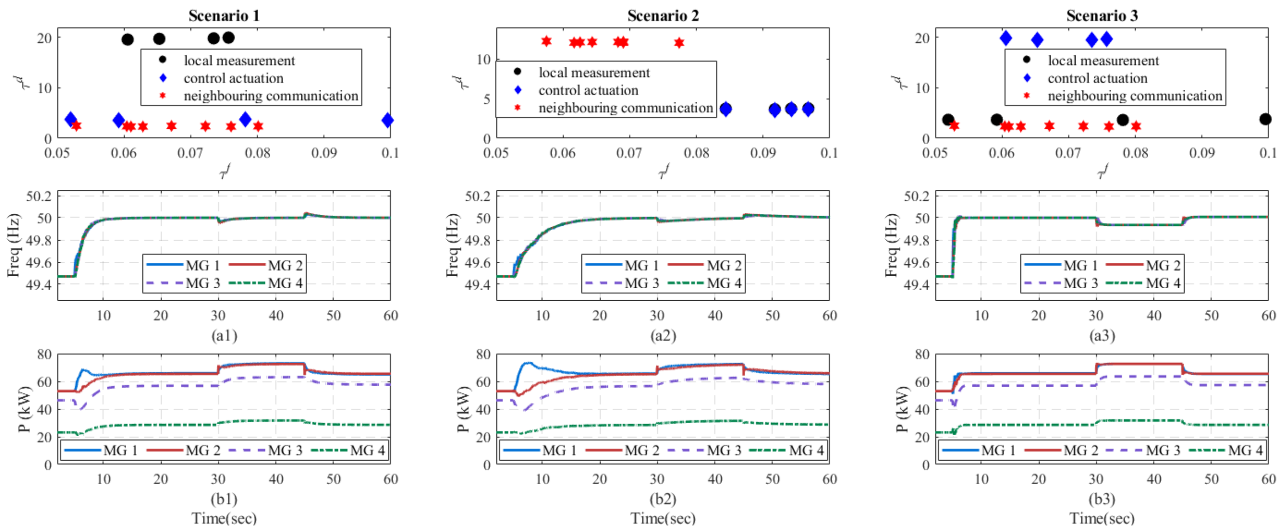

Figure 5.8: Performance comparisons with decreased DoS attacks on three type of channels separately: measurement (Scenario 1, 1st column), communication (Scenario 2, 2nd column) and actuation (Scenario 3, 3rd column).

secondary control strategy which is based on Corollary 5.2, we compare the performance with existing methods [1–4]. The results are shown in Figure 5.5, where each row corresponds to a typical controller and the three columns (from left to right) indicate the three simulation cases of different DoS attacks. As it can be seen, control performance deteriorates under either neighbouring DoS attacks or local DoS attacks (see (a) to (b)), and the degradation becomes more significant when local DoS attacks are introduced (see (b) to (c)). Considering only the neighbouring-communication-attack can not nullify the effects of local DoS attacks (see (e) to (f)). The resulting undesired oscillations may trigger the power grid protection mechanism, and consequently, lead to large-scale load shedding or power outage. Hence, the resilience against multi-layer DoS attacks is of great significance for enhancing the reliability of the networked

MGs. The results presented in the third row (i.e., (g), (h) and (i)) show that system resilience is preserved by the proposed DoS-resilient control method although the multi-layer DoS attacks slow down the frequency convergence speed. Moreover, frequency synchronisation and active power sharing are shown by equivalence inside each MG in Figure 5.6, where the accuracy is also guaranteed in a hierarchical framework. Take MG 2 as an example, the active power sharing is kept at all stages by a fixed ratio $4 : 4 : 3 : 3 : 2$, as specified by their power ratings.

5.4.2 Benefits of the Self-Adaptive Scheme

Under the DoS attacks of Figure 5.4, we evaluate the performance of the controller designed in line with the global consensus criteria (see Theorem 5.1), which considers the worst scenario of DoS attacks by PoDF. The results are shown in Figure 5.7(a). In contrast to Figure 5.5(i) that is obtained using the self-adaptive scheme, the steady state consensus error in Figure 5.7(a) is much greater due to the fact that the sensitivity parameter, ε, has to be set to a conservative value $\varepsilon = 1.2624\,(\Phi^{\max}_{\mathcal{I}=\mathcal{I}0} = 0.0526)$ to satisfy the global design criterion Eq. (5.15). If DoS attacks become less severe and intensive, after re-designing the sensitivity parameter, the consensus accuracy is improved for both control designs, as can be seen in Figure 5.7(b) and Figure 5.7(c). However, enhanced consensus accuracy is guaranteed in both cases by the less conservative design criteria given in Corollary 5.2.

5.4.3 Impacts of Attacks in Different Channels

The proposed DoS-resilient control framework gives different mitigation methods for identifiable and non-identifiable DoS attacks as described in Remark 5.3. In order to evaluate the impacts of both types of attacks and to what extent each attack can be mitigated, we successively decrease the frequency and duration for measurement, communication or actuation DoS attacks based on the original setting given in Figure 5.4. The resulting multi-layer DoS attacks are characterised in the first row of Figure 5.8. The corresponding performances of each scenario are shown in 2nd and 3rd rows of the same column. As discussed in Remark 5.3, the mitigation of the non-identifiable attacks is more conservative compare to that of identifiable ones. This is explicitly reflected in Figure 5.8, as the extenuation (by frequency and duration reduction) of the actuation attacks (which certainly bring non-identifiable effects) yields the most noticeable improvements in terms of frequency tracking among the three cases (see Scenario 3). In other words, under the proposed resilient self-triggered method based on Corollary 5.2, a sequence of DoS attack that acts on actuation channels has the most significant impact on the control performance, therefore, it is more beneficial to harden cybersecurity of actuation channels compared to the other two.

5.5 Conclusion

In this chapter, we propose a DoS resilient distributed self-triggered control method of networked systems. Multi-layer DoS attacks on different channels of data flow are considered: DoS attacks on neighbouring communication, measurement and control actuation channels. The quantitative description of such attacks, named by PoDF is employed to analyse the global stability criteria and convergence time of the consensus evolution. Then, the conservativeness induced by control design in the worst case is overcome by a self-adaptive scheme which classifies effects of DoS attacks into identifiable and non-identifiable parts. Through simulations conducted by MATLAB/Simulink, the effectiveness of such a multi-layer-DoS resilient strategy is illustrated with separate analysis of DoS attacks on local or neighbouring data transmissions.

Chapter 6

Cyber-Physical Post-Contingency Service Restoration of Power Networks: A UAV Assisted Communication Coverage Approach

6.1 Introduction

Existing climate change leads to an increase in the frequency, intensity and duration of severe weather events [147]. Extreme weather conditions pose huge threats to power supply infrastructures, thereby leading to undesired power interruptions or blackouts. Hence, the concept of resilience under contingencies has been gradually recognized as a key requirement for future energy systems [12, 148]. The trend of cyber-physical power systems or power system digitization [10], which emphasizes the high interdependence of communication system and power network, discloses that both communication infrastructure and power lines are vulnerable to increasing disasters [12]. Therefore, a cyber-physical resilience should receive more attention than before.

Currently, there are several research directions trying to enhance cyber-physical power system resilience. Network reconfiguration [149] is one of widely investigated methods but relies on the operational information of power network. Once contingencies with adverse cyber-physical effects occur, the lack of information exchange makes power-and-communication service restoration difficult. Another method to enhance post-contingency cyber-physical resilience is the technology of microgrid (MG) [41, 43, 67]. During post-contingency periods, MGs with distributed generators (DGs) could lose the centralized control owing to the disabled communication-system functionality. Although MGs can be controlled only by the primary control of DGs in a localized way without communication network [33], the optimality and sustainability are unable to achieve due to the lack of information sharing among controllers of DGs and MGs. In other words, MGs close to heavy load will consume more energy without appropriate power sharing scheme, leading to localized and regional energy shortage. Therefore, a post-contingency critical power supply through network reconfiguration or islanded MGs requires essential information exchange that can ensure an operational optimality.

The power network cyber-physical collaborative recovery [150, 151] have already been investigated to enhance cyber-physical power system resilience. A post-disaster cyber-physical interdependent restoration scheduling framework is proposed based on ad-hoc wireless device-to-device communication considering simultaneous damages on cyber and physical networks [151]. Communication failure is mitigated by the utilization of drone small cells for wireless communication recovery to enable power network reconfiguration after faults [151]. Such work considers one or some cyber-physical dependencies during the post-contingency restoration period, yet a comprehensive ad-hoc communication network formation supporting cyber-physical service restoration of power networks has not been fully investigated. Furthermore, during the post-contingency response period, existing DGs installed in the power network have limited capability, hence the portable storage of different carriers, e.g., mobile storage vehicles is utilized as an important optional extension of power supply. Such time-varying dispatchable energy resources require time-varying communication network topology to ensure an efficient coordination. Therefore, the cyber-layer response should be emphasized as important as the power supply response itself, especially the time-varying communication topology formation.

This chapter introduces a UAV (Unmanned Aerial Vehicle)-aided cyber-physical response to maintain critical power supply after adverse cyber-physical effects on power networks. The UAV positioning problem prioritizes full coverage of all dispatchable DGs and also considers the communication connectivity among networked MGs. Based on such UAV-assisted communication, a two-level event-triggered mechanism is proposed to regulate frequency and voltage, as well as to achieve a prioritized capacity-based active power sharing. More specifically, in each triggering instant, the bottom level dynamically updates the communication network and corresponding control laws, while the upper level considers the potential communication failure (caused by inter-MG long-distance data sharing) using a self-triggered request-then-response data exchange. The main contributions are outlined:

1. A UAV-assisted interconnected communication network formation is proposed to enable an effective data exchange both inside each MG and among networked MGs. The UAV positioning problem considers two scenarios in terms of the sufficiency of UAVs. Adequate UAVs can act as both base stations (BSs) and relay nodes to enable a full coverage, while the UAV positioning will prioritize the BSs to enable intra-MG operations in case of UAV insufficiency.

2. UAVs as mobile BSs enable event-based resource allocation considering mobile energy resources (MERs), thus ensuring communication coverage among post-contingency power network devices. UAV BSs, triggered by plug-and-play operations, update the communication topology and also design a prioritized capacity-based control law of each MG to guarantee the stability under time-delayed communication.

3. UAVs, as relay nodes enable enough information circulations among networked MGs, leading to effective power sharing among networked MGs. This can make the best of MERs to supply all critical loads in the power network. In virtue of UAV BSs and relay nodes, a self-triggered mechanism is employed to enable an energy-efficient UAV-based information circulation.

The rest of this chapter is organized as follows. Section 6.2 introduces the proposed framework and also details the UAV positioning problem, while Section 6.3 gives a two-level event-based control scheme. Simulation results are detailed in Section 6.4, and Section 6.5 concludes this chapter.

6.2 Post-Contingency UAV-Assisted Cyber-Physical Service Restoration Framework

The proposed post-contingency response framework focuses on the dynamic scheduling and control of the cyber-physical power network that has been split into several islanded MGs owing to damaged cyber-physical infrastructure. As shown in Figure 6.1, after contingencies (e.g., flooding and earthquake) occur, the power supply from the main grid is not available leading to the blackout, and the communication network supporting power system operation is out of service leading to information islands. Such cyber-physical out-of-service conditions normally cannot be repaired and recovered immediately. Hence, depending on wireless communication infrastructure (e.g., D2D wireless communication [14]), the power system dominated by power electronic devices is split into multiple MGs to maintain the critical power supply. At this stage, to enlarge the cyber-physical service coverage and to prolong the power supply, UAVs are deployed to rapidly create ad-hoc communication owing to its flexible placement in the air, thus supporting the operation of digitalized power networks. However, it is costly to deploy UAVs restoring the full communication during the pre-contingency period. Thus, analyzing the functionality of UAVs enabling its optimized deployment is necessary and economical. The functions of UAVs are two aspects: base station UAVs (BS-UAVs) to schedule the cyber-layer topology considering MERs in a regional MG (i.e., dynamically allocate communication resource for D2D wireless communication), and relay UAVs (R-UAVs) to enable inter-regional data exchange for further optimizing multi-MG operations.

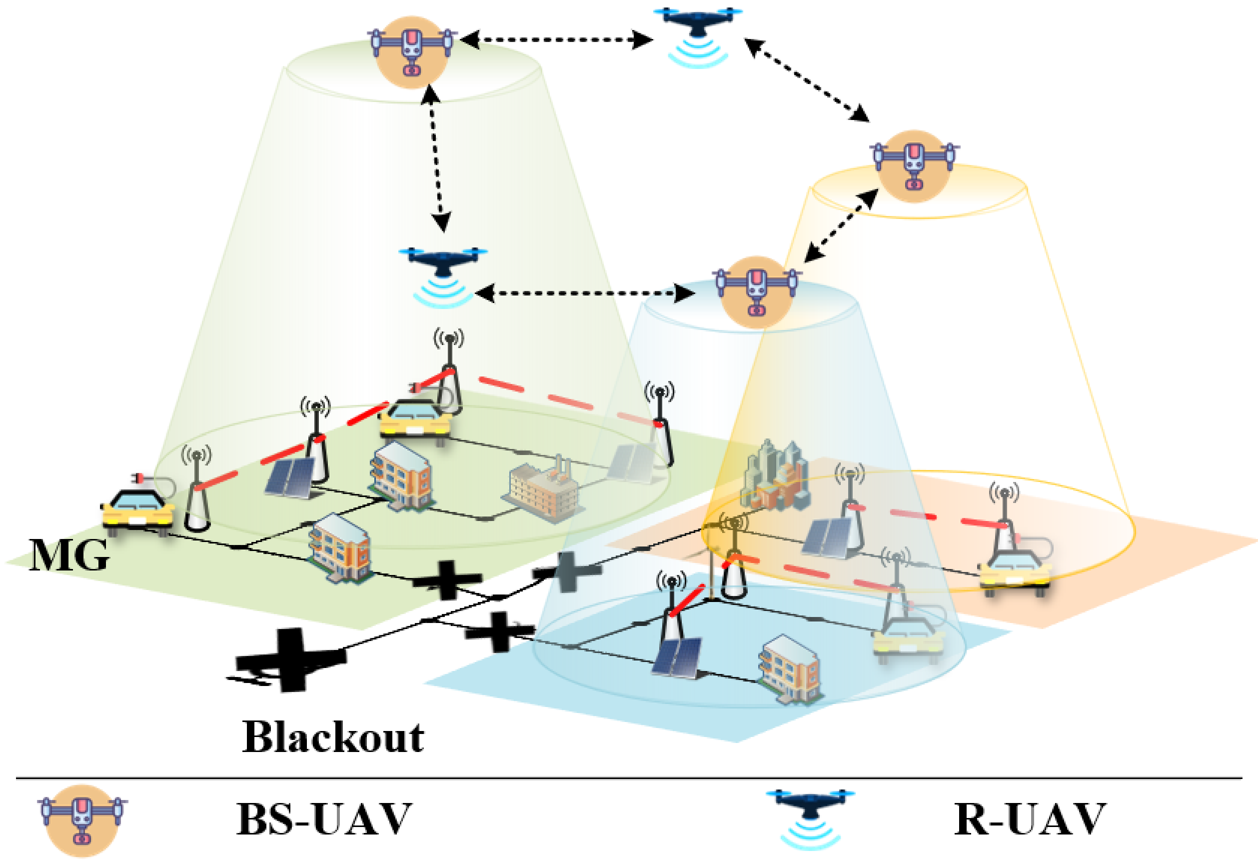

Figure 6.1: Diagram of UAV-aided post-contingency response.

6.2.1 Analysis of UAV functionality

In the post-contingency condition, there are two main wireless communication requirements to enlarge power network service coverage, i.e., management and transmission. In the management scenario, BS-UAVs manage communication resource, i.e., bandwidth between D2D users (DGs with D2D communication capability), while R-UAVs relay operational information among different power supply regions in the transmission scenario.

Combining two functional UAVs, the problem of UAV deployment can be summarized as Figure 6.2. Meshed dots model geographical locations of network users (e.g., DG users, smart load users, smart switches, ad-hoc plug-and-play points etc.), and red dots represent the UAV service range with radius r. Besides UAV service covering local users in each MG, interconnected network enabled by R-UAV of interconnection distance d_{ij} is considered. In addition, the charging cost efficiency of UAVs is considered through charging distance d_i^c to green-dot

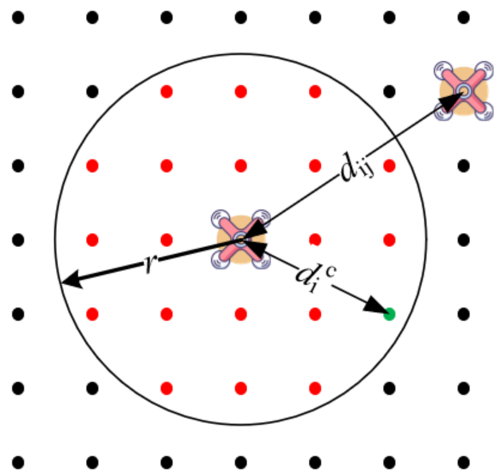

Figure 6.2: Post-contingency deployment of UAVs: r denotes the coverage radius of UAV; d_{ij} denotes the maximal UAV interconnection distance between UAV i and j; d_i^c denotes the recharging distance of UAV i.

charging points.

6.2.2 Post-Contingency Cyber-Physical Service Oriented UAV Deployment Optimization

As discussed in Section 6.2.1, we model the UAV deployment optimization with a meshed node set, i.e., possible UAV placement $\mathcal{N} = \{1, 2, \ldots, n\}$ and a UAV set $\mathcal{U} = \{1, 2, \ldots, u\}$ that is available to be deployed.

We first model the BS-UAVs covering aggregated local network users, and the coverage can be expressed as

$$\sum_{i=1}^{n} \sum_{k=1}^{u} \mu_{ik}\nu_{ij} \geq M_j, \forall j \in \mathcal{N} \tag{6.1}$$

where the binary variable $\mu_{ik} = 1$ if the placement i is deployed with the UAV k, otherwise $\mu ik = 0$; the binary variable $\nu_{ij} = 1(\nu_{ij} = 0)$ if the placement j is inside(outside) the coverage of the UAV deployed at placement i; $M_j = 1$ means that the placement j has a network user. Eq. (6.1) ensures that each user is served by at least one BS-UAV.

In terms of post-contingency service cost, it is necessary to limit the number of the deployed

UAVs. However, in the sense of resilience, the power network operator should guarantee the critical power supply, leading to enough UAVs in the case of emergency use. Hence, we have

$$\sum_{i=1}^{n}\sum_{k=1}^{u}\mu_{ik} \leq u \tag{6.2}$$

where u equals to the cardinality if the set of $\mathcal{U}$. To be more realistic, the pre-evaluation planning or forecasting algorithms should be well designed to decide the UAV numbers.

Each UAV is assigned to at most one potential placement, while each potential placement is deployed at most one UAV. This can be mathematically modelled by

$$\sum_{i=1}^{n}\mu_{ik} \leq 1, \forall k \in \mathcal{U}, \quad \sum_{k=1}^{u}\mu_{ik} \leq 1, \forall i \in \mathcal{N} \tag{6.3}$$

Eq. (6.1)–Eq. (6.3) mathematically summarize the network service coverage constraints. To further ensure the interconnectivity as discussed before, more UAVs may be required to serve as relay nodes in a large-scale power network. The intuitive method to express such interconnectivity is to use the connected graph constraint as [57], where the connected graph constraint is not linear, so that cannot be directly handled.

Hence, inspired by [152], we artificially set two successively indexed UAVs interconnected, which can be modelled with an auxiliary binary variable $\zeta_{ijk} = \mu_{ik}\mu_{j(k+1)}, , \forall i, j \in \mathcal{N}, \forall k \in \mathcal{U} \setminus \{u\}$. Only if $\mu_{ik} = 1$ and $\mu_{j(k+1)} = 1$, $\zeta_{ijk} = 1$ means the potential placements i and j are both deployed a UAV. Such nonlinearity can be easily linearized as

$$\begin{cases} \zeta_{ijk} \leq \mu_{ik} \\ \zeta_{ijk} \leq \mu_{j(k+1)} \qquad \forall i, j \in \mathcal{N}, \forall k \in \mathcal{U} \setminus \{u\} \\ \zeta_{ijk} \geq \mu_{ik} + \mu_{j(k+1)} \end{cases} \tag{6.4}$$

Since the number of UAVs in service is lower than the available ones in $\mathcal{U}$, the interconnection may not exist if the UAVs that are in emergency use are not successively indexed as Eq. (6.5).

The constraint (6.5) ensures that UAV $k+1$ is deployed only if UAV k is also in service.

$$\sum_{i=1}^{n} \mu_{ik} \geq \sum_{i=1}^{n} \mu_{i(k+1)}, \forall k \in \mathcal{U} \setminus \{u\} \tag{6.5}$$

So far, Eq. (6.1)–Eq. (6.5) ensure that all users are covered in the communication service while information exchange among deployed UAVs is feasible. Then, the objective of UAV deployment optimization is to minimize the cost of UAV placement which is reflected by two parts: total number of deployed UAVs and UAV total charging distances, i.e.,

$$\min_{\mu_{ik}} \sum_{i=1}^{n} \sum_{k=1}^{u} (w_u \mu_{ik} + w_c d_i^c) \quad \text{s.t. Eq. (6.1)} - \text{Eq. (6.5)} \tag{6.6}$$

where w_u and w_c are weighted factors of UAV deployment cost and UAV charging distance respectively. The UAV deployment optimization (6.6) optimizes the UAV placement enabling full service coverage of power users within an interconnected communication network. However, the optimization result may result in few R-UAVs if power network users are geographically centralized. This means that BS-UAVs can almost achieve information circulation without R-UAVs.

The UAV deployment optimization is based on the assumption that UAVs are enough to enable communication full coverage and connectivity as stated previously. However, if a more extreme condition with limited UAVs occurs, i.e. the optimization (6.6) is infeasible, the MG coverage should be guaranteed through giving up multi-MG power sharing, i.e., we transfer optimization (6.6) to

$$\min_{\mu_{ik}} \sum_{i=1}^{n} \sum_{k=1}^{u} (w_u \mu_{ik} + w_c d_i^c) \quad \text{s.t.} \quad \text{Eq. (6.1)} - \text{Eq. (6.3)} \tag{6.7}$$

which will lead to a network service coverage without connectivity. Furthermore, there may be more extreme conditions that optimization problem (6.7) is infeasible, i.e., not all network users can be covered by UAVs. Under this circumstance, it should be emphasized that users inside the MGs with plug-and-play operation needs, which also can be solved by (6.7). To summarize, the UAV positioning algorithm is detailed in Algorithm 6.1. After UAV deployment in the cyber layer, a two-level cyber-physical solution is required to be investigated and will be discussed in Section 6.3.

Algorithm 6.1: Post-Contingency Service Oriented UAV Positioning Algorithm

1 **Initialization:** set a meshed grid and define parameters and variables;
2 Solve optimization problem (6.6);
3 **if** *Problem in Line 2 is infeasible* **then**
4   Solve optimization problem (6.7);
5   **if** *Problem in Line 4 is infeasible* **then**
6   Prioritize network users of MGs requiring plug-and-play operations;
7   Update and re-initialize optimization problem, i.e., return to Line 1;
8   **end**
9 **end**

6.3 A Two-Level Event Based Solution Assisted by UAVs

In this section, we design an event based control scheme to coordinate power network dispatchable resources, i.e. users, in two levels with the assistance of ad-hoc communication network investigated in Section 6.2.2. According to two different functions of deployed UAVs, a bottom-level solution (corresponding to BS-UAV) targets at coordinate local dispatchable resources inside one MG, while an upper-level solution (relying on information circulation) focuses on multi-MG energy-efficient cyber-physical operation with poor communication.

6.3.1 Bottom-Level: Event-Triggered Dynamic Bandwidth Allocation and Prioritized Distributed Control Design

Event-Triggered Cyber-Layer Dynamic Resource Allocation

A mobile BS-UAV acts as a bandwidth manager of the regional power network to dynamically allocate communication resources considering time-varying physical-layer users [49]. The scenario that requires dynamic communication network formation is originated from time-varying dispatchable power network resources caused by plug-and-play operations (e.g., mobile emergency battery storage, electric vehicle cluster). Such add-on power injection is a pathway to support energy-deficient regions. In addition, The static storage of MGs can switch between charging state and discharging state to collaborate with the mobile one. In other words, mobile energy storage plug-in operation can both support regional loads and work as a charger for the localized static storage.

Once dispatchable devices vary among the power network, the BS-UAV re-schedules the topology according to the geographical distances, as shown in Figure 6.3. Then, in order to reduce the workload of bandwidth allocation under the post-contingency condition, the event-triggered mechanism is designed, i.e., plug-and-play operation triggering dynamic communication network formation. Specifically, the dynamic communication formation depends on efficient bandwidth allocation algorithms that have been widely utilized in industrial applications, e.g., Internet of Vehicles [60, 153] and disaster rescue [154]. After applying the bandwidth allocation in the post-contingency power network recovery enabled by D2D neighbouring communication technology [14], we can obtain event-varying delay τ in the cyber layer. Although the bandwidth allocation for either distributed, centralized or hybrid structure can be achieved similarly, such communication design is independent of UAV placement problems. In this chapter, we apply the distributed structure [14] instead.

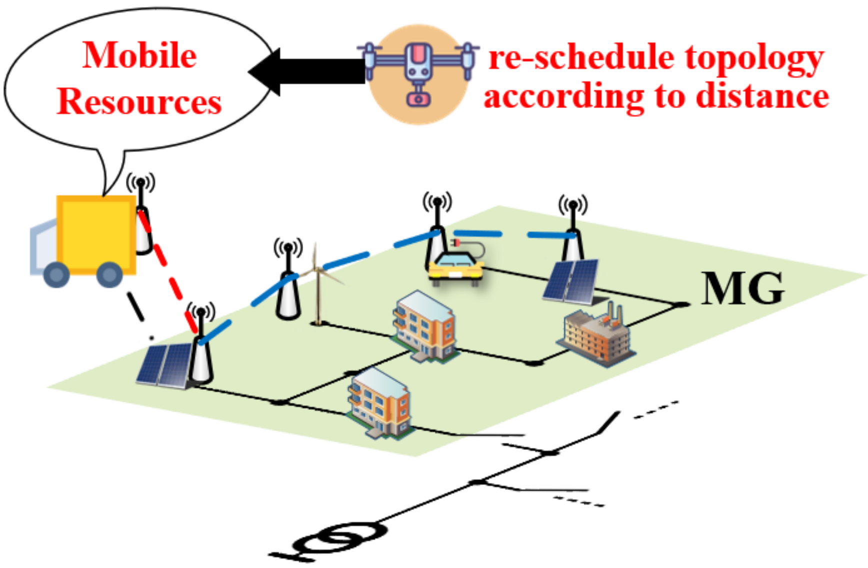

Figure 6.3: Communication topology re-scheduling with plug-and-play operations.

Depending on the time-varying delay τ obtained from bandwidth allocation, an adaptive distributed consensus based controller is designed to guarantee local stability of each MG. Apart from plug-and-play operations, different generators have diverse post-contingency priorities, e.g., the mobile energy storage enabling plug-and-play operation has higher service-providing priority so that it can be consumed firstly to restore more energy capacity of static storage, further extending the service of static storage. To be more specific, different from the traditional distributed control considers the averaging consensus among DGs [33, 67], we use prioritized droop coefficients to model the grid-forming inverter based DGs:

$$\omega_i = \omega_{ni} - m_{Pi}P_i, \quad V_i = V_{ni} - n_{Qi}Q_i \tag{6.8}$$

where ω_{ni}, V_{ni} are set points of primary frequency and voltage control; ω_i, V_i are angular frequency and voltage magnitude of DG i; P_i, Q_i are respectively active and reactive power outputs of DG i; m_{Pi}, n_{Qi} are droop coefficients and are selected based on the power ratings and priority levels. The primary controller consists of power control of Eq. (6.8) and inner control loops, through which the frequency and voltage deviations from the reference cannot be eliminated without effectively adjusting set-points. Hence, the proposed control is employed to achieve frequency regulation, accurate active power sharing, and voltage regulation, i.e., $\lim_{t\to\infty}\omega_i = \omega_{\text{ref}}, \lim_{t\to\infty}|m_{Pi}P_i - m_{Pj}P_j| = 0, \lim_{t\to\infty}V_i = V_{\text{ref}}$.

To achieve the control objective, an adaptive control law design adapting to time-varying delays can be obtained by the procedure as Section 4.2 of [14], which is triggered by the dynamic resource allocation. As a similar event-triggered manner, a prioritized active power sharing, i.e., frequency droop coefficient m_{Pi} also requires a reasonable update rule, which will be discussed as follows.

Each DG unit has two-dimensional adjustable parameter state indicator s_i and frequency droop coefficient m_{Pi}. $s_i \in \{-1, 0, 1\}$ is the plug-and-play condition of DG i: -1 means the MG charges DG units (normally energy storage); 0 means DG units are disconnected; DG units labelled 1 are those injecting power into the MG. The choice of m_{Pi} is determined by available capacity static DG units with $s_i = 1$ and MERs. According to the backup requirements of critical loads such as data center and telecommunication tower [155], coordinating BS-UAVs can obtain these static DG units' capacity. Together with the capacity of available MERs, we can obtain the all available units' capacity P_i^c, which guides to choose m_{Pi} satisfying $m_{Pi}P_i^c = m_{Pj}P_j^c, \forall i, j \in \mathcal{N} \wedge s_i = 1 \wedge s_j = 1$, which leads to the power injections of both static and MERs shared by capacity availability.

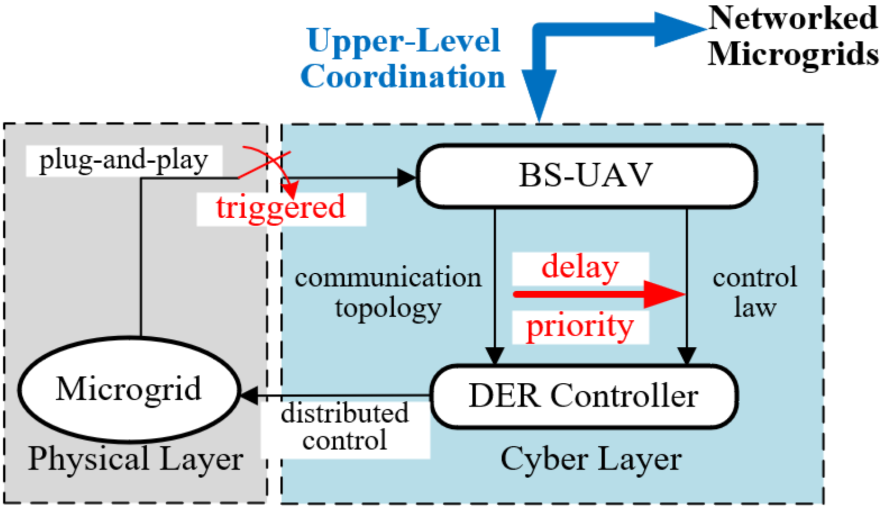

Figure 6.4: Framework of bottom-level UAV-aided post-contingency response.

To summarize, the work flow of the bottom-level cyber-physical post-contingency response of power networks is outlined in Figure 6.4. The UAV deployed for the bottom-level coordination utilizes a plug-and-play-driven event-triggered mechanism to enable dynamic communication topology and control law design, which is delay and priority driven. Such event-triggered mechanism leads to an energy-efficiency that is really vital in a post-contingency condition. Furthermore, BS-UAVs also acts interactive connector to enable upper-level multi-microgrid (networked microgrids) coordination, which will be investigated in Section 6.3.2.

6.3.2 Upper-Level: Self-Triggered Information Circulation

As depicted in Figure 6.4, bottom-level MGs could coordinate with each other achieving global energy sharing. However, such attractive aim cannot be reached directly without additional communication network coverage after contingencies. R-UAVs that have been deployed as Section 6.2.2 enable an inter-MG information circulation for multi-MG optimal operation. To allow multi-MG energy sharing, energy islands should be reconnected, which has been widely developed through power network reconfiguration algorithms [149,151,156] if the power network communication service is fully covered. Owing to the full communication coverage guaranteed by optimization (6.6), reconnections of islanded MGs can be completed. Hence, we focus on the communication-efficiency multi-MG coordination via a self-triggered scheme considering communication failure caused by poor post-contingency environments.

Aggregated Modelling of Available Dispatchable Energy Resources in MGs

The multi-MG coordination relies on the aggregated model of each MG, which reflects its dynamic capacity and performance. The aggregation model can be obtained by some equivalent methods [144, 157, 158], and this chapter adopts the following one especially for (6.8):

$$P_I = \sum_{j \in \mathcal{C}_I} P_j, m_{PI} = \frac{1}{\sum_{j \in \mathcal{C}_I} \frac{1}{m_{Pj}}}, \omega_I = \frac{\sum_{j \in \mathcal{C}_I} \frac{\omega_j}{\omega_{cj} m_{Pj}}}{\sum_{j \in \mathcal{C}_I} \frac{1}{\omega_{cj} m_{Pj}}} \tag{6.9}$$

where subscript I indexes the number of MGs; a dynamic set $\mathcal{C}_I$ obtained by the event-triggered manner of the bottom level contains real-time dispatchable resources inside MG I; ω_{cj} denotes the cut-off frequency of low-pass filter in the inverter control loop of DG j [33]. Eq. (6.9) only considers multi-MG frequency control and active power sharing, while the voltage regulation is a local problem solved inside each MG [43]. Based on (6.9), the MG can be aggregated as $\dot{\omega}_{nI} = \dot{\omega}_I + m_{PI}\dot{P}_I = u_{\omega I} + u_{PI}$ with $u_{\omega I}, u_{PI}$ being the auxiliary control inputs [66], i.e., $\dot{\omega}_I = u_{\omega I}$, $m_{PI}\dot{P}_I = u_{PI}$. Then, the upper-level coordination adopts an adaptive self-triggered mechanism [4, 157] that will be discussed next.

Distributed Adaptive Self-Triggered Information Circulation With Ternary Control

The upper-level communication topology of UAVs as the top of Figure 6.1 can be modelled by an undirected graph $\mathcal{G} = \{\mathcal{I}, \mathcal{E}\}$ [146], where $\mathcal{I} = \{1, 2, \ldots, m\}$ is a set of MGs, $\mathcal{E} \subseteq \mathcal{I} \times \mathcal{I}$

is a set of edges, and m is the number of MGs. An edge (J, I) means that MG I can receive information from MG J and J is a neighbour of I. The set of neighbours of MG I is described by $\mathcal{N}_I = \{J : (J, I) \in \mathcal{E}\}$ with $d_I = |\mathcal{N}_I|$ denoting the cardinality of $\mathcal{N}_I$.

To make information circulation energy-efficient, a ternary control [4, 157] with $(x, u, \theta) \in \mathbb{R}^m \times \mathbb{R}^d \times \mathbb{R}^d$ is utilized to binarize upper-level control law, thus reducing the data transmission. x, u, θ are the vectors of node states (i.e., frequency ω_I or active power ratio $m_{PI}P_I$), controls and clock variables respectively. u, θ are both edge-based variables with $d := \sum_{I=1}^{m} d_I$. Then, the control law is governed by

$$\dot{x}_I = u_I = \sum_{J \in \mathcal{N}_I} u_{IJ}, \forall I \in \mathcal{I}, J \in \mathcal{N}_I \tag{6.10a}$$

$$\begin{cases} x_I(t) = x_I(t^-) \quad \forall I \in \mathcal{I} \\ u_{IJ}(t) = \begin{cases} \operatorname{sign}_\varepsilon\left(D_{IJ}(t)\right), & (I, J) \in \mathcal{J}_1(\theta, t) \\ 0, & (I, J) \in \mathcal{J}_0(\theta, t) \\ u_{IJ}(t^-), & \text{otherwise} \end{cases} \\ \theta_{IJ}(t) = \begin{cases} \dfrac{f_{IJ}\left(x(t)\right)}{2(d_I + d_J)}, & (I, J) \in \mathcal{J}_1(\theta, t) \\ \dfrac{\varepsilon}{2(d_I + d_J)}, & (I, J) \in \mathcal{J}_0(\theta, t) \\ \theta_{IJ}(t^-), & \text{otherwise} \end{cases} \\ \dot{\theta}_{IJ}(t) = -R \end{cases} \tag{6.10b}$$

$$f_{IJ}\left(x(t)\right) = \max\left\{|D_{IJ}(t)|, \varepsilon\right\} \tag{6.10c}$$

$$D_{IJ}(t) = x_J(t) - x_I(t) \tag{6.10d}$$

$$\operatorname{sign}_\varepsilon(z) := \begin{cases} \operatorname{sign}(z), & \text{if } |z| \geq \varepsilon \\ 0, & \text{otherwise} \end{cases} \tag{6.10e}$$

In (6.10), u_I aggregates contributions of all edges $(J, I) \in \mathcal{E}$, and u_{IJ} represents the control action on node I of the communication link from MG J to MG I. Through (6.10b), u_{IJ}, θ_{IJ} are updated only when the clock variable θ_{IJ} reaches zero, i.e., $(I, J) \in \mathcal{J}_*(\theta, t) =$

$\{(I,J) : J \in \mathcal{N}_I \wedge \theta_{IJ}(t^-) \leq 0\}$ (subscript $*$ denotes the communication availability) with $\theta_{IJ}(t^-) = \lim_{\xi \to t} \theta_{IJ}(\xi)$. The clock rate across all network links $R > 0$ determines the triggering frequency that is designed according to UAV-assisted upper-level communication capability. The consensus error bound $\varepsilon > 0$, a user designed sensitivity parameter represents the minimally acceptable consensus error that avoids Zeno-behaviour of all edges. $u_{IJ} \in \{-1, 0, 1\}$ from a quantizer $\text{sign}_\varepsilon(z)$. The stability of control law (6.10) for a specific interconnected communication network obtained by (6.6) is mainly dependent on communication failure frequency and user designed parameters R, ε, and those interested in theoretical analysis can refer to [4,157].

Algorithm 6.2: Two-Level Cyber-Physical Framework With Detailed Upper-Level Coordination

`/* Cyber-Physical Functional Logic */`

1 **if** *Algorithm 6.1 ends at Line 4* **then**

2   Apply bottom-level control (frequency, voltage and active power sharing) designed in Section 6.3.1 ;

3 **else if** *Algorithm 6.1 ends at Line 2* **then**

4   Apply bottom-level voltage regulation designed in Section 6.3.1 ;

5   Apply upper-level frequency regulation and active power sharing by (6.10), i.e.,

    `/* Upper-Level Coordination */`

    /* **begin**

        Initialization: for all $I \in \mathcal{I}$ and $J \in \mathcal{N}_I$, set $\theta_{IJ}(0^-) = 0$, $u_{IJ}(0^-) = 0$;

        foreach $I \in \mathcal{I}$ **do**

            foreach $J \in \mathcal{N}_i$ **do**

                while $\theta_{IJ}(t) > 0$ **do**

                    MG I applies the control $u_I(t) = \sum_{J \in \mathcal{N}_I} u_{IJ}(t)$;

                end

                if $\theta_{IJ}(t) \leq 0$ **then**

                    MG I requests information from MG J;

                    Determine $\mathcal{J}_*(\theta, t)$ by data availability;

                    MG I updates $u_{IJ}(t), \theta_{IJ}(t)$ using (6.10b) according to $\mathcal{J}_*(\theta, t)$;

            end

        end

    end

    `*/`

6 **end**

The procedure of the two-level coordination is detailed in Algorithm 6.2, where aggregated set-points ω_{nI} obtained from upper-level coordination are updated to each MG through one DG and other DGs can be informed through multi-hop communication in the bottom-level. Line 5 (upper-level coordination) in Algorithm 6.2 checks the data availability of upper-level data exchange with a request-then-response mechanism. Such data availability could be induced by random packet loss or R-UAV overload. Once the UAV deployment result of (Algorithm 6.1) is solved by (6.7), i.e., forming an incomplete interconnected network, only the bottom-level control regulates all dispatchable units instead of the upper-level coordination.

6.4 Case Study

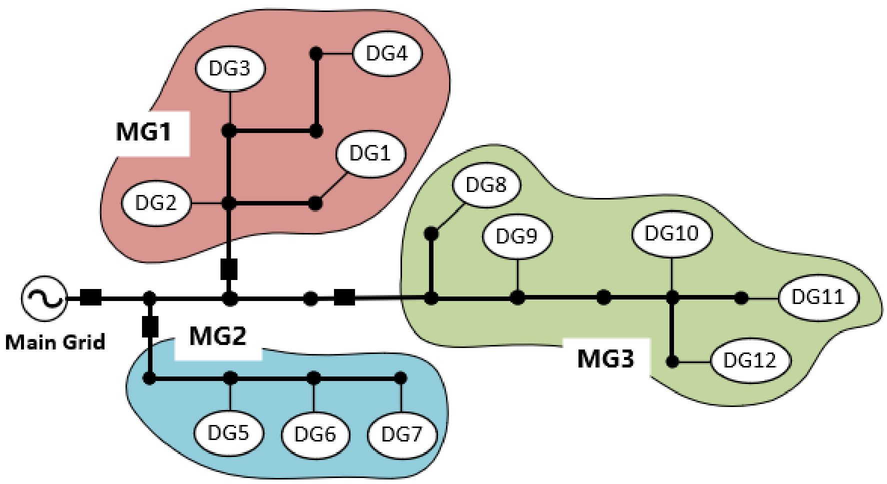

Figure 6.5: Diagram of the test power network: MG1, MG2 and MG3 coloured by red, blue and green respectively.

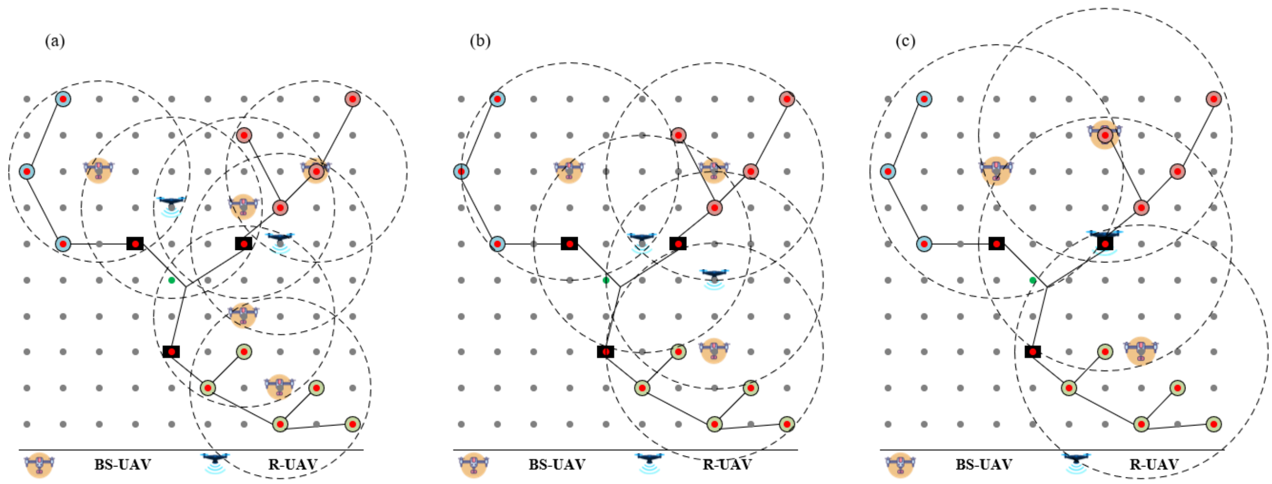

Figure 6.6: Result of UAV deployment optimization: (a) $r = 2.5$, (b) $r = 3$, (c) $r = 3.5$.

In this section, the proposed cyber-physical service restoration framework assisted by UAVs in post-contingency conditions will be verified by the power network detailed in Figure 6.5, where three emergency MGs formed after contingencies [14]. The test power network is consisted of 12 potential dispatchable DGs (network users), although some may be ad-hoc plug-and-play points. The results and performance of the proposed framework are discussed in details in terms of UAV deployment, bottom-level and upper-level solutions respectively.

6.4.1 Discussion of UAV Deployment Result

The layout of the test power network as Figure 6.5 is modelled by 10×10 meshed dots. The twelve (potential) dispatchable resources and three power grid interconnection switches are denoted by red dots as cyber-layer network users, while one UAV charging point is represented by a green dot. In practice, different geographical location and environments [159] (e.g., building height) will affect the coverage of UAVs, thus we optimize UAV deployment with three different coverage ranges $r = 2.5$, $r = 3$, $r = 3.5$ respectively, and the corresponding results are depicted in Figure 6.6.

The communication range of each UAV $r = 2.5$ including five BS-UAVs and two R-UAVs. More specifically, the blue-colour MG with DG5, DG6 and DG7 are served by only one BS-UAV and the others are both covered through two BS-UAVs, while another two R-UAVs relays the data among three MGs. The similar results are obtained for coverage ranges with $r = 3$ and $r = 3.5$ respectively, which are summarized in Table 6.1. All network users are covered by BS-UAVs, while all UAVs are interconnected through R-UAVs. In the case of $r = 3.5$, the UAV deployment (Figure 6.6(c)) shows only four UAVs required to be placed. Each MG is covered by one BS-UAV, while interconnection between MG2 and MG3 requires one R-UAV to enable network connectivity. The number of UAVs ensuring full coverage and connectivity decreases as the coverage range increases.

Table 6.1: Optimized UAV Numbers with Different Coverage Ranges

Coverage range	Total number	BS-UAV	R-UAV
$r = 2.5$	7	5	2
$r = 3$	5	3	2
$r = 3.5$	4	3	1

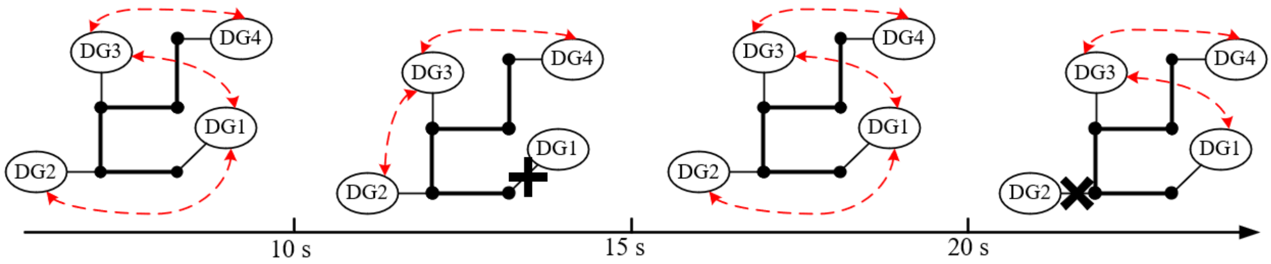

Figure 6.7: Bottom-level event-triggered topology optimization result.

6.4.2 Bottom-Level Event-Triggered Dynamic Communication and Control Design

Bottom-level communication-control design is a local management inside one MG, hence we take MG1 as an example to evaluate the proposed bottom-level solution, of which the performance is detailed in Figure 6.8. Once the plug-and-play operation after deploying BS-UAVs, the distributed control law is updated based on the bandwidth-allocation induced delay and capacity-driven priorities, of which the result is outlined in Table 6.2 and Figure 6.7. The islanded MG operates using droop principles with secondary control to regulate frequency and voltage, responding to the load disturbance during $0 < t \leq 10$. Then, DG1 is disconnected and one MER is plugged into the grid at $t = 10$, $t = 15$ respectively. Besides topology update, owing to the mobility, we prioritize its power output by updating $m'_{P1} = 0.5m_{P1}$, thus the active power output of MER increases to accommodate more load demands after $t = 15$. After $t = 20$, DG2 becomes load demand for charging to prolong the power supply service. As load demand, the power output of DG2 becomes negative in Figure 6.8(b) and the active power ratio becomes zero (i.e., not participating in intra-MG power sharing), leading to an increasing power output of other three DGs. During the whole period, the control performance (i.e., frequency regulation, active power sharing and voltage regulation) in the post-contingency period is all

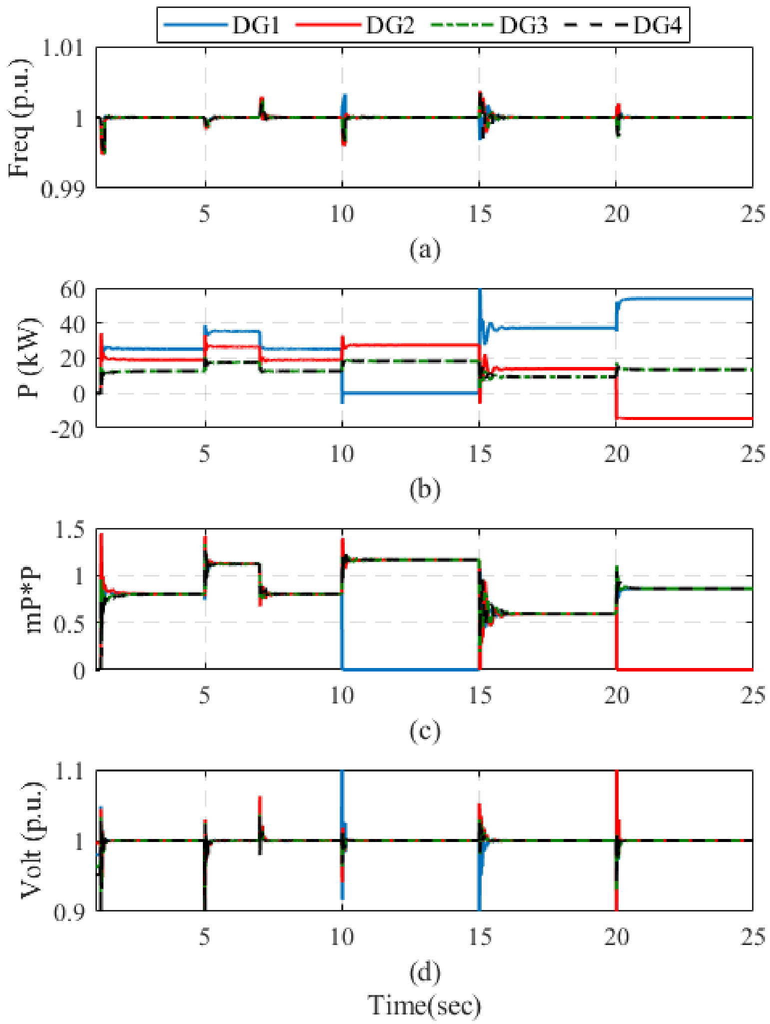

Figure 6.8: Bottom-level control performance of MG1: (a) frequency, (b) active power, (c) active power ratio, (d) voltage.

reached, showing the effectiveness of the proposed bottom-level cyber-physical post-contingency mitigation.

Table 6.2: Results of Dynamic Resource Allocation and Prioritized Control Design for MG1

Periods	Delay	Capacity ratio	m_{Pi} ratio
Load disturbance $0 < t \leq 10$	87.5ms	2 : 1.5 : 1 : 1	1 : 1.33 : 2 : 2
DG1 disconnection $10 < t \leq 15$	102.6ms	□ : 1.5 : 1 : 1	□ : 1.33 : 2 : 2
MER plug-in $15 < t \leq 20$	87.5ms	4 : 1.5 : 1 : 1	0.5 : 1.33 : 2 : 2
DG2 charging $20 < t \leq 25$	63.3ms	4 : □ : 1 : 1	0.5 : □ : 2 : 2

6.4.3 Upper-Level Coordination

The upper-level coordination is evaluated based on the communication solution in Section 6.4.1 (i.e., Figure 6.6(b)) and the same scenario in Section 6.4.2. The upper-level coordination is activated at $t = 10$, and the corresponding multi-MG power sharing is depicted in Figure 6.9 and Figure 6.10. Figure 6.9 outlines the power sharing comparison between the power network governed by upper-level coordination and only bottom-level control. The inter-MG active power sharing by bottom-level control is poor, hence more MERs are required to supply MGs individually leading to higher emergency response cost.

Besides frequency and voltage regulations guaranteed as that by the bottom-level control, the upper-level coordination achieves active power sharing through all DGs as Figure 6.10. Although there are not any load changes and plug-and-play operations after $t = 10$ in both MG2 and MG3, the active power outputs are adjusted responding to the plug-and-play operations in MG1. The MER plugging into the power network shares more load demands throughout the power network, showed by a decrease of active power ratios (row (c) in Figure 6.10) after $t = 15$. Therefore, through the upper-level coordination, plug-and-play operations such as MERs' connection and DGs' recharging provide grid flexibility that is really important during post-contingency emergency periods.

6.5 Conclusion

This chapter proposes a cyber-physical service restoration framework assisted by UAVs during emergency periods caused by adverse cyber-physical contingencies. The proposed framework employs UAVs to play two different roles, i.e., base station and relay node, thus forming an interconnected communication network that covers all controllable resources. By virtue of the information circulation, a two-level control scheme is designed to coordinate available resources including onsite dispatchable resources and MERs. Due to limited UAVs resulting in an incompletely full communication coverage, the UAV deployment optimization will prioritize the functionality of BS-UAVs to enable small-scale plug-and-play operations inside MGs. As such,

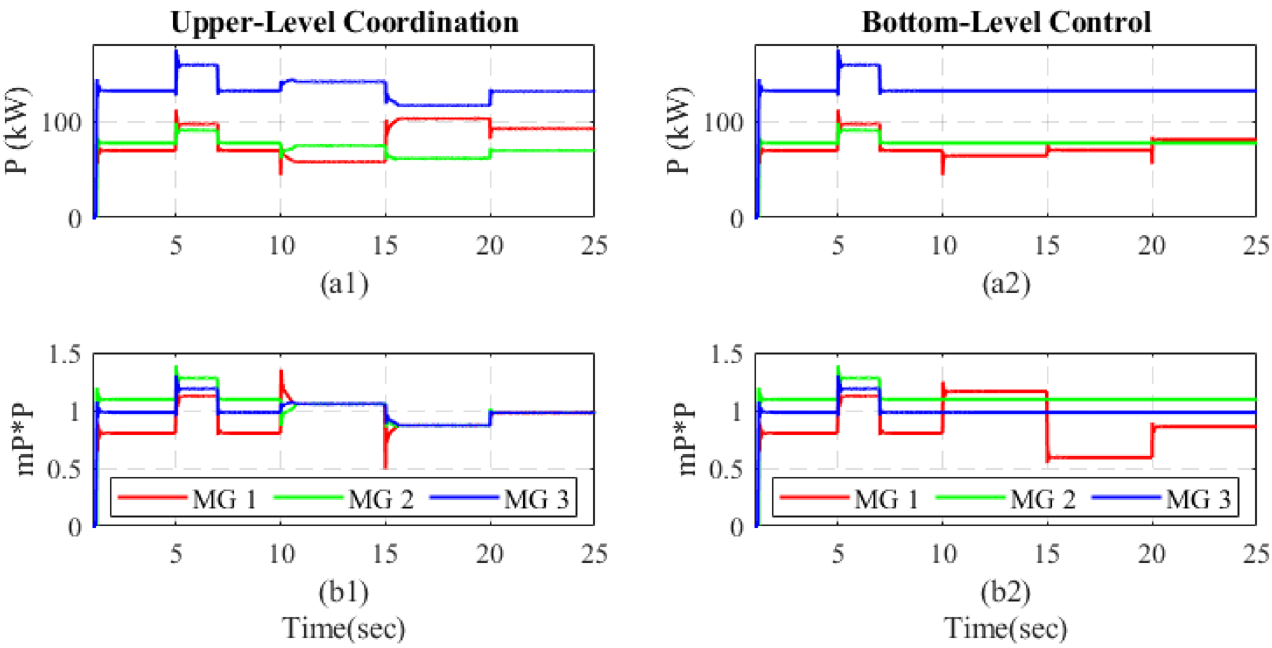

Figure 6.9: Active power sharing among MGs through upper-level coordination.

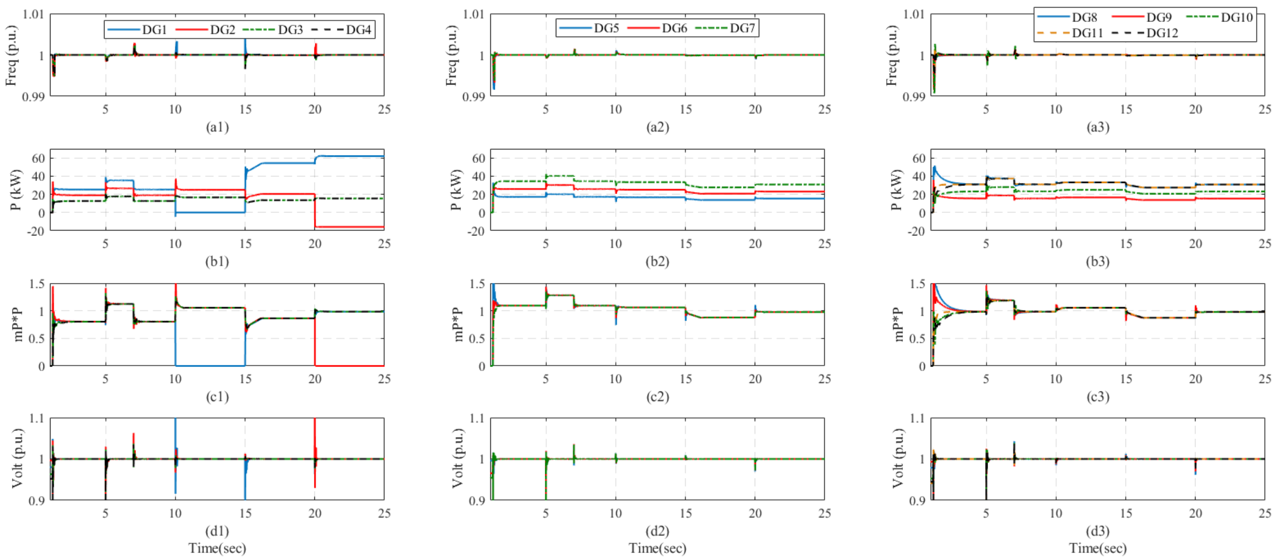

Figure 6.10: Upper-level coordination performance: row (a) frequency, row (b) active power, row (c) active power ratio, row (d) voltage; first column MG1, second column MG2, third column MG3.

the bottom-level control focuses on the intra-MG control, while the upper-level coordination investigates the inter-MG power sharing if possible. Finally, we design a case study with comprehensive scenarios validating its effectiveness.

Chapter 7

Fixed-Time Convergent Distributed Observer Design of Linear Systems: A Kernel-Based Approach

7.1 Introduction

Large scale systems are encountered more frequently in real-world applications, such as power networks, intelligent transportation systems and other cyber-physical systems. Such systems have an increasing demand for flexibility and scalability. The continuous growth of communication technology has enabled the development of decentralised and distributed solutions, which can perform collaborative tasks by using multi-agent communications. This has posed new challenges in control theory, including distributed consensus control, distribution estimation and so on [160, 161].

State estimation represents one of the most important problems in control. Motivated by previous developments in the centralised observer, this chapter focuses on the distributed observer, where the outputs of a large scale system are measured by a sensor network and only a small portion of the system output is available at each sensor node. Therefore, the main challenge is that the state of the system is not fully observable at any sensor node. The goal is to design a distributed observer, such that the full state of the system can be collaboratively reconstructed by each agent using local measurement and proper neighbouring communication [162–165].

A variety of distributed linear time-invariant (LTI) state estimation approaches have been reported in the literature under different formulations inherit from the centralised approaches, including the Kalman filter and Luenberger observer. A comprehensive overview of existing distributed observers can be found in [166]. It is noteworthy that the design of a distributed observer is highly influenced by the communication graph. In [167], a distributed Kalman filtering algorithm is proposed for an undirect and connected communication graph. With the same assumption on the communication graph, a distributed Luenberger-type observer is presented in [168]. More recently, research efforts are paid to more general directed graphs [5, 169–171]. Necessary and sufficient observability conditions for designing a distributed observer are stated in [169, 172, 173]. The study [174], on top of the Luenberger observer based scheme, introduces a multi-hop staircase decomposition mechanism, which makes it possible to lower information exchange and to relax the common assumptions of strongly connected graphs compared to the majority of distributed observers in the literature. Most of the existing methods are based on the Luenberger observer, which permits a single-agent-based design and implementation and ensures the local state estimate of each agent asymptotically converges the system state. On the other hand, [6, 175] propose alternative solutions to distributed state estimation by using the homogeneous technique [176]. As such, the state estimation error decays within a small finite time.

An important challenge in distributed estimation that has not been extensively addressed is the communication delay throughout the network. In the majority of existing works, the effect of delays is omitted, while its presence may drastically influence the estimation performance. Very recently, [177] proposes a time-delay distributed observer, which guarantees exponential stability in the presence of time-varying but conservatively known (upper bound is available) communication delays, and the convergence rate can be designed up to a maximum total delay.

In this chapter, we study the distributed observer problem of a continuous-time LTI system, where the communication between agents may involve time-varying delays, as assumed in [177]. The main contribution of the chapter lies in a novel fixed-time convergent distributed observer based on a cross-agent information sharing mechanism. The method provides an example of how distributed estimation systems can benefit from fixed-time convergence properties. The key to the fixed-time observer is the Volterra integral operators with specialised kernel functions, as inspired by the centralised counterpart [123]. In contrast to the majority of methods in the literature that require the full-dimensional state estimates to be shared among neighbouring nodes, the proposed scheme enables a reduction of the transmitted data over the communication links by invoking a rank-condition and the effect of delays in communication networks is compensated. Finally, the robustness of the proposed method against measurement noise and perturbations is characterised.

The outline of this chapter is as follows. The state estimation problem formulation and mathematical preliminaries are given in Section 7.2. Section 7.3 introduces the main algorithm, and its robustness against disturbances and measurement noise is analysed in Section 7.4. Simulation examples are presented in Section 7.5, and concluding remarks and future work are discussed in Section 7.6.

7.2 Problem Statement and Preliminary

7.2.1 Problem Setting

Notation: Let $\mathbb{R}$, $\mathbb{R}_{\geq 0}$ and $\mathbb{R}_{>0}$ denote the real, the non-negative real and the strict positive real sets of numbers, respectively. Given a vector $\boldsymbol{x} \in \mathbb{R}^n$, we denote $|\boldsymbol{x}|$ as the Euclidean norm of $\boldsymbol{x}$. Given a time-varying vector $\boldsymbol{x}(t) \in \mathbb{R}^n$, $t \in \mathbb{R}_{\geq 0}$, we will denote $\|\boldsymbol{x}\|_\infty$ as the quantity $\|\boldsymbol{x}\|_\infty = \sup_{t \geq 0} |\boldsymbol{x}(t)|$. Assuming $\boldsymbol{x}(t)$ is k-th order differentiable, the k-th order derivative signal of $\boldsymbol{x}(t)$ is denoted by $\boldsymbol{x}^{(k)}(t)$.

In this chapter, a directed graph is denoted by $\mathcal{G} = \{\mathcal{N}, \mathcal{E}, \mathcal{A}\}$, where $\mathcal{N} = \{1, 2, \cdots, N\}$ is a set of nodes, $\mathcal{E} \subseteq \mathcal{N} \times \mathcal{N}$ is a set of edges, and $\mathcal{A} = [a_{ij}] \in \mathbb{R}^{N \times N}$ denotes the adjacency matrix. The element a_{ij} is the weight of the edge (i,j), and $a_{ij}=1$ if and only if $(i,j)\in\mathcal{E}$ and $a_{ij}=0$ otherwise. Specifically, $(i,j)\in\mathcal{E}$ means that the i-th node can send information to the j-th node. The set of neighbours of node j is described by $\mathcal{N}_j=\{i:(i,j)\in\mathcal{E}\}$. A graph $\mathcal{G}$ is strongly connected if there exists a directed path between $\forall i,j\in\mathcal{N}, i\neq j$. Given a set $\{\boldsymbol{G}_1,\boldsymbol{G}_2,\cdots,\boldsymbol{G}_N\}$ of matrices with $\boldsymbol{G}_i\in\mathbb{R}^{m\times n}$, we use $\mathrm{col}(\boldsymbol{G}_1,\boldsymbol{G}_2,\cdots,\boldsymbol{G}_N)$ to denote the stacked matrix $[\boldsymbol{G}_1^\top,\boldsymbol{G}_2^\top,\cdots,\boldsymbol{G}_N^\top]^\top\in\mathbb{R}^{Nm\times n}$ and $\mathrm{diag}(\boldsymbol{G}_1,\boldsymbol{G}_2,\cdots,\boldsymbol{G}_N)\in\mathbb{R}^{Nm\times Nn}$ to denote the block diagonal matrix with the $\boldsymbol{G}$'s along the diagonal. The following definitions will also be used $\mathrm{col}_{i\in\mathcal{N}}(\boldsymbol{G}_i)\triangleq\mathrm{col}(\boldsymbol{G}_1,\boldsymbol{G}_2,\cdots,\boldsymbol{G}_N)$ and $\mathrm{diag}_{i\in\mathcal{N}}(\boldsymbol{G}_i)\triangleq\mathrm{diag}(\boldsymbol{G}_1,\boldsymbol{G}_2,\cdots,\boldsymbol{G}_N)$. $|\mathcal{N}|$ defines the cardinality of the set. $\mathrm{obsv}(\cdot,\cdot)$ and $\mathrm{rank}(\cdot)$ are used to define the observability matrix of the given system and matrix rank, respectively.

Consider the following continuous LTI system

$$\dot{\boldsymbol{x}}=\boldsymbol{A}\boldsymbol{x},\ \boldsymbol{y}=\boldsymbol{C}\boldsymbol{x} \tag{7.1}$$

where $\boldsymbol{x}\in\mathbb{R}^n$ is the state and $\boldsymbol{y}\in\mathbb{R}^m$ is the output, $\boldsymbol{A}\in\mathbb{R}^{n\times n},\boldsymbol{C}\in\mathbb{R}^{m\times n}$. The system (7.1) is sensed by N distributed agents $\boldsymbol{y}_i=\boldsymbol{C}_i\boldsymbol{x}$ with $\boldsymbol{y}=\mathrm{col}(\boldsymbol{y}_1,\boldsymbol{y}_2,\cdots,\boldsymbol{y}_N)$ where $\boldsymbol{y}_i\in\mathbb{R}^{m_i}$, $\sum_{i=1}^N m_i=m$ and $\boldsymbol{C}=\mathrm{col}(\boldsymbol{C}_1,\boldsymbol{C}_2,\cdots,\boldsymbol{C}_N)$. For each node/subsystem $i\in\mathcal{N}$, $\boldsymbol{y}_i$ is the only output that is available for node i. Neighbour relations between distinct pairs of agents are characterised by a directed graph $\mathcal{G}$. We assume throughout that $\boldsymbol{C}_i\neq 0,\forall i\in\mathcal{N}$ and $\boldsymbol{C}_i\neq\boldsymbol{C}_j$, $i\neq j$, $i,j\in\mathcal{N}$. For the sake of further analysis, let $\mathcal{O}\triangleq\mathrm{obsv}(\boldsymbol{A},\boldsymbol{C})$ and $\mathcal{O}_i\triangleq\mathrm{obsv}(\boldsymbol{A},\boldsymbol{C}_i)$ be the observability matrices of the pair $(\boldsymbol{A},\boldsymbol{C})$ and $(\boldsymbol{A},\boldsymbol{C}_i)$, respectively. The date transmission between agents may be impact by time-varying delays.

Assumption 7.1. *The pair $(\boldsymbol{A},\boldsymbol{C})$ is observable, but the pair $(\boldsymbol{A},\boldsymbol{C}_i)$ is not fully observable.*

The problem investigated in this article is defined as follows.

Problem 7.1. *Given the system* (7.1) *subject to a communication topology $\mathcal{G}$, how to design a distributed observer with the estimated state $\hat{\boldsymbol{x}}_i$, $\forall i\in\mathcal{N}$, such that the estimation error goes to 0 within a fixed time,*

$$|\hat{\boldsymbol{x}}_i(t)-\boldsymbol{x}(t)|=0,\ \forall t\geq\overline{\tau} \tag{7.2}$$

where $\overline{\tau} \in \mathbb{R}_{>0}$ is a known finite time.

7.2.2 The Volterra Operator and BF-NK

Volterra operator and non-asymptotic kernel functions are the key tools to the observer design in the chapter. To introduce later a distributed fixed-time observer, here we briefly recall the basic concepts [123].

Given a function belongs to the Hilbert space of locally integrable function with domain $\mathbb{R}_{\geq 0}$ and range $\mathbb{R}$, i.e., $w \in \mathcal{L}^2_{loc}(\mathbb{R}_{\geq 0})$, its image by the *Volterra operator* V_K induced by a Hilbert-Schmidt ($\mathcal{HS}$) Kernel Function $K : \mathbb{R} \times \mathbb{R} \to \mathbb{R}$ is denoted by $[V_K w]$ of the form

$$[V_K w]\,(t) \triangleq \int_0^t K(t,\tau) w(\tau) d\tau, \quad t \in \mathbb{R}_{\geq 0}$$

Definition 7.1 (BF-NK). *[123] If a kernel $K \in \mathcal{HS}$ which is at least $(i-1)$th order differentiable with respect to the second argument, verifies the conditions $K^{(j)}(t,0) = 0, \forall t \in \mathbb{R}_{\geq 0}$ and $K^{(j)}(t,t) \neq 0, \forall t \neq 0$ for all $j \in \{0, 1, \cdots, i-1\}$, it is called an ith order Bivariate Feedthrough Non-asymptotic Kernel (BF-NK).*

Lemma 7.1. *[178] For a given $i \geq 0$, consider a signal defined as a function of time $w \in \mathcal{L}^2(\mathbb{R}_{\geq 0})$ that admits the ith derivative in $\mathbb{R}_{\geq 0}$ and a kernel function $K \in \mathcal{HS}$, having the ith derivative with respect to the second argument, denoted as K. After successive integral by parts, it holds that*

$$\begin{aligned}\left[V_K w^{(i)}\right](t) = \sum_{j=0}^{i-1} (-1)^{i-j-1} w^{(j)}(t) K^{(i-j-1)}(t,t) \\ + \sum_{j=0}^{i-1} (-1)^{i-j} w^{(j)}(0) K^{(i-j-1)}(t,0) + (-1)^i \left[V_{K^{(i)}} w\right](t) \end{aligned} \tag{7.3}$$

which shows the function $\left[V_K w^{(i)}\right](t)$ is non-anticipative with respect to the lower-order derivatives $w, w^{(1)}, \cdots, w^{(i-1)}$.

Owing to the definition of the BF-NK, induced by a BF-NK K_h, the Volterra image (7.3) reduces to

$$\left[V_K w^{(i)}\right](t) = \sum_{j=0}^{i-1} (-1)^{i-j-1} w^{(j)}(t) K^{(i-j-1)}(t,t) + (-1)^i \left[V_{K^{(i)}} w\right](t) \tag{7.4}$$

A typical class of δth order BF-NKs that we will use in this chapter have the form of

$$K_h(t,\tau) = e^{-\omega_h(t-\tau)} \left(1 - e^{-\overline{\omega}\tau}\right)^{\delta}$$

which is parameterised by $\omega_h \in \mathbb{R}_{>0}$ and $\overline{\omega} \in \mathbb{R}_{>0}$. As it can be seen, all the non-asymptotic conditions up to the δ-th order are met thanks to the factor $(1 - e^{-\bar{\omega}\tau})^{\delta}$ regardless of the choice of ω_h and $\bar{\omega}$.

The Volterra image signal $\left[\mathcal{V}_{K_h^{(i)}} w\right](t), \forall\, i \in \{1, 2, \cdots, \delta\}$ can be obtained as the output of a linear time-varying scalar system. Letting $\xi(t) = \left[\mathcal{V}_{K_h^{(i)}} w\right](t)$, we have that

$$\dot{\xi}(t) = K_h^{(i)}(t,t) w(t) + \int_0^t \left(\frac{\partial}{\partial t} K_h^{(i)}(t,\tau)\right) w(\tau) d\tau - \omega_h \xi(t) + K_h^{(i)}(t,t) w(t) \tag{7.5}$$

with $\xi(0) = 0$. Being $K_h^{(i)}(t,t)$ bounded and ω strictly positive, it holds that the scalar dynamical system realization of the Volterra operators induced by the proposed kernels is BIBO stable with respect to w.

7.3 Fixed-Time Convergent Distributed Observer

In this section, the solution method to Problem 7.1 is presented. In the first instance, data transmission and communication delays within the sensor network are omitted. Under such a condition, a new distributed observer framework is designed. Then, the algorithm is modified to accommodate various network delays.

7.3.1 Delay-Free Case

From Assumption 7.1, the state vector $\boldsymbol{x}$ is not fully observable from a single sensor node. Nevertheless, by resorting to the commonly used observability decomposition technique of each subsystem [5, 168, 175], it is possible to partially estimate $\boldsymbol{x}$. Let n_i denotes the rank of the observability matrix of $(\boldsymbol{A}, \boldsymbol{C}_i)$, that is $n_i \triangleq \operatorname{rank}(\mathcal{O}_i) < n$. There exists an orthogonal matrix $\boldsymbol{T}_i \in \mathbb{R}^{n\times n}$ that enables the state transformation, $\bar{\boldsymbol{x}}_i = \boldsymbol{T}_i\boldsymbol{x}$, and $\bar{\boldsymbol{x}}_i$ admits the following decomposition $\bar{\boldsymbol{x}}_i = \begin{bmatrix} \bar{\boldsymbol{x}}_{io} & \bar{\boldsymbol{x}}_{iu} \end{bmatrix}^\top = \begin{bmatrix} \boldsymbol{T}_{io} & \boldsymbol{T}_{iu} \end{bmatrix}^\top \boldsymbol{x}$, where $\bar{\boldsymbol{x}}_{io}$ represents the observable part and $\bar{\boldsymbol{x}}_{iu}$ stands for the unobservable part. The dynamics of $\bar{\boldsymbol{x}}_i$ follows $\dot{\bar{\boldsymbol{x}}}_i = \bar{\boldsymbol{A}}_i\bar{\boldsymbol{x}}_i$, $\boldsymbol{y}_i = \bar{\boldsymbol{C}}_i\bar{\boldsymbol{x}}_i$, where

$$\bar{\boldsymbol{A}}_i = \boldsymbol{T}_i\boldsymbol{A}\boldsymbol{T}_i^\top = \begin{bmatrix} \boldsymbol{A}_{io} & \boldsymbol{0} \\ \boldsymbol{A}_{ir} & \boldsymbol{A}_{iu} \end{bmatrix}, \bar{\boldsymbol{C}}_i = \boldsymbol{C}_i\boldsymbol{T}_i^\top = \begin{bmatrix} \boldsymbol{C}_{io} & \boldsymbol{0} \end{bmatrix} \tag{7.6}$$

with $\boldsymbol{A}_{io} \in \mathbb{R}^{n_i\times n_i}$, $\boldsymbol{A}_{iu} \in \mathbb{R}^{(n-n_i)\times(n-n_i)}$, $\boldsymbol{A}_{ir} \in \mathbb{R}^{(n-n_i)\times n_i}$, $\boldsymbol{C}_{io} \in \mathbb{R}^{m_i\times n_i}$, , $\boldsymbol{T}_{io} \in \mathbb{R}^{n_i\times n}$, $\boldsymbol{T}_{iu} \in \mathbb{R}^{(n-n_i)\times n}$. Furthermore, $(\boldsymbol{A}_{io}, \boldsymbol{C}_{io})$ is observable, and the dynamics of the observer part is governed by

$$\dot{\bar{\boldsymbol{x}}}_{io} = \boldsymbol{A}_{io}\bar{\boldsymbol{x}}_{io},\ \boldsymbol{y}_i = \boldsymbol{C}_{io}\bar{\boldsymbol{x}}_{io}\,. \tag{7.7}$$

Next, a finite and fixed time convergent observer [123] is applied to estimate the observable part $\bar{\boldsymbol{x}}_{io} \in \mathbb{R}^{n_i}$, which will then be used to recover the full state vector through communication.

Thanks to the observability of $(\boldsymbol{A}_{io}, \boldsymbol{C}_{io})$, there exists a linear coordinates transformation $\boldsymbol{z}_i = \boldsymbol{T}_{iz}\bar{\boldsymbol{x}}_{io}$ with $\boldsymbol{T}_{iz} \in \mathbb{R}^{n_i\times n_i}$ such that the system (7.7) can be rewritten in the observer canonical form with respect to $\boldsymbol{z}_i$

$$\dot{\boldsymbol{z}}_i = \boldsymbol{A}_{i,z}\boldsymbol{z}_i,\ y_i = \boldsymbol{C}_{i,z}\boldsymbol{z}_i \tag{7.8}$$

where

$$\boldsymbol{A}_{i,z} = \boldsymbol{T}_{iz}\boldsymbol{A}_{io}\boldsymbol{T}_{iz}^{-1} = \begin{bmatrix} a_{n_i-1} & 1 & \cdots & 0 \\ \vdots & \vdots & \ddots & \vdots \\ a_1 & 0 & \cdots & 1 \\ a_0 & 0 & \cdots & 0 \end{bmatrix}$$

For simplicity, we herein assume (7.7) to be a single-output system, thereby $\boldsymbol{C}_{i,z} = \begin{bmatrix} 1 & 0 & \cdots & 0 \end{bmatrix}$. However, the method is not limited to single-output systems as the state vector of a multi-output observable system can be estimated by multiple observers individually designed for each single output utilising, for example, the technique described in Lemma 9.4.4 of [179]. The canonical-form subsystem (7.8) admits the following input-output realization

$$y_i^{(n_i)} = \sum_{p=0}^{n_i-1} a_p y_i^{(p)} \tag{7.9}$$

Let us consider the Volterra integral operator induced by $K_i = e^{-\omega_{i,h}(t-\tau)}\left(1 - e^{-\bar{\omega}_i \tau}\right)^{n_i}$, an n_i-th order BF-NK. Applying the Volterra integral operator introduced in Section 7.2.2 and recalling (7.4) for (7.9), we obtain

$$\begin{aligned} &\sum_{p=0}^{n_i-1} (-1)^{n_i-p-1} y_i^{(p)} K_i^{(n_i-p-1)}(t,t) + (-1)^{n_i}\left[V_{K_i^{(n_i)}} y_i\right](t) = \\ &\sum_{q=0}^{n_i-1} a_q \left((-1)^q \left[V_{K_i^{(q)}} y_i\right](t) + \sum_{p=0}^{q-1} (-1)^{p+q-1} y_i^p K_i^{q-p-1}(t,t) \right) \end{aligned} \tag{7.10}$$

Then, for all $r \in \{0, \cdots, n_i - 1\}$, the r-th state variable of (7.8) has the form of $z_{i,r} = y_i^{(r)} - \sum_{p=0}^{r-1} a_{n_i-r+p} y_i^{(p)}$, in terms of which we rearrange (7.10) after cumbersome algebra

$$\lambda_i = \boldsymbol{\gamma}_i \boldsymbol{z}_i \tag{7.11}$$

$$\lambda_i \triangleq (-1)^{n_i-1}\left[V_{K_i^{(n_i)}}y_i\right] + \sum_{p=0}^{n_i-1} a_p(-1)^p\left[V_{K_i^{(p)}}y_i\right]$$
$$\boldsymbol{\gamma}_i \triangleq \left[(-1)^{n_i-1}K_i^{(n_i-1)}(t,t),\cdots,K_i(t,t)\right]$$

Eq. (7.11) cannot be solved directly due to the rank-deficiency. However, by using n_i BF-NKs $K_{i,h}(t,\tau)$ with different $\omega_{i,h}$, $h \in \{0,\cdots,n_i-1\}$ but identical $\bar{\omega}_i$, it is possible to augment (7.11) into a matrix form

$$\boldsymbol{\Lambda}_i = \boldsymbol{\Gamma}_i\boldsymbol{z}_i \tag{7.12}$$

where $\boldsymbol{\Lambda}_i = [\lambda_{i,0},\lambda_{i,1},\cdots,\lambda_{i,n_i-1}]^\top$ and $\boldsymbol{\Gamma}_i = \left[\boldsymbol{\gamma}_{i,0}^\top,\boldsymbol{\gamma}_{i,1}^\top,\cdots,\boldsymbol{\gamma}_{i,n_i-1}^\top\right]^\top$. In addition, all transformed signals $\left[V_{K_{i,h}^{(p)}}y_i\right], \forall h \in \{0,\cdots,n_i-1\}, \forall p \in \{0,\cdots,n_i\}$ can be computed by (7.5). The invertibility of $\boldsymbol{\Gamma}$ is guaranteed for all $t>0$ thanks to the properties of the BF-NK [124, 180]. Therefore, the observable state vector is estimated by (7.8):

$$\hat{\boldsymbol{z}}_i = \boldsymbol{\Gamma}_i^{-1}\boldsymbol{\Lambda}_i, \forall t \geq t_\delta \tag{7.13}$$

where t_δ is a small time instant, provided that $\boldsymbol{\Gamma}_i$ is invertible for any $t \geq t_\delta$, so as to circumvent the singularity $\boldsymbol{\Gamma}_i(0) = 0$ as $K_{i,h}^{(h-1)}(0,0) = 0$. Note that, in the proposed distributed observer, t_δ is set uniformly across all agents whereas the kernel functions for each agent are independently designed.

From the coordinate transformations $\boldsymbol{T}_{i\alpha} \triangleq \boldsymbol{T}_{iz}\boldsymbol{T}_{io} \in \mathbb{R}^{n_i\times n}$, which is known, it is immediate to obtain:

$$\boldsymbol{z}_i = \boldsymbol{T}_{i\alpha}\boldsymbol{x}, \ \forall i \in \mathcal{N} \tag{7.14}$$

As $\boldsymbol{T}_{i\alpha}$ is not invertible, the global state vector $\boldsymbol{x}$ can not be estimated from local state estimate $\hat{\boldsymbol{z}}$ via (7.14) without further information. To establish the intercommunication requirements, the following results are shown.

Lemma 7.2 (Sylvester inequality). *[181] Let $\boldsymbol{G} \in \mathbb{R}^{m\times n}$ and $\boldsymbol{H} \in \mathbb{R}^{n\times p}$, it holds that*

$\text{rank}(\boldsymbol{G}) + \text{rank}(\boldsymbol{H}) - n \leq \text{rank}(\boldsymbol{GH}) \leq \min\{\text{rank}(\boldsymbol{G}), \text{rank}(\boldsymbol{H})\}$.

Proposition 7.1. *For any subset $\mathcal{N}_s \subset \mathcal{N}$, the observable matrix* $\text{obsv}\,(\boldsymbol{A}, \text{col}_{i\in\mathcal{N}_s}(\boldsymbol{C}_i))$ *determined by $(\boldsymbol{A}, \text{col}_{i\in\mathcal{N}_s}(\boldsymbol{C}_i))$ satisfies the following condition:*

$$\text{rank}\big(\text{obsv}\,(\boldsymbol{A}, \text{col}_{i\in\mathcal{N}_s}(\boldsymbol{C}_i))\,\big) = \text{rank}\big(\text{col}_{i\in\mathcal{N}_s}(\boldsymbol{T}_{i\alpha})\big).$$

Proof. From the definition of $\boldsymbol{T}_{i\alpha}$, we have $\text{col}_{i\in\mathcal{N}_s}(\boldsymbol{T}_{i\alpha}) = \text{diag}_{i\in\mathcal{N}_s}(\boldsymbol{T}_{iz})\text{col}_{i\in\mathcal{N}_s}(\boldsymbol{T}_{io})$. Owing to the decomposition (7.6),

$$\text{rank}[\text{col}_{i\in\mathcal{N}_s}(\boldsymbol{T}_{io})] = \text{rank}[\text{obsv}(\boldsymbol{A}, \text{col}_{i\in\mathcal{N}_s}(\boldsymbol{C}_i))]$$

From Lemma 7.2 and the fact that $\boldsymbol{T}_{iz}$ is full rank, we have

$$\begin{aligned}
&\text{rank}[\text{diag}_{i\in\mathcal{N}_s}(\boldsymbol{T}_{iz})] + \text{rank}[\text{col}_{i\in\mathcal{N}_s}(\boldsymbol{T}_{io})] - \sum_{i\in\mathcal{N}_s} n_i \\
&\leq \text{rank}[\text{col}_{i\in\mathcal{N}_s}(\boldsymbol{T}_{i\alpha})] = \text{rank}[\text{diag}_{i\in\mathcal{N}_s}(\boldsymbol{T}_{iz})\text{col}_{i\in\mathcal{N}_s}(\boldsymbol{T}_{io})] \\
&\leq \min\{\text{rank}[\text{diag}_{i\in\mathcal{N}_s}(\boldsymbol{T}_{iz})], \text{rank}[\text{col}_{i\in\mathcal{N}_s}(\boldsymbol{T}_{io})]\} \\
&\qquad\qquad\qquad\qquad \Downarrow\ (a) \\
&\text{rank}[\text{col}_{i\in\mathcal{N}_s}(\boldsymbol{T}_{io})] \leq \text{rank}[\text{col}_{i\in\mathcal{N}_s}(\boldsymbol{T}_{i\alpha})] \leq \text{rank}[\text{col}_{i\in\mathcal{N}_s}(\boldsymbol{T}_{io})] \\
&\qquad\qquad\qquad\qquad \Downarrow \\
&\text{rank}[\text{col}_{i\in\mathcal{N}_s}(\boldsymbol{T}_{i\alpha})] = \text{rank}[\text{col}_{i\in\mathcal{N}_s}(\boldsymbol{T}_{io})] = \text{rank}[\text{obsv}(\boldsymbol{A}, \text{col}_{i\in\mathcal{N}_s}(\boldsymbol{C}_i))]
\end{aligned}$$

where (a) comes from the fact that

$$\max_{i\in\mathcal{N}_s} n_i \leq \text{rank}[\text{col}_{i\in\mathcal{N}_s}(\boldsymbol{T}_{io})] \leq \text{rank}[\text{diag}_{i\in\mathcal{N}_s}(\boldsymbol{T}_{iz})] = \sum_{i\in\mathcal{N}_s} n_i$$

This completes the proof. □

Proposition 7.1 bridges the gap between traditional observability conditions based on the system matrices and the invertibility of the transformation matrix $\boldsymbol{T}_{i\alpha}$, which is instrumental for the following analysis.

Lemma 7.3. *[182] For a given directed graph $\mathcal{G} = \{\mathcal{N}, \mathcal{E}, \mathcal{A}\}$, $\mathcal{C} = [c_{ij}] \in \mathbb{R}^{N\times\ N} = \mathcal{A}^L$ denotes the Lth power of the adjacency matrix, then c_{ij} is equal to the number of available paths from node i to node j in L steps (across L edges).*

From Lemma 7.3, we define $\mathcal{D}^L = \text{bool}\left(\sum_{i=1}^{L} \mathcal{A}^i\right)$ the L-step data flow matrix with bool$(\cdot)$ the boolean function, and the non-zero elements in $\mathcal{D}^L(:,i)$ (ith column of $\mathcal{D}^L$) indicate the nodes available to node i in L steps. Let $\mathcal{N}_i^L \subseteq \mathcal{N} \setminus i$, $\forall i \in \mathcal{N}$ be the L-step reachable set of node i with $\mathcal{N}_i^0 = \emptyset$. Note that $\mathcal{N}_i^L$ can be inferred from $\mathcal{D}^L$ by $\mathcal{N}_i^L = \{i | \mathcal{D}^L(:,i) \neq 0\}$.

Without considering the network delays, each subsystem i is able to acquire $\boldsymbol{T}_{j\alpha}$ and up-to-date local state estimate $\hat{\boldsymbol{z}}_j$ from any other sensor node $j \in \mathcal{N}_i^L$ through cross-agent communication. Next, we introduce a definition and a necessary assumption for the solvability of Problem 7.1.

Definition 7.2 (Complementary Neighbouring (CN) set)**.** *Assume $\mathcal{CN}_i \subseteq \mathcal{N}_i^L$, $\forall\, L$, it is said to be a CN set of node i if the matrix $\begin{bmatrix} \boldsymbol{T}_{i\alpha} \\ \text{col}_{j\in\mathcal{CN}_i}(\boldsymbol{T}_{j\alpha}) \end{bmatrix} \in \mathbb{R}^{(\sum n_j + n_i)\times n}$ is full rank, i.e.,*

$$\text{rank}\left(\begin{bmatrix} \boldsymbol{T}_{i\alpha} \\ \text{col}_{j\in\mathcal{CN}_i}(\boldsymbol{T}_{j\alpha}) \end{bmatrix}\right) = n\,. \tag{7.15}$$

Assumption 7.2. *Each node $i \in \mathcal{N}$ of the system* (7.1) *has at least one CN set.*

As it can be noticed, the common assumptions of strongly connected graphs [5, 6, 177] are relaxed in this chapter by Assumption 7.2, which can hold in the absence of strong connectivity. Assumption 7.2 guarantees the existence of a CN set for each node. Nevertheless, without imposing further constraints, for any agent i, its CN set may not be unique and redundant information might be exchanged. In sequel, we show how to find a class of optimised CN sets $\boldsymbol{\mathcal{CN}}^{opt} = \{\mathcal{CN}_1^{opt}, \cdots, \mathcal{CN}_N^{opt}\}$ in terms of the communication cost for the proposed distributed observer, and how to avoid redundant data exchange.

Assumption 7.3. *The graph $\mathcal{G}$ modelling the communication network of the distributed system* (7.1) *has an equal communication cost across all edges.*

Consider h_i^L the L-step neighbouring set of node i required for exchanging data (possibly cross-agent) with agent i, $\min \left|\mathcal{CN}_i^{opt}\right|$ is found according to

$$\{h_i^1, h_i^2, \cdots, h_i^P\} = \underset{h_i^L \subseteq \mathcal{N}_i^L}{\arg\min} \left|\mathcal{CN}_i^{opt}\right|, \text{ such thatrank}\left(\begin{bmatrix} \boldsymbol{T}_{i\alpha} \\ \mathrm{col}_{j\in\mathcal{CN}_i^{opt}}(\boldsymbol{T}_{j\alpha}) \end{bmatrix}\right) = n \tag{7.16}$$

provided $P < |\mathcal{N}|$ the minimum step value to ensure the rank condition, such that

$$\mathrm{rank}\left(\begin{bmatrix} \boldsymbol{T}_{i\alpha} \\ \mathrm{col}_{j\in\mathcal{N}_i^P}(\boldsymbol{T}_{j\alpha}) \end{bmatrix}\right) = n > \mathrm{rank}\left(\begin{bmatrix} \boldsymbol{T}_{i\alpha} \\ \mathrm{col}_{j\in\mathcal{N}_i^{P-1}}(\boldsymbol{T}_{j\alpha}) \end{bmatrix}\right),$$

It is worth noting that the optimisation problem (7.16) does not necessarily lead to the minimum $\left|\mathcal{CN}_i^{opt}\right|$ in a global sense as a smaller $\left|\mathcal{CN}_i^{opt}\right|$ may be obtained by searching up to a step value great than P. However, by constraining the outreach step value at P, it is beneficial for mitigating the impact of cross-agent communication delay, as will be discussed later on in Section 7.3.2. By (7.16), we provide the offline optimisation algorithm for the selection of a CN set as summarised in Algorithm 7.1. It is noteworthy that under Assumption 7.3, the solution to the optimisation problem (7.16) may not be unique unless additional constraints are imposed. Moreover, in case that $\sum_j n_j > n - n_i$, $j \in \mathcal{CN}_i^{opt}$, the matrix $\begin{bmatrix} \boldsymbol{T}_{i\alpha} \\ \mathrm{col}_{j\in\mathcal{CN}_i^{opt}}(\boldsymbol{T}_{j\alpha}) \end{bmatrix}$ has more than n rows, which implies information redundancy. In this context, Algorithm 7.1 also extracts $n - n_i$ rows from $\mathrm{col}_{j\in\mathcal{CN}_i^{opt}}(\boldsymbol{T}_{j\alpha}) \in \mathbb{R}^{\sum_j n_j \times n}$, such that the resulting matrix $\begin{bmatrix} \boldsymbol{T}_{i\alpha} \\ \mathrm{col}_{j\in\mathcal{CN}_i^{opt}}(\boldsymbol{T}^*_{j\alpha}) \end{bmatrix} \in \mathbb{R}^{n\times n}$ with $\boldsymbol{T}^*_{j\alpha}$ the extracted row elements from $\boldsymbol{T}_{j\alpha}$, is rank of n.

Remark 7.1. *Algorithm 7.1 optimises the communication network under Assumption 3, which assumes a uniform weight across all edges. A more general framework can be modelled by utilising a weighted communication graph, where each edge is assigned a weight associated with an individual communication cost. This calls for an optimisation of the information exchange architecture to minimise the aggregated cost from* 1*-step reachable set to* P*-step reachable set rather than the cost for the* P*th step only as* (7.16)*, provided* P *the minimum step number to render the full rank condition* (7.15)*. A detailed discussion of this subject is beyond the scope*

Algorithm 7.1: Offline Optimisation of Data Acquisition Scheme

Input: system matrices $\boldsymbol{A}$ and $\boldsymbol{C}$; graph adjacency matrix $\mathcal{A}$; node number N
Output: optimised CN sets $\boldsymbol{\mathcal{CN}}^{opt}$

Initialisation: iteration index $k = 1, l = 1$;
while $\boldsymbol{\mathcal{CN}}^{opt}$ *is not obtained* **do**
  calculate $\mathcal{D}^l$;
  for $k \leftarrow 1$ **to** N **do**
    if $\mathcal{CN}_k^{opt}$ *is not obtained* **then**
      calculate $\mathcal{N}_k^l$ based on $\mathcal{D}^l$;
      optimise $\mathcal{CN}_k^{opt}$ using (7.16) and identify $\boldsymbol{T}_{j\alpha}^*$;
    end
  end
  $l = l + 1$;
end

of the present article, but it is envisaged to be done in future work.

As $\boldsymbol{T}_{j\alpha}^*$, $\forall j \in \mathcal{CN}_i^{opt}$ is determined offline, it is known to each node i when the communication network is initialised. Furthermore, the data sets required by each node i in real-time for global state observation is defined as

$$\mathcal{I}_{ij} = \{\hat{\boldsymbol{z}}_j^*\}, \, \forall j \in \mathcal{CN}_i^{opt} \tag{7.17}$$

where $\hat{\boldsymbol{z}}_j^*$ the local estimate of the $\boldsymbol{z}_j^*$ that fulfils $\boldsymbol{z}_j^* = \boldsymbol{T}_{j\alpha}^*\boldsymbol{x}$.

In view of the linear relation (7.14), each agent i can obtain the full state vector by

$$\hat{\boldsymbol{x}}_i = \begin{bmatrix} \boldsymbol{T}_{i\alpha} \\ \mathrm{col}_{j\in\mathcal{CN}_i^{opt}}(\boldsymbol{T}_{j\alpha}^*) \end{bmatrix}^{-1} \begin{bmatrix} \hat{\boldsymbol{z}}_i \\ \mathrm{col}_{j\in\mathcal{CN}_i^{opt}}(\hat{\boldsymbol{z}}_j^*) \end{bmatrix}, \forall t > 0 \tag{7.18}$$

provided the data sets $\mathcal{I}_{ij}$, $\forall j \in \mathcal{CN}_i^{opt}$ via communication. Hence, the fixed-time convergent condition (7.2) can be achieved. However, in practice, due to the various delays consist in the network, (7.18) will not work without further provisions, which will be provided in the next subsection.

7.3.2 Delayed Case

We now have all the ingredients to propose our main algorithm for the practical case, where network delays exist. For the sake of further analysis, let τ_{ij} be the time-varying delay consists in gathering the information set $\mathcal{I}_{ij}$ from j.

Assumption 7.4. *For any $i \in \mathcal{N}$, the accumulated delay is bounded, such that $\sum_j \tau_{ij} \leq \overline{\tau}$, $\forall j \in \mathcal{CN}_i^{opt}$, with $\overline{\tau}$ a known positive constant.*

Under Assumption 7.4, we assume that all the sensor nodes and observers have synchronized clocks and include time-stamps in the date transmission [183]. As such, each node i can identify at $t \geq \overline{\tau}$ a set of $\mathcal{I}_{ij}(t-\overline{\tau})$, $\forall j \in \mathcal{CN}_i^{opt}$ with synchronized delay. Combined with $\hat{\boldsymbol{z}}_i(t-\overline{\tau})$ the distributed observer can be designed, as shown in the following theorem.

Theorem 7.1 (Distributed Fixed-Time Observer)**.** *Under Assumptions 7.1, 7.2 and 7.4, given the distributed system* (7.1)*, the fixed-time estimation scheme* (7.13) *and the intercommunication mechanism determined by Algorithm 7.1, for each node $i \in \mathcal{N}$, the local state estimate $\hat{\boldsymbol{x}}_i(t), \forall t \geq \overline{\tau} + t_\delta$ obtained by*

$$\hat{\boldsymbol{x}}_i(t) = e^{\boldsymbol{A}\overline{\tau}} \begin{bmatrix} \boldsymbol{T}_{i\alpha} \\ \mathrm{col}_{j \in \mathcal{CN}_i^{opt}}(\boldsymbol{T}_{j\alpha}^*) \end{bmatrix}^{-1} \begin{bmatrix} \hat{\boldsymbol{z}}_i(t-\overline{\tau}) \\ \mathrm{col}_{j \in \mathcal{CN}_i^{opt}}(\hat{\boldsymbol{z}}_j^*(t-\overline{\tau})) \end{bmatrix} \tag{7.19}$$

for all $t \geq \overline{\tau} + t_\delta$ is equal to $\boldsymbol{x}(t)$, such that the condition (7.2) *is fulfilled.*

Proof. Thanks to the finite-time local observers (7.13) that is activated at $t = t_\delta$ and the information sets $\mathcal{I}_{ij}$ received from the CN set, node i is able to reconstruct delayed estimates

$$\begin{bmatrix} \hat{\boldsymbol{z}}_i(t-\overline{\tau}) \\ \mathrm{col}_{j \in \mathcal{CN}_i^{opt}}(\hat{\boldsymbol{z}}_j^*(t-\overline{\tau})) \end{bmatrix} = \begin{bmatrix} \boldsymbol{z}_i(t-\overline{\tau}) \\ \mathrm{col}_{j \in \mathcal{CN}_i^{opt}}(\boldsymbol{z}_j^*(t-\overline{\tau})) \end{bmatrix}, \forall t \geq \overline{\tau} + t_\delta.$$

Hence, from (7.18) and (7.1), it is immediate to show the following relationship by using (7.19)

$$\hat{\boldsymbol{x}}_i(t) = e^{\boldsymbol{A}\overline{\tau}} \boldsymbol{x}(t-\overline{\tau}) = \boldsymbol{x}(t), \, \forall t \geq \overline{\tau} + t_\delta \tag{7.20}$$

which completes the proof. □

Remark 7.2. *In contrast to the existing distributed observers (e.g., Luenberger-like observers) where agents only communicate with their neighbours (i.e., $\mathcal{N}_i$), the proposed method relies on a cross-agent communication strategy which enables an agent i to communicate with $j \notin \mathcal{N}_i$. This feature enables the optimisation Algorithm 7.1, and the resulting data flow may turn out to be efficient and useful in practice to reduce communication load. More specifically, in the proposed distributed observer, the accumulated data flows into a node is of dimension $(n - n_i)$, thus the dimension of the data flow through a communication channel (i.e., an edge, in one direction) is below $(n - n_i)$. However, in Luenberger-like distributed observers [5], the data transmitted along any edge is of dimension n, and each node has to manage to collect $n|\mathcal{N}_i|$-dimensional data. Despite the delay introduced by the cross-agent communication, the influence of a bounded delay can be compensated using an open-loop prediction scheme.*

Remark 7.3. *With the proposed cross-agent communication strategy, the proposed estimation scheme remains valid if the outputs y_i are shared instead of the local state estimates $\hat{\boldsymbol{z}}_j$ (see Proposition 7.1 that builds the connection between conventional observability and the invertibility of the coordinate transformation from $\boldsymbol{x}$ to $\boldsymbol{z}$). Nevertheless, sharing the outputs directly may sacrifice privacy-preserving properties of the method. Particularly, when one or more sensors/communication links are attacked, it could expose more sensor nodes to the attacker. For this reason, the state estimate sharing strategy is adopted in the proposed framework. Moreover, the cross-agent communication strategy may be applied to either Luenberger-type asymptotic [5] or finite-time [6] observers, which can also leads to reduced communication as discussed in Remark 7.2.*

7.4 Robustness Analysis of the Observer

This section analyses the robustness of the proposed observer against measurement and process disturbances. Assuming the presence of the bounded model uncertainty and sensor disturbance,

$\|\boldsymbol{d}_x\|_\infty \le \bar{d}_x, \|\boldsymbol{d}_{y,i}\|_\infty \le \bar{d}_y$ in (7.1), such that

$$\dot{\boldsymbol{x}}_d = \boldsymbol{A}\boldsymbol{x}_d + \boldsymbol{d}_x,\ \boldsymbol{y}_d = \boldsymbol{C}\boldsymbol{x}_d + \boldsymbol{d}_y \tag{7.21}$$

where $\boldsymbol{x}_d$ denotes state variable under the effect of $\boldsymbol{d}_x(t)$. In this context, for ith subsystem it holds that $\dot{\bar{\boldsymbol{x}}}_{i,d} = \bar{\boldsymbol{A}}_i\bar{\boldsymbol{x}}_{i,d} + \boldsymbol{T}_i\boldsymbol{d}_x, y_{i,d} = \bar{\boldsymbol{C}}_i\bar{\boldsymbol{x}}_{i,d} + d_{y,i}$ where $\bar{\boldsymbol{x}}_{i,d} = [\bar{\boldsymbol{x}}_{io,d}^\top \quad \bar{\boldsymbol{x}}_{iu,d}^\top]^\top$. By analogy to (7.8), the observable part follows

$$\dot{\boldsymbol{z}}_{i,d} = \boldsymbol{A}_{i,z}\boldsymbol{z}_{i,d} + \boldsymbol{d}_{z,i}, \boldsymbol{y}_{i,d} = \boldsymbol{C}_{i,z}\boldsymbol{z}_{i,d} + d_{y,i}, \tag{7.22}$$

where $\boldsymbol{d}_{z,i} \triangleq \boldsymbol{T}_{i\alpha}\boldsymbol{d}_x = [d_{z,i,0}, \cdots, d_{z,i,n_i-1}]^\top \in \mathbb{R}^{n_i}$ and the disturbance-effected state variable satisfies the identity that

$$\boldsymbol{\gamma}_{i,h}\boldsymbol{z}_{i,d} = \lambda_{i,h,d} \tag{7.23}$$

with

$$\lambda_{i,h,d} =(-1)^{n_i-1}\left[V_{K_{i,h}^{(n_i)}}\boldsymbol{C}_{i,z}\boldsymbol{z}_{i,d}\right] + \sum_{p=0}^{n_i-1} a_p(-1)^p\left[V_{K_{i,h}^{(p)}}\boldsymbol{C}_{i,z}\boldsymbol{z}_{i,d}\right] + \sum_{p=0}^{n_i-1}(-1)^p\left[V_{K_{i,h}^{(p)}}d_{z,i,n_i-1-p}\right].$$

In the noisy environment, the state estimator (7.13) gives

$$\hat{\boldsymbol{z}}_{i,d} = \boldsymbol{\Gamma}_i^{-1}\hat{\boldsymbol{\Lambda}}_{i,d}, \forall t \ge t_\delta \tag{7.24}$$

where $\hat{\boldsymbol{\Lambda}}_{i,d} = \left[\hat{\lambda}_{i,0,d}, \hat{\lambda}_{i,1,d}, \cdots, \hat{\lambda}_{i,n_i-1,d}\right]^\top$ and

$$\hat{\lambda}_{i,h,d} =(-1)^{n_i-1}\left[V_{K_{i,h}^{(n_i)}}y_{i,d}\right] + \sum_{p=0}^{n_i-1} a_p(-1)^p\left[V_{K_{i,h}^{(p)}}y_{i,d}\right].$$

Comparing (7.23) and (7.24), the estimation error of $\boldsymbol{z}_{i,d}$ takes on the form

$$\boldsymbol{\epsilon}_{z,i} \triangleq \boldsymbol{z}_{i,h,d} - \hat{\boldsymbol{z}}_{i,h,d} = \boldsymbol{\Gamma}_i^{-1}\boldsymbol{\epsilon}_{\Lambda,i} \tag{7.25}$$

where $\boldsymbol{\epsilon}_{\Lambda,i} = [\epsilon_{\lambda_i,0}, \epsilon_{\lambda_i,1}, \cdots, \epsilon_{\lambda_i,n_i-1}]^\top$, and

$$\epsilon_{\lambda_i,h} \triangleq \lambda_{i,h} - \hat{\lambda}_{i,h} = \sum_{p=0}^{n_i-1}(-1)^p \left[V_{K_{i,h}^{(p)}} d_{z,i,n_i-1-p}\right] - (-1)^{n_i-1}\left[V_{K_{i,h}^{(n_i)}} d_{y,i}\right] - \sum_{p=0}^{n_i-1} a_p(-1)^p \left[V_{K_{i,h}^{(p)}} d_{y,i}\right].$$

The effects of both measurement noise $d_{y,i}$ and model uncertainty $\boldsymbol{d}_x$ are embedded in $\boldsymbol{\epsilon}_{\Lambda,i}$ in the form of Volterra images, i.e. $\left[V_{K_{i,h}^{(p)}} d_{y,i}\right] \triangleq \epsilon_{d_{y,i},p,h}$ and $\left[V_{K_{i,h}^{(p)}} d_{z,i,p}\right] \triangleq \epsilon_{d_{z,i},p,h}, p \in \{0, \cdots, n_i\}, h \in \{0, \cdots, n_i - 1\}$. Recall the transformation of the Volterra operator, $\epsilon_{d_y,p,h}$ is the output of the LTV system

$$\dot{\epsilon}_{d_y,p,h} = -\omega_h \epsilon_{d_y,p,h} + K_{i,h}^{(p)}(t,t) d_y \tag{7.26}$$

Thanks to the Bounded-Input-Bounded-Output(BIBO) feature of (7.26), effects of the measurement noise can be bounded by

$$|\epsilon_{d_{y,i},p,h}| \leq \left|\frac{1}{\omega_h}\overline{d}_{y,i} \sup_{0<\tau\leq t} K_{i,h}^{(p)}(\tau,\tau)\right| \triangleq \overline{\epsilon}_{d_{y,i},p,h}$$

In the same line of reasoning, the Volterra images of the model uncertainty $\boldsymbol{d}_{z,i}$ have the upper bound $\overline{\epsilon}_{d_{z,i},p,h} \triangleq \|\boldsymbol{T}_{i\alpha}\|_\infty \left|\frac{1}{\omega_h}\overline{d}_{x,i} \sup_{0<\tau\leq t} K_{i,h}^{(p)}(\tau,\tau)\right|$. Therefore, the overall upper bound of the state estimation error $\overline{\epsilon}_{\lambda_i,h}$ for all $h \in \{0, 1, \cdots, n_i - 1\}$ can be written as

$$|\epsilon_{\lambda_i,h}| \leq \overline{\epsilon}_{d_{y,i},n,h} + \sum_{p=0}^{n_i-1} |a_p|\overline{\epsilon}_{d_{y,i},p,h} + \sum_{p=0}^{n_i-1} \overline{\epsilon}_{d_{z,i},p,h} \triangleq \overline{\epsilon}_{\lambda_i,h}.$$

As such, by stacking $\overline{\epsilon}_{\lambda_i,h}$ induced by different kernels, one can obtain the vector bound as $\overline{\boldsymbol{\epsilon}}_{\Lambda,i} \triangleq [\overline{\epsilon}_{\lambda_i,0}, \cdots, \overline{\epsilon}_{\lambda_i,n_i-1}]^\top$. Consequently, the observation error defined in (7.25) is bounded by $\overline{\boldsymbol{\epsilon}}_{z_i} \leq \|\boldsymbol{\Gamma}_i^{-1}\|_\infty \overline{\boldsymbol{\epsilon}}_{\Lambda,i}$.

Taking the communication delay into account, the compensation in (7.19) writes

$$\hat{\boldsymbol{x}}_{i,d}(t) = e^{\boldsymbol{A}\overline{\tau}} \begin{bmatrix} \boldsymbol{T}_{i\alpha} \\ \mathrm{col}_{j\in\mathcal{CN}_i^{opt}}(\boldsymbol{T}_{j\alpha}^*) \end{bmatrix}^{-1} \begin{bmatrix} \hat{\boldsymbol{z}}_{i,d}(t-\overline{\tau}) \\ \mathrm{col}_{j\in\mathcal{CN}_i^{opt}}(\hat{\boldsymbol{z}}_{j,d}^*(t-\overline{\tau})) \end{bmatrix} \tag{7.27}$$

However, recalling (7.21), during the delay $\overline{\tau}$, $\boldsymbol{d}_x$ introduce extra effects that can be expressed as

$$\boldsymbol{\epsilon}_{dx,\overline{\tau}} = \int_{t-\overline{\tau}}^{t} e^{\boldsymbol{A}(t-\tau)}\boldsymbol{d}_x(\tau)d\tau \tag{7.28}$$

Being $\boldsymbol{A}$ Hurwitz, it is straightforward to conclude that $\epsilon_{dx,\overline{\tau}}$ is bounded with an upper bound $\overline{\epsilon}_{dx,\overline{\tau}} \geq \left\| \int_{t-\overline{\tau}}^{t} e^{\boldsymbol{A}(t-\tau)}\boldsymbol{d}_x(\tau)d\tau \right\|_{\infty}$.

Notably, for any $i \in \mathcal{N}$ in (7.18), $\boldsymbol{\Gamma}_i$ and $\boldsymbol{T}_{i\alpha}$ are not affected by model uncertainty and disturbances. Therefore, the distributed observation of $\boldsymbol{x}_{i,d}$ in (7.27) remains bounded as long as $\boldsymbol{d}_x, d_y$ are bounded, i.e., for all $t \geq \overline{\tau} + t_\delta$,

$$|\boldsymbol{\epsilon}_{\hat{x}_i}| \leq \begin{bmatrix} \boldsymbol{T}_{i\alpha} \\ \mathrm{col}_{j\in\mathcal{CN}_i^{opt}}(\boldsymbol{T}_{j\alpha}^{*}) \end{bmatrix}^{-1} \begin{bmatrix} \overline{\boldsymbol{\epsilon}}_{z_i} \\ \mathrm{col}_{j\in\mathcal{CN}_i^{opt}}(\overline{\boldsymbol{\epsilon}}_{z_j^*}) \end{bmatrix} + \overline{\epsilon}_{dx,\overline{\tau}}, \tag{7.29}$$

7.5 Numerical Examples

In this section, the effectiveness of the proposed distributed observer is examined by a few numerical examples. Consider a linear system [5] of order $n = 6$ with four local sensors, i.e., $N = 4$ and $[n_1\ n_2\ n_3\ n_4] = [2\ 5\ 1\ 5]$. System parameters are given as follows

$$\boldsymbol{A} = \begin{bmatrix} -1 & 0 & 0 & 0 & 0 & 0 \\ -1 & 1 & 1 & 0 & 0 & 0 \\ 1 & -2 & -1 & -1 & 1 & 1 \\ 0 & 0 & 0 & -1 & 0 & 0 \\ -8 & 1 & -1 & -1 & -2 & 0 \\ 4 & -0.5 & 0.5 & 0 & 0 & -4 \end{bmatrix}, \boldsymbol{C} = \left[\begin{array}{cccccc} 1 & 0 & 0 & 2 & 0 & 0 \\ 2 & 0 & 0 & 1 & 0 & 0 \\ \hdashline 2 & 0 & 1 & 0 & 0 & 1 \\ \hdashline 0 & 0 & 0 & 2 & 0 & 0 \\ \hdashline 1 & 0 & 2 & 0 & 0 & 0 \\ 2 & 0 & 4 & 0 & 0 & 0 \end{array}\right] = \begin{bmatrix} \boldsymbol{C}_1 \\ \boldsymbol{C}_2 \\ \boldsymbol{C}_3 \\ \boldsymbol{C}_4 \end{bmatrix}$$

with the communication network described by

$$\mathcal{A}=\begin{bmatrix}0&0&1&1\\1&0&1&0\\0&1&0&0\\1&0&0&0\end{bmatrix}. \tag{7.30}$$

From (7.30) and Algorithm 7.1, it is straightforward to obtain $\mathcal{CN}_1^{opt}=\{2\}$, $\mathcal{CN}_2^{opt}=\{3\}$, $\mathcal{CN}_3^{opt}=$

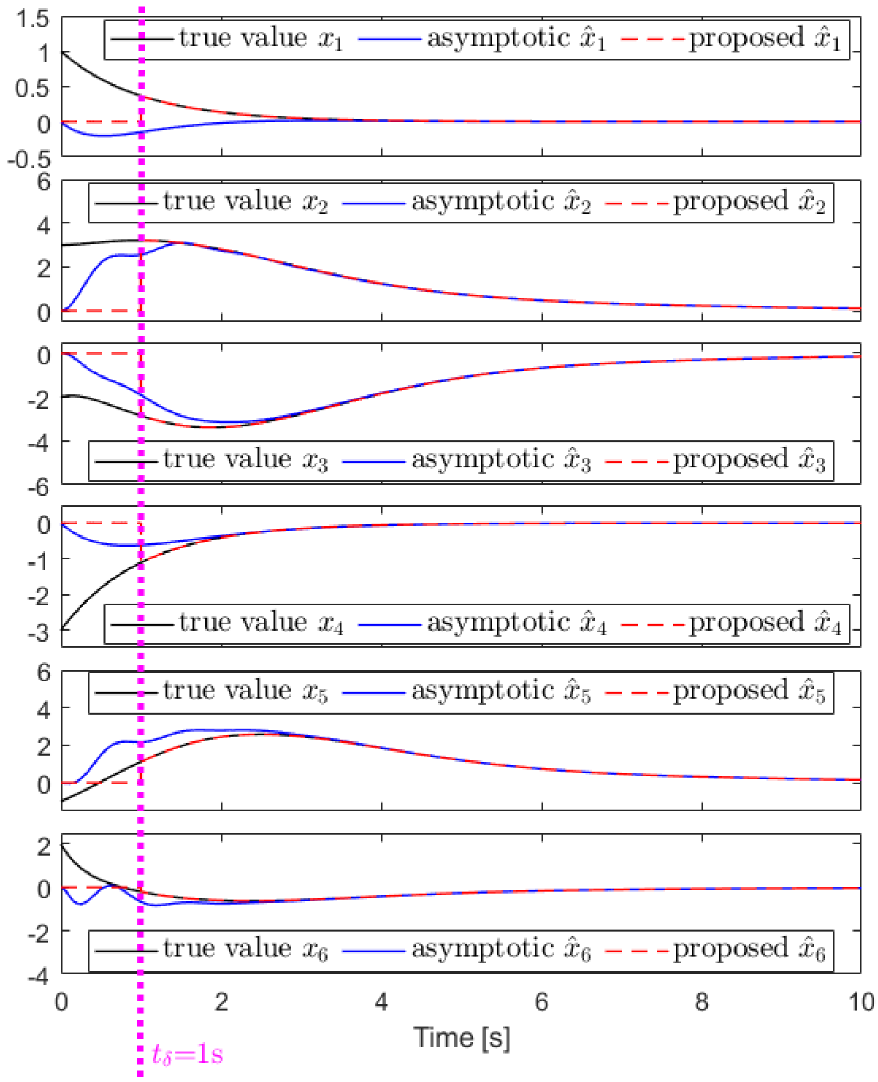

Figure 7.1: State estimates of method [5] and the proposed method in the delay-free and noise-free scenario.

$\{2\}$, $\mathcal{CN}_4^{opt}=\{1\}$. It is noteworthy that the redundant communication links which are $\{4\}$ in $\mathcal{CN}_1$ and $\{1\}$ in $\mathcal{CN}_2$ are removed at the design stage by Algorithm 7.1, thereby reducing the data transfer required by a distributed observer. Moreover, taking the subsystem 1 as an example, it does not require the full observable states of the subsystem 2 owing to the information redundancy $n_1 + n_2 > n$ as discussed in Section 7.3.1.

In the first instance, the communication delay is neglected throughout the network, and both process and measurement noises are not taken into account. The simulation results show that the state estimates of all agents can reach consensus immediately after the activation time $t_\delta = 1$s. For benchmarking purposes, the estimation results of the proposed method is compared with a recently proposed Luenberger-like approach [5]. Taking the 1st subsystem as an example, the comparative results are plotted in Figure 7.1. As it can be seen, all estimates of the proposed method converge to the actual state within a fixed time, showing a much faster convergence speed than the method in [5]. Next, a uniform delay is added to each network edge with an

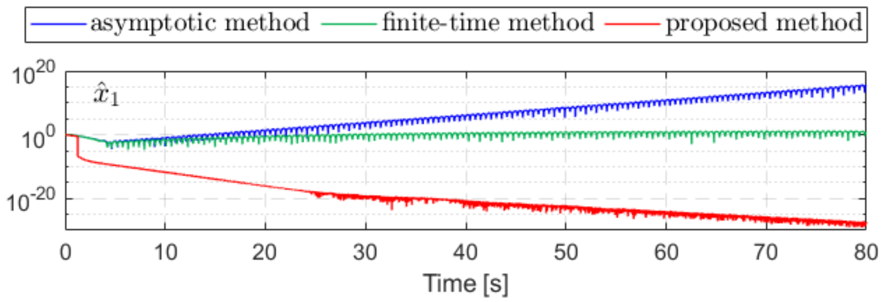

Figure 7.2: State estimation errors of methods [5, 6] and the proposed method in the delayed and noise-free scenario.

upper bound $\overline{\tau} = 0.27$s. In addition to [5], we further compare the proposed method with a finite-time distributed observer that has been shown robust against communication delays [6]. The errors of the state estimates are given in Figure 7.2. Under the delayed network, the asymptotic method [5] shows the non-convergent performance, while the error of the finite-time observer [6] stays bounded. However, the proposed method demonstrates its advantage in terms of dealing with network delays by showing the most accurate state estimation.

Finally, a noisy scenario is simulated where the outputs are corrupted by a uniformly distributed random noise within $[-0.2 \quad 0.2]$ and the system dynamic are perturbed by a sinusoidal uncertainty $0.1\sin(50t)$. Under the effects of both disturbances and the same delay considered in the previous example, the estimation error of all three methods are compared in Figure 7.3,

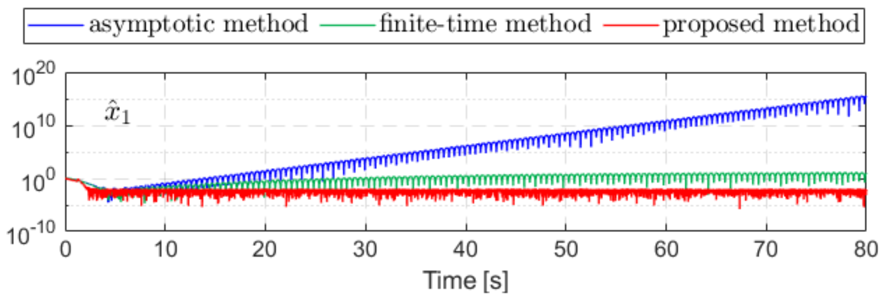

Figure 7.3: State estimation errors of methods [5, 6] and the proposed method in the delayed and noisy scenario.

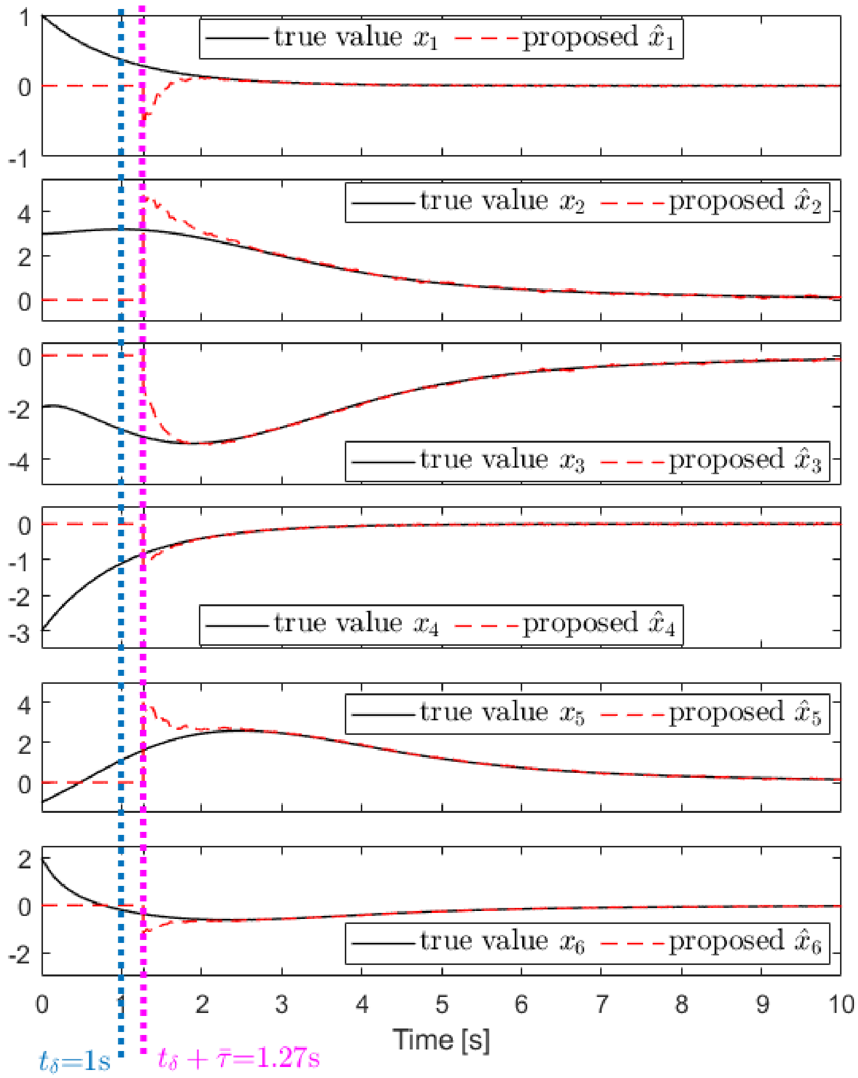

Figure 7.4: State estimates of the proposed method in the delayed and noisy scenario.

where the proposed method outperforms the other two in terms of steady-state accuracy. From the state estimates shown in Figure 7.4, the proposed method converges within a fixed time $t_\delta + \bar{\tau} = 1.27$s. This arises from that once the proposed observer is activated at $t_\delta = 1$s, it requires at most $\bar{\tau}$ to transmitting neighbouring information ensuring the fully observable in each subsystem.

7.6 Conclusion

A fixed-time convergent observer is proposed for distributed state estimation of a large scale system with directed communication typologies. The fast convergence properties enable the data transmission delay being compensated a posteriori. As such, cross-agent communication is utilised, and it yields a more effective data exchange mechanism with an optimised (minimised) data flow. The boundedness of the estimation error has been confirmed subject to bounded measurement and process disturbances. Numerical examples and comparisons with the existing method have been shown to verify the effectiveness of the proposed method. It should be noted that the property of fixed-time convergence needs high-frequency output sampling, which can be achieved by advanced information and communication technology.

Chapter 8

Conclusion

8.1 Summary of Thesis Achievements

This thesis investigates a resilient communication and control framework for cyber-physical energy systems using a concept of "microgrid". The proposed resilient framework tackles several challenging problems with exhaustive numerical tests, simulation results and experimental validations towards future "cyber-physical energy resilience" targeting at a zero-carbon society, generally including a centralised-to-decentralised transitional framework, a systematic analysis of cyber-resilient distributed control methods for networked MGs, a cyber-physical post-contingency service restoration based on UAVs and a theoretical distributed dynamic situational awareness algorithm for large-scale systems.

- Chapter 2 answers a question that whether to utilise a centralised control solution or a decentralised one to accommodate massive renewables, given their distinguished advantages on optimality and resilience. Instead of choosing one, blending them under the centralised-to-decentralised resilient control framework for energy systems is feasible and of great benefits in terms of operational optimality, resilience and cost-effectiveness.
- Chapters 3 to 5 elaborate a systematic analysis of cyber-resilient distributed control methods for MGs against multiple uncertainty and disturbance, random communication failure

and DoS attacks respectively. To be more specific, multiple uncertainty and disturbance are handled by a unified and linearised control-oriented model for grid-forming inverters; random communication failure is coped with a prediction horizon embedded with MPC; DoS attacks are dealt with an intelligence of data flow and control logic by theoretical proof.

- Chapter 6 utilizes mobile resources in both cyber side (i.e., UAV/drone) and physical side (i.e., MER) to improve the cyber-physical service level. i.e., UAVs function as wireless base station and relay while MERs provide incremental energy sources.

- Chapter 7 provides a kernel-based solution for fixed-time global state estimation in a distributed manner, which explicitly analyses distributed observability in terms of communication network topology.

8.2 Future Work

There are different areas that can be explored and investigated to enhance the research in this thesis, the main directions are identified chapter-by-chapter as follows.

- Chapter 2 only enhances power supply resilience from a centralised framework to a decentralised framework, corresponding to the stages of resistance and mitigation in Figure 1.3, but has not fully considered a cyber-physical cooperative recovery process, restoring system's full functionalities and further enabling system upgrading in terms of resilience. Hence, future research directions lie in post-contingency recovery and after-contingency upgrading and rebuilding.

  In the proposed centralised-to-decentralised framework of Chapter 2, the triggering conditions of both cyber and physical layers are key to resilience enhancement, though the seamless transition of MG islanding operation has been investigated widely. It still has improvements in increasing the efficiency (e.g., contingency detection sensitivity and accuracy) of the triggering conditions in not only physical islanding but cyber-layer emergency communication formation.

- The multi-disturbance resilient observer in Chapter 3 based on the unified modelling assumes the output measurement and system dynamics only containing Gaussian noise. However, sensors may induce non-Gaussian noise which requires further research on adaptive and intelligent observer design.

- In Chapter 4, the prediction horizon in DMPC, which is critical to communication failure-tolerance is determined based on the worst scenario of failure time. However, this is a robustness design mechanism inducing conservativeness. Future work could consider an intelligent, maybe learning-based decision-making method of prediction horizon to minimise communication and computation burdens on cyber-layer devices.

- Chapter 5 assumes all channels in information systems vulnerable to DoS attacks. However, in some cases, if the attacker has limited resources, there is an optimization problem to allocate attack resources to maximise/minimise the consequences, which in turn suggests an optimization problem for the defender to allocate the defense resources.

  Chapter 5 only investigates the system dynamics that are modelled by the first-order, and it is interesting to conduct research on more accurately modelled networked MGs and large-scale power systems, further comprehensively investigating cybersecurity issues not only including DoS, but deception attacks such as false data injection (FDI).

- Chapter 6 improves the power network resilience after contingencies and a detailed two-level design fully considers cyber-physical resource shortage to prioritize users and critical power supply of high importance. However, the proposed framework is service-oriented only without full cost consideration. The response cost-effectiveness during post-contingency periods could be a meaningful research direction in the future.

- Chapter 7 involves a fundamental distributed dynamic state estimation problem which has many future directions: the current work conducts research on those systems with a connected communication graph, while a time-varying communication graph or optimised communication topology design based on observability can be dug deeper; more general nonlinear systems and cybersecurity issues can be considered theoretically; multifarious applications in resilient energy systems can be further investigated.

- Beyond Chapters 2 to 7, although the cyber-physical interdependency has been considered, current work still models cyber-physical MGs as two layers, i.e. power transmission and data transmission. However, if we could model it as a whole named power-communication unified transmission model for instance, the critical vulnerability could be revealed and the globally optimal resilience could be achieved.

  The comprehensive evaluation of cybersecurity issues is difficult in practice because we are not willing to implement an intentional cyber attack in the real world, hence a cyber-physical testbed validation is essential. For example, current power-hardware-in-the-loop (PHIL) simulation can be extended through a practical communication network emulation as a powerful tool.

Bibliography

[1] Claudio De Persis and Paolo Frasca. Robust Self-Triggered Coordination With Ternary Controllers. *IEEE Transactions on Automatic Control*, 58(12):3024–3038, December 2013.

[2] Zhi Feng and Guoqiang Hu. Secure Cooperative Event-Triggered Control of Linear Multiagent Systems Under DoS Attacks. *IEEE Transactions on Control Systems Technology*, 28(3):1–12, 2019.

[3] Wenying Xu, Guoqiang Hu, Daniel WC Ho, and Zhi Feng. Distributed secure cooperative control under denial-of-service attacks from multiple adversaries. *IEEE Transactions on Cybernetics*, 50(8):3458–3467, 2019.

[4] Danial Senejohnny, Pietro Tesi, and Claudio De Persis. A Jamming-Resilient Algorithm for Self-Triggered Network Coordination. *IEEE Transactions on Control of Network Systems*, 5(3):10, 2018.

[5] Weixin Han, Harry L Trentelman, Zhenhua Wang, and Yi Shen. A simple approach to distributed observer design for linear systems. *IEEE Transactions on Automatic Control*, 64(1):329–336, 2019.

[6] Haik Silm, Rosane Ushirobira, Denis Efimov, Jean-Pierre Richard, and Wim Michiels. A note on distributed finite-time observers. *IEEE Transactions on Automatic Control*, 64(2):759–766, 2019.

[7] Shan Zuo, Ali Davoudi, Yongduan Song, and Frank L. Lewis. Distributed Finite-Time Voltage and Frequency Restoration in Islanded AC Microgrids. *IEEE Transactions on Industrial Electronics*, 63(10):5988–5997, October 2016.

[8] Earth Science Communications Team (NASA's Jet Propulsion Laboratory, California Institute of Technology). Scientific consensus: Earth's climate is warming. `https://climate.nasa.gov/scientific-consensus/`, 2021.

[9] Felix Creutzig, Jan Christoph Goldschmidt, Paul Lehmann, Eva Schmid, Felix von Blücher, Christian Breyer, Blanca Fernandez, Michael Jakob, Brigitte Knopf, Steffen Lohrey, et al. Catching two european birds with one renewable stone: Mitigating climate change and eurozone crisis by an energy transition. *Renewable and Sustainable Energy Reviews*, 38:1015–1028, 2014.

[10] Maria Luisa Di Silvestre, Salvatore Favuzza, Eleonora Riva Sanseverino, and Gaetano Zizzo. How decarbonization, digitalization and decentralization are changing key power infrastructures. *Renewable and Sustainable Energy Reviews*, 93:483–498, 2018.

[11] Alyson Kenward, Urooj Raja, et al. Blackout: Extreme weather, climate change and power outages. *Climate Central*, 10:1–23, 2014.

[12] Mathaios Panteli and Pierluigi Mancarella. Influence of extreme weather and climate change on the resilience of power systems: Impacts and possible mitigation strategies. *Electric Power Systems Research*, 127:259–270, 2015.

[13] Benzhi Zhou, Lianhong Gu, Yihui Ding, Lan Shao, Zhongmin Wu, Xiaosheng Yang, Changzhu Li, Zhengcai Li, Xiaoming Wang, Yonghui Cao, et al. The great 2008 chinese ice storm: Its socioeconomic–ecological impact and sustainability lessons learned. *Bulletin of the American meteorological Society*, 92(1):47–60, 2011.

[14] Pudong Ge, Fei Teng, Charalambos Konstantinou, and Shiyan Hu. A resilience-oriented centralised-to-decentralised framework for networked microgrids management. *Applied Energy*, 308:118234, 2022.

[15] Charalambos Konstantinou. Towards a secure and resilient all-renewable energy grid for smart cities. *IEEE Consumer Electronics Magazine*, 2021.

[16] Yezhou Wang, Chen Chen, Jianhui Wang, and Ross Baldick. Research on resilience of power systems under natural disasters—a review. *IEEE Transactions on Power Systems*, 31(2):1604–1613, 2016.

[17] Ekundayo Shittu, Abhijai Tibrewala, Swetha Kalla, and Xiaonan Wang. Meta-analysis of the strategies for self-healing and resilience in power systems. *Advances in Applied Energy*, 4:100036, 2021.

[18] NREL. Power system resilience. `https://www.nrel.gov/research/power-system-resilience.html`.

[19] CIGRE. Defining power system resilience. `https://www.cigre.org/article/defining-power-system-resilience`, 2019.

[20] NOAA NCEI. Noaa national centers for environmental information (ncei) us billion-dollar weather and climate disasters. `https://www.ncdc.noaa.gov/billions/`, 2021.

[21] Met Office. Past weather events. `https://www.metoffice.gov.uk/weather/learn-about/past-uk-weather-events`, 2021.

[22] Narayan Bhusal, Michael Abdelmalak, Md Kamruzzaman, and Mohammed Benidris. Power system resilience: Current practices, challenges, and future directions. *IEEE Access*, 8:18064–18086, 2020.

[23] United States. Executive Office of the President, et al. *The federal response to Hurricane Katrina: Lessons learned.* Government Printing Office, 2006.

[24] CNN.com. Rita's impact, city by city. `http://www.cnn.com/2005/US/09/24/rita.assess/index.html`, 2005.

[25] Hitoshi Yamamura, Kazuhisa Kaneda, and Yasumitsu Mizobata. Communication problems after the great east japan earthquake of 2011. *Disaster medicine and public health preparedness*, 8(4):293–296, 2014.

[26] Alexis Kwasinski. Hurricane sandy effects on communication systems. *The University of Texas at Austin, Tech. Rep. PR-AK-0112-2012*, 2012.

[27] Christine Hauser. Louisiana floods lead to 8 deaths. `https://www.nytimes.com/2016/08/16/us/louisiana-floods-deaths.html`, 2016.

[28] NOAA National Weather Service. Midwest derecho, august 10, 2020,. `https://storymaps.arcgis.com/stories/f98352e2153b4865b99ba53b86021b65`, 2021.

[29] Barbados Today. Elsa was a major test of island's telecommunications infrastructure. `https://barbadostoday.bb/2021/07/04/elsa-was-a-major-test-of-islands-telecommunications-infrastructure/`, 2021.

[30] Peter Palensky and Siem Bruijns. Cyber-physical system resilience challenges. `https://electra.cigre.org/319-december-2021/global-connections/cyber-physical-system-resilience-challenges.html`, 2021.

[31] Zhiyi Li, Mohammad Shahidehpour, Farrokh Aminifar, Ahmed Alabdulwahab, and Yusuf Al-Turki. Networked microgrids for enhancing the power system resilience. *Proceedings of the IEEE*, 105(7):1289–1310, 2017.

[32] Yuhua Du, Xiaonan Lu, Jianhui Wang, Bo Chen, Hao Tu, and Srdjan Lukic. Dynamic microgrids in resilient distribution systems with reconfigurable cyber-physical networks. *IEEE Journal of Emerging and Selected Topics in Power Electronics*, 2020.

[33] D. E. Olivares, A. Mehrizi-Sani, A. H. Etemadi, C. A. Cañizares, R. Iravani, M. Kazerani, A. H. Hajimiragha, O. Gomis-Bellmunt, M. Saeedifard, R. Palma-Behnke, G. A. Jiménez-Estévez, and N. D. Hatziargyriou. Trends in Microgrid Control. *IEEE Transactions on Smart Grid*, 5(4):1905–1919, July 2014.

[34] Florian Dörfler, John W Simpson-Porco, and Francesco Bullo. Breaking the hierarchy: Distributed control and economic optimality in microgrids. *IEEE Transactions on Control of Network Systems*, 3(3):241–253, 2015.

[35] Dimitra Apostolopoulou, Shay Bahramirad, and Amin Khodaei. The interface of power: Moving toward distribution system operators. *IEEE Power and Energy Magazine*, 14(3):46–51, 2016.

[36] Jianhui Wang and Xiaonan Lu. Sustainable and resilient distribution systems with networked microgrids. *Proceedings of the IEEE*, 108(2):238–241, 2020.

[37] Jeffrey Marqusee, William Becker, and Sean Ericson. Resilience and economics of microgrids with pv, battery storage, and networked diesel generators. *Advances in Applied Energy*, 3:100049, 2021.

[38] Robert Panora, Joseph E Gehret, Melinda M Furse, and Robert H Lasseter. Real-world performance of a certs microgrid in manhattan. *IEEE Transactions on Sustainable Energy*, 5(4):1356–1360, 2014.

[39] Chris Marnay, Hirohisa Aki, Keiichi Hirose, Alexis Kwasinski, Saori Ogura, and Takao Shinji. Japan's pivot to resilience: How two microgrids fared after the 2011 earthquake. *IEEE Power and Energy Magazine*, 13(3):44–57, 2015.

[40] Simone Polimeni, Lorenzo Meraldi, Luca Moretti, Sonia Leva, and Giampaolo Manzolini. Development and experimental validation of hierarchical energy management system based on stochastic model predictive control for off-grid microgrids. *Advances in Applied Energy*, 2:100028, 2021.

[41] Pudong Ge, Boli Chen, and Fei Teng. Event-triggered distributed model predictive control for resilient voltage control of an islanded microgrid. *International Journal of Robust and Nonlinear Control*, 31(6):1979–2000, 2021.

[42] Andrea Monforti Ferrario, Andrea Bartolini, Francisca Segura Manzano, Francisco José Vivas, Gabriele Comodi, Stephen John McPhail, and José Manuel Andujar. A model-based parametric and optimal sizing of a battery/hydrogen storage of a real hybrid microgrid supplying a residential load: Towards island operation. *Advances in Applied Energy*, 3:100048, 2021.

[43] Pudong Ge, Yue Zhu, Tim C. Green, and Fei Teng. Resilient secondary voltage control of islanded microgrids: An eskbf-based distributed fast terminal sliding mode control approach. *IEEE Transactions on Power Systems*, 36(2):1059–1070, March 2021.

[44] Palak P Parikh, Mitalkumar G Kanabar, and Tarlochan S Sidhu. Opportunities and challenges of wireless communication technologies for smart grid applications. In *IEEE PES General Meeting*, pages 1–7. IEEE, 2010.

[45] Xinghuo Yu and Yusheng Xue. Smart grids: A cyber–physical systems perspective. *Proceedings of the IEEE*, 104(5):1058–1070, 2016.

[46] Philip W.T. Pong, Anuradha M. Annaswamy, Benjamin Kroposki, Yingchen Zhang, Ram Rajagopal, Gil Zussman, and H. Vincent Poor. Cyber-enabled grids: Shaping future energy systems. *Advances in Applied Energy*, 1:100003, 2021.

[47] Abdulaziz Alqahtani, Rohit Abhishek, David Tipper, and Deep Medhi. Disaster recovery power and communications for smart critical infrastructures. In *2018 IEEE International Conference on Communications (ICC)*, pages 1–6, 2018.

[48] Ioannis Zografopoulos, Juan Ospina, Xiaorui Liu, and Charalambos Konstantinou. Cyber-physical energy systems security: Threat modeling, risk assessment, resources, metrics, and case studies. *IEEE Access*, 9:29775–29818, 2021.

[49] GC Deepak, Alexandros Ladas, Yusuf Abdulrahman Sambo, Haris Pervaiz, Christos Politis, and Muhammad Ali Imran. An overview of post-disaster emergency communication systems in the future networks. *IEEE Wireless Communications*, 26(6):132–139, 2019.

[50] Charalambos Konstantinou and Olugbenga Moses Anubi. Resilient cyber-physical energy systems using prior information based on gaussian process. *IEEE Transactions on Industrial Informatics*, 2021.

[51] Lalit Chettri and Rabindranath Bera. A comprehensive survey on internet of things (iot) toward 5g wireless systems. *IEEE Internet of Things Journal*, 7(1):16–32, 2019.

[52] Qingqing Wu, Geoffrey Ye Li, Wen Chen, Derrick Wing Kwan Ng, and Robert Schober. An overview of sustainable green 5g networks. *IEEE Wireless Communications*, 24(4):72–80, 2017.

[53] Daquan Feng, Chenzi Jiang, Gubong Lim, Leonard J Cimini, Gang Feng, and Geoffrey Ye Li. A survey of energy-efficient wireless communications. *IEEE Communications Surveys & Tutorials*, 15(1):167–178, 2012.

[54] Lin Chen and Kaigui Bian. Neighbor discovery in mobile sensing applications: A comprehensive survey. *Ad Hoc Networks*, 48:38–52, 2016.

[55] Arash Asadi, Qing Wang, and Vincenzo Mancuso. A survey on device-to-device communication in cellular networks. *IEEE Communications Surveys & Tutorials*, 16(4):1801–1819, 2014.

[56] Peng-Yong Kong. Multicell d2d communications for hierarchical control of microgrid system. *IEEE Systems Journal*, 15(2):1929–1938, 2020.

[57] Qian Hu, Siqi Bu, Zilin Li, Bowen Zhou, and Dongsheng Yang. Cost-effective communication network planning considering performance of pinning-based secondary control in microgrids. *International Journal of Electrical Power & Energy Systems*, 133:107269, 2021.

[58] Mohammad Rafiee and Alexandre M Bayen. Optimal network topology design in multi-agent systems for efficient average consensus. In *49th IEEE Conference on Decision and Control (CDC)*, pages 3877–3883. IEEE, 2010.

[59] Andrea Goldsmith. *Wireless communications.* Cambridge university press, 2005.

[60] Le Liang, Geoffrey Ye Li, and Wei Xu. Resource allocation for d2d-enabled vehicular communications. *IEEE Transactions on Communications*, 65(7):3186–3197, 2017.

[61] Atefeh Termehchi and Mehdi Rasti. Joint sampling time and resource allocation for power efficiency in industrial cyber–physical systems. *IEEE Transactions on Industrial Informatics*, 17(4):2600–2610, 2021.

[62] Johan Lofberg. Yalmip: A toolbox for modeling and optimization in matlab. In *2004 IEEE international conference on robotics and automation (IEEE Cat. No. 04CH37508)*, pages 284–289. IEEE, 2004.

[63] Mosek ApS (version 9.2.40). `https://www.mosek.com/`, 2021.

[64] Josep M. Guerrero, Juan C. Vasquez, José Matas, Luis García de Vicuna, and Miguel Castilla. Hierarchical Control of Droop-Controlled AC and DC Microgrids—A General Approach Toward Standardization. *IEEE Transactions on Industrial Electronics*, 58(1):158–172, January 2011.

[65] Huaguang Zhang, Sunghyok Kim, Qiuye Sun, and Jianguo Zhou. Distributed Adaptive Virtual Impedance Control for Accurate Reactive Power Sharing Based on Consensus Control in Microgrids. *IEEE Transactions on Smart Grid*, 8(4):1749–1761, July 2017.

[66] Ali Bidram, Ali Davoudi, and Frank L. Lewis. A Multiobjective Distributed Control Framework for Islanded AC Microgrids. *IEEE Transactions on Industrial Informatics*, 10(3):1785–1798, August 2014.

[67] Pudong Ge, Xiaobo Dou, Xiangjun Quan, Qinran Hu, Wanxing Sheng, Zaijun Wu, and Wei Gu. Extended-State-Observer-Based Distributed Robust Secondary Voltage and Frequency Control for an Autonomous Microgrid. *IEEE Transactions on Sustainable Energy*, 11(1):195–205, January 2020.

[68] Yu-Ping Tian and Cheng-Lin Liu. Consensus of multi-agent systems with diverse input and communication delays. *IEEE Transactions on Automatic Control*, 53(9):2122–2128, 2008.

[69] Zhiyun Lin, Bruce Francis, and Manfredi Maggiore. Necessary and sufficient graphical conditions for formation control of unicycles. *IEEE Transactions on Automatic Control*, 50(1):121–127, 2005.

[70] Xiwei Liu, Wenlian Lu, and Tianping Chen. Consensus of multi-agent systems with unbounded time-varying delays. *IEEE Transactions on Automatic Control*, 55(10):2396–2401, 2010.

[71] Ulrich Münz, Antonis Papachristodoulou, and Frank Allgöwer. Delay robustness in consensus problems. *Automatica*, 46(8):1252–1265, 2010.

[72] Fei Teng, Marko Aunedi, and Goran Strbac. Benefits of flexibility from smart electrified transportation and heating in the future uk electricity system. *Applied Energy*, 167:420–431, 2016.

[73] Guannan He, Jeremy Michalek, Soummya Kar, Qixin Chen, Da Zhang, and Jay F Whitacre. Utility-scale portable energy storage systems. *Joule*, 5(2):379–392, 2021.

[74] Kyriaki E. Antoniadou-Plytaria, Iasonas N. Kouveliotis-Lysikatos, Pavlos S. Georgilakis, and Nikos D. Hatziargyriou. Distributed and Decentralized Voltage Control of Smart Distribution Networks: Models, Methods, and Future Research. *IEEE Transactions on Smart Grid*, 8(6):2999–3008, November 2017.

[75] Dan T. Ton and Merrill A. Smith. The U.S. Department of Energy's Microgrid Initiative. *The Electricity Journal*, 25(8):84–94, October 2012.

[76] Mostafa Farrokhabadi, Claudio A. Canizares, John William Simpson-Porco, Ehsan Nasr, Lingling Fan, Patricio Mendoza-Araya, Reinaldo Tonkoski, Ujjwol Tamrakar, Nikos D. Hatziargyriou, Dimitris Lagos, Richard W. Wies, Mario Paolone, Marco Liserre, Lasantha Meegahapola, Mahmoud Kabalan, Amir H. Hajimiragha, Dario Peralta, Marcelo Elizondo, Kevin Paul Schneider, Frank Tuffner, and James T. Reilly. Microgrid Stability Definitions, Analysis, and Examples. *IEEE Transactions on Power Systems*, pages 1–1, 2019.

[77] T. Wu, G. Bao, Y. Chen, and J. Shang. A Review for Control Strategies in Microgrid. In *2018 37th Chinese Control Conference (CCC)*, pages 30–35, July 2018.

[78] X. Yu, A. M. Khambadkone, H. Wang, and S. T. S. Terence. Control of Parallel-Connected Power Converters for Low-Voltage Microgrid—Part I: A Hybrid Control Architecture. *IEEE Transactions on Power Electronics*, 25(12):2962–2970, December 2010.

[79] G. Diaz, C. Gonzalez-Moran, J. Gomez-Aleixandre, and A. Diez. Scheduling of Droop Coefficients for Frequency and Voltage Regulation in Isolated Microgrids. *IEEE Transactions on Power Systems*, 25(1):489–496, February 2010.

[80] Cuo Zhang, Yan Xu, Zhaoyang Dong, and Jayashri Ravishankar. Three-Stage Robust Inverter-Based Voltage/Var Control for Distribution Networks With High-Level PV. *IEEE Transactions on Smart Grid*, 10(1):782–793, January 2019.

[81] Zhengmao Li and Yan Xu. Dynamic dispatch of grid-connected multi-energy microgrids considering opportunity profit. In *2017 IEEE Power & Energy Society General Meeting*, pages 1–5, Chicago, IL, July 2017. IEEE.

[82] N. L. Díaz, A. C. Luna, J. C. Vasquez, and J. M. Guerrero. Centralized Control Architecture for Coordination of Distributed Renewable Generation and Energy Storage in Islanded AC Microgrids. *IEEE Transactions on Power Electronics*, 32(7):5202–5213, July 2017.

[83] Q. Zhong. Robust Droop Controller for Accurate Proportional Load Sharing Among Inverters Operated in Parallel. *IEEE Transactions on Industrial Electronics*, 60(4):1281–1290, April 2013.

[84] Frank L. Lewis, Zhihua Qu, Ali Davoudi, and Ali Bidram. Secondary control of microgrids based on distributed cooperative control of multi-agent systems. *IET Generation, Transmission & Distribution*, 7(8):822–831, August 2013.

[85] Stanton T. Cady, Alejandro D. Domínguez-García, and Christoforos N. Hadjicostis. A Distributed Generation Control Architecture for Islanded AC Microgrids. *IEEE Transactions on Control Systems Technology*, 23(5):1717–1735, September 2015.

[86] Amir H. Etemadi, Edward J. Davison, and Reza Iravani. A Decentralized Robust Control Strategy for Multi-DER Microgrids—Part I: Fundamental Concepts. *IEEE Transactions on Power Delivery*, 27(4):1843–1853, October 2012.

[87] Chunxia Dou, Dong Yue, Josep M. Guerrero, Xiangpeng Xie, and Songlin Hu. Multiagent System-Based Distributed Coordinated Control for Radial DC Microgrid Consid-

ering Transmission Time Delays. *IEEE Transactions on Smart Grid*, 8(5):2370–2381, September 2017.

[88] Ali Bidram, Ali Davoudi, Frank L. Lewis, and Josep M. Guerrero. Distributed Cooperative Secondary Control of Microgrids Using Feedback Linearization. *IEEE Transactions on Power Systems*, 28(3):3462–3470, August 2013.

[89] Amir H. Etemadi, Edward J. Davison, and Reza Iravani. A Generalized Decentralized Robust Control of Islanded Microgrids. *IEEE Transactions on Power Systems*, 29(6):3102–3113, November 2014.

[90] Shafiqul Islam, Peter X. Liu, and Abdulmotaleb El Saddik. Distributed robust adaptive finite-time voltage control for microgrids with uncertainty. In *2017 IEEE International Conference on Systems, Man, and Cybernetics (SMC)*, pages 2200–2202, Banff, AB, October 2017. IEEE.

[91] Nima Mahdian Dehkordi, Hamid Reza Baghaee, Nasser Sadati, and Josep M. Guerrero. Distributed Noise-Resilient Secondary Voltage and Frequency Control for Islanded Microgrids. *IEEE Transactions on Smart Grid*, 10(4):3780–3790, July 2019.

[92] Nima Mahdian Dehkordi, Nasser Sadati, and Mohsen Hamzeh. Distributed Robust Finite-Time Secondary Voltage and Frequency Control of Islanded Microgrids. *IEEE Transactions on Power Systems*, 32(5):3648–3659, September 2017.

[93] Alessandro Pilloni, Alessandro Pisano, and Elio Usai. Robust Finite-Time Frequency and Voltage Restoration of Inverter-Based Microgrids via Sliding-Mode Cooperative Control. *IEEE Transactions on Industrial Electronics*, 65(1):907–917, January 2018.

[94] Junyong Sun, Zhiyong Geng, Yuezu Lv, Zhongkui Li, and Zhengtao Ding. Distributed Adaptive Consensus Disturbance Rejection for Multi-Agent Systems on Directed Graphs. *IEEE Transactions on Control of Network Systems*, 5(1):11, 2018.

[95] Xiaocheng Zhang, Wenchao Xue, Haitao Fang, and Xingkang He. On Extended State Based Kalman-Bucy Filter. In *2018 IEEE 7th Data Driven Control and Learning Systems Conference (DDCLS)*, pages 1158–1163, Enshi, May 2018. IEEE.

[96] R. Madoński and P. Herman. Survey on methods of increasing the efficiency of extended state disturbance observers. *ISA Transactions*, 56:18–27, May 2015.

[97] Zhihua Qu. *Cooperative Control of Dynamical Systems: Applications to Autonomous Vehicles*. Springer-Verlag, London, 2009.

[98] Joan Rocabert, Alvaro Luna, Frede Blaabjerg, and Pedro Rodríguez. Control of Power Converters in AC Microgrids. *IEEE Transactions on Power Electronics*, 27(11):4734–4749, November 2012.

[99] Zongyu Zuo and Lin Tie. Distributed robust finite-time nonlinear consensus protocols for multi-agent systems. *International Journal of Systems Science*, 47(6):1366–1375, April 2016.

[100] Hassan K. Khalil. *Nonlinear Systems*. Pearson, Upper Saddle River, N.J, 3 edition edition, December 2001.

[101] X. He, X. Zhang, W. Xue, and H. Fang. Distributed Kalman Filter for A Class of Nonlinear Uncertain Systems: An Extended State Method. In *2018 21st International Conference on Information Fusion (FUSION)*, pages 78–83, July 2018.

[102] Junkang Ni, Ling Liu, Chongxin Liu, Xiaoyu Hu, and Shilei Li. Fast Fixed-Time Nonsingular Terminal Sliding Mode Control and Its Application to Chaos Suppression in Power System. *IEEE Transactions on Circuits and Systems II: Express Briefs*, 64(2):151–155, February 2017.

[103] Zongyu Zuo. Non-singular fixed-time terminal sliding mode control of non-linear systems. *IET Control Theory & Applications*, 9(4):545–552, February 2015.

[104] Wei Gu, Guannan Lou, Wen Tan, and Xiaodong Yuan. A Nonlinear State Estimator-Based Decentralized Secondary Voltage Control Scheme for Autonomous Microgrids. *IEEE Transactions on Power Systems*, 32(6):4794–4804, November 2017.

[105] Yu Wang, Tung Lam Nguyen, Yan Xu, Zhengmao Li, Quoc-Tuan Tran, and Raphael Caire. Cyber-Physical Design and Implementation of Distributed Event-Triggered Sec-

ondary Control in Islanded Microgrids. *IEEE Transactions on Industry Applications*, 55(6):5631–5642, November 2019.

[106] John W. Simpson-Porco, Qobad Shafiee, Florian Dörfler, Juan C. Vasquez, Josep M. Guerrero, and Francesco Bullo. Secondary Frequency and Voltage Control of Islanded Microgrids via Distributed Averaging. *IEEE Transactions on Industrial Electronics*, 62(11):7025–7038, November 2015.

[107] Sara Nourollah, Abolfazl Pirayesh, and Farrokh Aminifar. Combinational scheme for voltage and frequency recovery in an islanded distribution system. *IET Generation, Transmission & Distribution*, 10(12):2899–2906, September 2016.

[108] Nagaraju Pogaku, Milan Prodanovic, and Timothy C. Green. Modeling, Analysis and Testing of Autonomous Operation of an Inverter-Based Microgrid. *IEEE Transactions on Power Electronics*, 22(2):613–625, March 2007.

[109] Chengshan Wang, Tianyu Zhang, Fengzhang Luo, Fangxing Li, and Yanzhang Liu. Impacts of Cyber System on Microgrid Operational Reliability. *IEEE Transactions on Smart Grid*, 10(1):105–115, January 2019.

[110] A. Mehrizi-Sani and R. Iravani. Potential-Function Based Control of a Microgrid in Islanded and Grid-Connected Modes. *IEEE Transactions on Power Systems*, 25(4):1883–1891, November 2010.

[111] Yousef Khayat, Qobad Shafiee, Rasool Heydari, Mobin Naderi, Tomislav Dragičević, John W. Simpson-Porco, Florian Dörfler, Mohammad Fathi, Frede Blaabjerg, Josep M. Guerrero, and Hassan Bevrani. On the Secondary Control Architectures of AC Microgrids: An Overview. *IEEE Transactions on Power Electronics*, 35(6):6482–6500, June 2020.

[112] Stefano Riverso and Giancarlo Ferrari-Trecate. Plug-and-play distributed model predictive control with coupling attenuation. *Optimal Control Applications and Methods*, 36(3):292–305, May 2015.

[113] Shankar Abhinav, Ioannis D. Schizas, Frank L. Lewis, and Ali Davoudi. Distributed Noise-Resilient Networked Synchrony of Active Distribution Systems. *IEEE Transactions on Smart Grid*, 9(2):836–846, March 2018.

[114] Quan Zhou, Mohammad Shahidehpour, Mingyu Yan, Xi Wu, Ahmed Alabdulwahab, and Abdullah Abusorrah. Distributed Secondary Control for Islanded Microgrids With Mobile Emergency Resources. *IEEE Transactions on Power Systems*, 35(2):1389–1399, March 2020.

[115] Sean Anderson, Patricia Hidalgo-Gonzalez, Roel Dobbe, and Claire J. Tomlin. Distributed Model Predictive Control for Autonomous Droop-Controlled Inverter-Based Microgrids. In *2019 IEEE 58th Conference on Decision and Control (CDC)*, pages 6242–6248, December 2019.

[116] W.P.M.H. Heemels, K.H. Johansson, and P. Tabuada. An introduction to event-triggered and self-triggered control. In *2012 IEEE 51st IEEE Conference on Decision and Control (CDC)*, pages 3270–3285, Maui, HI, USA, December 2012. IEEE.

[117] D. Lehmann, E. Henriksson, and K. H. Johansson. Event-triggered model predictive control of discrete-time linear systems subject to disturbances. In *2013 European Control Conference (ECC)*, pages 1156–1161, July 2013.

[118] W P Maurice H Heemels, Andrew R Teel, Nathan van de Wouw, and Dragan Nešić. Networked Control Systems With Communication Constraints: Tradeoffs Between Transmission Intervals, Delays and Performance. *IEEE Transactions on Automatic Control*, 55(8):1781–1796, August 2010.

[119] Bo Zhang, Chunxia Dou, Dong Yue, Zhanqiang Zhang, and Tengfei Zhang. A Packet Loss-Dependent Event-Triggered Cyber-Physical Cooperative Control Strategy for Islanded Microgrid. *IEEE Transactions on Cybernetics*, pages 1–16, 2019.

[120] Alessandro Floriduz, Michele Tucci, Stefano Riverso, and Giancarlo Ferrari-Trecate. Approximate Kron Reduction Methods for Electrical Networks With Applications to Plug-

and-Play Control of AC Islanded Microgrids. *IEEE Transactions on Control Systems Technology*, 27(6):2403–2416, November 2019.

[121] Florian Dorfler and Francesco Bullo. Kron Reduction of Graphs With Applications to Electrical Networks. *IEEE Transactions on Circuits and Systems I: Regular Papers*, 60(1):150–163, January 2013.

[122] Peng Li, Francesca Boem, Gilberto Pin, and Thomas Parisini. Distributed Fault Detection and Isolation for Interconnected Systems: a Non-Asymptotic Kernel-Based Approach. *IFAC-PapersOnLine*, 50(1):1013–1018, July 2017.

[123] Gilberto Pin, Marco Lovera, Andrea Assalone, and Thomas Parisini. Kernel-based non-asymptotic state estimation for linear continuous-time systems. In *2013 American Control Conference*, pages 3123–3128. IEEE, June 2013.

[124] Gilberto Pin, Boli Chen, and Thomas Parisini. Robust deadbeat continuous-time observer design based on modulation integrals. *Automatica*, 107:95–102, September 2019.

[125] Lei Ding, Qing-Long Han, Boda Ning, and Dong Yue. Distributed resilient finite-time secondary control for heterogeneous battery energy storage systems under denial-of-service attacks. *IEEE Transactions on Industrial Informatics*, 16(7):4909–4919, 2019.

[126] Thomas Morstyn, Branislav Hredzak, and Vassilios G. Agelidis. Distributed Cooperative Control of Microgrid Storage. *IEEE Transactions on Power Systems*, 30(5):2780–2789, September 2015.

[127] Jing Wang, Rawad El Kontar, Xin Jin, and Jennifer King. Electrifying high-efficiency future communities: Impact on energy, emissions, and grid. *Advances in Applied Energy*, 6:100095, 2022.

[128] Amin Gholami and Andy Sun. Stability of multi-microgrids: New certificates, distributed control, and braess's paradox. *IEEE Transactions on Control of Network Systems*, 2021.

[129] Fabio Pasqualetti, Florian Dorfler, and Francesco Bullo. Control-Theoretic Methods for Cyberphysical Security: Geometric Principles for Optimal Cross-Layer Resilient Control Systems. *IEEE Control Systems Magazine*, 35(1):110–127, February 2015.

[130] Chao Deng, Fanghong Guo, Changyun Wen, Dong Yue, and Yu Wang. Distributed resilient secondary control for dc microgrids against heterogeneous communication delays and dos attacks. *IEEE Transactions on Industrial Electronics*, 2021.

[131] Zhijie Lian, Fanghong Guo, Changyun Wen, Chao Deng, and Pengfeng Lin. Distributed resilient optimal current sharing control for an islanded dc microgrid under dos attacks. *IEEE Transactions on Smart Grid*, 12(5):4494–4505, 2021.

[132] Pietro Danzi, Marko Angjelichinoski, Čedomir Stefanović, Tomislav Dragičević, and Petar Popovski. Software-defined microgrid control for resilience against denial-of-service attacks. *IEEE Transactions on Smart Grid*, 10(5):5258–5268, 2019.

[133] Shichao Liu, Zhijian Hu, Xiaoyu Wang, and Ligang Wu. Stochastic Stability Analysis and Control of Secondary Frequency Regulation for Islanded Microgrids Under Random Denial of Service Attacks. *IEEE Transactions on Industrial Informatics*, 15(7):4066–4075, July 2019.

[134] Songlin Hu, Fuyi Yang, Sergey Gorbachev, Dong Yue, Victor Kuzin, and Chao Deng. Resilient control design for networked dc microgrids under time-constrained dos attacks. *ISA Transactions*, 2022.

[135] Ying Wan, Cheng Long, Ruilong Deng, Guanghui Wen, Xinghuo Yu, and Tingwen Huang. Distributed event-based control for thermostatically controlled loads under hybrid cyber attacks. *IEEE Transactions on Cybernetics*, 51(11):5314–5327, 2021.

[136] Bo Zhang, Chunxia Dou, Dong Yue, Ju H Park, and Zhanqiang Zhang. Attack-defense evolutionary game strategy for uploading channel in consensus-based secondary control of islanded microgrid considering dos attack. *IEEE Transactions on Circuits and Systems I: Regular Papers*, 69(2):821–834, 2022.

[137] Zhijian Hu, Shichao Liu, Wensheng Luo, and Ligang Wu. Resilient distributed fuzzy load frequency regulation for power systems under cross-layer random denial-of-service attacks. *IEEE Transactions on Cybernetics*, 2020.

[138] Songlin Hu, Ping Yuan, Dong Yue, Chunxia Dou, Zihao Cheng, and Yunning Zhang. Attack-resilient event-triggered controller design of dc microgrids under dos attacks. *IEEE Transactions on Circuits and Systems I: Regular Papers*, 67(2):699–710, 2020.

[139] Xiao-Kang Liu, Changyun Wen, Qianwen Xu, and Yan-Wu Wang. Resilient control and analysis for dc microgrid system under dos and impulsive fdi attacks. *IEEE Transactions on Smart Grid*, 12(5):3742–3754, 2021.

[140] Martine Chlela, Diego Mascarella, Geza Joos, and Marthe Kassouf. Fallback control for isochronous energy storage systems in autonomous microgrids under denial-of-service cyber-attacks. *IEEE Transactions on Smart Grid*, 9(5):4702–4711, 2018.

[141] Pengcheng Chen, Shichao Liu, Bo Chen, and Li Yu. Multi-agent reinforcement learning for decentralized resilient secondary control of energy storage systems against dos attacks. *IEEE Transactions on Smart Grid*, 2022.

[142] Dimos V Dimarogonas, Emilio Frazzoli, and Karl H Johansson. Distributed event-triggered control for multi-agent systems. *IEEE Transactions on Automatic Control*, 57(5):1291–1297, 2011.

[143] Scott N Backhaus, Larisa Dobriansky, Steve Glover, Chen-Ching Liu, Patrick Looney, Salman Mashayekh, Annabelle Pratt, Kevin Schneider, Michael Stadler, Michael Starke, et al. Networked microgrids scoping study. Technical report, Los Alamos National Lab.(LANL), Los Alamos, NM (United States), 2016.

[144] Junru Chen, Muyang Liu, and Federico Milano. Aggregated model of virtual power plants for transient frequency and voltage stability analysis. *IEEE Transactions on Power Systems*, 36(5):4366–4375, 2021.

[145] Martijn H Roos, Phuong H Nguyen, Johan Morren, and JG Slootweg. Aggregation of component-based grid-feeding der and load models for simulation of microgrid islanding transients. *Electric Power Systems Research*, 189:106759, 2020.

[146] Wei Ren, Randal W Beard, and Ella M Atkins. A survey of consensus problems in multi-agent coordination. In *Proceedings of the 2005, American Control Conference, 2005.*, pages 1859–1864. IEEE, 2005.

[147] Zhaoyu Wang and Jianhui Wang. Service restoration based on ami and networked mgs under extreme weather events. *IET Generation, Transmission & Distribution*, 11(2):401–408, 2017.

[148] Shanshan Ma, Liu Su, Zhaoyu Wang, Feng Qiu, and Ge Guo. Resilience enhancement of distribution grids against extreme weather events. *IEEE Transactions on Power Systems*, 33(5):4842–4853, 2018.

[149] Shunbo Lei, Chen Chen, Yue Song, and Yunhe Hou. Radiality constraints for resilient reconfiguration of distribution systems: Formulation and application to microgrid formation. *IEEE Transactions on Smart Grid*, 11(5):3944–3956, 2020.

[150] Chongyu Wang, Mingyu Yan, Kaiyuan Pang, Fushuan Wen, and Fei Teng. Cyber-physical interdependent restoration scheduling for active distribution network via ad hoc wireless communication. *IEEE Transactions on Smart Grid*, 2023.

[151] Haochen Zhang, Chen Chen, Shunbo Lei, and Zhaohong Bie. Resilient distribution system restoration with communication recovery by drone small cells. *IEEE Transactions on Smart Grid*, 14(2):1325–1328, 2023.

[152] Michael Heise, Martin Pietsch, Florian Steinke, Maximilian Bauer, and Burak Yilmaz. Optimized uav placement for resilient crisis communication and power grid restoration. In *2022 IEEE PES Innovative Smart Grid Technologies Conference Europe (ISGT-Europe)*, pages 1–5. IEEE, 2022.

[153] Le Liang, Hao Ye, Guanding Yu, and Geoffrey Ye Li. Deep-learning-based wireless resource allocation with application to vehicular networks. *Proceedings of the IEEE*, 108(2):341–356, 2020.

[154] Maurilio Matracia, Mustafa A Kishk, and Mohamed-Slim Alouini. On the topological aspects of uav-assisted post-disaster wireless communication networks. *IEEE Communications Magazine*, 59(11):59–64, 2021.

[155] Pei Yong, Ning Zhang, Qingchun Hou, Yuxiao Liu, Fei Teng, Song Ci, and Chongqing Kang. Evaluating the dispatchable capacity of base station backup batteries in distribution networks. *IEEE Transactions on Smart Grid*, 12(5):3966–3979, 2021.

[156] Zekai Wang, Tao Ding, Chenggang Mu, Yuhan Huang, Miao Yang, Yueyang Yang, Yi Lin, and Meng Li. A distributionally robust resilience enhancement model for transmission and distribution coordinated system using mobile energy storage and unmanned aerial vehicle. *International Journal of Electrical Power & Energy Systems*, 152:109256, 2023.

[157] Pudong Ge, Boli Chen, and Fei Teng. Cyber-resilient self-triggered distributed control of networked microgrids against multi-layer dos attacks. *IEEE Transactions on Smart Grid*, 14(4):3114–3124, 2022.

[158] Amin Gholami and Xu Andy Sun. Stability of multimicrogrids: New certificates, distributed control, and braess's paradox. *IEEE Transactions on Control of Network Systems*, 9(1):308–319, 2022.

[159] Anzar Mahmood, Nadeem Javaid, and Sohail Razzaq. A review of wireless communications for smart grid. *Renewable and Sustainable Energy Reviews*, 41:248–260, 2015.

[160] Bo Liu, Tianguang Chu, Long Wang, and Guangming Xie. Controllability of a leader–follower dynamic network with switching topology. *IEEE Transactions on Automatic Control*, 53(4):1009–1013, 2008.

[161] Xueji Zhang, Kristian Hengster-Movric, Michael Sebek, Wim Desmet, and Cassio Faria. Distributed observer and controller design for spatially interconnected systems. *IEEE Transactions on Control Systems Technology*, 27(1):1–13, 2019.

[162] Lei Zou, Zidong Wang, Jun Hu, and Donghua Zhou. Moving horizon estimation with unknown inputs under dynamic quantization effects. *IEEE Transactions on Automatic Control*, 65(12):5368–5375, 2020.

[163] Marcello Farina, Giancarlo Ferrari-Trecate, and Riccardo Scattolini. Distributed moving horizon estimation for linear constrained systems. *IEEE Transactions on Automatic Control*, 55(11):2462–2475, 2010.

[164] L Wang, Daniel Fullmer, Fengjiao Liu, and A Stephen Morse. Distributed control of linear multi-channel systems: summary of results. In *2020 American Control Conference (ACC)*, pages 4576–4581. IEEE, 2020.

[165] Shinkyu Park and Nuno C Martins. Necessary and sufficient conditions for the stabilizability of a class of lti distributed observers. In *2012 IEEE 51st IEEE Conference on Decision and Control (CDC)*, pages 7431–7436. IEEE, 2012.

[166] Stefan Knotek, Kristian Hengster-Movric, and Michael Sebek. Distributed estimation on sensor networks with measurement uncertainties. *IEEE Transactions on Control Systems Technology*, 29(5):1997–2011, 2021.

[167] Reza Olfati-Saber. Distributed kalman filtering for sensor networks. In *2007 46th IEEE Conference on Decision and Control*, pages 5492–5498. IEEE, 2007.

[168] Taekyoo Kim, Hyungbo Shim, and Dongil Dan Cho. Distributed luenberger observer design. In *2016 IEEE 55th Conference on Decision and Control (CDC)*, pages 6928–6933. IEEE, 2016.

[169] Shinkyu Park and Nuno C Martins. Design of distributed lti observers for state omniscience. *IEEE Transactions on Automatic Control*, 62(2):561–576, 2017.

[170] A. Mitra and S. Sundaram. Distributed observers for lti systems. *IEEE Transactions on Automatic Control*, 63(11):1024–1029, 2018.

[171] Lili Wang and A. Stephen Morse. A distributed observer for a time-invariant linear system. *IEEE Transactions on Automatic Control*, 63(7):2123–2130, 2018.

[172] Valery Ugrinovskii. Conditions for detectability in distributed consensus-based observer networks. *IEEE Transactions on Automatic Control*, 58(10):2659–2664, 2013.

[173] Usman A Khan, Soummya Kar, Ali Jadbabaie, and José MF Moura. On connectivity, observability, and stability in distributed estimation. In *49th IEEE Conference on Decision and Control (CDC)*, pages 6639–6644. IEEE, 2010.

[174] Álvaro Rodríguez del Nozal, Pablo Millán, Luis Orihuela, Alexandre Seuret, and Luca Zaccarian. Distributed estimation based on multi-hop subspace decomposition. *Automatica*, 99:213–220, 2019.

[175] Haik Silm, Rosane Ushirobira, Denis Efimov, Wim Michiels, and Jean-Pierre Richard. Design of a distributed finite-time observer using observability decompositions. In *2019 18th European Control Conference (ECC)*, pages 1816–1821. IEEE, 2019.

[176] W. Perruquetti, T. Floquet, and E. Moulay. Finite-time observers: Application to secure communication. *IEEE Transactions on Automatic Control*, 53(1):356–360, 2008.

[177] Haik Silm, Rosane Ushirobira, Denis Efimov, Emilia Fridman, Jean-Pierre Richard, and Wim Michiels. Distributed observers with time-varying delays. *IEEE Transactions on Automatic Control*, pages 1–1, 2020.

[178] Gilberto Pin, Andrea Assalone, Marco Lovera, and Thomas Parisini. Non-asymptotic kernel-based parametric estimation of continuous-time linear systems. *IEEE Transactions on Automatic Control*, 61(2):360–373, 2016.

[179] Jan C Willems and Jan W Polderman. *Introduction to mathematical systems theory: a behavioral approach*, volume 26. Springer Science & Business Media, 1998.

[180] Peng Li, Francesca Boem, Gilberto Pin, and Thomas Parisini. Kernel-based simultaneous parameter-state estimation for continuous-time systems. *IEEE Transactions on Automatic Control*, 65(7):3053–3059, 2020.

[181] Roger A Horn and Charles R Johnson. *Matrix analysis*. Cambridge university press, 2012.

[182] Béla Bollobás. *Modern graph theory*, volume 184. Springer Science & Business Media, 2013.

[183] Alexandre Kruszewski, Wenjuan-J Jiang, Emilia Fridman, Jean Pierre Richard, and Armand Toguyeni. A switched system approach to exponential stabilization through communication network. *IEEE Transactions on Control Systems Technology*, 20(4):887–900, 2012.